Fabrication of Vanadium Dioxide Thin Films and their Structural, Optical and Electrical Characterization for Optoelectronic Applications

A Thesis Submitted to the

College of Graduate and Postdoctoral Studies

In Partial Fulfillment of the Requirements

for the Degree of

Doctor of Philosophy

In the Department of Electrical and Computer Engineering

University of Saskatchewan

Saskatoon

by

OZAN GUNES

© Copyright Ozan Gunes, February, 2023.

Unless otherwise noted, the copyright of the material in this thesis belongs to the author.

Permission to Use

In presenting this dissertation in partial fulfillment of the requirements for a Postgraduate degree from the University of Saskatchewan, I agree that the Libraries of this University may make it freely available for inspection. I further agree that permission for copying of this dissertation in any manner, in whole or in part, for scholarly purposes may be granted by the professor or professors who supervised my dissertation work or, in their absence, by the Head of the Department or the Dean of the College in which my dissertation work was done. It is understood that any copying or publication or use of this dissertation or parts thereof for financial gain shall not be allowed without my written permission. It is also understood that due recognition shall be given to me and to the University of Saskatchewan in any scholarly use which may be made of any material in my dissertation.

Requests for permission to copy or to make other uses of materials in this dissertation in whole or part should be addressed to:

Head of the Department of Electrical and Computer Engineering
57 Campus Drive
University of Saskatchewan
Saskatoon, Saskatchewan, Canada
S7N 5A9

OR

Dean
College of Graduate and Postdoctoral Studies
University of Saskatchewan
116 Thorvaldson Building, 110 Science Place
Saskatoon, Saskatchewan, Canada
S7N 5C9

Abstract

Vanadium dioxide (VO_2) is a transition metal oxide that is well known for its metal-to-insulator phase transition (MIT). One of the most common forms of VO_2 that has been generally studied is the thin film form. VO_2 thin films are considered a strong candidate in various new-generation optical, electronic, and optoelectronic (photonic) applications. From the technology perspective, the fabrication of single-crystal VO_2 thin films appears to be challenging. Up to now, research on the preparation of VO_2 thin films has focused on employing different material fabrication techniques to produce high-quality VO_2 thin films. The stoichiometry and quality of VO_2 thin films strongly depend on the fabrication process. There is still a need to study the production of near-single-crystal, high-quality VO_2 thin films and their structural, optical and electrical characterization. Secondly, the metal-to-insulator phase transition phenomenon in VO_2 is a topical research field. The percolation theory has introduced some rigor in explaining the phase transition. This dissertation focuses on two aspects of research on VO_2 thin films. The first aspect focuses on studying the effect of specific deposition parameters such as substrate biasing and substrate temperature on the quality of VO_2 thin films. Also, the synthesis of high-quality VO_2 thin films prepared on single-crystal silicon, quartz and sapphire substrates is investigated. The films are examined using various analysis techniques including Raman spectroscopy, scanning electron microscopy (SEM), x-ray diffraction (XRD), x-ray photoelectron spectroscopy (XPS), transmission electron microscopy (TEM) and energy-dispersive x-ray spectroscopy (EDS). The optical constants, namely the refractive index (n) and the extinction coefficient (K), and the optical bandgap (E_g) of the films are extracted using the Swanepoel and Manifacier techniques. The second aspect of this dissertation covers the application of percolation theory on the phase transition in VO_2 thin films. Accordingly, the topology of conducting clusters during the IMT and MIT is investigated by means of optical and electrical switching in a high-quality VO_2 thin film. Additionally, self-heating-induced electrical and optical switching in VO_2 thin films prepared on sapphire substrates under constant applied current pulses has been studied. The difference in the two switching dynamics is explained by a simple model based on the percolation theory.

Acknowledgements

I would like to begin by expressing my deepest gratitude to Dr. Safa O. Kasap, who has given me the opportunity to pursue a Ph.D. degree under his supervision. I thank him for his guidance and patience, and for being a role model as a distinguished scientist. Secondly, I would like to sincerely thank Dr. Chunzi Zhang, whom I had the opportunity to work with during my Ph.D., for helping me with thin film depositions and carrying out experiments. I would like to acknowledge Dr. Qiaoqin Yang for granting me access to the SPT-320 magnetron sputter deposition system to prepare my samples. I would like to thank Dr. Robert E. Johanson for the training on the RF magnetron sputtering system. I would like to express my appreciation to Dr. Cyril Koughia for his supervision and assistance with the experimental methodology and analysis as well as for the intellectual discussions. I would like to extend my gratitude to Dr. George Belev, for the most valuable assistance on the technical issues and for the discussions about the philosophical side of research. Furthermore, I am profoundly thankful to Dr. Shi-Jie Wen at Cisco Systems, San Jose, California, for his collaboration and financial support to conduct research on vanadium dioxide. I would also like to thank Dr. Rick Wong, for the stimulating discussions on our projects. In addition, I am truly grateful to all my peers and friends that I have met in Saskatoon during my life as a graduate student. They have given me the most memorable moments of my early adulthood.

I would like to acknowledge Cisco Systems and Natural Sciences and Engineering Research Council of Canada (NSERC) for funding my Ph.D. work. Also, I would like to acknowledge the University of Saskatchewan which has been my home for the eight years of my graduate studies.

Finally, I would like to thank my mother Hatice, my father Mehmet, and my sister Derya, who have always supported me throughout the years, even during the most uncertain and desperate times of the Covid-19 lockdown.

Table of Contents

Permission to Use ... i

Abstract ... ii

Acknowledgements ... iii

Table of Contents ... iv

List of Figures ... ix

List of Tables ... xxiii

List of Abbreviations ... xxv

1. Introduction ... 1

  1.1 Introduction ... 1

  1.2 VO_2 as a Transition Metal Oxide ... 2

    1.2.1 Introduction ... 2

    1.2.2 The Phase Transition Phenomenon in VO_2 ... 5

    1.2.3 Phases of VO_2 ... 9

    1.2.4 Percolation Theory ... 10

    1.2.5 Manipulation of Phase Transition Properties of VO_2 ... 12

    1.2.6 Forms of VO_2 ... 13

  1.3 Applications of VO_2 Thin Films ... 17

    1.3.1 VO_2 Films in Smart Windows ... 17

    1.3.2 VO_2 Films in Optical Switches ... 19

    1.3.3 VO_2 Films in Mott-Field Effect Transistors ... 21

    1.3.4 VO_2 Films in Threshold Switches ... 22

    1.3.5 VO_2 Films in Neuromorphic Devices ... 23

  1.4 Fabrication of VO_2 Thin Films by DC Magnetron Sputtering ... 25

  1.5 Motivation of Research ... 27

  1.6 Objective of Research and the Thesis ... 27

  1.7 References ... 30

2. Experimental Procedures ... 44

  2.1 Introduction ... 44

2.2 Magnetron Sputtering and Fabrication of VO_2 Thin Films 44
2.2.1 Magnetron Sputtering Technique 44
2.2.2 SPT-320 Magnetron Sputtering System 49
2.2.3 Fabrication of VO_2 Thin Films 52
2.3 Optical and Electro-Optical Characterization of VO_2 Thin Films 53
2.3.1 Optical Characterization of VO_2 Films 53
2.3.2 Electro-Optical Characterization of VO_2 Films 54
2.4 Structural Characterization of VO_2 Thin Films 55
2.4.1 Introduction 55
2.4.2 Raman Spectroscopy 55
2.4.3 Scanning Electron Microscopy (SEM) 57
2.4.4 X-ray Diffraction (XRD) 59
2.4.5 Transmission Electron Microscopy (TEM) 61
2.4.6 Electron Diffraction Spectroscopy (EDS) 62
2.4.7 Selected Area Electron Diffraction (SAED) 62
2.4.8 X-ray Photoelectron Spectroscopy (XPS) 63
2.5 References 65
3. Optical Transmittance of Thin Films and the Extraction of Optical Properties 68
3.1 Introduction 68
3.2 Light Transmission in Thin Films 68
3.3 Optical Constants of Semi-Transparent Media 76
3.3.1 Introduction 76
3.3.2 The Complex Refractive Index 76
3.3.3 The Attenuation Coefficient of a Medium 78
3.3.4 The Optical Band Gap 82
3.4 Calculation of Optical Constants-Analysis Techniques 85
3.4.1 The Swanepoel Technique 85
3.4.2 The Manifacier Technique 100
3.5 Summary 101
3.6 References 102

4. The Effect of Substrate Biasing During DC Magnetron Sputtering on the Quality of VO_2 Thin Films and their Insulator-Metal Transition Behavior ... 104
4.1 Abstract ... 104
4.2 Introduction ... 104
4.3 Materials and Methods ... 105
4.4 Results ... 106
4.4.1 Microstructure Characterization by Raman ... 106
4.4.2 Surface Morphology Characterization by SEM ... 108
4.4.3 Chemical States Characterization by XPS ... 109
4.4.4 Optical Measurements ... 110
4.5 Discussion ... 117
4.6 Conclusions ... 122
4.7 References ... 124
5. Effect of Substrate Temperature on the Structural, Optical and Electrical Properties of DC Magnetron Sputtered VO_2 Thin Films ... 128
5.1 Abstract ... 128
5.2 Introduction ... 128
5.3 Materials and Methods ... 130
5.4 Results ... 131
5.4.1 Microstructural Characterization by Raman Spectroscopy and XRD ... 131
5.4.2 Surface Morphology and Roughness Characterization by SEM and Profilometry 133
5.4.3 Optical Characterization by Spectrophotometry ... 138
5.4.4 Electrical MIT Characterization ... 148
5.5 Discussion ... 150
5.6 Conclusion ... 156
5.7 References ... 157
6. Synthesis, Structure and Optical Properties of High-Quality VO_2 Thin Films Grown on Silicon, Quartz and Sapphire Substrates by High Temperature Magnetron Sputtering: Properties Through the Transition Temperature ... 163
6.1 Abstract ... 163
6.2 Introduction ... 164
6.3 Experimental Procedure ... 166

6.4 Results and Discussion 167
6.4.1 Microstructure Characterization by Raman 167
6.4.2 Surface Morphology Characterization by SEM 170
6.4.3 Chemical State Characterization by XPS 171
6.4.4 Optical Properties Through Insulator-Metal-Insulator Transition 172
6.4.5 Optical Constants *n*, *K* and Bandgap 177
6.4.6 Interface Characterization by XRD, EDS, and HRTEM 181
6.4.7 Mapping of Phase Transition of VO_2 by Raman Spectroscopy 185
6.5 Conclusions 188
6.6 References 189
7. Topology of Conductive Clusters in Sputtered High-Quality VO_2 Thin Films on the Brink of Percolation Threshold During Insulator-to-Metal and Metal-to-Insulator Transitions 195
7.1 Abstract 195
7.2 Introduction 195
7.3 Experimental Procedure 197
7.4 Physical Model and Discussion 204
7.4.1 Metallic Content 204
7.4.2 Conductivity of VO_2 and Effective Medium Approximation 204
7.4.3 Conductivity in VO_2 and Percolation Theory 207
7.4.4 Percolation Threshold in Metal-to-Insulator Transition 210
7.4.5 Difference in the Topology of the ICCs in IMT and MIT of VO_2 216
7.5 Conclusions 219
7.6 References 221
8. Self-Heating-Induced Electrical and Optical Switching in High-Quality VO_2 Films Controlled with Current Pulses 229
8.1 Abstract 229
8.2 Introduction 230
8.3 Experimental Procedure 230
8.4 Results 233
8.5 Discussion 244
8.6 Summary 247

8.7 References 248
9. Conclusions and Future Work 252
9.1 Conclusions 252
9.1.1 Fabrication of VO_2 Thin Films Under Different Deposition Conditions 252
9.1.2 Investigation of Phase Transition in VO_2 Thin Films 254
9.2 Future Works 255
9.2.1 Elemental Doping in VO_2 Thin Films 255
9.2.2 Excess Noise in VO_2 Thin Films 256
9.2.3 VO_2 Thin Film-Based Diffraction Gratings 256
9.2.4 Multilayered VO_2 Thin Film Structures 257
9.3 References 258
Appendix A 259
Appendix B 273

List of Figures

Figure 1.1 (a) The metal-to-insulator phase transition temperature (T_{MIT}) distribution of selected transition metal oxides. (b) Various application fields of transition metal oxides with fast transition capability. Diagrams partially adapted from Yang et al. [14]. 3

Figure 1.2 Oxidation states of vanadium (V). The V-oxides indicated in blue refer to the Magnéli series, V_nO_{2n+1}. The ones indicated in green refer to the Wadsley series, V_nO_{2n-1}. After Bahlawane and Lenoble [15]. 4

Figure 1.3 Crystal structure of monoclinic insulator and rutile metallic phases VO_2. After Wegkamp and Stähler [25]. 6

Figure 1.4 (a) A sketch of the resistivity of VO_2 (or any transition metal oxide) which undergoes insulator-to-metal (IM) and metal-to-insulator (MI) phase transitions. (b) A circular diagram that represents triggering of phase transition in Mott insulators. In the figure, the inner circle shows the coupling of the different degrees of freedom. The middle ring presents various ways of triggering the phase transitions in VO_2. The outer ring shows the physical properties that can be changed during phase transitions. (a) and (b) are partially extracted from Zhou and Ramanathan [46]. 8

Figure 1.5 (a) A unit cell of VO_2 with oxygen octahedra and tilted vanadium sublattices. (b) Position of V atoms at monoclinic 1 (M_1, blue), monoclinic 2 (M_2, gray and blue), where the arrows indicate the intermediate triclinic (T') phase. (c) Shifting of critical Raman peak (ω_o) with respect to tensile strain at temperatures 293 K, 303 K and 313 K and the transition from M_1 to M_2 phase. (d) Relative strain versus temperature phase diagram of the VO_2 represented via the phonon frequency shift (ω_o) (red data). After Atkin et al. [47]. 10

Figure 1.6 Site percolation on a square lattice: The small circles represent the occupied sites for three different concentrations: $p = 0.2$, 0.59, and 0.80. Nearest-neighbor cluster sites are connected by lines representing the bonds. Filled circles represent finite clusters, while open circles mark the large infinite clusters. After Bunde and Kantelhardt [54]. 11

Figure 1.7 (a) VO_2 microrods, after Zhang et al. [99], (b) VO_2 nanorods, after Zhang et al. [100] (c) VO_2 nanowires, after Bae et al. [101]. (d) VO_2 nanoplates, after Liang et al. [102] (e) VO_2 nanobelts, after Sediri and Gharbi [103]. (f) VO_2 nanoribbons, after Sreekanth et al. [104]. 14

Figure 1.8 (a) VO_2 nanoparticle-based thermochromic smart window. After Granqvist [128] (b) Transmission of light through photochromic or thermochromic laminate. After Wang

et al. [122] (c) Schematic of an electrochromic smart window. After Pehlivan et al. [129] (d) Transmission of light through an electrochromic laminate. After Wang et al. [122]....... 19

Figure 1.9 (a) A Si/VO_2hybrid electro-optical modulator on top of 2 μm-thick SiO_2 thermally grown on a Si substrate. After Joushaghani et al. [118]. (b) An optical switch based on a VO_2 film grown on a Si_3N_4 waveguide on top of a SiO_2 substrate. A control beam is used to regulate the transmission of the incoming signal beam. After Wong et al. [140], in Ref. [141]....... 20

Figure 1.10 (a) A schematic of all-optical tunable coding metasurfaces based on Al–VO_2 hybrid resonators for modulation of linearly polarized terahertz waves. (b) Schematic of all-optical tunable coding metasurfaces based on Al−VO_2 hybrid resonators for modulation of circularly polarized terahertz waves. After Li et al. [142]....... 21

Figure 1.11 (a) Two-terminal and three-terminal configurations of Mott FET devices proposed by Kim et al. [143]. (b) A three-terminal Mott FET proposed by Ruzmetov et al. [148]. (c) VO_2 FETs with high-k oxide/organic parylene-C hybrid gate dielectric. After Wei et al. [149]. (d) Optical microscope (left) and atomic force microscope (right) images of a VO_2 nanobeam-based Mott FET with HfO_2 as the gate oxide material. After Sengupta et al. [147]....... 22

Figure 1.12 (a) A proposed InGaAs quantum well (QW) FinFET with VO_2 films as a reversible switch. After Shukla et al. [150]. (b) A proposed GaN phase-transition FET with ultralow off-state leakage. After Verma et al. [151]....... 23

Figure 1.13 (a) A membrane of the biological neuron and its electronic circuit representation. Under stimulation, the trans-membrane potential (V_M) and membrane conductance (G_M) oscillates. (b) A lateral VO_2 device and a capacitor are used as an artificial neuron circuit. After Lin et al. [152]....... 25

Figure 2.1 (a) Energy transfer from incident ions to sputtered atoms. (b) A planar magnetron in a sputtering system. $d\Omega_{sek}$ represents the solid angle and E_{sek} is the energy of secondary particles created from the collisions of the incident ions on the surface of the material. Here, R represents the sputtering radius, W is the width of the magnetic field ring and r_{CE} is the height of the ring. After Frey [7]....... 47

Figure 2.2 Sputter yield (Y) of different materials as a function of Ar ion energies. After Matsunami et al. [9]....... 48

Figure 2.3 An illustration of a magnetron sputtering event. Partially extracted from Shaat [10]. 49

Figure 2.4 A view of the Plasmionique SPT-320 Magnetron sputter deposition system. (b) Inside view of the sputter chamber. The substrate cradle is positioned on the substrate holder. The loading process is commanded from the software control window. The fork is moved back to the load-lock chamber after the substrate plate is loaded. Taken from Plasmionique Inc. [11]. 51

Figure 2.5 Sputtering process control window. Desired magnetron is enabled through an "enable" button. Substrate temperature, position, rotation speed, chamber pressure can be adjusted. A stopwatch is used to set up a time to monitor the period of deposition. Taken from Plasmionique Inc. [11]. 52

Figure 2.6 Perkin Elmer Lambda 900 UV-Vis-NIR spectrophotometer. 54

Figure 2.7 Renishaw Invia Reflex Raman Microscope as used in the Saskatchewan Structural Sciences Centre, Vibrational Spectroscopy Laboratory [17] 57

Figure 2.8 (a) A schematic diagram of an SEM. Taken from Nanoimages [20]. (b) A Hitachi SU8010 FE SEM, University of Saskatchewan, Western College of Veterinary Medicine [21]. 59

Figure 2.9 Diffraction of x-rays incident in a crystalline material. The interference of the x-rays reflected from adjacent atomic planes construct a diffracted beam at certain angles. Interatomic separation can be determined using Bragg's law. After Kasap [22]. 60

Figure 2.10 (a) A schematic diagram of an XRD in operation [24]. (b) A Rigaku Ultima IV XRD [23]. 61

Figure 2.11 FEI Talos F200X G2 used for HRTEM, EDS and SAED imaging. Taken from Thermofisher Scientific [25] 62

Figure 2.12 (a) Representation of the emission of electrons from various orbitals due to the interaction with incoming light at a certain energy. Depending on the energy of the incoming light the technique is categorized as ultra-violet spectroscopy (UPS), x-ray photo spectroscopy (XPS) and Auger electron spectroscopy (AES). After Hollas [26]. 63

Figure 2.13 (a) A schematic of a typical XPS. (b) SXRMB high-energy XPS at the Canadian Light Source used for XPS measurements [27]. 64

Figure 3.1 Light as an electromagnetic wave propagating at an instant in a homogeneous and isotropic medium with a velocity v. After Kasap [1]. 69

Figure 3.2 Reflection and transmission of light as a sum of reflected and transmitted beams within and throughout the thin film and substrate. After S. O. Kasap lecture notes [2]. 70

Figure 3.3 (a) Direct band-to-band transition of electron. E_c, E_v, and E_g is the conduction energy, valance energy and energy band gap, respectively. (b) Indirect band-to-band transition with additional energy absorption by phonon through lattice vibration. After Mistrik et al. [5]. 82

Figure 3.4 (a) Tauc's plot of an amorphous semiconductor which the energy region where the absorption edge is taken into consideration. Region A ($\alpha \geq 10^4$ cm^{-1}) is the fundamental absorption edge. Region B is the Urbach edge, (exponential change in α occurs). Region C represents the weak absorption (Urbach) tail. (b) The absorption edge of a-Se at various temperatures between −200 °C and 400 °C. After Tauc [6] in Ref. [8]. 83

Figure 3.5 Bandgap estimation (a) of single-crystal GaAs, a direct semiconductor, from $(\alpha h\nu)^2$ vs. $h\nu$ (b) Si a well-known indirect semiconductor from $(\alpha h\nu)^{1/2}$ vs. $h\nu$. (a) and (b) are partial extraction from Mistrik et al. [5]. 84

Figure 3.6 Swanepoel technique flow chart for calculating the attenuation coefficient and the optical bandgap. 88

Figure 3.7 Schematic sketch of the typical behavior of light passing through a thin film with uniform thickness on a thick substrate. On the left, the oblique incidence is shown to demonstrate the multiple reflections. In most measurements, the incident beam is nearly normal to the film as shown on the right. After Ref. [8]. 90

Figure 3.8 The construction of envelopes around the transmission spectrum of a uniform a-Se thin film of 0.9687μm. The extreme points, the maximum transmittance (T_M) and minimum transmittance (T_m) values are indicated with blue and gray dots, respectively. The spectrum consists of strong absorption ($\lambda < 600$ nm), absorption (600 nm $< \lambda <$ 1610 nm) and transparent regions (1610 nm $< \lambda <$ 2500 nm). After Ref. [8]. 91

Figure 3.9 The flow chart of the Swanepoel technique applied for a thin film with uniform thickness 94

Figure 3.10 Schematic sketch of the typical behavior of light passing through a thin film with a non-uniform thickness on a thick substrate. In most measurements, the incident beam is almost normal to the film. After Ref. [8]. 95

Figure 3.11 A regenerated transmission spectrum of a sample with an average thickness of 1 μm average thickness (d_{avg}) of 30 nm, and a refractive index fitted to a Cauchy equation. After Ref. [8]........ 98

Figure 3.12 The flow chart of Swanepoel technique applied for a thin film with non-uniform thickness........ 99

Figure 4.1 Raman spectra of the as-deposited VO_2 thin films with substrate biasing: (a) 89 V; (b) 126 V; (c) 146 V; (d) 173 V. 107

Figure 4.2 SEM images of VO_2 thin films deposited on Si substrates for 2 h with bias voltage of: (a) 89 V; (b) 126 V; (c) 146 V; (d) 173 V; (e) no bias on a sample prepared as in [23]. 109

Figure 4.3 XPS spectra of the as-deposited VO_2 thin films with substrate biasing. 110

Figure 4.4 Optical transmittance of the as-deposited VO_2 thin films with a substrate bias voltage of: (a) 89 V; (b) 126 V; (c) 146 V; (d) 173 V; (e) bare Si substrate; (f) no bias (data extracted from Ref. [23] and replotted). 112

Figure 4.5 Optical transmittance of VO_2 thin films deposited under different bias voltages at (a) 300 K and (b) 368 K. 113

Figure 4.6 Optical transmittance at a wavelength of 2000 nm in the insulator and semiconductor phases (300 and 368 K, respectively) and contrast $\Delta\tilde{T}$ vs. thickness on a semilogarithmic plot. The dashed lines are exponential fits. The attenuation coefficient of the metal phase $\alpha \approx 3.1 \times 10^7$ m^{-1}. 113

Figure 4.7 Optical transmittance of the as-deposited VO_2 thin films under heating (red) and cooling (black): (a) 89 V; (b) 126 V; (c) 146 V; (d) 173 V; (e) no bias (data extracted from Ref. [23] and replotted). 115

Figure 4.8 Optical transmittance of the as-deposited VO_2 thin films with biasing: (a) under heating and (b) under cooling. 116

Figure 4.9 (a) X-ray diffraction patterns and (b) Raman spectra of VO_2 thin films (red) and VO_2 thin films deposited with 173 V bias (black). 117

Figure 4.10 The transmittance vs. wavelength for the 102 nm VO_2 thin film with various contributions. The orange curve is the Swanepoel transmittance with no attenuation. Other colored curves are selected fits to the data as follows: blue: E_g = 0.70 eV, A_a =

0.0070 nm^{-1}·eV^{-1}, p = 2.6, A_s = 5.9 × 10^5 nm$^{1.6}$; magenta: E_g = 0.60 eV, A_a = 0.0048 nm^{-1}·eV^{-1}, p = 2.4, A_s = 1.3 × 10^5 nm$^{1.4}$; green: E_g = 0.55 eV, A_a = 0.0038 nm^{-1}·eV^{-1}, p = 2.4, A_s = 1.30 × 10^5 nm$^{1.4}$; black: E_g = 0.50 eV, A_a = 0.0035 nm^{-1}·eV^{-1}, p = 2.4, A_s = 1.25 × 10^5 nm$^{1.4}$. 121

Figure 5.1 Raman spectra of VO_2 and V_2O_5 thin films prepared at various substrate temperatures (T_S) on (a) Si and (b) sapphire substrates. Note that the vertical axes are in arbitrary units (a.u.), so the relative magnitudes of the spectra cannot be compared. 132

Figure 5.2 XRD spectra of VO_2 and V_2O_5 thin films prepared at various substrate temperatures (T_S) on (a) Si and (b) sapphire substrates. Note that the vertical axes are in arbitrary units (a.u.). 133

Figure 5.3 Surface images of VO_2 and V_2O_5 thin films prepared at various substrate temperatures (T_S) (a) 350 °C, (b) 400 °C, (c) 450 °C, (d) 500 °C, (e) 550 °C, and (f) 600 °C obtained by SEM. 136

Figure 5.4 Surface profile images of VO_2 thin films deposited on Si and sapphire substrates at (a) 500 °C, (b) 550 °C, (c) 600 °C and (d) 650 °C [17]. The roughness of the surface is indicated by color mapping, where the maximum (peak), median and minimum (depth) points on the surface are indicated in red, green and blue, respectively. The scale bars are used as a measure of the peaks and depths on the surface of the films. 136

Figure 5.5 Average grain size (GS_{avg}) of VO_2 thin films prepared on (a) Si and (b) sapphire substrates. In (b) the dashed vertical line is an asymptote that indicates the near-epitaxial almost flat surface of the film prepared at 650 °C [17]. (c,d) present the average (R_a) and root-mean-square (R_q) roughness of films prepared on Si and sapphire substrates, respectively. The dashed lines between the data points are guides to the eye. The data points shown in hollow symbols belong to the films pre-pared at 650 °C (prepared as described in Ref. [17] but not reported therein). 137

Figure 5.6 Optical transmittance ($\tilde{T}$) spectra of VO_2 thin films deposited at (a) 500 °C, (b) 550 °C, and (c) 600 °C and (d) 650 °C [17] on Si and sapphire substrates at 300 K (insulating phase) and 368 K (metallic phase). 140

Figure 5.7 (a) Temperature dependence (T) of optical transmittance ($\tilde{T}$) obtained at a light wavelength of λ = 2500 nm for VO_2 thin films deposited at 500, 550, 600 and 650 °C [17]. The phase transition characteristics for heating and cooling cycles for films prepared at (b) 500 °C, (c) 550 °C, (d) 600 °C, and (e) 650 °C [17] on Si and sapphire substrates at 300 K (insulating phase) and 368 K (metallic phase). 145

Figure 5.8 (a) Critical temperatures (T_{IMT}, T_{MIT} and T_t) of the VO_2 films on Si and sapphire prepared at various substrate temperatures (T_S) obtained at a light wavelength of λ = 2500 nm. (b) Hysteresis (ΔH) and sharpness (FWHM) of the Gaussian curves obtained from $d\tilde{T} / dT$ vs. T plots in Figure 5.7. In (a) and (b) the data points for films prepared at 650 °C [17] are shown in hollow symbols. (c) Comparison of optical transmittance contrast, $\Delta\tilde{T} = \tilde{T}(300\text{ K}) - \tilde{T}(368\text{ K})$, obtained at NIR wavelengths λ = 1500 nm, 2000 nm and 2500 nm for films prepared at T_S = 500 (olive), 550 (orange), 600 (navy) and 650 [17] (magenta) °C. 146

Figure 5.9 (a) Luminous transmittance ($\tilde{T}_{lum}$) at 300 K and 368 K and luminous modulation efficiency ($\Delta\tilde{T}_{lum}$) obtained for films deposited at various substrates temperatures (T_S). (b) Solar transmittance ($\tilde{T}_{sol}$) at 300 K and 368 K and solar modulation efficiency ($\Delta\tilde{T}_{sol}$) obtained for films deposited at various substrates temperatures (T_S). Data for the substrate temperature (T_S) of 650 °C [17] are presented in hollow symbols. 147

Figure 5.10 Temperature (T) dependence of electrical conductivity (σ) of VO_2 films prepared at various substrate temperatures (T_S). (a) Comparison of T dependence of σ of films prepared at T_S = 500 °C, 550 °C, 600 °C, and 650 °C [32]. The phase transition characteristics for heating and cooling cycles for films prepared at T_S = (b) 500 °C, (c) 550 °C, (d) 600 °C and (e) 650 °C [32]. 149

Figure 5.11 Electrical conductivity phase transition properties of VO_2 films prepared on sapphire substrates at various substrate temperatures (T_S). (a) Critical temperatures of the phase transition (T_{IMT}, T_{MIT} and T_t). (b) Phase transition parameters (ΔH, FWHM (IMT), and FWHM (MIT)) and the contrast of conductivity, $\Delta\sigma = \sigma(368\text{ K}) / \sigma(300\text{ K})$. The data points for the substrate temperature 650 °C are from Ref. [32] and displayed in hollow symbols. 150

Figure 5.12 Arrhenius plot of conductivity (σ) data obtained from VO_2 films in their insulating phases. Data set for VO_2 film prepared at 650 °C is extracted from the σ vs. T plot in Ref. [32]. 153

Figure 5.13 X-ray diffraction of (011) planes of VO_2 thin films deposited at T_S = 500, 550, and 600 °C on (a) Si and (b) sapphire substrates. 154

Figure 5.14 Comparison of VO_2 thin films deposited at various temperatures studied in different works. (a) Comparison of T_t obtained from optical (O-) switching measurements. (b) Hysteresis width (ΔH) of the films that are obtained from the temperature (T) dependence of optical transmittance ($\tilde{T}$). (c) Comparison of phase transition

temperature (T_t) obtained from electrical (E-) switching. (d) Hysteresis width (ΔH) of the films that are obtained from the T-dependence of electrical conductivity or resistance. Note that Kana et al. (2010) is [30]; Kang et al. (2019) is [57]; Koughia et al. (2020) is [32]; Lee et al. (2020) is [28]; Melnik et al. (2012) is [26]; Sato et al. (2012) is [21]; Zhang et al. (2015) is [36]; Zhang et al. (2020) is [17]. 155

Figure 6.1 Raman spectra of the as-deposited VO_2 thin films on Si, quartz and sapphire substrates with sputtering power of (a) 90 W, (b) 95 W, (c) 100 W. 170

Figure 6.2 SEM images of VO_2 thin films deposited on (a) Si, (b) quartz, and (c) sapphire. 171

Figure 6.3 XPS spectra of the as-deposited VO_2 thin films on Si (red), quartz (blue), and sapphire (black). (For interpretation of the references to color in this figure legend, the reader is referred to the Web version of this article.) 172

Figure 6.4 Optical transmittance of the as-deposited VO_2 thin films on (a) Si, (b) quartz, (c) sapphire, (d) optical transmittance of substrates. 174

Figure 6.5 Optical transmittance of the as-deposited VO_2 thin films on Si, quartz and sapphire at (a) 300 K, (b) 368 K. 175

Figure 6.6 Optical transmittance of the as-deposited VO_2 thin films on (a) Si, (b) quartz, and (c) sapphire at a wavelength of 2500 nm, (d) on sapphire at a wavelength of 1500 nm under heating (red) and cooling (black), (e) optical transmittance hysteresis of the VO_2 thin film on sapphire compared with reproduced results from published works [19,27,34] (Optical transmittance hysteresis of this work, [19] and [34] were taken at wavelength of 2500 nm, [27] was taken at 2000 nm.) 176

Figure 6.7 Comparison of model predictions with experimental data collected for VO_2 films of varying thicknesses on different substrates in the semiconducting (300 K) and metallic (368 K) phases. The inset to Figure 6.7 (a) shows the schematic of measurements. The film with thickness d has complex refractive index $n^*(\lambda) = n(\lambda) + jK(\lambda)$ where λ is the wavelength light and the absorption in the substrate is negligible ($\alpha_S(\lambda) = 0$). The reader should not be confused by the "noise" around 1380 nm, 1870 nm and 2700 nm, which is an artifact appearing most likely from IR absorption of water vapor. 178

Figure 6.8 Real (n) and imaginary (K) parts of complex refractive index n^* of VO_2 measured in the semiconducting phase (at 300 K) and metallic phase at (368 K). The plots compare present data with previously data extracted from Refs. [55,58]. 179

Figure 6.9 (a) Comparison of optical absorption coefficients of VO_2 films measured in semiconducting (300 K) and metallic (368 K) phases. (b) The corresponding plots for indirect ($\alpha(h\nu)^{1/2}$) and direct ($\alpha(h\nu)^2$) optical band gaps for semiconducting state. One indirect optical bandgap at ~ 0.52 eV and one direct bandgap at ~ 2.6 eV is observed. Straight lines are guides to the eye to illustrate the direct and indirect theoretical predictions. 180

Figure 6.10 X-ray diffraction pattern of VO_2 thin film on sapphire. 183

Figure 6.11 EDS (a) mapping and (b) depth profile of VO_2 thin film on sapphire substrate. 184

Figure 6.12 (a) HRTEM and (b) SAED patterns of VO_2 thin film on sapphire substrate. 185

Figure 6.13 Raman spectra in the region of the peaks at around (a) 600 cm^{-1} and (b) 220 cm^{-1} at different temperatures under heating (marked "h" in the legend) and cooling (marked "c" in legend). The data collected over a square area of 25 × 25 pixels. The size of every pixel is 1.2 μm × 1.2 μm. 186

Figure 6.14 Temperature dependences of optical transmittance (a) and integral Raman intensities of peaks at around 600 cm^{-1} (b) and 220 cm^{-1} (c). Heating curves are in blue. Cooling curves are in red. Integral Raman intensities are found by the integration of Raman signal (as shown in Figure 6.13) from 525 to 750 cm^{-1} and from 210 to 245 cm^{-1} at corresponding temperatures, respectively. Dashed lines in (b) and (c) are guides to eye. 187

Figure 6.15 Maps of VO_2 conversion from the semiconducting to metallic phase under heating (upper row) and under cooling (lower row) derived from Raman scattering as explained in Appendix B. The temperature increases from left to right (upper row) and decreases from right to left (lower row). The values of temperature are shown inside of the large image squares (bottom right corner). The size of every big square is 25 × 25 pixels. The size of every pixel is 1.2 mm × 1.2 mm. Blue color marks the pixels showing semiconducting properties. Red color marks the pixels with metallic properties. Pink and greyish colors mark mixed metal/semiconductor pixels with the dominance of metal or semiconductor, respectively. See Appendix B for the criteria used to identify the phase composition of the imaged VO_2 region. (For interpretation of the references to color in this figure legend, the reader is referred to the Web version of this article.) 187

Figure 7.1 (a) Simplified schematic diagram of the experimental setup used for simultaneous measurements of electrical conductivity (σ) and optical transmittance ($\tilde{T}$). Operational wavelength of the laser diode is 1550 nm. (b) A schematic geometry of the sample used in our experiments. The black masks limit the passage of light. Au contacts are sufficiently thick (~54 nm) to be optically non-transparent. The red spot shows the illumination region. 199

Figure 7.2 Experimental results of (a) conductivity and (b) optical transmittance as a function of temperature during heating (red curves) and cooling (blue curve). Magenta dotted curve is the best fit approximation to the conductivity of VO_2 in the insulating (semiconducting) state by the equation $(2.0 \times 10^6\ \Omega^{-1}\ \text{cm}^{-1})\exp[-(0.3\ \text{eV})/k_BT]$. The horizontal cyan dotted curve is the approximation for the relatively temperature independent conductivity of VO_2 in the metallic state. 200

Figure 7.3 (a) Dependence of conductivity (σ) on the partial concentration of metal (X_m) in a VO_2 film under heating (red symbols) and cooling (blue symbols). Estimations of conductivity using the effective medium approximations (EMAs). The curves 1, 2, and 3 are obtained using Equations (7.3), (7.4), and (7.6), respectively. (b) The derivatives of conductivity vs. metallic phase content for heating (red) and cooling (blue). Symbols are the results of numerical differentiation. The curves are guides to the eye. The maxima indicate the percolation thresholds (X_c) of heating and cooling scans (a.u. represents arbitrary units with the maximum set to 100). 201

Figure 7.4 Normalized derivatives of conductivity (σ) in (a) and transmittance ($\tilde{T}$) in (b) as a function of temperature (T) during heating (red) and cooling (blue). Vertical lines mark the positions of maxima in the optical transmittance related curves in (b) (a.u. represents arbitrary units). 202

Figure 7.5 Dependence of conductivity vs. partial content of metallic phase (X_m) under heating (red symbols) and cooling (blue symbols) scans. The crosses mark the critical concentrations corresponding to the appearance (upon heating) and disappearance (upon cooling) of the infinite conductive cluster. Magenta and navy curves show the approximation functions explained in the text and defined in accordance with Efros–Shklovskii (ES) percolation theory (Ref. [47]). 203

Figure 7.6 Map of the VO_2 phase structure during thermal cycling. The results are obtained using Raman spectroscopy. The data have been extracted from our previous paper (Ref. [16]) where one can find a detailed explanation of the mapping procedure. Every large square is 25 × 25 pixels with each pixel having a size of $1.2 \times 1.2\ \mu\text{m}^2$. The numbers in the maps refer to the substrate temperature in degrees Celsius (°C). 207

Figure 7.7 Simplified views of the appearance of 2D infinite conductive cluster at heating (a), (b) and disappearance of 3D infinite conductive cluster at cooling (c), (d). In (a) and (b), brownish color marks the appearance and disappearance of the metallic phase respectively. White shows the initial insulating phase. In (c) and (d), violet spheres show the appearance and disappearance of the insulating phase, respectively. White shows the remaining metallic phase. The red arrows show possible current paths in 2D (b) and 3D (d) infinite conductive clusters. 210

Figure 7.8 Cross sections of the cube of $70 \times 70 \times 70$ used in modeling where (a) and (d) are the first layer; (b) and (e) are the 28th; (c) and (f) are the 70th layer. The first row (a)–(c) shows the metallic sites (i.e., containing 1 in computations) in blue. The second row (d)–(f) shows the wet sites (i.e., containing 2) in blue color. Figure (e) shows the gorge (the narrowest cross section) of the conductive cluster. The red arrow in figure (e) enables the reader to see the position of the gorge which is only one pixel. In all figures, white pixels denote voids, i.e., insulating sites (containing 0). The inset to figure (f) schematically shows the infinite percolation cluster as two vortexes with common gorge marked with a red arrow. No information is blocked by the inset: all pixels behind the inset are white. The results shown here represent one of the possible outcomes of the numerical simulations. 214

Figure 7.9 Cross-sectional area of the critical infinite conductive percolation cluster presented in Figure 7.8. Cross section is a number of wet sites, i.e., belonging to the conductive cluster. The size of the model is $70 \times 70 \times 70$. The gorge (with a width of one site) is on 28th and 29th layers. 215

Figure 7.10 (a) Width of the gorge (the narrowest cross-sectional area) of the infinite conductive cluster [schematically shown in the inset of Figure 7.8 (f) and in Figure 7.7 (d)] as a function of partial concentration of remaining metal. The results of the Swiss cheese model where the initial metal is substituted by spherical nonconductive voids. (b) The comparison of the Swiss cheese numerical model predictions with the measured VO_2 conductivity during sample cooling. The details of model are explained in the text. 216

Figure 7.11 Schematic presentation of IMT and MIT. 219

Figure 8.1 (a). Front view of VO_2 film on c-cut sapphire. 2 mm × 2mm gold contacts separated by 0.5 mm are covered by black non-conductive opaque tapes, above and below, to limit the light passing through the gap. (b) Rear view of VO_2 film on c-cut sapphire. Two platinum Pt-100 thermistors (PR1 and PR2) are attached on thermally conductive tapes which are also attached to the sapphire substrate. The PR1 thermistor is used simultaneously as a heater to pre-heat the sample and as a thermometer to stabilize the

substrate temperature. The PR2 thermistor is used to measure the temperature of the sample. (c) Outline of the experimental setup. The size of the sample is grossly exaggerated. LD is laser diode operating at 1550 nm, PD is the photodiode sensitive at 1550 nm, PR1 and PR2 are platinum thermistors shown in (b). 232

Figure 8.2 (a) Optical transmission spectrum of VO_2 films grown on c-cut sapphire at 27 °C and 95 °C. (b) Raman spectrum of VO_2 film taken at room temperature. (c) SEM surface image of the VO_2 film under 3 kV operation. (d) Cross sectional SEM image of VO_2 film under 3 kV operation. The thickness of the sample is measured as 190 nm ± 10 nm. (e) The temperature dependence of electrical conductivity at heating and cooling cycles. The inset shows the calculated T_{IMT} and T_{MIT} which are 67.2 °C and 62.5 °C, respectively. The hysteresis width (ΔH_{elec}) is 4.7 °C. (f) The temperature dependence of relative optical transmittance ($\tilde{T}_r$) at heating and cooling cycles. The T_{IMT} and T_{MIT} are calculated as 66.2 °C and 61.3 °C. The hysteresis width (ΔH_{opt}) is approximately 4.9 °C. 235

Figure 8.3 The conductivity (a), the optical transmittance (normalized to that of the film in semiconducting phase) (b) and the temperature (c) of the VO_2 film sample sketched in Figure 8.1 (a) in function of time before, during and after application of driving pulses with varying value of electrical current passed through the VO_2 and fixed duration of 5 seconds. The sample was kept at 57 °C before and after application of the pulse. The time discretization of the experiments was 2.5 ms and therefore all faster processes appear on graphs as vertical lines. The σ_m value shows fully metallic conductivity. The optical transmittance of the VO_2 in metallic phase is zero and in semiconducting phase is taken to be 100%. 238

Figure 8.4 (a), (b) The dynamics of conductivity normalized to that of VO_2 in metallic phase ($\sigma(t)/\sigma_m$) and partial concentration of the metallic phase (X_m) before, during and after application of I_D pulses with electrical current of 125 mA (a), (c) and 175 mA (b), (d). The pulse duration is 5 seconds and the time position is marked by the blue rectangular on the lower time axis. (b), (d) The corresponding dynamics of VO_2 temperature. All data are re-calculated from Figure 8.3. The time scale in (a) and (c) is split into time intervals $A - E$ with varying highlighting. The meaning of the intervals $A - E$ is explained in the text. The size of big squares is 25 × 25 pixels. The size of single pixel is 1.2 × 1.2 μm. The legend shows the color coding of the partial concentration of the metallic phase (X_m) in single pixel. The numbers in the maps refer to the substrate temperature (°C). 240

Figure 8.5 The simplified model of the events happening during the time intervals $A - E$ in Figure 8.4 and time intervals $A - C$ and $D' - F'$ in Figure 8.6. Blue color corresponds to the semiconducting phase and the red color to the metallic one. Broken arrows

schematically show the flow and the spatial distribution of the driving electrical current I_D. All other necessary explanations are given in the text. 242

Figure 8.6 (a) – (c) The dynamics of conductivity normalized to that of VO_2 in metallic phase ($\sigma(t)/\sigma_m$) and partial concentration of the metallic phase (X_m) before, during and after application of driving pulses with electrical current of 225 mA in (a) and (d), 250 mA in (b) and (e), and 275 mA in (c) and (f). The pulse duration is 5 seconds. Broken magenta lines present the same data as thick red lines but with (× 20) magnification. (d) – (f) show the corresponding dynamics of VO_2 temperature. The pulse duration is 5 seconds, and the time position is marked by the blue rectangular on the lower time axis. All data are re-calculated from Figure 8.1. The time scale in (c) and (f) is split into time intervals *A*, *B, D'– F'* with varying highlighting. The meaning of the intervals *A*, *B, D'– F'* is explained in the text. 243

Figure 8.7 The conductivity versus partial concentration of metallic phase (X_m). The data are taken from Figure 8.6 (a) – (c) when σ and X_m are relaxing when I_D is off. Note that both X_m and σ/σ_m are measured in non-steady-state conditions while the sample, previously heated by the driving pulse, is uncontrollably cooling down to 57 °C. 244

Figure 9.1 (a) Simple sketch of electrochromic diffraction gratings of electric constants for switches using electric field induced MIT (b) thermochromic diffraction gratings for thermally induced MIT. Black layers represent the gratings, and the red layers represent VO_2 films. 257

Figure A.1 Process flow diagram of SPT-320 magnetron sputter deposition system produced by Plasmionique Inc. for the Department of Mechanical Engineering at the University of Saskatchewan. 259

Figure A.2 Electrical circuit designed to pass constant current through a VO_2 film. 260

Figure A.3 The circuit used to measure the transmittance of VO_2 thin films. The light incident on the photodiode produces a photocurrent that is fed into a large load resistor, which is 1 MΩ. The photocurrent and hence the voltage across the load resistor is a function of incident light power, light wavelength, and responsivity. 262

Figure A.4 The circuit used to measure the temperature of the VO_2 sample. 263

Figure A.5 An image of a Digilent Analog Discovery 2. (b) A block diagram of the Digilent Analog Discovery 2. 264

Figure A.6 The front panel of PID control. GDP4304 COM Port is used to communicate with the GW Instek GDP4304 DC voltage supply. COM3 port is used to communicate with the Omega® PID temperature controller. 267

Figure A.7 Block diagram of the Labview program used to control the substrate temperature. 268

Figure A.8 The user interface of the Labview program is used to measure the substrate temperature (top reading). Significant noise in the temperature reading, which is inevitable, may be due to the vibrations coming from the temperature measuring circuit. The bottom reading (red data) shows the voltage across a 5 Ω-5 W resistor connected in series to the VO_2 film. 270

Figure A.9 Square pulse of a total amplitude of 1.5 V set to generate 300 mA with a 5 s-pulse period. 271

Figure A.10 Scope panel was used to monitor the change in optical transmittance (blue) and voltage reading across the sample (yellow). 272

Figure B.1 (a) Raman spectrum measured for an array of 25 × 25 = 625 pixels at 24 °C. (b) – (d) Typical Raman spectra collected at different temperatures for an individual pixel as it undergoes a transformation from semiconducting (b) to metallic (d) phase. 275

Figure B.2 Histograms of correlation coefficients (CC) of the Raman spectra in Figure B.1, measured at different temperatures. 276

List of Tables

Table 1.1 Space group and cell parameters (*a*, *b*, *c*) of insulating (monoclinic) and metallic (rutile) phases of VO_2. After Shao et al. [23]. 6

Table 1.2 Comparison of similarities and differences between the phase transition in VO_2 and the classical phase transition mechanisms. After Nag [37]. 7

Table 1.3 Forms of VO_2, selected examples of their preparation methods, potential applications, and the triggering of the phase transition. 16

Table 2.1 The ionization energy regimes. After Rossnagel [6]. 46

Table 3.1 Relations of reflection and transmission coefficients under various scattering conditions. 72

Table 3.2 Waves reflected in thin film medium (n_2) from film-substrate interface. 73

Table 3.3 Reflected waves in the thin-film-substrate and thin-film-air interfaces. 74

Table 3.4 Representation of reflected waves by means of transmission and reflection coefficients that constitute the reflected beam. 74

Table 3.5 Well known dispersion models to examine the wavelength dependence of refractive index of materials. 78

Table 3.6 Parameters defined in transmittance ($\tilde{T}$) equation of Swanepoel technique [10]. 86

Table 3.7 Parameters defined in transmittance ($\tilde{T}$) equation of the Manifacier technique [13]. 100

Table 4.1 Grain size and thickness of the as-deposited VO_2 thin films with substrate biasing.. 107

Table 4.2 The scattering contribution to attenuation in VO_2 films on Si, given E_g = 0.60 eV and A_a = 0.0048 $nm^{-1}\cdot eV^{-1}$. 122

Table 5.1 Deposition conditions of the as-prepared thin films on Si and sapphire substrates. .. 130

Table 5.2 Average grain size (GS_{avg}), average (R_a) and root-mean square (R_q) roughness of VO_2 thin films prepared at various substrate temperatures (T_S). 138

Table 5.3 Optical transmittance ($\tilde{T}$) and transmittance contrast ($\Delta\tilde{T}$) values of VO_2 films prepared at different substrate temperatures (T_S) obtained at 300 K (insulating) and 368 K (metallic) for λ = 1500 nm, 2000 nm and 2500 nm. 141

Table 5.4 Luminous and solar modulation efficiencies of VO_2 films prepared on sapphire substrates at various T_S. 147

Table 6.1 Deposition conditions of VO_2 thin films on Si, quartz and sapphire......................... 167

Table 7.1 Comparison of experimental results with theoretical predictions of paper [47]. X_c is percolation threshold, T_c is temperature corresponding to percolation threshold, $\sigma(X_c)$ is the conductivity at percolation threshold, σ_s is the conductivity of VO_2 in semiconducting phase at temperature T, σ_m is the conductivity of VO_2 in metallic phase. The values marked with asterisk (*) are the published results of computer simulations and may be considered as approximate (for details see Refs. [47,65] and references herein]). 209

List of Abbreviations

AC	Alternating Current
AFM	Atomic Force Microscopy
AP	Action Potential
Ar	Argon
CB	Conduction Band
CC	Correlation Coefficient
CCD	Charge-Coupled Device
CVD	Chemical Vapor Deposition
D	Deuterium
DC	Direct Current
DG	Diffraction Grating
EHP	Electron-Hole Pair
EM	Electro-Magnetic Wave
EMA	Effective Mass Approximation
FEG	Field Emission Gun
GaAs	Gallium Arsenide
HL	Halogen Light
HRTEM	High Resolution Transmission Electron Microscopy
ICC	Infinite Conductive Cluster
IM	Insulator-to-Metal
IMI	Insulator-Metal-Insulator
IMT	Insulator-to-Metal Transition
InGaAs	Indium Gallium Arsenide
IR	Infrared
LD	Laser Diode
Li	Lithium
MI	Metal-to-Insulator

MIT	Metal-to-Insulator Transition
MOSFET	Metal-Oxide-Semiconductor Field-Effect Transistor
NIR	Near Infrared Light Spectrum
O	Oxygen
O_2	Oxygen Gas
PID	Proportional–Integral–Derivative
PLD	Pulsed Laser Deposition
PR	Platinum Thermistor
Pt	Platinum
PVC	Polyvinyl Chloride
RF	Radio Frequency
SCCM	Standard Cubic Centimeters Per Minute
SEM	Scanning Electron Microscopy
SH	Self-Heating
SPT	Sputtering System
TCR	Temperature Coefficient of Resistance
TEM	Transmission Electron Microscopy
TMO	Transition Metal Oxide
UV	Ultraviolet
VB	Valence Band
Vis	Visible Light Spectrum
VO_2	Vanadium Dioxide
W	Tungsten
Xe	Xenon
XPS	X-Ray Photoelectron Spectroscopy
XRD	X-Ray Diffraction
Zn	Zinc

1. Introduction

1.1 Introduction

Vanadium dioxide (VO_2) is a well-known multifunctional transition metal oxide (TMO) with distinguished switching properties that have attracted attention for various electrical, optical and optoelectronic applications. At room temperature, the material is an insulator, more precisely a semiconductor. When heated, VO_2 undergoes an insulator-to-metal (IMT) phase transition and transforms into a metallic phase. This transition occurs at a critical temperature of around 67-68 °C (340– 341 K) [1]. On the contrary, upon cooling, the metallic phase VO_2 goes through a metal-to-insulator phase transition (MIT). Ideally, in chemically pure stoichiometric single-crystal VO_2 the IM/MI, transitions occur almost at the same temperature. Polycrystalline VO_2 films, exhibit IM and MI phase transitions at different critical temperatures (T_c). Compared with the IMT, the MIT occurs at a substantially lower temperature. The temperature difference between the occurrence of IMT and MIT is known as thermal hysteresis (ΔH). The phase transition sharpness, the transition contrast, and the critical temperature separation between IMT and MIT depend on the quality of the prepared VO_2 films. Under phase transition, the optical and electrical properties of the material experience dramatic changes. The IMT in VO_2 can be induced by means of heating [2], applying an electric field [3], photoexcitation [4−8] and mechanical stress [9−10]. Due to the many ways of triggering its phase transition, VO_2 has been proposed for a number of thermal, optical, electrochemical and electronic applications, such as IR sensors, smart windows, Li-ion batteries and optoelectronic switches.

In real life, producing ideally stoichiometric and single-crystal VO_2 is quite difficult, which bares challenges related to the fabrication process. There are many fabrication methods and procedures that have been under investigation to grow high-quality VO_2 films. The type of crystalline structure and the quality of the desired films depend on the type of application. For optical applications, normally a high optical transmission contrast ($\Delta\tilde{T}$) between the insulating and metallic phases with a narrow ΔH is desired. On the other hand, in certain electrical applications such as (e.g., memristor, RRAM), a high conductivity contrast ($\Delta\sigma$) with a broader ΔH is preferred [11−12]. The obscure nature of the phase transition in VO_2 has long been studied

but has not been fully understood. To date, two theoretical models (Mott-Hubbard and Peierls) are found to have validity, as supported by certain experimental data. However, a more comprehensive model of the phenomenon, as applied to VO_2, has not yet been developed.

This chapter introduces a concise account of the synthesis and properties of VO_2 films based on the reports in the literature. Initially, a brief review of VO_2 as a transition metal oxide is provided. Then, the phase transition phenomenon in VO_2 is covered, as well as certain intermediate phases of the material. Following the latter, specific forms of VO_2 and their potential applications are introduced. Next, certain structural modification techniques of the phase transition temperature are discussed such as doping the film or inducing strain in the film through the choice of substrate material. Subsequently, potential application fields of VO_2 films are reviewed. Finally, the motivation and the objective of the Ph.D. research are given. Eventually, the content of the Ph.D. dissertation is introduced.

1.2 VO_2 as a Transition Metal Oxide

1.2.1 Introduction

TMOs have been of much interest in the past few decades due to their switching functionality which can be utilized in numerous (optical and electrical) applications. Such distinguished transition metal oxides and their metal-to-insulator phase transition temperatures (T_{MIT}) are given in Figure 1.1 (a). TMOs such as NbO_2, NiO, CoO, SnO, FeO, CuO, ZnO and MnO_2 have been gaining interest for their potential in applications such as optoelectronics, energy harvesting and storage, sensing, electronics, magneto-electronics, and thermo-electronic applications. More details on the advantages of emerging two-dimensional (2D) metal oxides and prospective development techniques can be found in the review of Kumbhakar et al. [13]. Figure 1.1 shows the various fields of transition metal oxides with fast switching characteristics.

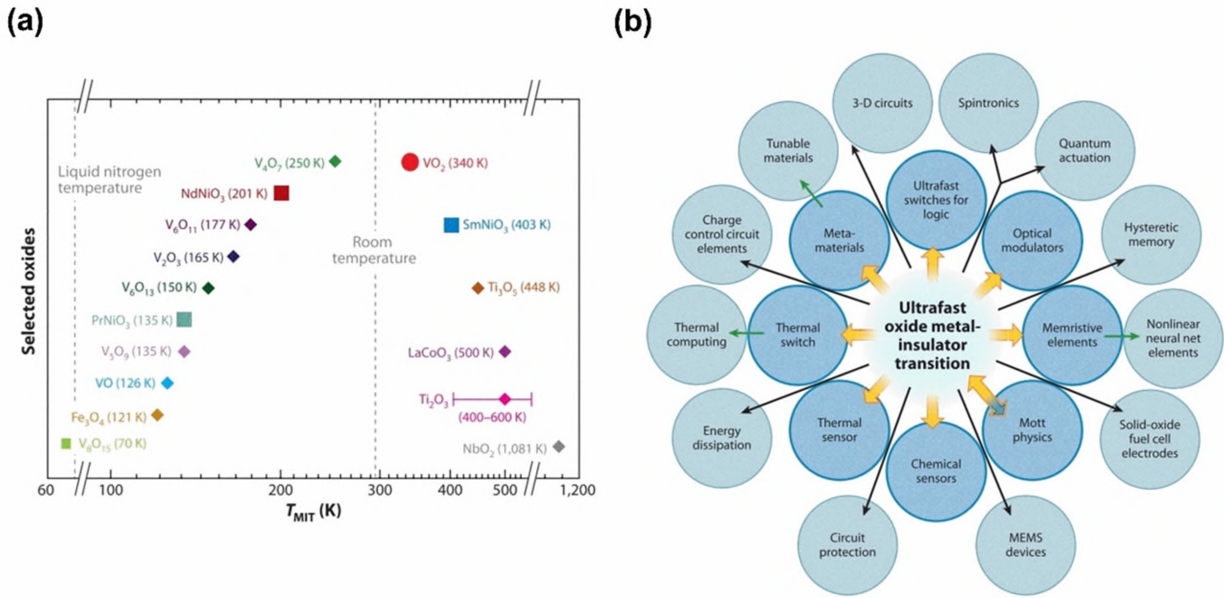

Figure 1.1 (a) The metal-to-insulator phase transition temperature (T_{MIT}) distribution of selected transition metal oxides. (b) Various application fields of transition metal oxides with fast transition capability. Diagrams partially adapted from Yang et al. [14].

Vanadium (V) as an element, is a transition metal with an atomic number of 23 and is placed in the 4th period group 5 elements. The electron configuration of V is [Ar] $3d^3$ $4s^2$ with an atomic weight of 50.94 amu. Due to its multivalence electronic state V can form various compositions with oxygen (O). Figure 1.2 presents various oxidation states of V.

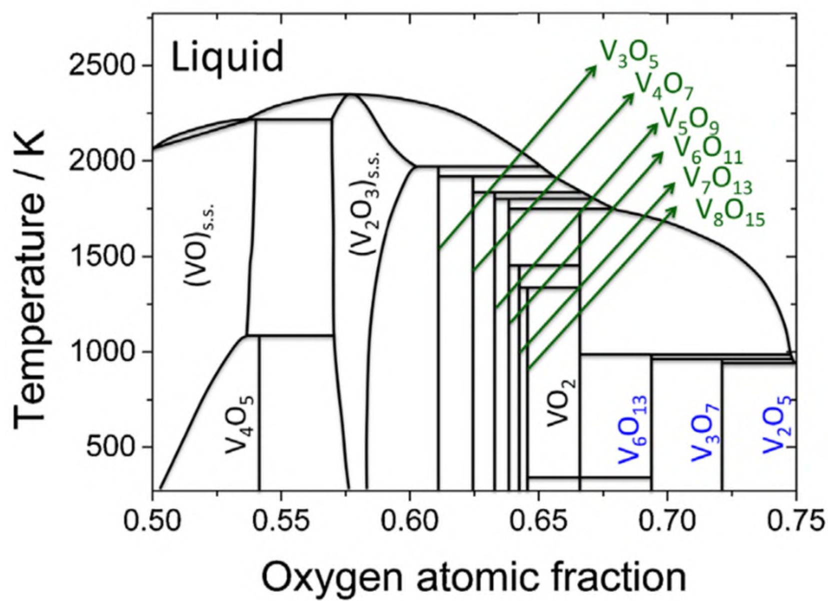

Figure 1.2 Oxidation states of vanadium (V). The V-oxides indicated in blue refer to the Magnéli series, V_nO_{2n+1}. The ones indicated in green refer to the Wadsley series, V_nO_{2n-1}. After Bahlawane and Lenoble [15].

A few noteworthy oxides of V are VO, VO_2, V_2O_5, V_5O_9, V_2O_3, V_6O_{11} and V_4O_7. Vanadium oxides are preferable in mainly electrical applications, and a few of them are worth mentioning. V_2O_3 is a vanadium oxide that is a candidate for utilization in lithium (Li)-ion batteries as anode materials [16] as well as in functional positive temperature coefficient (PTC) materials in nanobelt, nanosphere and nanosheet forms [17]. V_6O_{13} is another oxide of V that is utilized in Li-ion cells [18,19]. V_5O_9 is known for its super capacitive behavior which can be utilized in energy storage devices. [20] V_4O_7 is a third oxide of vanadium that has the potential to be employed as a cathode material in Li-ion batteries. V_2O_5 is another vanadium oxide that has been found to be suitable for certain electrical switching applications. This oxide can also be utilized in Li-ion batteries, as high-performance anodes in the form of nanobelts. [21] Another potential application field of V_2O_5 is electromechanical actuators for its highly sensitive Young's modulus under an applied voltage [22].

Compared to other V-oxides, VO_2 stands as the most popular material with the highest potential to be employed in electrical, optical and optoelectronic devices. This is due to the distinctive change in the electrical and optical properties during phase transition. In such

applications, the metal-to-insulator phase transition lies in the main interest and establishes the benchmark for the utilization of the material. A concise explanation of the phase transition in VO_2 films is delivered in the next section.

1.2.2 The Phase Transition Phenomenon in VO_2

The phase transition in VO_2 is a first-order thermodynamic transition which involves latent heat. In the metallic phase of VO_2, the crystal structure of the material is tetragonal rutile with a symmetry space group P42/mnm (No. 136), in which the unit cell of the metallic phase consists of straight V-V bonds that occupy the outermost boundaries. In the metallic phase, the crystal structure consists of V^{4+} ions occupying the body center and the vertex of the tetragonal structure, and all the V^{4+} ions and O^{2-} ions form an octahedral VO_6 unit [23]. When heat is extracted from the rutile VO_2 the material undergoes dimerization, and which the outermost V-V bonds become tilted (zigzag-like). During the MIT, the unit cell doubles in size with the conversion of space symmetry to P21/c (No. 14). According to the aspects of classical band theory [24], the 3d band splits, and a bandgap appears between the π^* and $d_{//}$ bands. As a result, the material transitions into the semiconducting phase. Figure 1.3 shows the crystal and electronic band structure of the insulating (monoclinic) and metallic (rutile) phases.

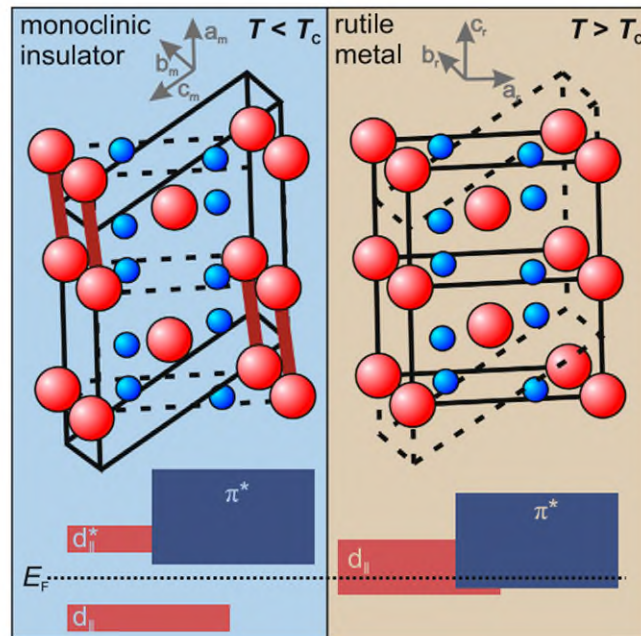

Figure 1.3 Crystal structure of monoclinic insulator and rutile metallic phases VO_2. After Wegkamp and Stähler [25].

During the reverse phase transition (insulator-to-metal transition (IMT)), the tilted bonds between the V-V dimers delocalize and the angle between the V atoms that are located at the corner and middle of the crystal structure straighten (β = 122.6°→180°). The bandgap between π^* and $d_{//}$ bands disappears and the split 3d bands reunite. Consequently, a highly symmetric tetragonal structure of metallic (rutile) phase VO_2 is formed. The crystalline properties of the insulating and metallic phases of VO_2 are given in Table 1.1.

Table 1.1 Space group and cell parameters (*a*, *b*, *c*) of insulating (monoclinic) and metallic (rutile) phases of VO_2. After Shao et al. [23].

	Insulating phase	**Metallic phase**
Space group	P21/c (No.14)	P42/mnm (No.136)
a (nm)	0.575	0.455
b (nm)	0.452	0.455
c (nm)	0.538	0.286
β (°)	122.6	180

The physics of the phase transition in VO_2 has not been fully resolved. Since the discovery of this phenomenon [1] there has been a growing interest to identify the driving mechanism of the phase transition. Theoretical discussions on the transition mechanism of VO_2 have not been able to reach a consensus on whether the transition is purely structural (Peierls type) or electrical (Mott-Hubbard type) [26–31]. The Peierls model states that the phase transition is caused by electron-

phonon interactions (lattice distortion) [24,29]. This view has found support from certain theoretical works [25,26] and experiments focusing on the structural dynamics of the phase transition in VO_2 by photoexcitation [4,5]. Also, Goodenough's [24] qualitative work on the electronic structure of the monoclinic and rutile phases of VO_2 using crystal field and molecular orbital theories suggested that the lattice distortion in the VO_2 unit cell is the main cause of the MIT, which is based on the Peierls model. On the contrary, the Mott-Hubbard model relates the phase transition to electron-electron correlations in partially filled d-bands separated by a band gap [27,28]. Unlike Peierls' view, the Mott-Hubbard model has been able to explain the electrical band gap of VO_2, which has been experimentally obtained around 0.7 eV [32–34]. Additionally, experiments on the electrical [3] and optical excitation of VO_2 have claimed that the phase transition is of the Mott-Hubbard type [35]. Nevertheless, more recent studies point out that Mott- and Peierls-type transitions occur interdependently [36]. Table 1.2 presents a comparison of the Peierls (structural) and Mott-Hubbard (electrical) mechanisms and the aspects of the phase transition phenomenon in VO_2 they are consistent and/or inconsistent with.

Table 1.2 Comparison of similarities and differences between the phase transition in VO_2 and the classical phase transition mechanisms. After Nag [37].

Features of phase transition in VO_2	**Peierls transition**	**Mott-Hubbard transition**
Consistent with:	Doubling of unit cell	Existence of M_2 phase
	Pairing of metal atoms	Narrowing of d-bands
	Large lattice transition latent heat	Ultrafast phase transition
Inconsistent with:	Large bandgap (0.7 eV)	Structural change
	Conductivity jump 10^{-2} – 10^{-3} times smaller than experiment	Phonon scattering
	$\frac{dT_c}{dP} > 0$	$\frac{dT_c}{dP} > 0$

The phase transition in VO_2 is known to be a very fast transition. With the application of a high electric field (E) across the material, the phase transition appears in an ultrafast time scale.

Related work has revealed with THz spectroscopy that the transition occurs in less than 2 ns [38]. This ultrafast on/off electrical (and optical) switching property of VO_2 has made the material particularly attractive for memory devices [39–42].

When VO_2 undergoes IMT the optical transmittance ($\tilde{T}$) of the material decreases significantly, and the material becomes almost completely opaque. Also, the material becomes highly conductive. The electrical conductivity of the material changes by 3−5 orders of magnitude [43–45]. Typical ways of externally triggering phase transition in VO_2 are heating, and applying electric field, inducing strain etc. Figure 1.4 (a) presents a simple sketch of the IM/MI phase transitions in terms of the resistivity of VO_2 which may be induced by certain types of external excitation.

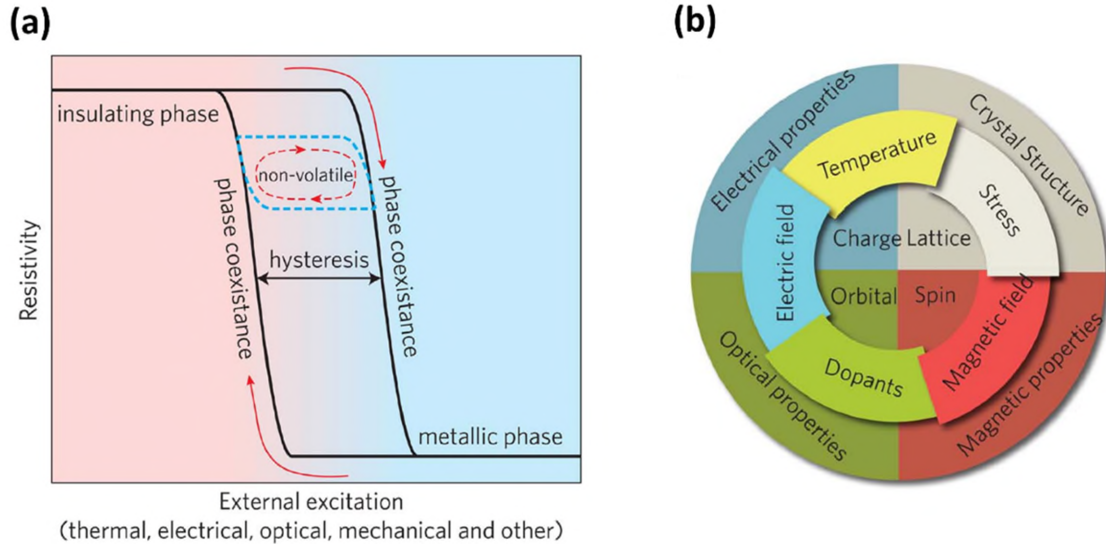

Figure 1.4 (a) A sketch of the resistivity of VO_2 (or any transition metal oxide) which undergoes insulator-to-metal (IM) and metal-to-insulator (MI) phase transitions. (b) A circular diagram that represents triggering of phase transition in Mott insulators. In the figure, the inner circle shows the coupling of the different degrees of freedom. The middle ring presents various ways of triggering the phase transitions in VO_2. The outer ring shows the physical properties that can be changed during phase transitions. (a) and (b) are partially extracted from Zhou and Ramanathan [46].

It's now a strongly supported view that the phase transition starts to appear locally. Wherefore, during the IM and MI phase transitions both insulating and metallic phases coexist. In

polycrystalline films, the ΔH is related to the induced strains in the crystal caused by grain size or lattice mismatch between the film and the substrate. The phase transition is a reproducible process in which the resistivity follows the same heating and cooling characteristics back and forth when the external excitation is applied and removed. As given in Figure 1.4 (b) there are different ways of triggering the phase transition (e.g., IMT). To induce phase transition in VO_2, four degrees of freedom, (charge, lattice, orbital and spin) may be coupled in different ways to trigger the phase transition (e.g., temperature), which eventually leads to the change in physical properties.

1.2.3 Phases of VO_2

At room temperature, VO_2 is in an insulating, more precisely in a semiconducting phase. When the material is heated, it undergoes IMT around 68 °C (341 K), and transitions into a metallic phase. The insulating phase is also referred to as the monoclinic phase due to its monoclinic crystal structure. On the contrary, the metallic phase is also described as the rutile or tetragonal phase. In the metal phase, VO_2 has a tetragonal crystal structure. VO_2 has three monoclinic phases which are known to be M_1, M_2 and T' (triclinic) phase respectively. The M_1 phase represents the stable structure of the semiconducting phase of VO_2. The second monoclinic (M_2) phase exists as a semiconducting phase, where the position of the vanadium atoms is twisted compared to that for the M_1 phase. The T' phase appears as an intermediate (metastable) phase that exists between two M_1 and M_2 monoclinic phases. Structural studies with strain-induced phase transition have been effective in revealing different monoclinic phases. Figure 1.5 presents a concise explanation of the monoclinic phases of VO_2. Figure 1.5 (a) illustrates a unit cell of VO_2 with oxygen octahedra and tilted vanadium sublattices. Under applied strain, the position of V atoms shifts to a certain angle, transforming the M_1 phase into the M_2 phase. Figure 1.5 (b) gives the position of V atoms at M_1 and M_2 at two different sublattices. The arrows indicate the intermediate triclinic (T') phase that appears between M_1 and M_2 phases. Given in Figure 1.5 (c) the structural characterization of the monoclinic phases elucidates the difference in the critical Raman peak with respect to tensile strain at certain temperatures [45].

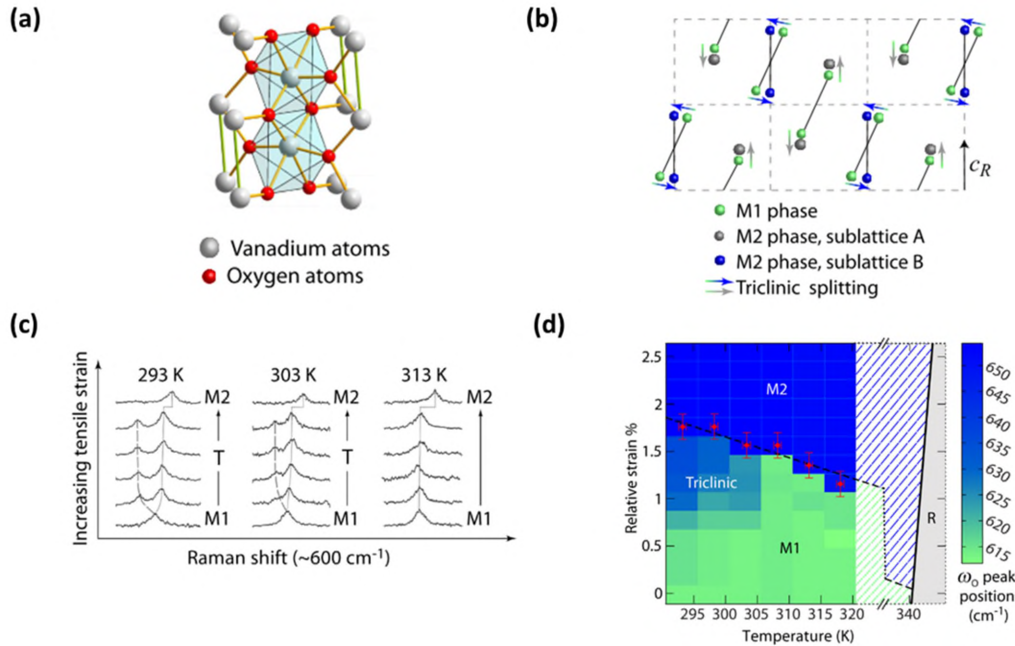

Figure 1.5 (a) A unit cell of VO_2 with oxygen octahedra and tilted vanadium sublattices. (b) Position of V atoms at monoclinic 1 (M_1, blue), monoclinic 2 (M_2, gray and blue), where the arrows indicate the intermediate triclinic (T') phase. (c) Shifting of critical Raman peak (ω_o) with respect to tensile strain at temperatures 293 K, 303 K and 313 K and the transition from M_1 to M_2 phase. (d) Relative strain versus temperature phase diagram of the VO_2 represented via the phonon frequency shift (ω_o) (red data). After Atkin et al. [47].

1.2.4 Percolation Theory

Percolation theory is a well-known concept in the study of electrical conduction of semiconductor materials. It has been established by Broadbent and Hammersley [48] and is based on a simple mechanism which describes the critical behavior of the physical properties of a material when a critical point is reached. This theory is fundamentally considered in two-dimensional space (Z^2) and used to explain phase transition in terms of cluster formation (i.e., growth of infinite clusters within a finite cluster system). In particular, the probability of nearest neighbors during cluster formation is considered to analyze the transition. The percolation theory has found much interest in material science as well as numerous other fields of research such as in astrophysical problems (star formation), binary systems, glass transition and in biological

problems. [49] Specifically, it has been used in the study of the electrical conduction of chalcogenide glasses [50]. It has been a well-recognized phenomenon in the phase transition which occurs in TMOs (e.g., Percolation-induced two-dimensional metal-insulator transition has been revealed in Si MOSFETs [51]). In the utilization of TMOs in resistive random-access memories (RAM), the formation of filamentary percolation path is one of the important considerations to engineer reliable non-volatile memory devices. [52] This theory has been improved for TMOs by the Efros-Shklovskii model [53] which analyzes the electrical conductivity of a strongly inhomogeneous media. Figure 1.6 illustrates site percolation on a square lattice of finite and infinite clusters at concentrations (a) $p = 0.2$, (b) $p = 0.59$ and (c) $p = 0.8$.

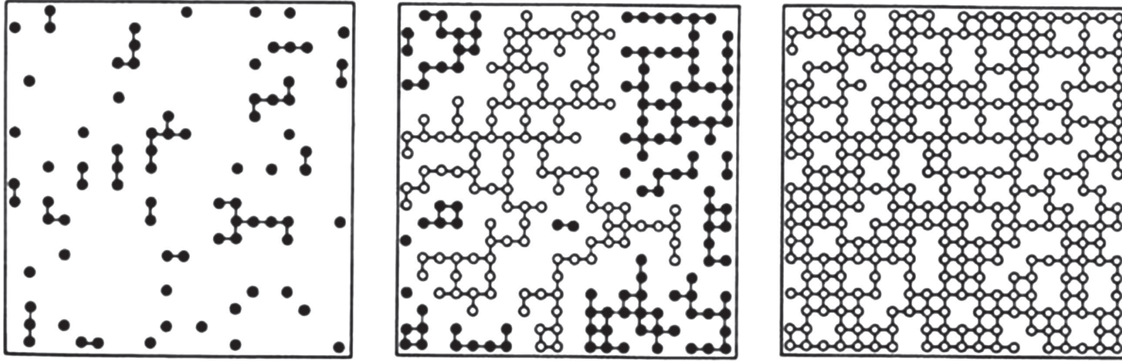

Figure 1.6 Site percolation on a square lattice: The small circles represent the occupied sites for three different concentrations: $p = 0.2$, 0.59, and 0.80. Nearest-neighbor cluster sites are connected by lines representing the bonds. Filled circles represent finite clusters, while open circles mark the large infinite clusters. After Bunde and Kantelhardt [54].

Percolation theory has been considered for the phase transition in VO_2 [55]. However, until now, the number of limited works requires more efforts to examine and analyze the insight into the formation and growth of insulating and metallic phases during the IM and MI phase transitions, respectively.

1.2.5 Manipulation of Phase Transition Properties of VO_2

One of the main interests in research on VO_2 is the manipulation of phase transition properties. In polycrystalline films, these can be categorized separately as optical and electrical switching properties. Phase transition properties include critical temperatures such as T_{IMT} and T_{MIT}, as well as ΔH and the sharpness of the IM and MI phase transitions. Different methods are used to manipulate IMT/MIT of VO_2 films which depend on the type of optical and electrical application. Such ways of manipulating the phase transitions may involve the choice of substrate, elemental doping, self-heating etc. The crystallinity, hence, the phase transition of VO_2 films is influenced by substrate/film mismatch. In experimental studies, the single-crystal sapphire substrate is found to be effective in reducing the structural mismatch at the sapphire/VO_2 interface, facilitating near-epitaxial VO_2 nucleation and growth leading to near-epitaxial VO_2 structure. There are numerous works covering different aspects of VO_2 deposition on sapphire substrates [45,56–60].

Also, the optical and electrical switching properties of VO_2 can be manipulated by elemental doping. Dopants which include W, Al, Au, B, Nb and Li are reported to reduce the T_{MIT} [61–81] whereas dopants such as Ti, Cr, Ga, Ge, and Sn elevate the T_{MIT} [82–87]. Co-doping is another method to manipulate the T_{MIT} which additionally aims to optimize the optical and electrical switching properties of VO_2 for optoelectronic applications. A few examples of elements that are co-doped in VO_2 include Ce-W, Mg-W, Ti-W, Ti-F, W-Sr, and Ni-Cr [88-96].

Another way of manipulating the phase transition in VO_2 is inducing self-heating in the material. This may be achieved by applying sufficiently large voltage or passing a large electric current. However, in this type of manipulation, there has been a challenge in identifying, hence controlling the main factor that triggers the phase transition in VO_2. One view suggests that the phase transition under a high electric field is related to potential breakdown due to high carrier injection (e.g., Ref. [97]). A different view suggests that the triggering is caused by local heating as a result of the Joule effect that is caused by the applied electric field (e.g., Ref. [98]). The difficulty in identifying the main triggering factor may be attributed to the unavailability of monitoring rapid electrical and structural changes in the material that leads to the IM/MI phase transitions in nano- or micro-scale VO_2-based devices under applied high electric field.

1.2.6 Forms of VO_2

VO_2 can be fabricated in various forms. These forms mainly fall under two different categories: thin films and micro/nano-scale structures. Thin films are the most popular form of VO_2 in various applications. Also, micro/nano-scale structures have significance for utilization in recent integrated circuits and nanotechnology applications. These forms may be classified under one-dimensional structures (e.g., microrods, nanorods, nanobelts) and nearly-two-dimensional structures (e.g., nanoplates and thin films). The synthesis of each form is a unique process. In addition, most of these forms can be utilized in various applications. Figure 1.7 presents various forms of VO_2.

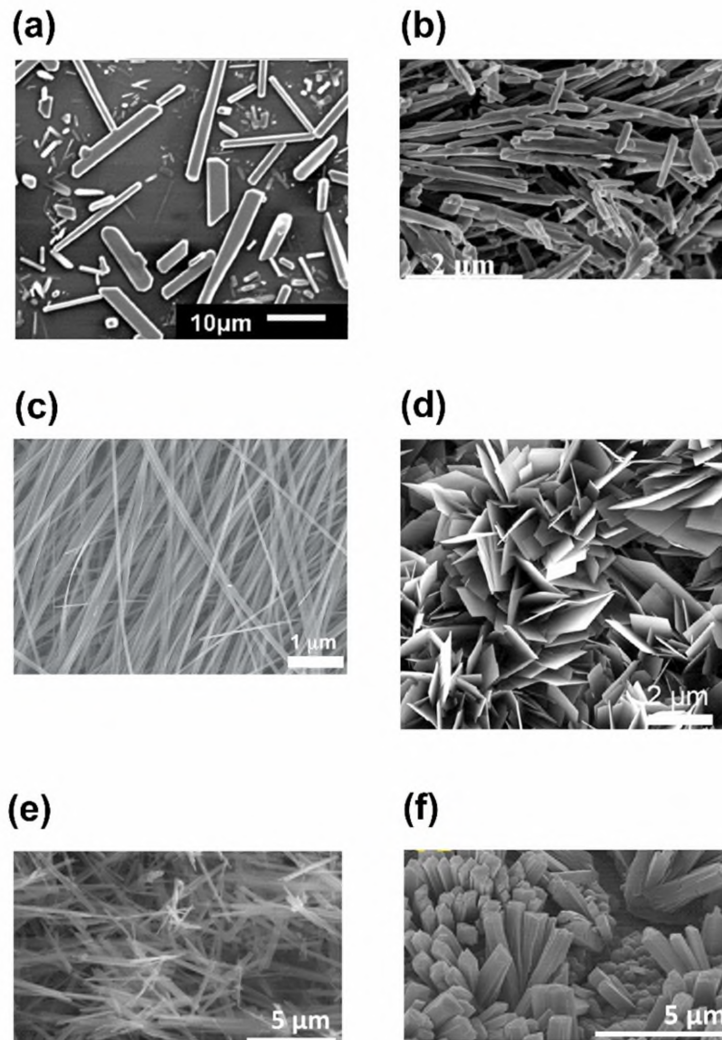

Figure 1.7 (a) VO_2 microrods, after Zhang et al. [99], (b) VO_2 nanorods, after Zhang et al. [100] (c) VO_2 nanowires, after Bae et al. [101]. (d) VO_2 nanoplates, after Liang et al. [102] (e) VO_2 nanobelts, after Sediri and Gharbi [103]. (f) VO_2 nanoribbons, after Sreekanth et al. [104].

VO_2 microrods are generally considered to be quasi-one-dimensional VO_2 rod-like structures that have a length in the micrometer range in which the length is greater than the diameter. These rods have the potential to be utilized in memory devices, strain and gas sensors, and actuators. The preparation of such VO_2 structures involves a reduction process. Zhang et al. [105] have synthesized VO_2 microrods from annealing precursor V_2O_5 films grown on Si (100) substrates. Various experimental studies on VO_2 microrods have demonstrated structural change during IM and MI phase transitions [99]. Further investigations have found a size-dependent phase transition in microrods by means of monitoring the light scattered from microrods [106]. Experiments have revealed that the IM and MI transitions become sharper with decreasing size of microrods (i.e., for sizes below 1 μm-height, and 10 μm-length) having a T_{IMT} between 58–76 °C and a T_{MIT} between 31−64 °C. It was observed that larger microrods (4 μm-height, and 40 μm-length) would display a sharp IMT around 68 °C but have an MIT that is stretched over a wide temperature with a distinctive low-temperature shoulder between 35–50 °C which is related to the substrate-induced mechanical stress in the rod.

One-dimensional VO_2 nanostructures, on the other hand, have a high potential to be used as nanoscale devices such as supercapacitors, memristive and storage devices. VO_2 nanowires are cylindrical-shaped wires that have a diameter and length on the order of nanometers. VO_2 nanowires can be utilized in gas sensors. Strelcov et al. [107] have demonstrated the high sensitivity of resistivity of VO_2 nanowires on SiO_2/Si substrates due to external physical factors such as pressure, temperature and molecular composition. Alternatively, VO_2 nanowires can be used in the realization of high-rate and long-life Li-ion batteries. Niu et al. [108] have assembled VO_2 nanowires into hollowed microspheres which function as a capacitor. It was shown that such structures have high capacitance and cyclability (charge and discharge performance) which were related to high self-response to mechanical strain that results in the expansion and compression in the volume.

VO_2 nanobelts are another type of nanoscale structure that can be utilized in various applications. Geometrically, these structures have a rectangular cross-section and a longer length compared to nanowires, which resemble a belt. The VO_2 nanobelts can be obtained in a metastable (B) phase where the phase transition is realized between (B) and (A) or (B) and (M) phases [102,109–111]. VO_2 nanobelts can be Li-ion batteries as cathode material.

VO_2 nanorods are another type of popular nanostructure which have the potential of being utilized in Li-ion batteries [112]. Compared to microrods, the length and width of these rod-shaped structures are on the order of nanometers. VO_2 nanorods, can be prepared in the metastable (B). or in monoclinic phase of VO_2. nanorods may be prepared. Such structures may demonstrate thermochromic phase transition at temperatures (e.g., 10 °C) higher than that in VO_2 films [113].

As a two-dimensional nanostructure of VO_2, nanoplates (nanosheets) and thin films can be given as examples. VO_2 nanoplates (nanosheets) are another form of VO_2 that can be utilized in applications such as gas sensors. A related work [102], B-phase VO_2 nanosheets have shown high sensitivity to NO_2 adsorption which regulates the phase transition in the material. As a two-dimensional microstructure, VO_2 can also be fabricated in microwire form which is proposed for emerging field-effect transistor applications. In a related work, VO_2 microwire has been implemented as a drain contact in a WSe_2 transistor to control the drain current through the thermal phase transition of VO_2 [114].

Table 1.3 summarizes the forms of VO_2 that are reviewed in this section.

Table 1.3 Forms of VO_2, selected examples of their preparation methods, potential applications, and the triggering of the phase transition.[1]

VO_2 form	Preparation method	Potential application	Triggering of the phase transition
Microrod	Reduction of V_2O_5 films [105]	Mott transistors, memory devices, strain and gas sensors, and actuators [115–117]	Heat, electric field, mechanical stress
Microwire	Electron-beam (e-beam) lithography and reactive ion etching of VO_2 film [118]	Hybrid optoelectronic devices for optical switches, modulators and detectors	Heat, electric field
Microbeam	Self-flux growth [119],	Strain sensors, micro-cantilevers and actuators	Mechanical stress
Nanorod	Hydrothermal reduction of V_2O_5 [100]	Ion cathode for Li-ion batteries	Electrochemical
Nanowire	Vapor solid method on Si/SiO_2 [107]	Gas sensors, microbolometers, thermistors	Heat
Nanosheet	Hydrothermal method [102]	Gas sensors	Electrochemical

[1] The preparation methods, applications, and ways of triggering the MIT of different forms of VO_2 are one or a few examples and are not limited to these.

Nanobelt	Hydrothermal method [103]	Cathode electrodes for Li-ion batteries	Electrochemical
Nanobeam	Chemical treatment in aqueous solution [120]	Bolometric infrared detector	Heat
Nanoribbon	In situ growth via microwave assisted synthesis [104]	Optical switches, sensors, aqueous Zn-ion batteries	Heat, electric field, electrochemical
Nanoneedle	Sol-gel and hydrothermal treatment [121]	Cathode for Li-ion batteries	Electrochemical
Thin Films	Section 1.3		

1.3 Applications of VO_2 Thin Films

VO_2 thin films have a broad range of applications. As mentioned in the previous sections, due to the change in its physical properties during phase transition and its ultra-fast switching characteristics, VO_2 films have been proposed for a number of optoelectronic and photonic device applications. Recently, this material has also gained much interest in neuromorphic devices. This section provides a concise review of the current and potential applications of VO_2 films. Only a few major or significant applications are reviewed and presented.

1.3.1 VO_2 Films in Smart Windows

Smart windows are new-generation windows with chromogenic glazing in which the light transmission can be modulated by light (photochromic), voltage (electrochromic) or heat (thermochromic). Smart windows are utilized for reducing energy consumption in tall buildings

(e.g., skyscrapers) and for decreasing the cost of heating, ventilation and air conditioning. Physical properties such as colour contrast, switching rate and durability are crucial in the performance of smart windows [122]. Chromogenic materials become reflective (opaque or cloudy) when transitioned into a metallic phase. The transition can be induced in different ways such as photochromic, electrochromic and thermochromic switching. Electrochromic materials are switched to the opaque metallic phase by the application of an electric field, which typically requires low voltages (up to ~ 2−3 V) across very thin VO_2 films (nanoscale) for electrochromic switching [123−125]. Photochromic windows are made of materials that undergo a phase transformation upon excitation by light. Injection of photocarriers leads to a bandgap collapse in the material (specifically for VO_2) which then leads to a transformation from the insulator to the metal phase. In a photochromic phase transformation, the material undergoes a chemical bond rearrangement with respect to the excitation of molecules under illumination. The photoinduction of the phase transition in VO_2 films is carried out by applying light pulses at THz frequencies with wavelengths between 500− 700 nm [25]. Among metal oxides MoO_3, WO_3, V_2O_5, Nb_2O_5, ZnO, and TiO_2 are used as photochromic switching materials. VO_2 is used as a switching material in thermochromic windows. Nb^+ and W^+ doping is preferred to reduce the thermochromic switching temperature from 68 °C down to room temperature. Studies have shown that 3 at. % Nb doping the temperature is reduced to around 303 K (30 °C) depending on the amount of doping [126]. Other selected studies have reported that the phase transition temperature is dropped down to nearly 25 °C with 4 at. % W doping [127]. Figure 1.8 shows an example of the structure and operation of thermochromic and electrochromic smart windows.

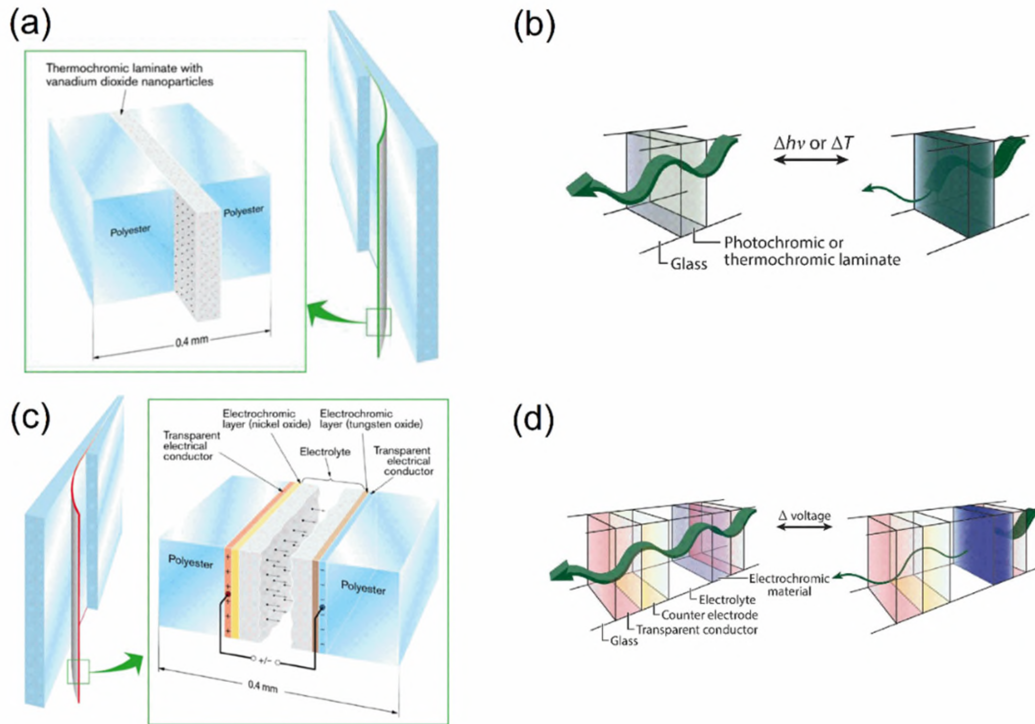

Figure 1.8 (a) VO_2 nanoparticle-based thermochromic smart window. After Granqvist [128] (b) Transmission of light through photochromic or thermochromic laminate. After Wang et al. [122] (c) Schematic of an electrochromic smart window. After Pehlivan et al. [129] (d) Transmission of light through an electrochromic laminate. After Wang et al. [122].

1.3.2 VO_2 Films in Optical Switches

Optical switches, also known as optical transistors, are devices that are used to switch or amplify optical (analog and/or digital) signals. Research on optical switches is based on the need to switch data streams at higher speeds efficiently (i.e., 1–4 Tbps [130]) to comply with the demands of computer and communications services for higher transmission and switching rates. The optical switching applications generally involve the NIR [131] and mid-IR [132], wavelength regions. Optical switches are integrated in optical transducers which are used in data centers. Efforts have been made to increase the efficiency of data transfer and storage in such devices [133]. VO_2 films have also shown promise as a medium for optical switching [134]. This material can be utilized in different types of switching applications namely all-optical switches [135−136] and

electro-optical switches [137−138], due to the ability of inducing thermochromic, photochromic and electrochromic switching capability.

In all-optical switches, the material regulates the transmission of information carried by light (photons). This is done by photoexciting the material at a certain wavelength by using a very short-duration pulse (femtosecond range) and short pulse repetition rate (on the order of Hz) to control the incoming signal (either blocking it or regulating its direction). A related work [135] has shown a switching in VO_2 films using light at a wavelength of 800 nm, with femtosecond-range pulses. In electro-optical switches, light (information) transfer is regulated by the optical switching in VO_2 films [139]. Such applications may require operations at elevated temperatures due to heating that arise in transducers and data centers. This has led to the research interests in increasing the phase transition temperature by elemental doping of VO_2 films as discussed in Section 1.2.5.

Figure 1.9 provides a representation of VO_2-based waveguides that are constructed for optical switching applications. Figure 1.9 (a) shows a hybrid Si/VO_2 electro-optical modulator where the modulation of light is actualized by applying an electric field between two coplanar Au electrodes on the opposite side of the waveguide plane [118]. Figure 1.9 (b) shows a VO_2-based Si_3N_4-SiO_2 all-optical switch, where SiO_2 is the substrate, Si_3N_4 is the waveguide and VO_2 acts as a switching surface for the optical switching process [140].

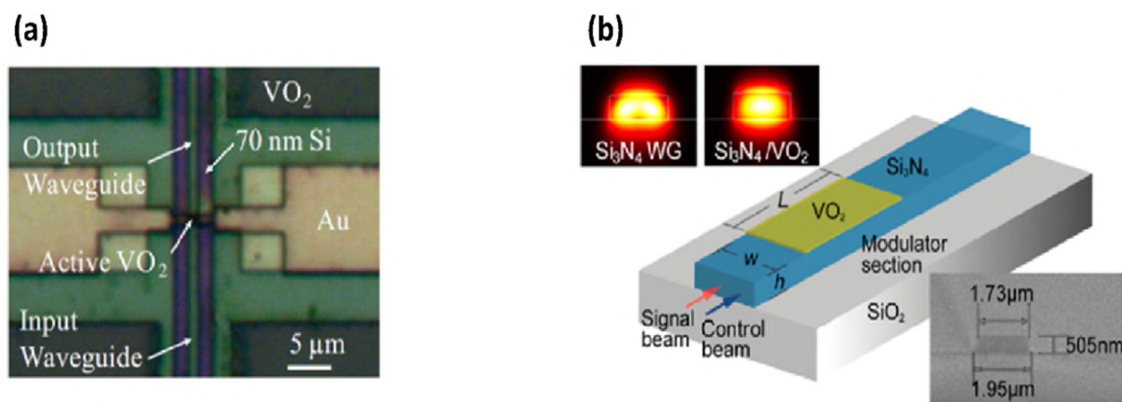

Figure 1.9 (a) A Si/VO_2hybrid electro-optical modulator on top of 2 µm-thick SiO_2 thermally grown on a Si substrate. After Joushaghani et al. [118]. (b) An optical switch based on a VO_2 film

grown on a Si_3N_4 waveguide on top of a SiO_2 substrate. A control beam is used to regulate the transmission of the incoming signal beam. After Wong et al. [140], in Ref. [141].

As mentioned above, new-generation communication systems demand faster data transfer times with a light frequency in the THz range. Figure 1.10 shows an illustration of (a) linear and (b) circular tuning of polarized light in VO_2-based programmable metasurfaces that are functionalized as switching devices for light modulation and data processing in the microwave band [142].

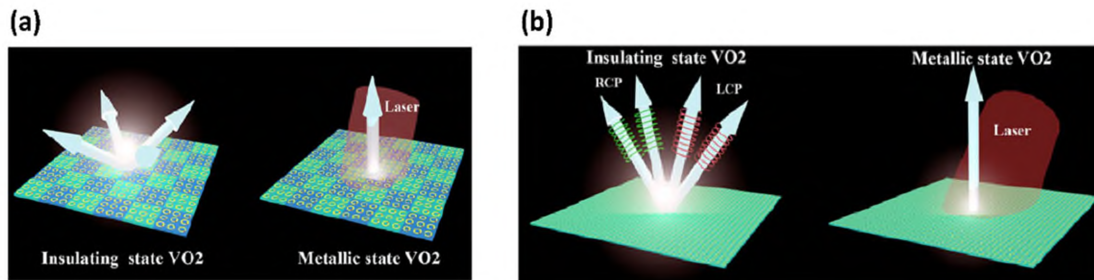

Figure 1.10 (a) A schematic of all-optical tunable coding metasurfaces based on Al–VO_2 hybrid resonators for modulation of linearly polarized terahertz waves. (b) Schematic of all-optical tunable coding metasurfaces based on Al–VO_2 hybrid resonators for modulation of circularly polarized terahertz waves. After Li et al. [142].

1.3.3 VO_2 Films in Mott-Field Effect Transistors

By definition, Mott insulators are materials that conduct electricity under conventional band theories but are insulators (semiconductors) at low temperatures. The functionality of Mott FETs is based on the Mott-Hubbard transition, which occurs due to electron-electron interactions, which is not considered in conventional band theory. The electronic (Mott-Hubbard) transition occurs between two split bands that are of the same character, i.e., 3d band in VO_2, namely π and // bands [143]. Mott FETs are considered as an alternative to conventional Si-based FETs due to the scaling limitations of the latter (i.e., with a minimum channel available to be around 300–400 Å [144]. The scaling problem in Si-based FETs can be overcome down to the nanometer scale using Mott field-effect transistors. The Mott insulators offer non-volatile storage capability which makes it possible to integrate the Mott FETs in multilayer device structures [145]. In Mott FETs,

the channel consists of a Mott insulator where the controlling mechanism of the channel conductivity is the MI phase transition, which is induced by applying voltage [146]. Recent advances have shown that single-crystal VO_2 nanobeams that exhibit intrinsic phase transition can be utilized in Mott FETs to eliminate the percolative domain structures that are present in VO_2 films [147].

Figure 1.11 presents selected designs of VO_2-based Mott FETs.

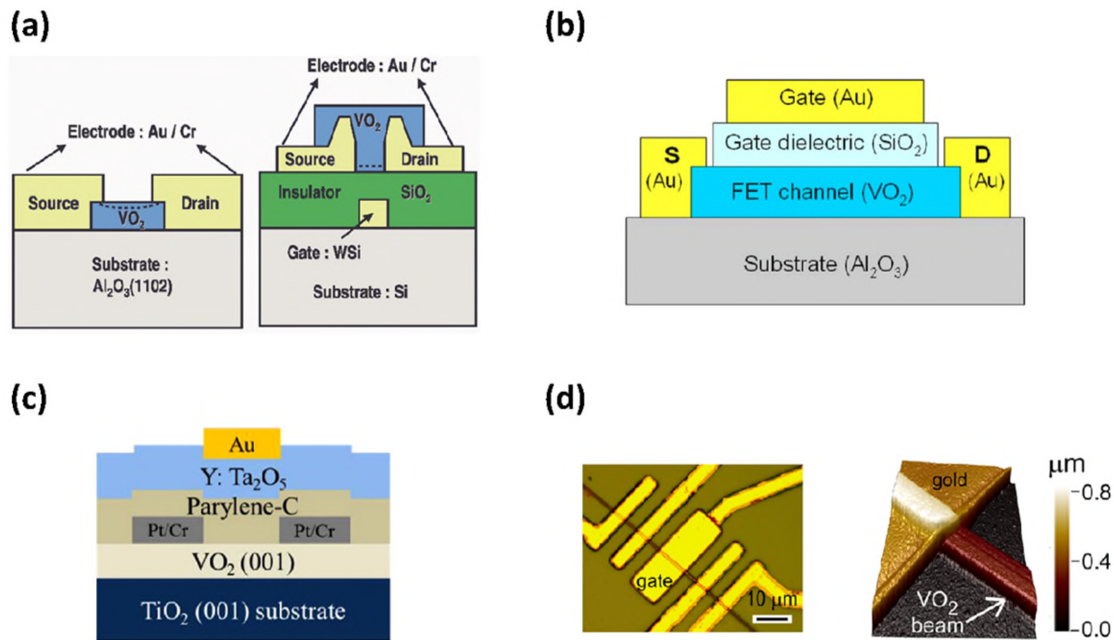

Figure 1.11 (a) Two-terminal and three-terminal configurations of Mott FET devices proposed by Kim et al. [143]. (b) A three-terminal Mott FET proposed by Ruzmetov et al. [148]. (c) VO_2 FETs with high-k oxide/organic parylene-C hybrid gate dielectric. After Wei et al. [149]. (d) Optical microscope (left) and atomic force microscope (right) images of a VO_2 nanobeam-based Mott FET with HfO_2 as the gate oxide material. After Sengupta et al. [147].

1.3.4 VO_2 Films in Threshold Switches

Field effect transistors are currently used in various digital electronic applications. The advancement of the FET technology has miniaturized every electronic component in a circuit in compliance with Moore’s law. The requirements of rapidly advancing technology include faster

and controllable FET response times. Many conventional metal oxide semiconductors have not been able to provide such fast FET dynamics. New metal oxide semiconductor (MOS) materials such as VO_2 have been a candidate for next-generation FETs (e.g., phase-FETs, hyper-FETs, FinFETs) with improved device features such as faster response time and limited drain current, due to the ultrafast IM and MI phase transition characteristics. A common application is to integrate a VO_2 layer in the gate of a FET device. As shown in Figure 1.12 (a), VO_2-based hybrid-phase transition field effect transistors is designed as a next-generation transistor to eliminate the Boltzmann limit (60 mV/decade limit) which restricts V_{GS} in conventional MOSFETs [150]. Also, shown in Figure 1.12 (b), the I_{DS} in the proposed device is controlled by the ultrafast electrical switching in VO_2. AlGaN/GaN phase FETs have also implemented VO_2 films as a load resistor for steep on/off switching [151].

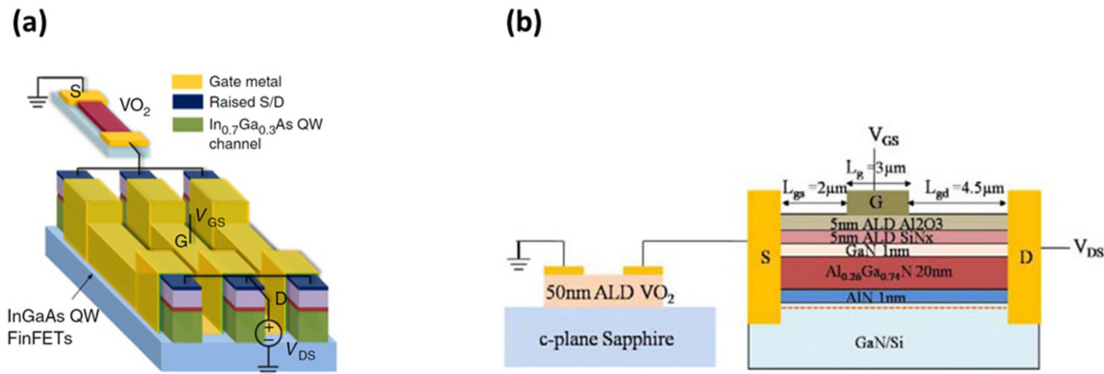

Figure 1.12 (a) A proposed InGaAs quantum well (QW) FinFET with VO_2 films as a reversible switch. After Shukla et al. [150]. (b) A proposed GaN phase-transition FET with ultralow off-state leakage. After Verma et al. [151].

1.3.5 VO_2 Films in Neuromorphic Devices

Neuromorphology is an emerging field that is based on electronic circuits (systems) that replicate neurological systems. The research in this area is focused on the investigation of memristive materials and the development of electronic neural devices and oscillatory neural networks. The crucial consideration in such neuromorphic systems is the provision of an efficient on/off response time. Important neuromorphic device features include the switching speed, switching energy of phase transition, reliability, and non-volatility of state [44]. VO_2 can also be

applied as memristive material for oscillatory systems due to its ultrafast volatile switching properties. The ultra-fast reversible memristive switching capability of VO_2 has been reported to be a critical feature for large coupled oscillatory systems used for computing complex algorithms, developed for biological behaviors (i.e., pattern recognition). Such selective works have reported the use of VO_2 in (neural) oscillatory circuits as in Refs. [152–155]. Figure 1.13 gives a comparison of a biological neuron and a lateral VO_2 film device and a capacitor utilized as an artificial neuron circuit. Figure 1.13 (a) shows a membrane of a biological neuron which is considered as a parallel connection of a membrane capacitance (C_M) and a membrane conductance (G_M) which changes by MI phase transition. The membrane is activated through steady current clamping which generates continuous action potential (AP). This results in the oscillation of trans-membrane potential (V_M) and the G_M. The AP can propagate along the axon and where the signal is transmitted to the other connected neurons. Figure 1.13 (b) shows the VO_2 device with two collateral electrodes used as an artificial neuron circuit. The reversible electrical MIT of VO_2 functions as an oscillator by changing the conductance to imitate the biological neuron. The change in material resistance (±1R in the figure) due to time-related degradation can be used to study neural disorders with respect to spike time.

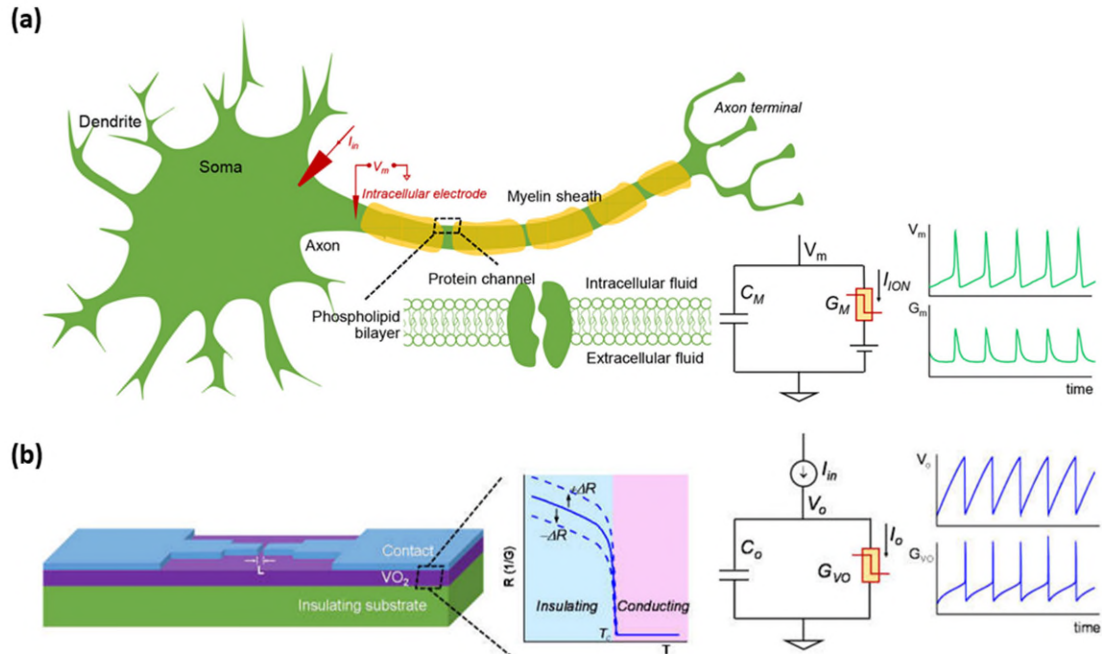

Figure 1.13 (a) A membrane of the biological neuron and its electronic circuit representation. Under stimulation, the trans-membrane potential (V_M) and membrane conductance (G_M) oscillates. (b) A lateral VO_2 device and a capacitor are used as an artificial neuron circuit. After Lin et al. [152].

1.4 Fabrication of VO_2 Thin Films by DC Magnetron Sputtering

Fabrication of high-quality films with near-single-crystal switching properties is of crucial importance in VO_2 research. To fabricate high-quality VO_2 films various fabrication methods have been employed. The most pronounced methods in VO_2 film fabrication include sol-gel, DC and RF (reactive) magnetron sputtering, chemical vapour deposition (CVD), pulsed laser deposition (PLD) and molecular beam epitaxy (MBE). Although there have been numerous studies on fabricating VO_2 films, to this date there is no certainty on which fabrication method could deliver the near-single-crystal VO_2 thin films. Nevertheless, as a conventional method, magnetron sputtering is widely referred to in thin film fabrication.

Magnetron sputtering technique is a common thin film deposition method used in vacuum technology. It has several advantageous features over other vacuum deposition methods such as

high deposition rates, low operating voltage and operating pressures (a few mTorr). This deposition is based on the sputtering of target ions from a cathode target material in a plasma environment. The plasma environment is generated by ionizing an inert gas (in this work, argon (Ar)) under an applied voltage difference between the cathode target and anode substrate. Magnetron is used to contain a stable glow discharge during the sputtering process and enhance the sputter yield of target ions. The target ions are extracted from the bombardment of Ar ions on the surface of the target material. The extracted target ions with sufficient kinetic energy travel across the deposition chamber and deposit on the substrate. A detailed explanation of the magnetron sputtering technique is discussed in Chapter 2.

Deposition parameters are of crucial importance in the preparation of thin films. Such parameters are substrate temperature, substrate biasing and oxygen (O_2) flow rate. Specifically, in the fabrication of VO_2 thin films by magnetron sputtering, the O_2 rate plays an important role in growing VO_2 films. This is due to its unstable electronic state of V which can combine with O in many different ways to form various oxides as shown in Figure 1.2. A small deviation in the oxygen content may lead to a non-uniformity of the vanadium oxidation state (V_2O_5, V_3O_6) and thereby result in a non-stoichiometric compound. This situation makes it quite difficult to obtain highly stoichiometric VO_2 films. Other aforementioned parameters also play an important role in the quality and stoichiometry of VO_2 thin films. As a motivation for the research covered in this dissertation, the fabrication of VO_2 films under different deposition conditions has been a main interest. We focus our interest on studying the effect of selected deposition parameters which are substrate biasing and substrate temperature on the phase transition properties of VO_2 thin films.

1.5 Motivation of Research

VO_2 thin films have been studied for many decades. Nevertheless, growing high-quality purely stoichiometric single-crystal films has been a quest in scientific research. On the other hand, depending on the type of application, the fabrication of VO_2 films is substrate specific. Until now, research has been carried out to deliver VO_2 films with distinguished phase transition properties on single-crystal p-Si, quartz and sapphire substrates. Also, research conducted on deposition techniques and conditions has attempted to deliver high-quality VO_2 films. There is wide literature available for research in this area to grow high-quality VO_2 films along with physical and structural characterization. In addition, the unresolved nature of the MI phase transition permits more experimental work to find an improved theoretical explanation that would elucidate this phenomenon. Moreover, the differences between electrical and structural MITs have been much debated. There is therefore still much interest in experimental work that uncovers the differences and similarities between the IM and MI transitions and between different external excitations of the transition. Given that there is no definitive consensus and many aspects of the phase transition in VO_2 films are not well-understood, especially the nature of carrier dynamics in the two phases, it is highly desirable to carry out as many structural, electrical, and optical experiments as possible on high-quality films through the IM/MI phase transitions. The latter has been the main motivation of this research in terms of advancing our knowledge of VO_2 films and providing new insights.

1.6 Objective of Research and the Thesis

This dissertation aims to study the fabrication and physical and structural characterization of VO_2 thin films along with a number of electrical and optical properties. The first objective of the research is to study the effect of the fabrication parameters of DC magnetron sputtering on the quality of VO_2 thin films. The quality of the film depends on the polycrystallinity, defects and residual strains present in the material, which affects the IM/MI phase transition characteristics. Indeed, the sharpest IM/MI transitions are observed in single-crystal VO_2 [156] with a non-existent hysteresis. The phase transition characteristics of VO_2 films may thus be manipulated for specific applications. In this regard, one of the interests focuses on examining the effect of substrate biasing during the sputtering of VO_2 thin films at a high deposition (substrate) temperature of 650 °C with

the goal of elevating the phase transition temperature of VO_2 films for hybrid optoelectronic devices. Also, there is still a demand for experimental work on VO_2 film production at more practical deposition conditions while maintaining film quality. Accordingly, the next interest focuses on the systematic investigation of the effect of substrate temperature on the growth of VO_2 thin films with the goal of producing high-quality films at more feasible temperatures.

The second objective is to study the synthesis, structure and optical properties of high-quality VO_2 thin films grown on silicon, quartz and sapphire substrates by high-temperature DC magnetron sputtering. It is well known that the choice of substrate has a large effect on the defects and the residual stress in the film, hence its quality. Ideally, the VO_2 films should be grown on single-crystal silicon wafers if VO_2 films are to be integrated into conventional microelectronics as part of integrated photonic devices. However, there are previous studies where sapphire and quartz crystals have been used and suggested as a good choice of substrate for high-quality VO_2 film growth. In nearly all cases, the films grown have been polycrystalline.

The third objective is to investigate the phase transition in VO_2 from a structural transition perspective based on the percolation theory. This theory has been effective in explaining many physical processes that undergo a transition. Fundamentally, percolation occurs in a solid with a predominantly phase A structure (e.g., insulating phase in VO_2) and a small amount of phase B (e.g., metallic phase in VO_2). When the volume of phase B reaches a critical threshold value (= 0.5) it becomes the dominant phase. Our objective has been to examine whether relevant classical effective medium approximations (EMA) or the percolation theory can be applied to VO_2 films and whether one can deduce the critical threshold values of the IM/MI phase transitions.

The fourth objective of this research is to examine the difference between the structural and electrical IM/MI transitions in VO_2 by passing sufficiently high electric current in a high-quality film. The net heat generated by self (joule)-heating, increases the temperature of the film which eventually undergoes IMT. There has been very limited past work in this area and our objective was to demonstrate the characteristics of electrical and optical switching under Joule-heating-induced IMT/MIT and explain their difference by considering percolation theory.

This dissertation follows a manuscript-style format. Chapter 2 covers the experimental procedures that are referred to in the fabrication and characterization of VO_2 thin films. Chapter 3

presents the technical analysis of the optical properties of thin films. In other words, it presents the fundamentals of light transmission, dispersion relations, definitions of optical constants and Swanepoel and Manifacier techniques that are commonly used in analyzing optical transmission (or, transmittance) spectra. Chapters 4 to 8 consist of works that have been published as manuscripts in four peer-reviewed journals. Finally, Chapter 9 compiles the outcomes of the conducted research and conclusions and proposes recommendations for future research.

Chapter 2 covers the fabrication method as well as the structural and physical characterization techniques of VO_2 films selected in the research. The chapter begins with introducing the DC magnetron sputtering with a concise explanation of the theory of the technique. Following the film fabrication, optical and electro-optical characterizations of VO_2 films are explained separately. Chapter 3 introduces the optical characterization methods of the Swanepoel and Manifacier techniques to extract the optical constants from the optical transmission spectra of VO_2 films on a transparent substrate. Chapter 4 includes the manuscript (Materials) on the effect of substrate biasing during DC magnetron sputtering on the quality of VO_2 thin films deposited on p-Si substrates and their insulator-metal transition behavior. Chapter 5 includes the manuscript (Materials) on the effect of substrate temperature on the structural, optical and electrical properties of DC magnetron sputtered VO_2 thin films. Chapter 6 (Journal of Alloys and Compounds) covers the manuscript based on the synthesis, structure and optical properties of high-quality VO_2 thin films grown on silicon, quartz and sapphire substrates by high-temperature magnetron sputtering: properties through the transition temperature. Chapter 7 includes the manuscript (Journal of Vacuum Science and Technology A) on the topology of conductive clusters in sputtered high-quality VO_2 thin films on the brink of percolation threshold during insulator-to-metal and metal-to-insulator transitions. Chapter 8 (Journal of Materials Science: Materials in Electronics) includes the self-heating-induced electrical and optical switching in high-quality VO_2 films controlled with current pulses. Chapter 9 summarizes the conducted research and provides conclusions with possible research related to VO_2 films and related devices.

1.7 References

[1] F. J. Morin, "Oxides Which Show a Metal-to-Insulator Transition at the Neel Temperature," *Physical Review Letters*, vol. 3, pp. 34-36, 1959.

[2] Y. Ke, S. Wang, G. Liu, M. Li, T. J. White and Y. Long, "Vanadium dioxide: The multi stimuli responsive material and its applications," *Small*, vol. 14, no. 39, p. 1802025, 2018.

[3] C. Ko and S. Ramanathan, "Observation of electric field-assisted phase transition in thin film vanadium oxide in a metal-oxide-semiconductor device geometry," *Applied Physics Letters*, vol. 93, no. 25, p. 252101, 2008.

[4] A. Cavalleri, C. Tóth, C. W. Siders, J. A. Squier, F. Ráksi, P. Forget and J. C. Kieffer, "Femtosecond structural dynamics in VO 2 during an ultrafast solid-solid phase transition," *Physical Review Letters*, vol. 87, no. 23, p. 237401, 2001.

[5] A. Cavalleri, T. Dekorsy, H. H. Chong, J. C. Kieffer and R. W. Schoenlein, "Evidence for a structurally-driven insulator-to-metal transition in VO 2: A view from the ultrafast timescale," *Physical Review B*, vol. 70, no. 16, p. 161102, 2004.

[6] J. Kim, K. Park, S. Jo, B. J. Kim, H. W. Kang, S. Y. Nam, ... and Y. W. Lee, "Memristive states in vanadium-dioxide-based planar devices stimulated by 966 nm infrared laser pulses," *Japanese Journal of Applied Physics*, vol. 54, no. 10, p. 102601, 2015.

[7] S. Wall, S. Yang, L. Vidas, M. Chollet, J. M. Glownia, M. Kozina, ... and M. Trigo, "Ultrafast disordering of vanadium dimers in photoexcited VO2," *Science*, vol. 362, no. 6414, pp. 572-576, 2018.

[8] A. Pashkin, C. Kübler, H. Ehrke, R. Lopez, A. Halabica, R. F. Haglund Jr., ... and A. Leitenstorfer, "Ultrafast insulator-metal phase transition in VO 2 studied by multiterahertz spectroscopy," *Physical Review B*, vol. 83, no. 19, p. 195120, 2011.

[9] X. Li, Y. Wang, B. X. Y. Chen, Z. Tian, G. Huang and Y. Mei, "Growth and stress analyses of vanadium dioxide nanomembranes for controllable rolling," *Journal of Physics D: Applied Physics*, vol. 53, no. 45, p. 455105, 2020.

[10] J. Cao, Y. Gu, W. Fan, L. Q. Chen, D. F. Ogletree, K. Chen, ... and J. Wu, "Extended mapping and exploration of the vanadium dioxide stress-temperature phase diagram," *Nano Letters*, vol. 10, no. 7, pp. 2667-2673, 2010.

[11] T. Driscoll, H. T. Kim, B. G. Chae, M. D. Ventra and D. N. Basov, "Phase-transition driven memristive system," *Applied Physics Letters*, vol. 95, no. 4, p. 043503, 2009.

[12] A. Rana, C. Li, G. Koster and H. Hilgenkamp, "Resistive switching studies in VO2 thin films," *Scientific Reports*, vol. 10, no. 1, pp. 1-6, 2020.

[13] P. Kumbhakar, C. C. Gowda, P. L. Mahapatra, M. Mukherjee, K. D. Malviya, M. Chaker, ... and C. S. Tiwary, "Emerging 2D metal oxides and their applications," *Materials Today*, vol. 45, pp. 142-168, 2021.

[14] Z. Yang, C. Ko and S. Ramanathan, "Oxide Electronics Utilizing Ultrafast Metal-Insulator Transitions," *Annual Review of Materials Research*, vol. 41, no. 1, p. 337, 2011.

[15] N. Bahlawane and D. Lenoble, "Vanadium oxide compounds: structure, properties, and growth from the gas phase," *Chemical Vapor Deposition*, vol. 20, no. 7-8-9, pp. 299-311, 2014.

[16] Y. Zhang, A. Pan, S. Liang, T. Chen, Y. Tang and X. Tan, "Reduced graphene oxide modified V2O3 with enhanced performance for lithium-ion battery," *Materials Letters*, vol. 137, pp. 174-177, 2014.

[17] Y. Zhang, F. Zhang, L. Yu, M. Fan, Y. Zhong, X. Liu, ... and C. Huang, "Synthesis and characterization of belt-like VO2(B)@carbon and V2O3@carbon core–shell structured composites," *Colloids and Surfaces A: Physicochemical and Engineering Aspects*, vol. 396, pp. 144-152, 2012.

[18] K. West, B. Zachau-Christiansen, T. Jacobsen and S. Atlung, "V6O13 as cathode material for lithium cells," *Journal of Power Sources*, vol. 14, no. 1-3, pp. 235-245, 1985.

[19] Y. L. Ding, Y. Wen, C. Wu, P. A. van Aken, J. Maier and Y. Yu, "3D V6O13 nanotextiles assembled from interconnected nanogrooves as cathode materials for high-energy lithium ion batteries," *Nano Letters*, vol. 15, no. 2, pp. 1388-1394, 2015.

[20] M. Isacfranklin, G. Ravi, R. Yuvakkumar, P. Kumar, D. Velauthapillai, B. Saravanakumar and E. S. Babu, "Vanadium oxide nanostructures for electrochemical supercapacitor applications," in *AIP Conference Proceedings*, 2020.

[21] L. Zhang, M. Yang, S. Zhang, Z. Wu, A. Amini, Y. Zhang, ... and C. Cheng, "V2O5-C-SnO2 hybrid nanobelts as high performance anodes for lithium-ion batteries," *Scientific Reports*, vol. 6, no. 1, pp. 1-9, 2016.

[22] G. Gu, M. Schmid, P. W. Chiu, A. Minett, J. Fraysse, G. T. Kim, ... and R. H. Baughman, "V2O5 nanofibre sheet actuators," *Nature Materials*, vol. 2, no. 5, pp. 316-319, 2003.

[23] Z. Shao, X. Cao, H. Luo and P. Jin, "Recent progress in the phase-transition mechanism and modulation of vanadium dioxide materials," *NPG Asia Materials*, vol. 10, no. 7, pp. 581-605, 2018.

[24] J. B. Goodenough, "The two components of the crystallographic transition in VO2," *Journal of Solid State Chemistry*, vol. 3, no. 4, pp. 490-500, 1971.

[25] D. Wegkamp and J. Stähler, "Ultrafast dynamics during the photoinduced phase transition in VO2," *Progress in Surface Science*, vol. 90, no. 4, pp. 464-502, 2015.

[26] H. A. Jahn and E. Teller, "Stability of polyatomic molecules in degenerate electronic states-I—Orbital degeneracy," *Proceedings of the Royal Society of London. Series A-Mathematical and Physical Sciences*, vol. 161, no. 905, pp. 220-235, 1937.

[27] R. M. Wentzcovitch, W. W. Schulz and P. B. Allen, "VO 2: Peierls or Mott-Hubbard? A view from band theory," *Physical Review Letters*, vol. 72, no. 21, p. 3389, 1994.

[28] V. Eyert, "VO2: A novel view from band theory," *Physical Review Letters*, vol. 107, no. 1, p. 016401, 2011.

[29] N. F. Mott, "Metal-insulator transition," *Reviews of Modern Physics*, vol. 40, no. 4, p. 677, 1968.

[30] J. Hubbard, "Electron correlations in narrow energy bands," *Proceedings of the Royal Society of London. Series A. Mathematical and Physical Sciences*, vol. 276, no. 1365, pp. 238-257, 1963.

[31] R. Peierls and R. E. Peierls, *Quantum theory of solids*, Oxford: Oxford University Press, 1955.

[32] R. J. O. Mossanek and M. Abbate, "Evolution of the d‖ band across the metal–insulator transition in VO2," *Solid State Communications*, vol. 135, no. 3, pp. 189-192, 2005.

[33] B. Rajeswaran, I. J. Tadeo and A. M. Umarji, "IR photoresponsive VO 2 thin films and electrically assisted transition prepared by single-step chemical vapor deposition," *Journal of Materials Chemistry C*, vol. 8, no. 36, pp. 12543-12550, 2020.

[34] D. Fu, K. Liu, T. Tao, K. Lo, C. Cheng, B. Liu, ... and J. Wu, "Comprehensive study of the metal-insulator transition in pulsed laser deposited epitaxial VO2 thin films," *Journal of Applied Physics*, vol. 113, no. 4, p. 043707, 2013.

[35] M. M. Qazilbash, M. Brehm, B. G. Chae, P. C. Ho, G. O. Andreev, B. J. Kim, ... and D. N. Basov, "Mott transition in VO2 revealed by infrared spectroscopy and nano-imaging," *Science*, vol. 318, no. 5857, pp. 1750-1753, 2007.

[36] S. Kumar, J. P. Strachan, Pickett, M. D., A. Bratkovsky, Y. Nishi and R. S. Williams, "Sequential electronic and structural transitions in VO2 observed using X-ray absorption spectromicroscopy," *Advanced Materials*, vol. 26, no. 44, pp. 7505-7509, 2014.

[37] J. Nag, "The solid-solid phase transition in vanadium dioxide thin films: synthesis, physics and application," Ph.D. Dissertation, Dept. Phys., Vanderbilt Univ., Nashville, TN, 2011.

[38] Y. Zhou, X. Chen, C. Ko, Z. Yang, C. Mouli and S. Ramanathan, "Voltage-triggered ultrafast phase transition in vanadium dioxide switches," *IEEE Electron Device Letters*, vol. 34, no. 2, pp. 220-222, 2013.

[39] M. Soltani, M. Chaker, E. Haddad, R. Kruzelecky, J. Margot, P. Laou and S. Paradis, "Fabrication of stationary micro-optical shutter based on semiconductor-to-metallic phase transition of W-doped VO 2 active layer driven by an external voltage," *Journal of Vacuum Science & Technology A: Vacuum, Surfaces, and Films*, vol. 26, no. 4, pp. 763-767, 2008.

[40] F. Chudnovskiy, S. Luryi and B. Spivak, "Switching device based on first-order metal-insulator transition induced by external electric field. Future trends in microelectronics: the nano millennium," *Future trends in microelectronics: The Nano Millennium*, p. 148, 2002.

[41] J. J. Yang, D. B. Strukov and D. R. Stewart, "Memristive devices for computing," *Nature Nanotechnology*, vol. 8, no. 1, pp. 13-24, 2013.

[42] M. J. Lee, Y. Park, D. S. Suh, E. H. Lee, S. Seo, D. C. Kim, ... and B. H. Park, "Two series oxide resistors applicable to high speed and high density nonvolatile memory," *Advanced Materials*, vol. 19, no. 22, pp. 3919-3923, 2007.

[43] V. P. Melnik, I. M. Khatsevych, Y. V. Goltvyanskyi, V. A. Nikirin, B. M. Romanyuk, V. G. Popov, ... and A. V. Kuchuk, "Thermochromic Properties of Vanadium Dioxide Films Obtained by Magnetron Sputtering," *Ukrainian Journal of Physics*, vol. 56, no. 6, pp. 535-541, 2011.

[44] S. Lee, T. L. Meyer, S. Park, T. Egami and H. N. Lee, "Growth control of the oxidation state in vanadium oxide thin films," *Applied Physics Letters*, vol. 105, no. 22, p. 223515, 2014.

[45] Y. Zhao, J. H. Lee, Y. Zhu, M. Nazari, C. Chen, H. Wang, ... and Z. Fan, "Structural, electrical, and terahertz transmission properties of VO2 thin films grown on c-, r-, and m-plane sapphire substrates," *Journal of Applied Physics*, vol. 111, no. 5, p. 053533, 2012.

[46] S. Zhou and Y. Ramanathan, "Mott memory and neuromorphic devices," *Proceedings of the IEEE*, vol. 103, no. 8, pp. 1289-1310, 2015.

[47] J. M. Atkin, S. Berweger, E. K. Chavez, M. B. Raschke, J. Cao, W. Fan and J. Wu, "Strain and temperature dependence of the insulating phases of VO 2 near the metal-insulator transition," *Physical Review B*, vol. 85, no. 2, p. 020101, 2012.

[48] S. R. Broadbent and J. M. Hammersley, "Percolation processes: I. Crystals and mazes," in *Mathematical proceedings of the Cambridge philosophical society*, Cambridge University Press, vol. 53, no. 3, pp. 629-641, 1957.

[49] M. Sahimi. (April, 2014). *Applications of percolation theory* [Online]. Taylor&Francis Ltd. Available: https://www.taylorfrancis.com/books/mono/10.1201/9781482272444/applications-percolation-theory-sahimi

[50] K. Shimakawa and S. Nitta, "Percolation-controlled conduction in chalcogenide glass semiconductors," *Physical Review B*, vol. 17, no. 10, p. 3950, 1978.

[51] L. A. Tracy, E. H. Hwang, K. Eng, G. A. T. Eyck, E. P. Nordberg, K. Childs, ... and S. D. Sarma, "Observation of percolation-induced two-dimensional metal-insulator transition in a Si MOSFET," *Physical Review B*, vol. 79, no. 23, p. 235307, 2009.

[52] B. Magyari-Köpe, M. Tendulkar, S. G. Park, H. D. Lee and Y. Nishi, "Resistive switching mechanisms in random access memory devices incorporating transition metal oxides: TiO2, NiO and Pr0. 7Ca0. 3MnO3," *Nanotechnology*, vol. 22, no. 25, p. 254029, 2011.

[53] B. I. Shklovskiĭ and A. L. V. Éfros, "Percolation theory and conductivity of strongly inhomogeneous media," *Soviet Physics Uspekhi*, vol. 18, no. 11, p. 845, 1975.

[54] A. Bunde and J. W. Kantelhardt, "Diffusion and conduction in percolation systems," in *Diffusion in Condensed Matter*, Heidelberg, Berlin, Springer, 2005, pp. 895-914.

[55] A. R. Gentle, G. B. Smith and A. I. Maaroof, "Frequency and percolation dependence of the observed phase transition in nanostructured and doped VO2 thin films," *Journal of Nanophotonics,* vol. 3, no. 1, p. 031505, 2009.

[56] T. H. Yang, R. Aggarwal, A. Gupta, H. Zhou, R. J. Narayan and J. Narayan, "Semiconductor-metal transition characteristics of VO 2 thin films grown on c-and r-sapphire substrates," *Journal of Applied Physics*, vol. 107, no. 5, p. 053514, 2010.

[57] K. Shibuya, J. Y. Tsutsumi, T. Hasegawa and A. Sawa, "Fabrication and Raman scattering study of epitaxial VO2 films on MgF2 (001) substrates," *Applied Physics Letters*, vol. 103, no. 2, p. 021604, 2013.

[58] J. Ma, G. Xu, L. Miao, M. Tazawa and S. Tanemura, "Thickness-dependent structural and optical properties of VO2 thin films," *Japanese Journal of Applied Physics*, vol. 50, no. 2, p. 020215, 2011.

[59] G. J. Kovács, D. Bürger, I. Skorupa, H. Reuther, R. Schmidt and H. Heller, "Effect of the substrate on the insulator–metal transition of vanadium dioxide films," *Journal of Applied Physics*, vol. 109, no. 6, p. 063708, 2011.

[60] J. A. Creeden, S. E. Madaras, D. B. Beringer, M. R. Beebe, I. Novikova and R. Lukaszew, "Structural and photoelectric properties of epitaxially grown vanadium dioxide thin films on c-plane sapphire and titanium dioxide," *Scientific Reports*, vol. 9, no. 1, pp. 1-9, 2019.

[61] A. Paone, R. Sanjines, P. Jeanneret, H. J. Whitlow, E. Guibert, G. Guibert, ... and A. Schüler, "Influence of doping in thermochromic V1− xWxO2 and V1− xAlxO2 thin films: Twice improved doping efficiency in V1− xWxO2.," *Journal of Alloys and Compounds*, vol. 621, pp. 206-211, 2015.

[62] S. Wang, W. Wei, T. Huang, M. Yuan, Y. Yang, W. Yang, ... and N. Dai, "Al-Doping-Induced VO2 (B) Phase in VO2 (M) Toward Smart Optical Thin Films with Modulated ΔTvis and ΔTc," *Advanced Engineering Materials*, vol. 21, no. 12, p. 1900947, 2019.

[63] E. Cavanna, J. P. Segaud and J. Livage, "Optical switching of Au-doped VO2 sol-gel films," *Materials Research Bulletin*, vol. 34, no. 2, pp. 167-177, 1999.

[64] Y. Zhu, F. He and J. Na, "Au doping effects on electrical and optical properties of vanadium dioxides," *Science China Physics, Mechanics and Astronomy*, vol. 55, no. 3, pp. 409-412, 2012.

[65] T. Hajlaoui, N. Emond, C. Quirouette, B. L. Drogoff, J. Margot and M. Chaker, "Metal–insulator transition temperature of boron-doped VO2 thin films grown by reactive pulsed laser deposition," *Scripta Materialia*, vol. 177, pp. 32-37, 2020.

[66] L. Song, Y. Zhang, W. Huang, Q. Shi, D. Li, Y. Zhang and Y. Xu, "Preparation and thermochromic properties of Ce-doped VO2 films," *Materials Research Bulletin*, vol. 48, no. 6, pp. 2268-2271, 2013.

[67] C. Lu, W. Liang, M. Gao, S. N. Luo and Y. Lin, "Terahertz Transmittance of Cobalt-Doped VO2 Thin Film: Investigated by Terahertz Spectroscopy and Effective Medium Theory," *IEEE Transactions on Terahertz Science and Technology*, vol. 9, no. 2, p. 177–185, 2019.

[68] L. Lu, Z. Wu, C. Ji, M. Song, H. Feng, X. Ma and Y. Jiang, "Effect of Fe doping on thermochromic properties of VO2 films," *Journal of Materials Science: Materials in Electronics*, vol. 29, no. 7, pp. 5501-5508, 2018.

[69] M. Panagopoulou, E. Gagaoudakis, N. Boukos, E. Aperathitis, G. Kiriakidis, D. Tsoukalas and Y. S. Raptis, "Thermochromic performance of Mg-doped VO2 thin films on functional substrates for glazing applications," *Solar Energy Materials and Solar Cells*, vol. 157, pp. 1004-1010, 2016.

[70] M. Wan, M. Xiong, N. Li, B. Liu, S. Wang, W. Y. Ching and X. Zhao, "Observation of reduced phase transition temperature in N-doped thermochromic film of monoclinic VO2," *Applied Surface Science*, vol. 410, pp. 363-372, 2017.

[71] R. Zhang, C. Yin, Q. Fu, C. Li, G. Qian, X. Chen, ... and H. Tao, "Metal-to-insulator transition and its effective manipulation studied from investigations in V1-xNbxO2 bulks," *Ceramics International*, vol. 44, no. 3, pp. 2809-2813, 2018.

[72] X. Lv, Y. Cao, L. Yan, Y. Li, Y. Zhang and L. Song, "Atomic Layer Deposition of V1–x Mo x O2 Thin Films, Largely Enhanced Luminous Transmittance, Solar Modulation," *ACS Applied Materials & Interfaces*, vol. 10, no. 7, pp. 6601-6607, 2018.

[73] D. Gu, X. Zhou, Z. Sun and Y. Jiang, "Influence of Gadolinium-doping on the microstructures and phase transition characteristics of VO2 thin films," *Journal of Alloys and Compounds*, vol. 705, pp. 64-69, 2017.

[74] W. A. N. G. Bin, E. H. Li, J. J. Du, Z. H. U. Jun, L. B. Li and T. T. Zhou, "Effects of heat treatment conditions and Y-doping on structure and phase transition temperature of VO2 powders," *Transactions of Nonferrous Metals Society of China*, vol. 30, no. 4, pp. 1038-1045, 2020.

[75] X. Wu, Z. Wu, H. Zhang, R. Niu, Q. He, C. Ji, ... and Y. Jiang, "Enhancement of VO2 thermochromic properties by Si doping," *Surface and Coatings Technology*, vol. 276, pp. 248-253, 2015.

[76] Z. Huang, Z. Wu, C. Ji, J. Dai, Z. Xiang, D. Wang, ... and Y. Jiang, "Improvement of phase transition properties of magnetron sputtered W-doped VO2 films by post-annealing approach," *Journal of Materials Science: Materials in Electronics*, vol. 31, no. 5, pp. 4150-4160, 2020.

[77] A. Romanyuk, R. Steiner, L. Marot and P. Oelhafen, "Temperature-induced metal–semiconductor transition in W-doped VO2 films studied by photoelectron spectroscopy," *Solar Energy Materials and Solar Cells*, vol. 91, no. 19, pp. 1831-1835, 2007.

[78] W. Lu, G. Zhao, B. Song, J. Li, X. Zhang and G. Han, "Preparation and thermochromic properties of sol-gel-derived Zr-doped VO2 films," *Surface and Coatings Technology*, vol. 320, pp. 311-314, 2017.

[79] B. Li, S. Tian, Z. Wang, B. Liu, X. Gong and X. Zhao, "Thermochromic Ta Doped VO2 Films: Enhanced Luminous Transmittance, Significantly Depressed Phase Transition Temperature and Hysteresis Width.," *Applied Surface Science*, vol. 568, p. 150959, 2021.

[80] Z. Gao, Z. Liu, Y. Ping, Z. Ma, X. Li, C. Wei, ... and Y. Liu, "Low metal–insulator transition temperature of Ni-doped vanadium oxide films," *Ceramics International*, vol. 47, no. 20, pp. 28790-28796, 2021.

[81] Y. Chen, Z. Wang, S. Chen, H. Ren, B. Li, W. Yan, ... and C. Zou, "Electric-field control of Li-doping induced phase transition in VO2 film with crystal facet-dependence," *Nano Energy*, vol. 51, pp. 300-307, 2018.

[82] Y. Hu, Q. Shi, W. Huang, H. Zhu, F. Yue, Y. Xiao, ... and T. Lu, "Preparation and phase transition properties of Ti-doped VO2 films by sol–gel process," *Journal of Sol-Gel Science and Technology*, vol. 78, no. 1, pp. 19-25, 2016.

[83] M. Marezio, D. B. McWhan, J. P. Remeika and P. D. Dernier, "Structural Aspects of the Metal-Insulator Transitions in Cr-Doped VO2," *Physical Review B*, vol. 5, no. 7, p. 2541, 1972.

[84] B. L. Brown, M. Lee, P. G. Clem, C. D. Nordquist, T. S. Jordan, S. L. Wolfley, ... and J. A. Custer, "Electrical and optical characterization of the metal-insulator transition temperature in Cr-doped VO2 thin films," *Journal of Applied Physics*, vol. 113, no. 17, p. 173704, 2013.

[85] Y. Zhang, J. Zhang, X. Zhang, C. Huang, Y. Zhong and Y. Deng, "The additives W, Mo, Sn and Fe for promoting the formation of VO2 (M) and its optical switching properties," *Materials Letters*, vol. 92, pp. 61-64, 2013.

[86] A. Krammer, A. Magrez, W. A. Vitale, P. Mocny, P. Jeanneret, E. Guibert, ... and A. Schüler, "Elevated transition temperature in Ge doped VO2 thin films," *Journal of Applied Physics*, vol. 122, no. 4, p. 045304, 2017.

[87] M. H. Lee, M. G. Kim and H. K. Song, "Thermochromism of rapid thermal annealed VO2 and Sn-doped VO2 thin films," *Thin Solid Films*, vol. 290, pp. 30-33, 1996.

[88] I. J. Tadeo, B. Rajeswaran and A. M. Umarji, "Influence of Ce–W co-doping on phase transition temperature of VO2 thin films deposited by ultrasonic nebulized spray pyrolysis of aqueous combustion mixture," *Journal of Physics D: Applied Physics*, vol. 53, no. 18, p. 185104, 2020.

[89] L. Fan, Y. Zhu, S. Zhao, Z. Wang, Z. Liu, L. Zhu, ... and Q. Zhang, "Modulation of VO2 metal-insulator transition by co-doping of hydrogen and oxygen vacancy," *Solar Energy Materials and Solar Cells*, vol. 212, p. 110562, 2020.

[90] N. Wang, S. Liu, X. T. Zeng, S. Magdassi and Y. Long, "Mg/W-codoped vanadium dioxide thin films with enhanced visible transmittance and low phase transition temperature," *Journal of Materials Chemistry C*, vol. 3, no. 26, pp. 6771-6777, 2015.

[91] Z. Zhao, Y. Liu, Z. Yu, C. Ling, J. Li, Y. Zhao and H. Jin, "Sn–W Co-doping improves thermochromic performance of VO2 films for smart windows," *ACS Applied Energy Materials*, vol. 3, no. 10, pp. 9972-9979, 2020.

[92] M. Okada, A. Takeyama and Y. Yamada, "Thermal hysteresis control of VO2 (M) nanoparticles by Ti-F codoping," *Nano-Structures & Nano-Objects*, vol. 20, p. 100395, 2019.

[93] M. Soltani, M. Chaker, E. Haddad, R. V. Kruzelecky and J. Margot, "Effects of Ti–W codoping on the optical and electrical switching of vanadium dioxide thin films grown by a reactive pulsed laser deposition," *Applied Physics Letters*, vol. 85, no. 11, p. 1958, 2004.

[94] W. Burkhardt, T. Christmann, S. Franke, W. Kriegseis, D. Meister, B. K. Meyer, ... and A. Scharmann, "Tungsten and fluorine co-doping of VO2 films," *Thin Solid Films*, vol. 402, no. 1-2, pp. 226-231, 2002.

[95] M. K. Dietrich, F. Kuhl, A. Polity and P. J. Klar, "Optimizing thermochromic VO2 by co-doping with W and Sr for smart window applications," *Applied Physics Letters*, vol. 110, no. 14, p. 141907, 2017.

[96] Q. He, D. Zhang, Y. Huang, Y. Yang, H. Guan, J. Fan and P. Jin, "Employing Ni-Cr co-doping to prepare low phase transition temperature VO2 film," in *In Tenth International Conference on Thin Film Physics and Applications*, July 2019.

[97] X. Zhong, X. Zhang, A. Gupta and P. LeClair, "Avalanche breakdown in microscale VO2 structures," *Journal of Applied Physics*, vol. 110, no. 8, p. 084516, 2011.

[98] D. Li, A. A. Sharma, D. K. Gala, N. Shukla, H. Paik, S. Datta, ... and M. Skowronski, "Joule heating-induced metal–insulator transition in epitaxial VO2/TiO2 devices," *ACS Applied Materials & Interfaces*, vol. 8, no. 20, pp. 12908-12914, 2016.

[99] C. Zhang, O. Gunes, C. K. J. Peng, S. J. Wen, R. Wong, ... and S. O. Kasap, "Structural mapping of single-crystal VO2 microrods through metal-to-insulator phase transition," *Journal of Materials Science*, vol. 56, no. 1, pp. 260-268, 2021.

[100] L. Zhang, J. Yao, Y. Guo, F. Xia, Y. Cui and B. Liu, "VO 2 (A) nanorods : One-pot synthesis, formation mechanism and thermal transformation to VO 2 (M)," *Ceramics International*, vol. 44, no. 16, pp. 19301–19306, 2018.

[101] S. H. Bae, S. Lee, H. Koo, L. Lin, B. H. Jo, C. Park and Z. L. Wang, "The memristive properties of a single VO2 nanowire with switching controlled by self-heating," *Advanced Materials*, vol. 25, no. 36, pp. 5098-5103, 2013.

[102] J. Liang, Q. Lou, W. Wu, K. Wang, ... and C. Xuan, "NO2 gas sensing performance of a VO2 (B) ultrathin vertical nanosheet array: Experimental and DFT investigation," *ACS Applied Materials & Interfaces*, vol. 13, no. 27, pp. 31968-31977, 2021.

[103] F. Sediri and N. Gharbi, "Controlled hydrothermal synthesis of VO2 (B) nanobelts," *Materials Letters*, vol. 63, no. 1, pp. 15-18, 2009.

[104] T. V. M. Sreekanth, M. Tamilselvan, K. Yoo and J. Kim, "Microwave-assisted in situ growth of VO2 nanoribbons on Ni foam as inexpensive bifunctional electrocatalysts for

the methanol oxidation and oxygen evolution reactions," *Applied Surface Science*, vol. 570, p. 151119, 2021.

[105] C. Zhang, J. Wang, Y. Li, X. Li, C. Koughia, S. J. Wen, ... and S. Kasap, "VO2 microrods synthesized from V2O5 thin films," *Applied Surface Science*, vol. 476, pp. 259-264, 2019.

[106] C. Koughia, O. Gunes, C. Zhang, S. J. Wen, Q. Yang and S. O. Kasap, "Size-Dependent Insulator-to-Metal and Metal-to-Insulator Phase Transitions in VO2 Microrods Grown on a Silicon Substrate," *physica status solidi (a)*, vol. 218, no. 14, p. 2100165, 2021.

[107] E. Strelcov, Y. Lilach and A. Kolmakov, "Gas sensor based on metal− insulator transition in VO2 nanowire thermistor," *Nano Letters*, vol. 9, no. 6, pp. 2322-2326, 2009.

[108] C. Niu, J. Meng, C. Han, K. Zhao, M. Yan and L. Mai, "VO2 nanowires assembled into hollow microspheres for high-rate and long-life lithium batteries," *Nano Letters*, vol. 14, no. 5, pp. 2873-2878, 2014.

[109] S. Zhang, B. Shang, J. Yang, W. Yan, S. Wei and Y. Xie, "From VO2 (B) to VO2 (A) nanobelts: first hydrothermal transformation, spectroscopic study and first principles calculation," *Physical Chemistry Chemical Physics*, vol. 13, no. 35, pp. 15873-15881, 2011.

[110] Y. Zhang, "VO (B) conversion to VO (A) and VO (M) and their oxidation resistance and optical switching properties," *Materials Science-Poland*, vol. 34, no. 1, pp. 169-176, 2016.

[111] S. Ni, H. Zeng and X. Yang, "Fabrication of VO2 (B) nanobelts and their application in lithium ion batteries," *Journal of Nanomaterials*, 2011, pp.1-4.

[112] T. Luo, Y. Liu, H. Su, R. Xiao, L. Huang, Q. Q. Xiang, ... and C. Chen, "Nanostructured-VO2 (B): A high-capacity magnesium-ion cathode and its electrochemical reaction mechanism," *Electrochimica Acta*, vol. 260, pp. 805-813, 2018.

[113] K. C. Kam and A. K. Cheetham, "Thermochromic VO2 nanorods and other vanadium oxides nanostructures," *Materials Research Bulletin*, vol. 41, no. 5, pp. 1015-1021, 2006.

[114] M. Yamamoto, R. Nouchi, T. Kanki, A. N. Hattori, K. Watanabe, T. Taniguchi, ... and H. Tanaka, "Gate-tunable thermal metal–insulator transition in VO2 monolithically integrated into a WSe2 field-effect transistor," *ACS Applied Materials & Interfaces*, vol. 11, no. 3, pp. 3224-3230, 2019.

[115] L. Pellegrino, N. Manca, T. Kanki, H. Tanaka, M. Biasotti, E. Bellingeri, ... and D. Marré, "Multistate memory devices based on free-standing VO2/TiO2 microstructures driven by Joule self-Heating," *Advanced Materials*, vol. 24, no. 21, pp. 2929-2934, 2012.

[116] C. Cheng, H. Guo, A. Amini, K. Liu, D. Fu, J. Zou and H. Song, "Self-assembly and horizontal orientation growth of VO2 nanowires," *Scientific Reports*, vol. 4, no. 1, pp. 1-5, 2014.

[117] Y. Cheng, T. L. Wong, K. M. Ho and N. Wang, "The structure and growth mechanism of VO2 nanowires," *Journal of Crystal Growth*, vol. 311, no. 6, pp. 1571-1575, 2009.

[118] A. Joushaghani, J. Jeong, S. Paradis, D. Alain, J. S. Aitchison and J. K. Poon, "Characteristics of the current-controlled phase transition of VO2 microwires for hybrid optoelectronic devices," *Photonics*, vol. 2, no. 3, pp. 916-932, 2015.

[119] D. Singh and B. Viswanath, "In situ nanomechanical behavior of coexisting insulating and metallic domains in VO2 microbeams," *Journal of Materials Science*, vol. 52, no. 10, pp. 5589-5599, 2017.

[120] Z. Li, J. Wu, Z. Hu, Y. Lin, Q. Chen, Y. Guo, ... and Y. Xie, "Imaging metal-like monoclinic phase stabilized by surface coordination effect in vanadium dioxide nanobeam," *Nature Communications*, vol. 8, no. 1, pp. 1-7, 2017.

[121] F. Sediri, F. Touati and N. Gharbi, "From V2O5 foam to VO2 (B) nanoneedles," *Materials Science and Engineering: B*, vol. 129, no. 1-3, pp. 251-255, 2006.

[122] Y. Wang, E. L. Runnerstrom and D. J. Milliron, "Switchable materials for smart windows," *Annual Review of Chemical and Biomolecular Engineering*, vol: 7, pp. 283-304, 2016.

[123] C. Bechinger, J. N. Bullock, J. G. Zhang, C. E. Tracy, D. K. Benson, S. K. Deb and H. M. Branz, "Low-voltage electrochromic device for photovoltaic-powered smart windows," *Journal of Applied Physics*, vol. 80, no. 2, pp. 1226-1232, 1996.

[124] C. O. Avellaneda, "Electrochromic performance of sol–gel deposited V2O5: Ta films," *Materials Science and Engineering: B*, vol. 138, no. 2, pp. 118-122, 2007.

[125] G. A. Niklasson and C. G. Granqvist, "Electrochromics for smart windows: thin films of tungsten oxide and nickel oxide, and devices based on these," *Journal of Materials Chemistry*, vol. 17, no. 2, pp. 127-156, 2007.

[126] Z. L. Wang, R. Zhang, X. H. Chen, Q. S. Fu, C. L. Li, S. L. Yuan, ... and H. Z. Tao, "Nb doping effect in VO2 studied by investigations of magnetic behavior," *Ceramics International*, vol. 44, no. 7, pp. 8623-8627, 2018.

[127] D. Liu, H. Cheng, X. Xing, C. Zhang and W. Zheng, "Thermochromic properties of W-doped VO2 thin films deposited by aqueous sol-gel method for adaptive infrared stealth application," *Infrared Physics & Technology*, vol. 77, pp. 339-343, 2016.

[128] C. G. Granqvist, "Oxide-based chromogenic coatings and devices for energy efficient fenestration: brief survey and update on thermochromics and electrochromics," *Journal of Vacuum Science & Technology B, Nanotechnology and Microelectronics: Materials, Processing, Measurement, and Phenomena*, vol. 32, no. 6, p. 060801, 2014.

[129] I. B. Pehlivan, R. Marsal, E. Pehlivan, E. L. Runnerstrom, D. J. Milliron, C. G. Granqvist and G. A. Niklasson, "Electrochromic devices with polymer electrolytes functionalized by SiO2 and In2O3: Sn nanoparticles: Rapid coloring/bleaching dynamics and strong near-infrared absorption," *Solar Energy Materials and Solar Cells*, vol. 126, pp. 241-247, 2014.

[130] Q. Cheng, M. Bahadori, M. Glick, S. Rumley and K. Bergman, "Recent advances in optical technologies for data centers: a review," *Optica*, vol. 5, no. 11, pp. 1354-1370, 2018.

[131] S. Fardad, S. Das, A. Salandrino, E. Breckenfeld, H. Kim, J. Wu and R. Hui, "All-optical short pulse translation through cross-phase modulation in a VO 2 thin film," *Optics Letters*, vol. 41, no. 2, pp. 238-241, 2016.

[132] E. Azmoudeh and S. Farazi, "Ultrafast and low power all-optical switching in the mid-infrared region based on nonlinear highly doped semiconductor hyperbolic metamaterials," *Optics Express*, vol. 29, no. 9, pp. 13504-13517, 2021.

[133] V. Shukla, R. Srivastava and D. K. Choubey, "Optical switching in next-generation data centers: architectures based on optical switching," in *Contemporary developments in high-frequency photonic devices*, 2019.

[134] F. Beteille and J. Livage, "Optical switching in VO2 thin films," *Journal of Sol-Gel Science and Technology*, vol. 13, no. 1, pp. 915-921, 1998.

[135] F. Moradiani, M. Seifouri, K. Abedi and F. G. Gharakhili, "High extinction ratio all-optical modulator using a vanadium-dioxide integrated hybrid plasmonic waveguide," *Plasmonics*, vol. 16, no. 1, pp. 189-198, 2021.

[136] M. Soltani, M. Chaker, E. Haddad and R. Kruzelesky, "1× 2 optical switch devices based on semiconductor-to-metallic phase transition characteristics of VO2 smart coatings," *Measurement Science and Technology*, vol. 17, no. 5, p. 1052, 2006.

[137] M. Sun, M. Taha, S. Walia, M. Bhaskaran, S. Sriram, W. Shieh and R. R. Unnithan, "A photonic switch based on a hybrid combination of metallic nanoholes and phase-change vanadium dioxide," *Scientific Reports*, vol. 8, no. 1, pp. 1-9, 2018.

[138] L. Sanchez, S. Lechago, A. Gutierrez and P. Sanchis, "Analysis and design optimization of a hybrid VO 2/Silicon2 $\times $2 microring switch," *IEEE Photonics Journal*, vol. 8, no. 2, pp. 1-9, 2016.

[139] S. Chen, H. Ma, X. Yi, H. Wang, X. Tao, M. Chen, ... and C. Ke, "Optical switch based on vanadium dioxide thin films," *Infrared Physics & Technology*, vol. 45, no. 4, pp. 239-242, 2004.

[140] H. M. Wong, Z. Yan, K. A. Hallman, R. E. Marvel, R. P. Prasankumar, R. F. Haglund Jr and A. S. Helmy, "Broadband, integrated, micron-scale, all-optical Si3N4/VO2 modulators with pJ switching energy," *ACS Photonics*, vol. 6, no. 11, pp. 2734-2740, 2019.

[141] S. Cueff, J. John, Z. Zhang, J. Parra, J. Sun, R. Orobtchouk, ... and P. Sanchis, "VO2 nanophotonics," *APL Photonics*, vol. 5, no. 11, p. 110901, 2020.

[142] J. Li, Y. Yang, J. Li, Y. Zhang, Z. Zhang, H. Zhao, ... and J. Yao, "All-optical switchable vanadium dioxide integrated coding metasurfaces for wavefront and polarization manipulation of terahertz beams," *Advanced Theory and Simulations*, vol. 3, no. 1, p. 1900183, 2020.

[143] H. T. Kim, B. G. Chae, D. H. Youn, S. L. Maeng, G. Kim, K. Y. Kang and Y. S. Lim, "Mechanism and observation of Mott transition in VO2-based two-and three-terminal devices," *New Journal of Physics*, vol. 6, no. 1, p. 52, 2004.

[144] M. A. Belyaev, V. Putrolaynen, A. A. Velichko, G. B. Stefanovich and A. L. Pergament, "Field-effect modulation of resistance in VO2 thin film at lower temperature," *Japanese Journal of Applied Physics*, vol. 53, no. 11, p. 111102, 2014.

[145] D. M. Newns, J. A. Misewich, C. C. Tsuei, A. Gupta, B. A. Scott and A. Schrott, "Mott transition field effect transistor," *Applied Physics Letters*, vol. 73, no. 6, pp. 780-782, 1998.

[146] G. Stefanovich, A. Pergament and D. Stefanovich, "Electrical switching and Mott transition in VO2," *Journal of Physics: Condensed Matter*, vol. 12, no. 41, p. 8837–8845, 2000.

[147] S. Sengupta, K. Wang, K. Liu, A. K. Bhat, S. Dhara, J. Wu and M. M. Deshmukh, "Field-effect modulation of conductance in VO2 nanobeam transistors with HfO2 as the gate dielectric," *Applied Physics Letters*, vol. 99, no. 6, p. 062114, 2011.

[148] D. Ruzmetov, G. Gopalakrishnan, C. Ko, V. Narayanamurti and S. Ramanathan, "Three-terminal field effect devices utilizing thin film vanadium oxide as the channel layer," *Journal of Applied Physics*, vol. 107, no. 11, p. 114516, 2010.

[149] T. Wei, T. Kanki, K. Fujiwara, M. Chikanari and H. Tanaka, "Electric field-induced transport modulation in VO2 FETs with high-k oxide/organic parylene-C hybrid gate dielectric," *Applied Physics Letters*, vol. 108, no. 5, p. 053503, 2016.

[150] N. Shukla, A. V. Thathachary, A. Agrawal, H. Paik, A. Aziz, D. G. Schlom, ... and S. Datta, "A steep-slope transistor based on abrupt electronic phase transition," *Nature Communications*, vol. 6, no. 1, pp. 1-6, 2015.

[151] A. Verma, B. Song, B. Downey, V. D. Wheeler, D. J. Meyer, H. G. Jena and D. Xing, "Steep sub-Boltzmann switching in AlGaN/GaN phase-FETs with ALD VO 2," *IEEE Transactions on Electron Devices*, vol. 65, no. 3, pp. 945-949, 2018.

[152] J. Lin, S. Guha and S. Ramanathan, "Vanadium dioxide circuits emulate neurological disorders," *Frontiers in Neuroscience*, vol. 12, p. 856, 2018.

[153] W. Yi, K. K. Tsang, S. K. Lam, X. Bai, J. A. Crowell and E. A. Flores, "Biological plausibility and stochasticity in scalable VO2 active memristor neurons," *Nature Communications*, vol. 9, no. 1, pp. 1-10, 2018.

[154] M. D. Pickett, G. Medeiros-Ribeiro and R. S. Williams, "A scalable neuristor built with Mott memristors," *Nature Materials*, vol. 12, no. 2, pp. 114-117, 2013.

[155] E. Corti, B. Gotsmann, K. Moselund, A. M. Ionescu, J. Robertson and S. Karg, "Scaled resistively-coupled VO2 oscillators for neuromorphic computing," *Solid-State Electronics*, vol. 168, p. 107729, 2020.

[156] B. Fisher and L. Patlagan, "Switching VO2 single crystals and related phenomena: sliding domains and crack formation," *Materials*, vol. 10, no. 5, p. 554, 2017.

2. Experimental Procedures

2.1 Introduction

This chapter covers the experimental procedures that are carried out to prepare and characterize VO_2 films to study the research interests proposed in the previous chapter. It consists of three sections which explain the preparation, fabrication, electrical and optoelectronic characterization as well as structural characterization of VO_2 films. In the first section, the brief description of magnetron sputtering technique and the preparation of VO_2 films using DC magnetron sputtering is introduced. In the second section, the methods used for the optical and optoelectronic characterization of VO_2 films is presented. In the third section, the structural characterization techniques used in the examination of VO_2 films are introduced.

2.2 Magnetron Sputtering and Fabrication of VO_2 Thin Films

Sputtering is a commonly used technique in the fabrication of thin films [1,2]. It has many advantages over other deposition techniques. The distinct advantages are mainly high deposition rates, the convenience of sputtering metals, alloys and compounds, delivering highly adhesive and high-purity films with excellent uniformity on large-area substrates, ability to coat heat-sensitive substrates and easy accessibility [3]. In this section, the fundamental concepts of the magnetron sputtering technique are covered. Initially, a brief description of magnetron sputtering technique is given. Afterwards, the features of the sputtering system (SPT-320, Plasmionique) used in the preparation of VO_2 films are described. Lastly, the sputtering procedure followed for the fabrication of VO_2 films is explained.

2.2.1 Magnetron Sputtering Technique

In general, this method can be used for micromachining [4], wafer patterning [5], and depth profiling [3]. The method is based on the creation of surface erosion on a target material to extract energetic atoms or ions and deposit them on a hard surface, namely the substrate. The sputtering process is based on the transfer of the physical momentum and the kinetic energy of incident ions from the plasma onto the surface atoms of the target. Energetic particles (e.g., ions) are extracted

from the surface of the target material by use of plasma. Under plasma conditions, numerous amounts of energetic atoms/ions extracted from the target surface accelerate toward the substrate surface. The cloud of highly accelerated atoms/ions impinges on the substrate. A magnetron sputtering source takes advantage of the above phenomena by using magnets to confine the electrons in the plasma near the surface of the target. Magnetron sputtering deposition can be carried out using different power delivery systems such as DC, pulsed DC and RF sputtering.

One of the fundamental measures of the sputtering method is yield (Y). This parameter describes the ratio of the number of emitted particles from the target surface to the number of incident particles on the substrate.

$$Y = \frac{\text{Number of emitted particles}}{\text{Number of incident particles}} \tag{2.1}$$

The yield varies with respect to the ionization energy regime. In order to generate ionized particles from the target material, a certain amount of energy has to be applied through the cathode. The minimum amount of energy required to extract such an ionized particle is called the threshold energy (E_{th}). There are typically four different energy ranges for magnetron sputtering. These are classified as low-energy range (30– 50 eV), knock-on energy regime (40 eV−1 keV), collision cascade sputtering regime (1 keV− 50 keV), and high implantation regime (> 50 keV) as given in Table 2.1 below:

Table 2.1 The ionization energy regimes. After Rossnagel [6].

Range name	Ionization energy range (eV)
Low energies	30–50
Knock-on energy regime	40–1,000
Collision-cascade regime	1,000–50,000
High-energy implantation regime	≥ 50,000

In the low-energy regime, the extraction of ionized particles from the target is minimal. The yield in this regime is low, typically 10^{-2} or below [6]. In the knock-on regime there is sufficient energy around and just above the threshold energy level (E_{th}) to extract ions.

Maximum yield can be achieved for the best mass matching of the incident ions with the molar mass of the target material. Also increasing the angle of incidence (i.e., from normal incidence (0°) to 45°) significantly increases the yield by a factor (1.5 to 3) for most materials. The sputtering rate scales with discharge power involved in the plasma (i.e., doubling the discharge power in a sputtering system would result in a doubling of the deposition rate). In the collision-cascade sputtering regime, a sufficient amount of energy is delivered to break all bonds from the target surface at the site of impact.

In the high-energy implantation regime above 50 keV, the incident ions have enough energy to penetrate below the surface of the material and thereby cause damage at the surface. As a result, nearly no particles get extracted from the target material's surface, where the highly energetic beams are simply implanted (absorbed) within the target. Figure 2.1 (a) shows an illustration of the sputtering of ions from the surface of the target material.

Figure 2.1 (b) shows a sketch of a planar magnetron. A magnetron generates a magnetic field ($\vec{B}$) which confines the secondary electrons extracted from the target surface within the plasma. The secondary electrons close to the target surface drift in a closed loop due to the electric

field ($\vec{E}$) and strong $\vec{B}$ near the target surface. Thus, a highly dense plasma is maintained near the target surface which causes more ionization of the target atoms.

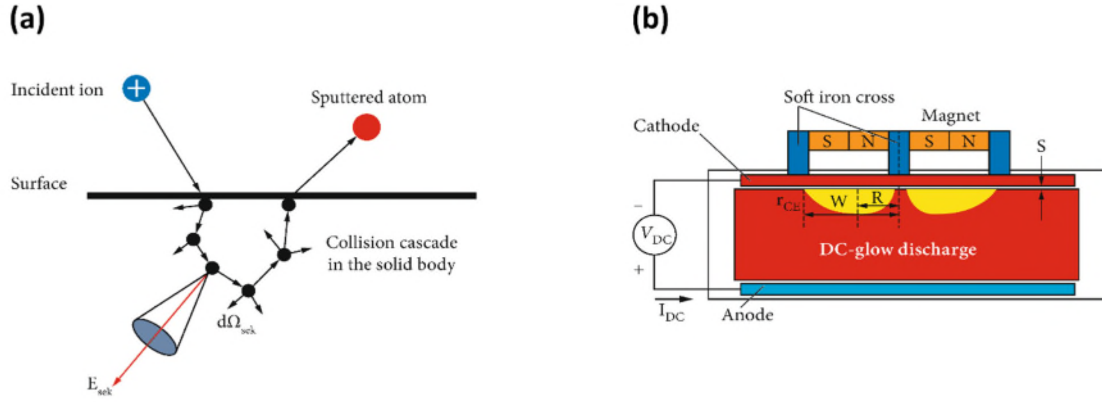

Figure 2.1 (a) Energy transfer from incident ions to sputtered atoms. (b) A planar magnetron in a sputtering system. $d\Omega_{sek}$ represents the solid angle and E_{sek} is the energy of secondary particles created from the collisions of the incident ions on the surface of the material. Here, R represents the sputtering radius, W is the width of the magnetic field ring and r_{CE} is the height of the ring. After Frey [7].

Bombardment angle plays an important role in the yield (Y) of sputtered atoms/ions [7]. The relation between the total sputter yield (Y_{total}) and the bombardment angle (Θ) is given as,

$$Y_{total}(\Theta) = Y_o + \Delta Y(\Theta) \tag{2.2}$$

where the change in the yield can be written as,

$$\Delta Y(\Theta) = c\sigma_d \frac{\gamma_{kin} E_o}{r_{atom}^2 U_o} \frac{\Theta^2}{\Theta_{opt}^2} \tag{2.3}$$

where σ_d represents the distance from the center of the incident ions with energy E_o to the target atom and r_{atom} the target atom radius. The c is a constant with a measured value of 0.0025 [7]. γ_{kin} is the kinematic factor, and the Θ_{opt} represents the optimal bombardment angle. At $\Theta = \Theta_{opt}$, the

yield becomes maximum. The optimal angle Θ_{opt} is different in every material and typically lies between 60–70°. Figure 2.2 gives the *Y* of several materials. For vanadium (not shown in the graph), the *Y* at 600 keV is 0.7 [8].

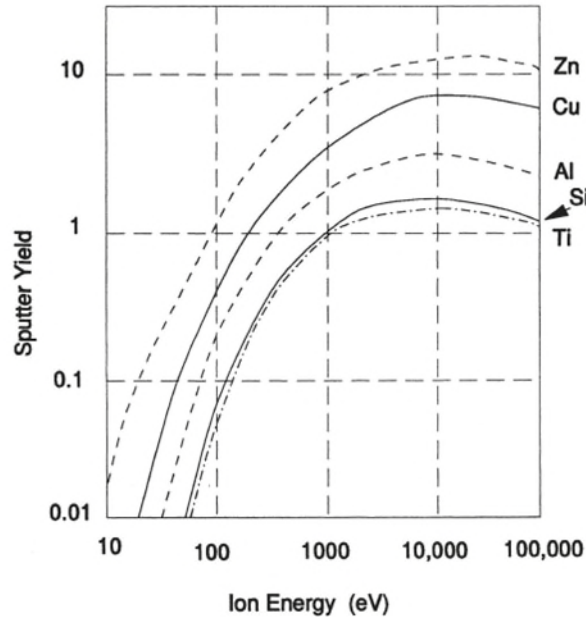

Figure 2.2 Sputter yield (*Y*) of different materials as a function of Ar ion energies. After Matsunami et al. [9].

Magnetron sputtering takes place under a stable plasma environment. To sustain a constant plasma during the sputtering process, the flow of inert or reactive gas should be maintained at a constant rate. Before the application of bias to the target cathode, inert or reactive gas (e.g., Ar or O_2) is brought into the sputtering chamber. The plasma environment is generated by ionizing the gas present in the chamber under an applied voltage difference between the cathode target and the anode substrate. Magnetron is used to contain a stable glow discharge during the sputtering process and enhance the sputter yield of target ions as mentioned earlier. The target ions are extracted from the bombardment of Ar ions on the surface of the target material. The extracted target ions with sufficient kinetic energy travel across the deposition chamber and deposit on the substrate. Figure 2.3. shows a typical magnetron sputtering event under stable plasma.

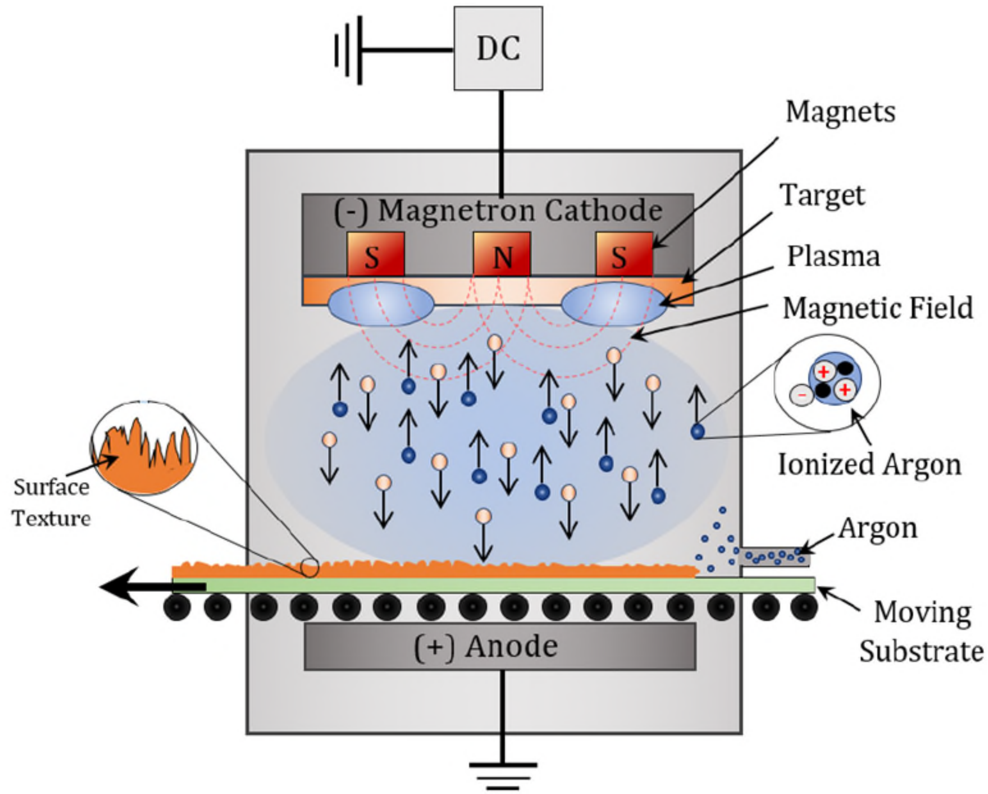

Figure 2.3 An illustration of a magnetron sputtering event. Partially extracted from Shaat [10].

To facilitate as many high-energy collisions as possible – leading to increased deposition rates – the sputtering gas is typically chosen to be a high molecular weight gas such as argon (Ar) or xenon (Xe). If a reactive sputtering process is desired, gases such as oxygen (O_2) or nitrogen (N) can also be introduced to the chamber during film growth.

2.2.2 SPT-320 Magnetron Sputtering System

The SPT-320 magnetron sputtering system consists of six parts. These are mainly the vacuum chamber, vacuum system, substrate holder, deposition sources, gas and fluid distribution system and control system [11]. The vacuum system consists of a main deposition chamber, where the sputtering takes place. Also, specific to the system, there may be an additional vacuum chamber called the load-lock chamber. This chamber is used to load substrates on a ceramic substrate cradle and transfer the substrates into the main chamber. The substrate holder hosts the substrate loaded on a cradle in the main chamber. This part can be rotated at a selected speed (rpm) and heated

during the sputtering process to allow the substrate to reach the desired substrate temperature. The deposition sources consist of magnetrons, remote plasma source and power generators. Gas/fluid distribution system is used to supply gas/fluid into the main deposition chamber during the sputtering process.

In the SPT-320 magnetron sputtering system there are three gas flow lines for oxygen (O_2), argon (Ar) and nitrogen (N) gas flow. Constant gas flow is regulated by calibrated mass flow controls (MFCs). Additionally, a control system is used to control the power distribution box, heater box, control box for general system control, gas distribution and motor control modules for substrate holder rotation. All the elements in the control system are commanded by an all-in computer Labview-built-in software with a graphical interface.

There are two ways to apply power to the cathode, either DC (direct current) or RF (radio frequency) power. Both biases are frequently used for fabricating VO_2 films (e.g., Refs. [12,13]). Sputtering can also be performed by applying pulsed DC for high-pulsed-power sputtering. During the preparation of VO_2 thin films, only DC power was used.

An overall view of the sputtering system used for VO_2 deposition can be found in Figure 2.4 (a). The system consists of a deposition chamber with three guns with selection for DC, pulsed-DC and RF sputtering, a load-lock chamber and an operation cabinet with all supply units and software set-up to control the deposition process. Figure 2.4 (b) shows a view of the deposition chamber. There are three targets that are available for deposition. The substrates are inserted onto the substrate holder from the load-lock chamber by a transfer fork. The transfer of the substrates takes place at pressures in the range of 1-3 mTorr. After the transfer of the substrates the gate between the deposition chamber and the load-lock chamber is closed. The deposition chamber is pumped down to a high vacuum level (4×10^{-7} torr) for the sputtering process.

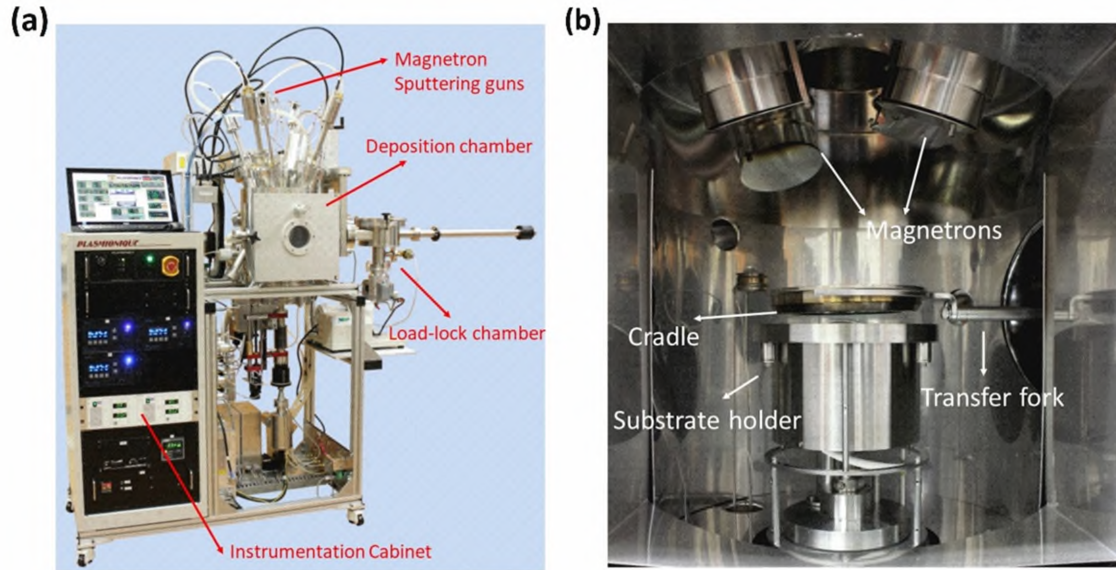

Figure 2.4 A view of the Plasmionique SPT-320 Magnetron sputter deposition system. (b) Inside view of the sputter chamber. The substrate cradle is positioned on the substrate holder. The loading process is commanded from the software control window. The fork is moved back to the load-lock chamber after the substrate plate is loaded. Taken from Plasmionique Inc. [11].

Figure 2.5 shows the front panel of the control software where the entire command of the sputtering process takes place. The software consists of four tabs: process control, gas & pressure, graphs and alarms. In the process control tab, the desired magnetron is selected for sputtering. Two targets are utilized for DC magnetron sputtering and the third target is used for RF magnetron sputtering. The substrate temperature, rotation speed and position can be adjusted using this tab. Chamber pressure and film thickness monitoring during the deposition chamber are also available tools. In the pressure & gas tab the pressure of the chamber and the flow rate of gases (Ar and O_2) are selected. The graphs tab displays and records the chamber pressure as well as the flow rate of Ar and O_2 during deposition and the substrate temperature during the deposition. The Alarm tab consists of a set of alarms to ensure communication between all the instruments and the control software.

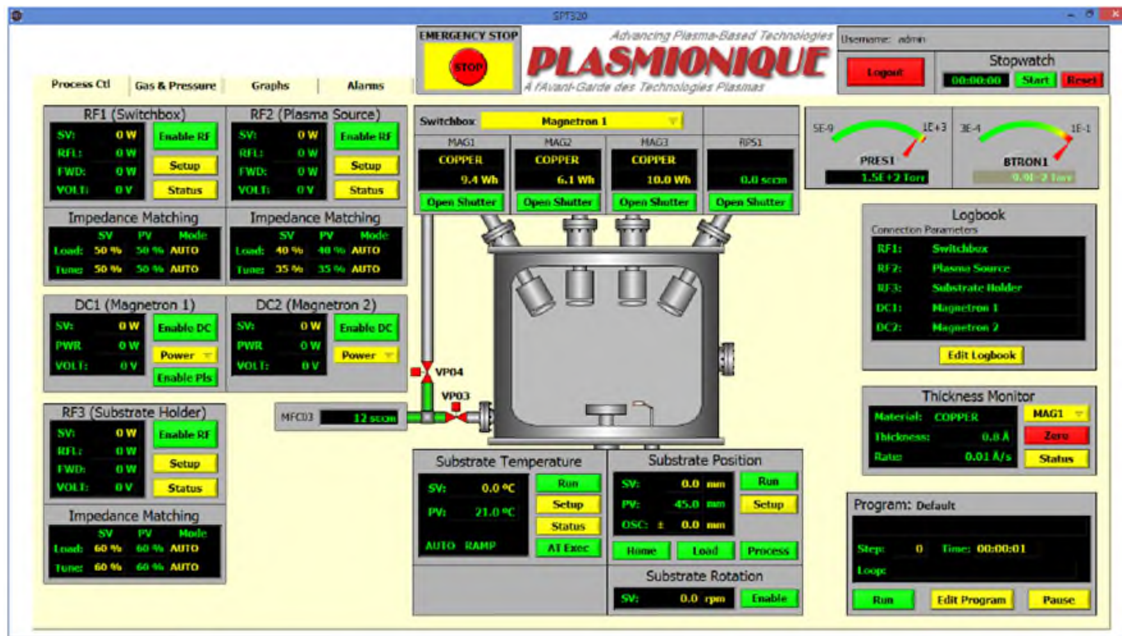

Figure 2.5 Sputtering process control window. Desired magnetron is enabled through an "enable" button. Substrate temperature, position, rotation speed, chamber pressure can be adjusted. A stopwatch is used to set up a time to monitor the period of deposition. Taken from Plasmionique Inc. [11].

2.2.3 Fabrication of VO_2 Thin Films

Preparation of VO_2 films consists of several steps. Initially, deep cleaning of the sputtering chamber is carried out for high-purity VO_2 deposition. In this process, the target gun shields, substrate holder and the inner shields protecting the side surface of the chamber are sandblasted and then cleaned with ethanol with the use of KimWipes™. A high-purity vanadium target (99.95%) is used for the deposition. The target is placed in a gun that was supplied to generate DC voltage between the substrate and the target. The system is pumped down to an ultra-high vacuum level where the chamber pressure is stabilized around 4×10^{-7} torr.

Selected substrates (i.e., sapphire) are ultrasonically cleaned with ethanol for approximately 15 minutes and then dried with Kimwipes™. Clean substrates are placed on a transfer cradle in a load-lock chamber. To transfer the substrates, Ar gas (5 SCCM) is purged into the sputtering chamber to increase the pressure and the load-lock chamber is pumped down to

avoid a large pressure difference between the two chambers. During the transfer of the substrates, the pressure in the two chambers is equal and in the mTorr range. The cradle is transferred to the sputtering chamber by use of a transfer arm and placed on the substrate holder.

VO_2 films are prepared by DC magnetron sputtering in a reactive environment. For deposition, Plasmionique SPT-320 magnetron sputter system. High-purity vanadium target (Plasmionique Inc., purity: 99.5%, diameter: 2″, thickness: 0.25″), was used and sputtered in an Ar and O_2 atmosphere at a low constant chamber pressure (1.33 Pa). The substrate temperature was 650 °C for the deposition of high-quality VO_2 thin films. Information about the preparation parameters is covered in Chapters 4 to 8.

2.3 Optical and Electro-Optical Characterization of VO_2 Thin Films

2.3.1 Optical Characterization of VO_2 Films

Optical spectrophotometry is a common technique used to characterize the optical transmission of the examined materials (e.g., transition metal oxides) in a light wavelength spectrum typically spanning ultraviolet (UV), visible (Vis) and near-infrared (NIR) regions. The optical transmittance, reflectance or absorbance of a thin film may be examined using a spectrophotometer. With the use of analysis techniques (e.g., Swanepoel model [14]) the optical constants of the material (i.e., optical absorption coefficient and refractive index) can be extracted from the spectrum. These parameters can later be used to calculate the optical band gap of the material as well as the complex refractive index. Detailed information on the analysis of optical the transmission spectrum of thin films and the extraction of optical constants is covered in Chapter 3.

The characterization of the optical spectrum of VO_2 films is carried out by use of a Perkin Elmer Lambda900 optical spectrophotometer, presented in Figure 2.6. The optical system of the spectrophotometer consists of two light sources (a deuterium (D) and a tungsten (W) lamp). The W-lamp is used to measure sample transmittance at visible (Vis) and near-infrared (NIR) regions. There are two monochromators and a set of mirrors to separate the incoming beam from the light source into two beams and guide them to the sample compartment. These are named reference and

sample beams which become incident on reference and sample slits, respectively. The examined film is mounted on the sample slit, where the reference slit is essentially empty. The transmitted beams enter the detector compartment. The transmittance of the sample is measured from the intensity ratio of the detected sample and reference beams.

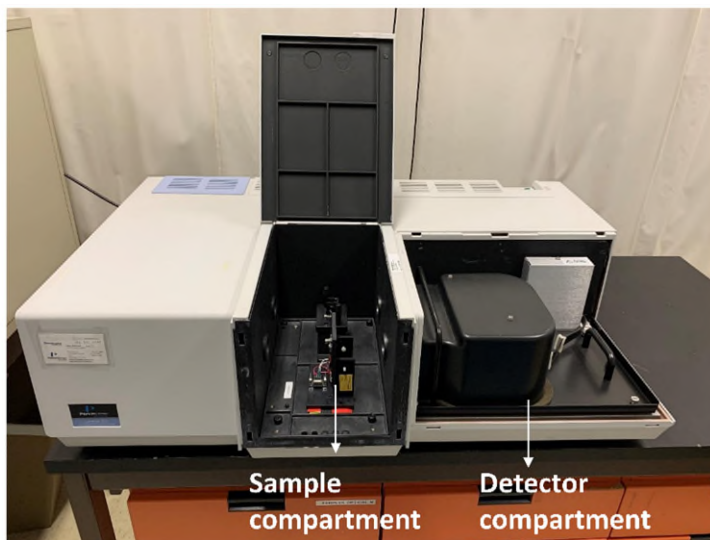

Figure 2.6 Perkin Elmer Lambda 900 UV-Vis-NIR spectrophotometer.

2.3.2 Electro-Optical Characterization of VO_2 Films

Simultaneous optical and electrical characterization of transition metal oxides such as vanadium dioxide is rarely reported; generally, the two characterizations are carried out separately. The importance of characterizing optical and electrical properties, which are optical transmittance and electrical resistivity (conductivity) respectively, may contribute to a better understanding and evaluation of the performance of the phase transition in VO_2 films. Specifically, investigating the optical and electrical switching in VO_2 films from the effect of self-heating carries particular interest. To examine such effects in VO_2 films, a purpose-built system which spontaneously monitors the changes in optical transmittance and electrical conductivity has been used. This system has been explained in Chapter 8, where the technical details can be found in Appendix A.

2.4 Structural Characterization of VO_2 Thin Films

2.4.1 Introduction

Material characterization plays a crucial role in determining the stoichiometry, homogeneity and crystallinity of materials. In this section, we cover the characterization techniques that have been used to characterize VO_2 films. Such characterization techniques involve Raman spectroscopy, XPS, XRD, and SEM. Additionally, more advanced techniques that have been used to examine the structure of such films are to be mentioned (i.e., EDS, HRTEM). These techniques used to characterize the VO_2 samples are explained concisely in the following.

2.4.2 Raman Spectroscopy

Raman spectroscopy is a technique for qualitative and quantitative investigation of the vibrational modes of bonds between atoms, which are distinctive to each material. It is used for characterizing inorganic and organic materials. This technique is essentially based on the Raman effect which is the outcome of inelastic (Raman) scattering of light in a medium. Examination of this effect provides information on vibrational modes that are unique in every material. This information is monitored by detecting the wavelength and intensity of the inelastically scattered light. In a Raman experiment, monochromatic light of known wavelength (generally in IR and Vis ranges) and polarization is incident on a sample. The light incident on the sample is either elastically (Rayleigh scattering) or inelastically scattered, resulting in a spectrum of the scattered light. The spectrum can be used to extract information on the composition and stoichiometry of the sample from expected vibrational mode signatures for the material under study. The Raman scattered light may either have lower or higher energy than the incident light, which is named Stokes and anti-Stokes emission, respectively. The relation between the energy of Raman scattered light and incident light can be given below:

$$\text{Stokes:} \qquad E_R = E_o - \Delta E_\lambda \tag{2.4}$$

$$\text{Anti-Stokes:} \qquad E_R = E_o + \Delta E_\lambda \tag{2.5}$$

where E_R is the energy of Raman scattered light, E_o is the energy of incident light and ΔE_λ is the change in energy. During Raman scattering, the change in energy in simple terms is related to energy absorption by or emission from local vibrational modes. For Stokes emission, the energy change can be written as $\Delta E_\lambda = hc(1/\lambda_o - 1/\lambda_R)$, where λ_o and λ_R are the wavelength of incident light and Raman scattered light, respectively. For the anti-Stoke case, the relation becomes $\Delta E_\lambda = hc(1/\lambda_R - 1/\lambda_o)$. The ΔE_λ is related to the deformation of the electron density (interatomic or intermolecular) in bonds during the interaction of incident light and the material. The deformed bonds change the polarizability of light, which results in the Raman shift of wavelength and energy. Until now there has been 25 different Raman techniques developed to overcome such weaknesses in Raman scattering experiments on various materials [15].

The experimental apparatus of a conventional Raman spectrometer consists of five main parts: a light source (laser), sample optics, spectral dispersion (Michelson or Fabry-Perot interferometer), spectral acquisition (CCD camera) and apparatus control. [16] The microscope is used to focus the incident light on the surface of the sample. The light is generated from the laser source and passes through the filters, polarizers and/or mirrors. The guided light impinges on the surface of the sample. The Raman scattered light is then guided to the CCD detector.

Raman characterization of VO_2 films was carried out using a Renishaw Invia™ Reflex Raman Microscope located at Saskatchewan Structural Sciences Centre (SSSC) [17]. The set-up consists of two different laser sources (514 nm and 785 nm), an xyz high-precision motorized stage (MS20 Encoded Stage, Renishaw, UK) with a step size of 100nm, a light microscope (Leica DC2500M) and a CCD detector. The detector is connected to a computer where the Raman spectrum is saved and analyzed in related software (WiRE^{TM} 3 by Renishaw). Figure 2.7 shows the Raman spectrometer used for measuring the Raman spectra of thin films presented in this dissertation.

Figure 2.7 Renishaw Invia Reflex Raman Microscope as used in the Saskatchewan Structural Sciences Centre, Vibrational Spectroscopy Laboratory [17].

In the Raman experiments, a VO_2 sample was placed on the xyz high precision motorized stage situated in the microscope cabinet. Before the experiment, a calibration scan (internal Si check) was carried out the check the internal Si peak at 520 cm^{-1} ± 2 cm^{-1}). A 514 nm-Ar^+ laser (Modulaser StellarPro-50) operating at 10 mW-laser power was used as an incident light source. The laser was guided through a laser pathway which consists of an edge filter 100 cm^{-1} and polarizers with $z(x,x)z'$ and $z(x,y)z'$- orientations and a selected grating of 1800 lines/mm. The light microscope equipped with various selections of lenses (5X (NA=0.12), 10X (NA = 0.25), 20X (NA = 0.40), 50X (NA = 0.75), 100X (NA = 0.85), 50X LWD (NA = 0.40)) was focused on the surface of the sample. The sample stage was used to meet a suitable alignment and distance with the microscope for focusing. When the microscope was properly focused and a perfect image was achieved, the acquisition of the Raman spectrum of VO_2 films was carried out.

2.4.3 Scanning Electron Microscopy (SEM)

Surface characterization and thickness measurements of VO_2 films were carried out by using field emission scanning electron microscopy (FE-SEM). For this purpose, a Hitachi SU8010

FE SEM, located at the University of Saskatchewan, Western College of Veterinary Medicine was used (See Figure 2.8). In general, SEM is used to examine the topography and morphology of organic and inorganic materials. It is an efficient tool to characterize not only the surface topography of thin films [18] but also the size of nanostructures [19]. This technique provides high-resolution images of the material surface. A typical SEM system consists of an electron gun, a set of limiting apertures and electromagnetic lenses, a sample stage and an Everhart-Thornley detector.

During the operation of SEM, an electric field is applied between the filament (cathode) and anode plates to accelerate the emitted electrons toward the sample. These anode plates are situated between the filament and the scanning coils. The electrons are focused on a target area of the sample with the use of limiting apertures and a condenser lens. Scanning coils are used to regulate the electron density per area to raster-scan the target surface. An Everhart-Thornley detector then collects electrons scattered from the surface of the sample. The energies of the collected electrons are digitized and amplified to form an image.

SEM measurements of VO_2 films were carried out using a semi-in-lens cold field emission Hitachi. This instrument delivers an ultra-high resolution of the sample surfaces with various selections of high and low magnification modes. Acceleration modes can be adjusted between 0.5 – 30 kV with a landing deceleration mode of 0.1 – 2.0 kV. The combination of a semi-in-lens type objective lens and cold FEG with small energy spread delivers ultra-high resolution imaging performance and flexible signal mixing for absolute surface information, Z-number contrast and charge suppression. High-resolution images were taken using image processing software SPIP (Version 5.1, Image Metrology, Copenhagen, Denmark).

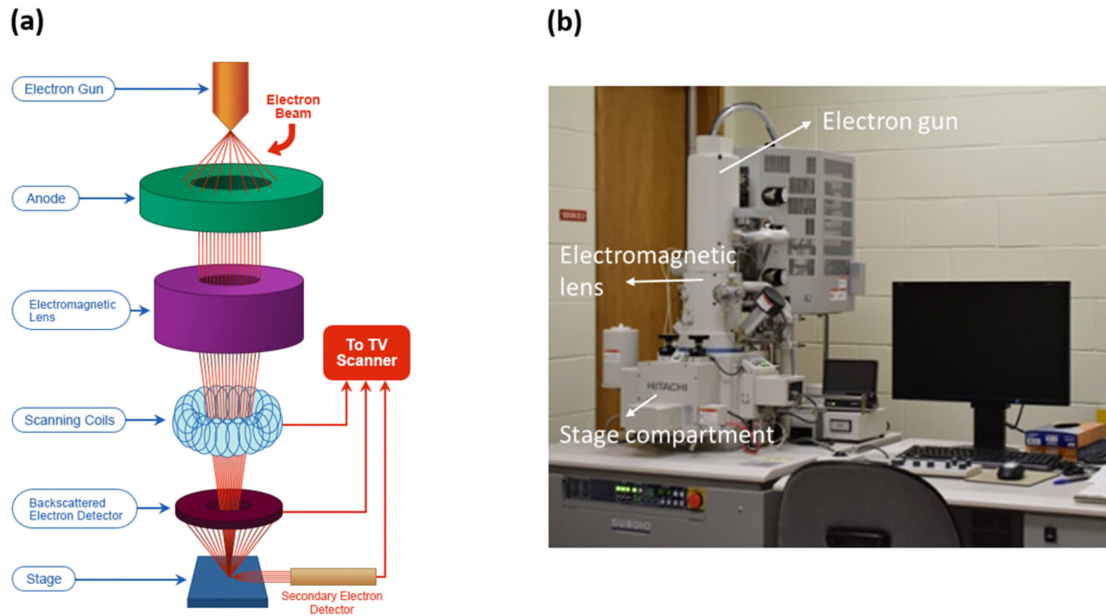

Figure 2.8 (a) A schematic diagram of an SEM. Taken from Nanoimages [20]. (b) A Hitachi SU8010 FE SEM, University of Saskatchewan, Western College of Veterinary Medicine [21].

2.4.4 X-ray Diffraction (XRD)

X-ray powder diffraction (XRD) is utilized to study the crystal structure of solid-state materials. With this technique properties such as crystallinity, crystal size and strain, phase transitions, and lattice parameters can be extracted. The theory of XRD is based on Bragg's law. According to Bragg's law, the wavelength of the observed interference fringes that are formed by the x-rays diffracted from the sample is related to the angle of incident x-rays to the normal of the sample surface. Bragg's law can be presented in the equation below:

$$n\lambda = 2d\sin\theta \tag{2.6}$$

where n is an integer (usually 1), λ is the wavelength of the interfered x-rays, θ is the angle of incidence with respect to the atomic planes involved in the diffraction, and d is the separation between atomic planes. Figure 2.9 shows the diffraction of x-rays in a crystalline material.

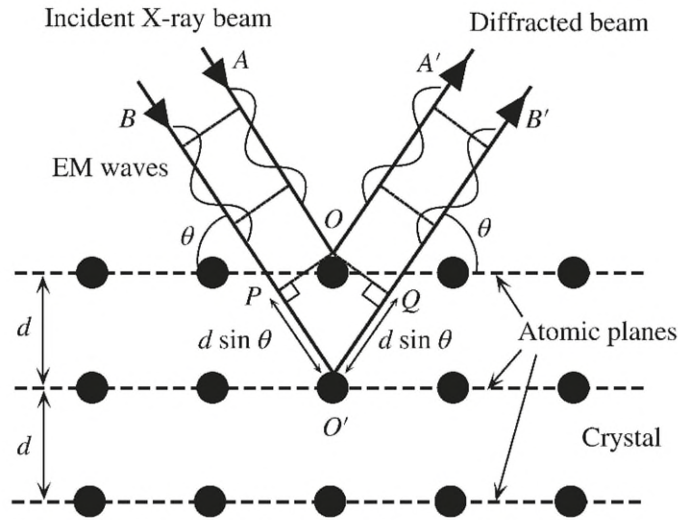

Figure 2.9 Diffraction of x-rays incident in a crystalline material. The interference of the x-rays reflected from adjacent atomic planes construct a diffracted beam at certain angles. Interatomic separation can be determined using Bragg's law. After Kasap [22].

An x-ray diffractometer consists of three main parts: an x-ray tube, a sample holder (goniometer) and an x-ray detector. A filament located in the x-ray tube is heated to generate x-rays from the cathode x-ray tube. A voltage is applied to accelerate the electrons toward the sample. Electrons with sufficient energies knock the electron in the inner shells of the sample material. The freed electrons produce x-ray spectra characteristic of the sample. In an XRD experiment, the sample is placed on a goniometer. This instrument is used to rotate the sample at a certain angle θ as the x-ray beams impinge on the sample. The diffracted x-rays are collected by the detector mounted on an arm which rotates at an angle 2θ. XRD measurements were carried out using a Rigaku Ultima IV XRD located at SSSC, Saskatchewan, Canada. (See Figure 2.10) [23].

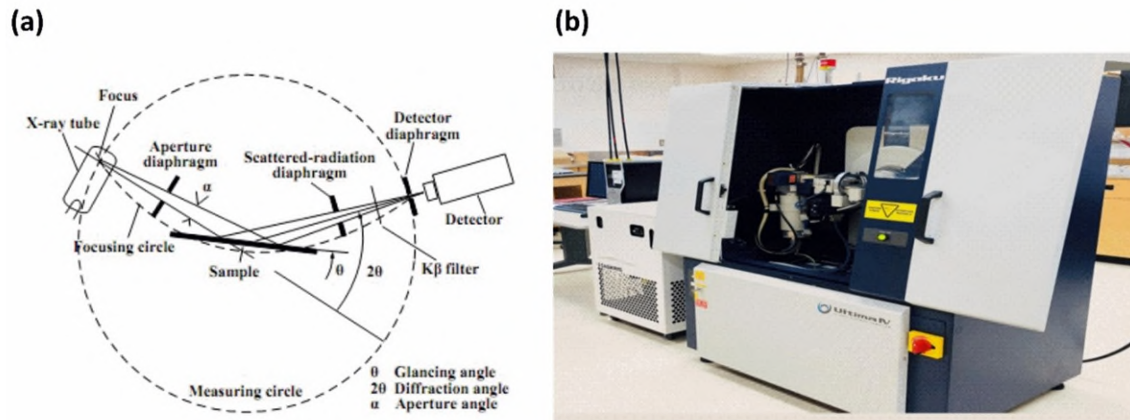

Figure 2.10 (a) A schematic diagram of an XRD in operation [24]. (b) A Rigaku Ultima IV XRD [23].

2.4.5 Transmission Electron Microscopy (TEM)

Transmission electron microscopy (TEM) was used to take high-resolution images of VO_2 films. With this technique layer growth, material composition and defect of thin films may be examined. A TE microscope uses high-energy electrons to obtain high-resolution images of a sample. Technical apparatus of a TEM resembles that of an SEM. It includes an electron gun, electromagnetic lenses and a detector. In TEM, the ultra-high-resolution image is constructed through the light transmitted through the sample, instead of reflected beams as in SEM.In a TEM experiment, electrons are generated by an electron gun and formed into an e-beam by use of condenser lenses. The beam impinges on the sample film. The transmitted portion of the beam is focused by objective lenses into a CCD detector. The electrons are converted to digital voltage and an image is constructed. TEM, EDS and SAED measurements were carried out in Key Laboratory of Microelectronics Devices and Integrated Technology, Institute of Microelectronics, Chinese Academy of Sciences (IMECAS), China. The instrument used is presented in Figure 2.11.

Figure 2.11 FEI Talos F200X G2 used for HRTEM, EDS and SAED imaging. Taken from Thermofisher Scientific [25].

2.4.6 Electron Diffraction Spectroscopy (EDS)

Energy dispersive spectroscopy is a technique that is particularly used for mapping the surface topography and depth profiling of thin films. This technique is typically delivered through TEM. The experiment is based on monitoring the characteristic x-rays that are emitted from the K, L and/or M shells from the surface of the material due excitation by incident x-rays. A detector measures the x-ray intensities emitted from the surface by counting pulses.

2.4.7 Selected Area Electron Diffraction (SAED)

Further investigations in TEM can be held using selected area electron diffraction (SAED) to examine the crystallinity of the VO_2 samples. The experiment is based on detecting the patterns of electrons diffracted from the sample. In a SAED experiment, a high-energy electron beam is applied on a selected area of the sample surface. The examined medium behaves as a diffraction grating due to larger atomic spacing with respect to electron wavelength. The obtained diffraction patterns appear as sharp diffraction spots. These spots project the reciprocal lattice of the examined sample, thus providing with information about the crystallinity of the VO_2 thin films.

2.4.8 X-ray Photoelectron Spectroscopy (XPS)

X-ray photoelectron spectroscopy (XPS) is a technique used to identify the composition and chemical state of thin films. This technique is based on the photoelectric effect, (i.e., ejection of photoelectrons from the core *K* shell from the surface of the examined material by incident monochromatic x-rays). Figure 2.12 (a) illustrates the excitation of electrons at either valence or core orbitals. Figure 2.12 (b) shows the band diagram of a sample material that is used for detection in an x-ray photospectrometer.

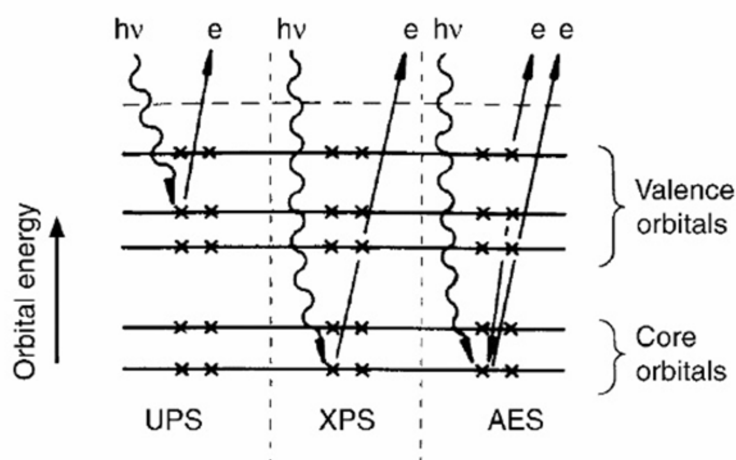

Figure 2.12 (a) Representation of the emission of electrons from various orbitals due to the interaction with incoming light at a certain energy. Depending on the energy of the incoming light the technique is categorized as ultra-violet spectroscopy (UPS), x-ray photo spectroscopy (XPS) and Auger electron spectroscopy (AES). After Hollas [26].

In an XPS experiment, monochromatic x-rays with certain photon energy are used to excite the surface of the examined films. Figure 2.13 (a) shows a sketch of an XPS operation. The interaction of x-rays with the surface of the thin film leads to the ejection of photoelectrons from the inner shells of the material. The energy of the photoelectrons is detected by a hemispherical analyzer. The chemical content of the surface is identified by examining the intensity of the photoelectrons as a spectrum of their binding energies. XPS experiments of VO_2 samples were performed using SXRMB high-energy XPS with x-rays supplied from the VLS-PGM beamline at

the Canadian Light Source (Figure 2.13 (b)). The experiments are carried out in an ultra-high vacuum environment.

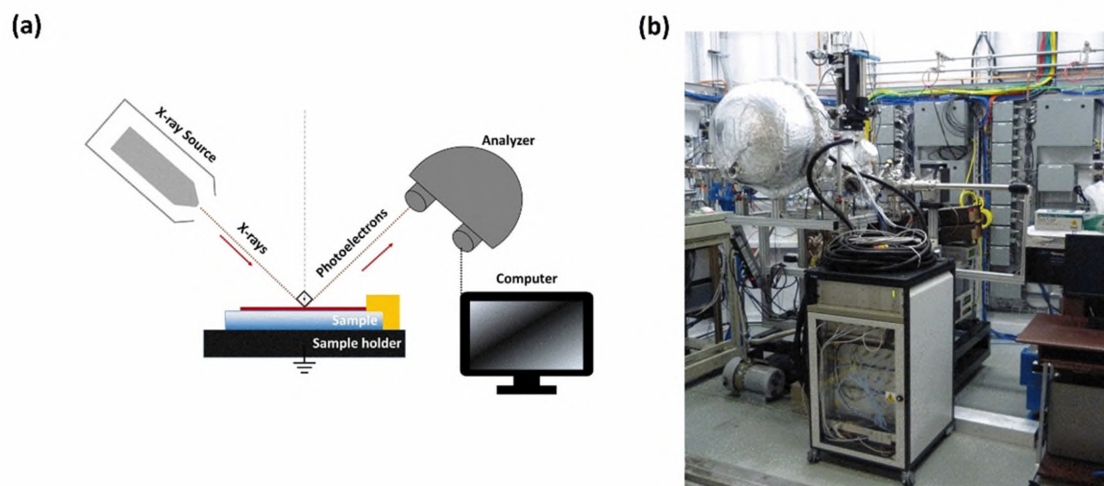

Figure 2.13 (a) A schematic of a typical XPS. (b) SXRMB high-energy XPS at the Canadian Light Source used for XPS measurements [27].

2.5 References

[1] M. Ohring, *Materials science of thin films: deposition and structure*, 2nd ed., San Diego, CA: Academic Press, 2002.

[2] S. M. Rossnagel, "Magnetron sputtering," *Journal of Vacuum Science & Technology A: Vacuum, Surfaces, and Films*, vol. 38, no. 6, p. 060805, 2020.

[3] S. Hofmann, "Sputter-depth profiling for thin-film analysis," *Philosophical Transactions of the Royal Society of London. Series A: Mathematical, Physical and Engineering Sciences*, vol. 362, no. 1814, pp. 55-75, 2004.

[4] S. Chandra, V. Bhatt and R. Singh, "RF sputtering: A viable tool for MEMS fabrication," *Sadhana*, vol. 34, no. 4, pp. 543-556, 2009.

[5] P. F. Cheng, S. M. Rossnagel and D. N. Ruzic, "Directional deposition of Cu into semiconductor trench structures using ionized magnetron sputtering," *Journal of Vacuum Science & Technology B: Microelectronics and Nanometer Structures Processing, Measurement, and Phenomena*, vol. 13, no. 2, pp. 203-208, 1995.

[6] S. Rossnagel, "Sputtering and Sputter Deposition," in *Handbook of thin film deposition processes and techniques: principles, methods, equipment and applications*, 2nd ed., K. Seshan, Ed. New York, NY: Noyes Publications/William Andrew Publishing, 2002 pp. 319-349.

[7] H. Frey, "Cathode Sputtering," in *Handbook of thin film technology*, H. Frey and H. R. Khan, Eds., Berlin: Springer, 2015.

[8] T. G. S. Semicore, "Sputtering Yield Rates," Semicore, [Online]. Available: http://www.semicore.com/reference/sputtering-yields-reference. [Accessed 5 February 2023].

[9] N. Matsunami, Y. Yamamura, Y. Itikawa, N. Itoh, Y. Kazumata, S. Miyagawa, ... and H. Tawara, "Energy dependence of the ion-induced sputtering yields of monatomic solids," *Atomic data and nuclear data tables*, vol. 31, no. 1, pp. 1-80, 1984.

[10] M. Shaat. (2017, December). "On performance of nano-resonators produced by magnetron sputtering deposition," *arXiv preprint* [Online]. Available: https://arxiv.org/abs/1801.06529

[11] *Magnetron Sputter Deposition System Model SPT320 Operation Manual*, Plasmionique Inc., Varennes, QC, 2015.

[12] D. P. Zhang, M. D. Zhu, Y. Liu, K. Yang, G. X. Liang, Z. H. Zheng, ... and P. Fan, "High performance VO2 thin films growth by DC magnetron sputtering at low

temperature for smart energy efficient window application," *Journal of Alloys and Compounds*, vol. 659, pp. 198-202, 2016.

[13] D. Lee, D. Yang, H. Kim, J. Kim, S. Song, K. S. Choi, ... and S. Park, "Deposition-temperature-mediated selective phase transition mechanism of VO2 films," *The Journal of Physical Chemistry C*, vol. 124, no. 31, pp. 17282-17289, 2020.

[14] R. Swanepoel, "Determination of the thickness and optical constants of amorphous silicon," *Journal of Physics E: Scientific Instruments*, vol. 16, no. 12, p. 1214, 1983.

[15] R. R. Jones, D. C. Hooper, L. Zhang, D. Wolverson and V. K. Valev, "Raman techniques: fundamentals and frontiers," *Nanoscale Research Letters*, vol. 14, no. 1, pp. 1-34, 2019.

[16] S. L. Zhang, "Experimental Foundation of Raman Spectroscopy," in *Raman spectroscopy and its application in nanostructures*, West Sussex, John Wiley & Sons, 2012, pp. 47-104.

[17] Saskatchewan Structural Sciences Centre. *Vibrational Spectroscopy Laboratory* [Online]. Available: https://sssc.usask.ca/vibrational-spectroscopy-laboratory.php#instruments. [Accessed 5 February 2023].

[18] T. Everhart, "Thin-film measurements in scanning electron microscope," *Journal of Vacuum Science & Technology,* vol. 6, no. 5, p. 899, 1969.

[19] W. Zhou and Z. L. Wang, Eds., "One-dimensional Wurtzite Semiconducting," in *Scanning microscopy for nanotechnology: techniques and applications*, New York, Springer science & business media, 2007, pp. 384-427.

[20] "SEM Technology Overview – Scanning Electron Microscopy," Nanoimages Perfect Focus, [Online]. Available: https://www.nanoimages.com/sem-technology-overview/. [Accessed 5 February 2023].

[21] University of Saskatchewan, Western College of Veterinary Medicine, *Hitachi SU8010 Field-Emission Scanning Electron Microscope (FE-SEM)* [Online]. Available: https://wcvm.usask.ca/research/image-centre/scanning-electronic-microscope.php#About. [Accessed 5 February 2023].

[22] S. O. Kasap, "Bragg's Diffraction Law and X-ray Diffraction," in *Principles of electronic materials and devices*, 4th ed., New York: McGraw-Hill, 2018, pp. 941-945.

[23] Saskatchewan Structural Sciences Centre, *X-ray Diffraction Analysis Laboratory* [Online]. Available: https://sssc.usask.ca/x-ray-diffraction-analysis-laboratory.php. [Accessed 5 February 2023].

[24] J. R. Connolly, "Introduction to X-ray Powder Diffraction," [Online], 2005. Available: https://www.ocf.berkeley.edu/~mwg/lab/xdocs/pxrdintro.pdf. [Accessed 5 February 2023].

[25] Thermofisher Scientific. *Thermofisher Scientific*™ *Talos™ F200X G2 TEM* [Online]. Available: https://www.thermofisher.com/order/catalog/product/TALOSF2OOX. [Accessed 5 February 2023].

[26] J. M. Hollas, "Photoelectron and Related Spectroscopies," in *Modern Spectroscopy*, West Sussex, John Wiley & Sons, 2004, p. 209.

[27] "High Energy XPS," [Online]. Available: https://sxrmb.lightsource.ca/about/high-energy-xps/. [Accessed 5 February 2023].

3. Optical Transmittance of Thin Films and the Extraction of Optical Properties

3.1 Introduction

This chapter covers the optical analysis techniques that have been used to extract the optical constants of VO_2 thin films studied in this dissertation. The chapter contains five sections. In the first section, the physical aspects of light transmission in thin films are explained in a concise manner. In the second section, the optical constants and optical band gap are defined. The third section is devoted to the description of dispersion in thin films, which is the wavelength dependence of the refractive index and the extinction coefficient. The fourth section covers the analysis techniques used to calculate the optical constants of thin films, specifically in the case of transmission spectra of VO_2 thin films. The last section provides a summary of the chapter.

3.2 Light Transmission in Thin Films

The optical properties of thin films are studied in the field of thin film optics. It provides relations between the dispersion, transmission and reflection phenomena of light in materials. It also offers analysis techniques which are used to extract the physical parameters that are known as the optical constants which display a unique spectrum, i.e., dependence on the light wavelength. This study focuses on the assessment of the interaction of the incident light with the thin film material and substrate. It is assumed that the thin film is deposited on the semi-transparent substrate. The analysis of such optical parameters is governed by the light-matter interaction in the film, which is examined by means of the electromagnetic (EM) wave nature of light. According to the EM wave theory, we can treat light as a travelling plane electromagnetic wave with orthogonal electric (E) and magnetic (B) fields as shown in Figure 3.1.

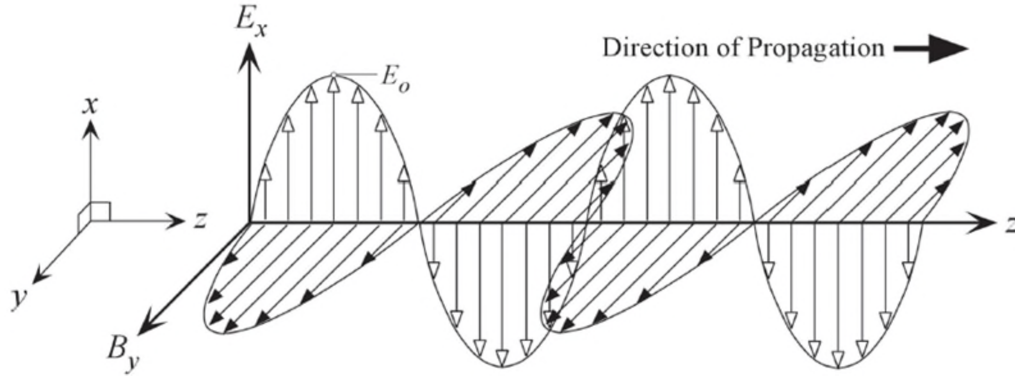

Figure 3.1 Light as an electromagnetic wave propagating at an instant in a homogeneous and isotropic medium with a velocity *v*. After Kasap [1].

For mathematical reasons, a collimated light beam at a single frequency can be simply represented by a traveling exponential wave as below:

$$E = E_o e^{j(\omega t - kz)} \tag{3.1}$$

where *E* describes the electric field of the electromagnetic wave, E_o is the amplitude of the EM wave, ω and *t* represent the angular frequency of the wave and time respectively, where *z* represents the direction of propagation. There is a similar expression for the magnetic field in an orthogonal direction, which also propagates along *z*. The optical characterization of a dielectric thin film material involves light transmission through the material, which can be carried out by using optical spectrophotometry. More information on the characterization method can be found in Chapter 2. The light-matter interaction in a thin film may lead to the absorption, reflection, and transmission of incident light. For a polycrystalline films, as incident light enters the film and travels through its medium, it experiences absorption and scattering. The wavelength dependence of the scattering of light is related to the size and distribution of grains in the film, their geometry, defects, as well as surface roughness. The dispersion or the frequency dependence of optical properties such as the refractive index depends on the crystal structure of the thin film material. In addition, there will be many internal reflections and these reflections interfere and give rise to maxima and minima in the transmitted light spectrum.

In a semitransparent thin film, incident light may undergo multiple reflections at air-thin film and thin film-substrate interfaces. Some proportion of the waves that are internally reflected would exit the film and enter the substrate and the rest of the light will be reflected as shown in Figure 3.2. The waves that are reflected from the thin film-substrate interface travel through the film and then become partially reflected again at the surface interface. Some light is transmitted as a reflected wave. All the reflected waves summed together to quantify the reflectance of the thin film. On the other hand, all the transmitted waves into the substrate are used to quantify the transmittance of the film. Apart from reflection and transmission, some portion of the light can be absorbed by either the film or the substrate. The energy of the absorbed light may be released as lattice vibrations (phonons) within the film. Figure 3.2 presents the interaction of incident light with the thin film and the substrate.

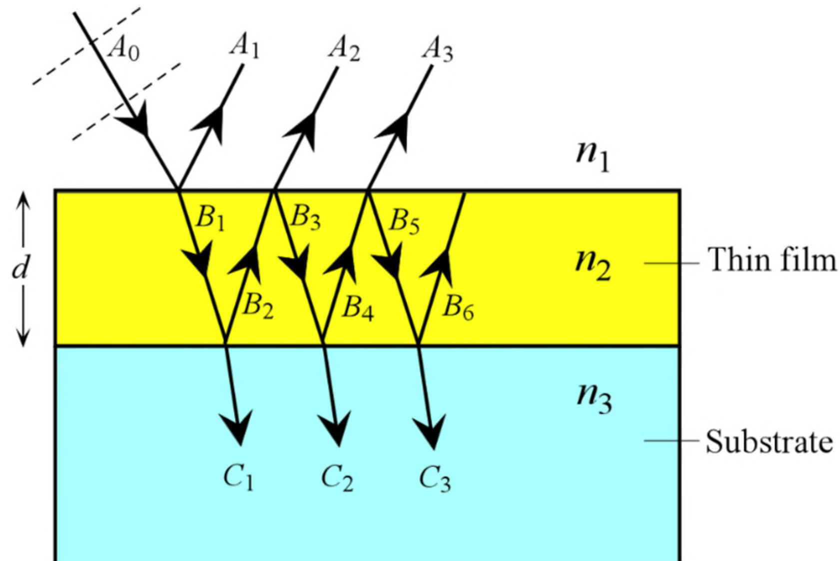

Figure 3.2 Reflection and transmission of light as a sum of reflected and transmitted beams within and throughout the thin film and substrate. After S. O. Kasap lecture notes [2].

As the incoming wave with an amplitude A_o impinges on the surface of the thin film, some portion is transmitted (with an amplitude B_1) and the remainder is reflected (with an amplitude A_1). Equation (3.2) presents the amplitudes of the reflected waves A_1 and A_2 in Figure 3.2. The amplitudes can be defined in terms of transmission and reflection coefficients as a multiplier to the amplitude (A_o) of the incident wave. It is appropriate to define the transmission and reflection

coefficients between different media, i.e., air-film, film-air and film-substrate as shown in Table 3.1. The reflected waves 1, 2, 3 and so on in Figure 3.2 have the amplitudes given by

$$\begin{aligned}
A_1 &= A_0 \times \tilde{r}_1 \\
A_2 &= A_0 \tilde{r}_2 \tilde{t}_1 \tilde{t}_1' e^{-j\phi} \\
A_3 &= A_0 \tilde{r}_2^2 \tilde{r}_1 \tilde{t}_1 \tilde{t}_1' e^{-j\phi} \\
A_4 &= A_0 \tilde{r}_2^3 \tilde{r}_1^2 \tilde{t}_1 \tilde{t}_1' e^{-j\phi} \\
&....
\end{aligned} \tag{3.2}$$

where the transmission and reflection coefficients are defined in Table 3.1 and ϕ is the phase change in one round trip from one surface, through the film and back to the same surface, i.e., phase change in traversing the thickness of the film $2d$. Thus, $\phi = 2(2\pi/\lambda)n_2d$. Table 3.1 summarizes the relations of reflected and transmitted waves that are involved in the air-film, film-air and film-substrate interfaces and relates these to the refractive indices of these media. The details of multiple orders of reflections and transmissions within a thin film-substrate system is given below:

Table 3.1 Relations of reflection and transmission coefficients under various scattering conditions.

Coefficients	Interface	Equation number
$\tilde{r}_1 = \tilde{r}_{12} = \frac{n_1 - n_2}{n_1 + n_2} = -\tilde{r}_{21}$	Air-thin film	(3.3)
$\tilde{r}_2 = \tilde{r}_{23} = \frac{n_2 - n_3}{n_2 + n_3}$	Thin film-substrate	(3.4)
$\tilde{t}_1 = \tilde{t}_{12} = \frac{2n_1}{n_1 + n_2}$	Air-thin film	(3.5)
$\tilde{t}_1' = \tilde{t}_{21} = \frac{2n_2}{n_1 + n_2}$	Thin film-air	(3.6)
$\tilde{t}_2 = \tilde{t}_{23} = \frac{2n_2}{n_2 + n_3}$	Thin film-substrate	(3.7)

The sum of the waves that are transmitted through the dielectric media (film and substrate) represents the transmitted light. The transmission coefficient ($\tilde{t}$) of the film, describes the total intensity of the EM waves that are transmitted through the thin film and substrate, relative to the incident EM wave, We need to add all the transmitted waves C_1, C_2, C_3 … to obtain the transmission coefficient, which is given in Equation (3.13). Table 3.2 presents the amplitudes of transmitted waves, the amplitude of the overall transmitted light ($C_{\text{transmitted}}$) and the transmission coefficient ($\tilde{t}$).

Table 3.2 Waves reflected in thin film medium (n_2) from film-substrate interface.

Relation of wave amplitude	Equation number
$C_1 = A_0 \tilde{t}_{12} \tilde{t}_{23} e^{j\phi_{C1}}$	(3.8)
$C_2 = A_0 \tilde{t}_{12} \tilde{r}_{23} \tilde{r}_{21} \tilde{t}_{23} e^{j\phi_{C2}}$	(3.9)
$C_3 = A_0 \tilde{t}_{12} \tilde{r}_{23} \tilde{r}_{21} \tilde{r}_{23} \tilde{r}_{21} \tilde{t}_{23} e^{j\phi_{C3}}$	(3.10)
$C_{\text{transmitted}} = \sum_{k=1}^{\infty} C_k = C_1 + C_2 + C_3 + \ldots$	(3.11)
$C_{\text{transmitted}} / A_0 = \tilde{t}_1 \tilde{t}_2 e^{-j\phi/2} - \tilde{t}_1 \tilde{t}_2 \tilde{r}_1 \tilde{r}_2 e^{-j3\phi/2} + \tilde{t}_1 \tilde{t}_2 \tilde{r}_1^{\,2} \tilde{r}_2^{\,2} e^{-j5\phi/2} + \ldots$	(3.12)
$\tilde{t} = \frac{C_{\text{transmitted}}}{A_0} = -\frac{\tilde{t}_1 \tilde{t}_2 e^{j\phi}}{\tilde{r}_1 \tilde{r}_2} \sum_{k=1}^{\infty} (-\tilde{r}_1 \tilde{r}_2 e^{-j2\phi})^k = \left(\frac{\tilde{t}_1 \tilde{t}_2 e^{j\phi}}{\tilde{r}_1 \tilde{r}_2} \right) \frac{\tilde{r}_1 \tilde{r}_2 e^{-j2\phi}}{1 + \tilde{r}_1 \tilde{r}_2 e^{-j2\phi}}$	(3.13)

The geometric series in Equation (3.13) gives the transmission coefficient as:

$$\tilde{t} = \frac{\tilde{t}_1 \tilde{t}_2 e^{-j\phi}}{1 + \tilde{r}_1 \tilde{r}_2 e^{-j2\phi}} \tag{3.14}$$

The reflected waves from thin-film-substrate and thin-film-air interfaces are presented below:

Table 3.3 Reflected waves in the thin-film-substrate and thin-film-air interfaces.

Relation of wave amplitude	Equation number
$B_1 = E_0 \tilde{t}_{12} e^{j\phi_{B1}}$	(3.15)
$B_2 = E_0 \tilde{t}_{12} \tilde{r}_{23} e^{j\phi_{B2}}$	(3.16)
$B_3 = E_0 \tilde{t}_{12} \tilde{r}_{23} \tilde{r}_{21} e^{j\phi_{B3}}$	(3.17)
$B_4 = E_0 \tilde{t}_{12} \tilde{r}_{23} \tilde{r}_{21} \tilde{r}_{23} e^{j\phi_{B4}}$	(3.18)
$B_5 = E_0 \tilde{t}_{12} \tilde{r}_{23} \tilde{r}_{21} \tilde{r}_{23} \tilde{r}_{21} e^{j\phi_{B5}}$	(3.19)
$B_6 = E_0 \tilde{t}_{12} \tilde{r}_{23} \tilde{r}_{21} \tilde{r}_{23} \tilde{r}_{21} \tilde{r}_{23} e^{j\phi_{B6}}$	(3.20)

In the case of reflection, the sum of the reflected waves from the thin film describes the reflection coefficient of the material which is the sum of the amplitudes A_1, A_2, A_3 etc. The relation for amplitudes A_1, A_2, A_3 are presented in Table 3.4 below:

Table 3.4 Representation of reflected waves by means of transmission and reflection coefficients that constitute the reflected beam.

Relation of wave amplitude and reflection coefficient	Equation number
$A_1 = E_0 \tilde{r}_{12} e^{j\phi_{A1}}$	(3.21)
$A_2 = E_0 \tilde{t}_{12} \tilde{r}_{23} \tilde{t}_{21} e^{j\phi_{A2}}$	(3.22)
$A_3 = E_0 \tilde{t}_{12} \tilde{r}_{23} \tilde{r}_{21} \tilde{r}_{23} \tilde{t}_{21} e^{j\phi_{A3}}$	(3.23)
$A_{\text{reflected}} = \sum_{k=1}^{\infty} A_k$	(3.24)
$A_{\text{reflected}} / A_0 = \tilde{r}_1 + \tilde{t}_1 \tilde{t}_1' \tilde{r}_2 \mathrm{e}^{-j\phi} - \tilde{t}_1 \tilde{t}_1' \tilde{r}_1 \tilde{r}_2^2 \mathrm{e}^{-2j\phi} + \tilde{t}_1 \tilde{t}_1' \tilde{r}_1^2 \tilde{r}_2^3 \mathrm{e}^{-3j\phi}$	(3.25)

The geometric series in Equation (3.25) gives the reflection coefficient as,

$$\tilde{r} = \frac{\tilde{r}_1 + \tilde{r}_2 e^{-j\phi}}{1 + \tilde{r}_1 \tilde{r}_2 e^{-j\phi}} \tag{3.26}$$

The square of the magnitude of the reflection coefficients defines the reflectance ($\tilde{R}$) of the film. Similarly, the square of the magnitude of the sum of all the transmitted waves ($C_1 + C_2 + C_3 + \ldots$ in Figure 3.2) represents the transmittance of the material. The transmittance ($\tilde{T}$) and reflectance ($\tilde{R}$) represent the total intensity of the transmitted and reflected beams. Hence, the transmittance and reflectance of the dielectric medium (semiconductor thin film) can be expressed in terms of the transmission and reflection coefficients, respectively, in Equation (3.27) below:

$$\tilde{R} = |\tilde{r}|^2 \text{ and } \tilde{T} = (n_3 / n_1)|\tilde{t}|^2 \tag{3.27}$$

The transmittance and reflectance of light must add to unity in the absence of any absorption and scattering in the thin film:

$$\tilde{T} + \tilde{R} = 1 \tag{3.28}$$

It should be emphasized that the absorption and scattering in the film medium will alter the above equations. The description of a finite extinction coefficient in the film is given in Section 3.4.1 in terms of the transmission spectrum. The relation between the refractive index and the wavelength can be established by a dispersion relation, which is presented in the next section.

3.3 Optical Constants of Semi-Transparent Media

3.3.1 Introduction

Optical constants are physical properties that characterize the response of the medium to an electromagnetic wave passing through it. There are two approaches to representing the optical constants: the complex refractive index $n*$ and the complex dielectric constant ε_r. In the case of the complex refractive index, the optical constants are the refractive index (n) and extinction coefficient (K). These optical constants are often extracted from the optical transmission and/or reflection spectrum of the thin film. Optical properties such as refractive index extinction coefficient, absorption coefficient (α) and optical bandgap (E_g) can be calculated by using the reflection or transmission spectra. The transmittance and reflectance of a dielectric thin film depend on the wavelength (λ) of the incident light as discussed above in Section 3.2. From the wavelength dependence of the spectra, we can extract the optical constants.

3.3.2 The Complex Refractive Index

The interaction of a dielectric medium with light can be identified in terms of its complex refractive index. The complex refractive index $n*$ can be represented in Equation (3.29) below:

$$n* = n - jK \tag{3.29}$$

where the real part n is the refractive index and the imaginary part K is the extinction coefficient. The real part n accounts for the phase change in the electromagnetic wave as it propagates through the medium. The imaginary part K accounts for the energy loss experienced by light as it passes through the medium. The complex refractive index $n*$ can be defined in terms of the complex dielectric constant or relative permittivity (ε_r) by using Maxwell's equations [3]. For non-magnetic materials, where μ_r is unity, and the relationship between N and ε_r is given in Equation (3.30):

$$n^* = n - jK = \sqrt{\varepsilon_r} = \sqrt{\varepsilon_r' + j\varepsilon_r''} \tag{3.30}$$

where ε_r' and ε_r'' are the real and imaginary parts of ε_r. Correspondingly, the n and K can be redefined in terms of real and imaginary parts of the dielectric permittivity in Equations (3.31) and (3.32):

$$n = (1/\sqrt{2})\left[(\varepsilon_r'^2 + \varepsilon_r''^2)^{1/2} + \varepsilon_r'\right]^{1/2} \tag{3.31}$$

$$K = (1/\sqrt{2})\left[(\varepsilon_r'^2 + \varepsilon_r''^2)^{1/2} - \varepsilon_r'\right]^{1/2} \tag{3.32}$$

If we know the dispersion relationship for the real part (or the imaginary part) of the dielectric constant over all frequencies, then we can find the dispersion of the imaginary part (or the real part) through the Kramers-Kronig relationship as shown in

Table 3.3. Similar relationships hold for relating the real (n) and imaginary part (K) of the complex refractive index n^*. In addition, there are various empirical equations for the dispersion of the refractive index n as summarized in Table 3.5.

Table 3.5 Well known dispersion models to examine the wavelength dependence of refractive index of materials.

Model	Relation	Equation number
Kramers-Kronig	$\varepsilon_r' = 1 + \frac{2}{\pi} P \int_0^\infty \frac{\omega' \varepsilon_r''(\omega')}{\omega'^2 - \omega^2} d\omega'$ $\varepsilon_r'' = 1 + \frac{2}{\pi} P \int_0^\infty \frac{\omega' [\varepsilon_r'(\omega') - 1]}{\omega'^2 - \omega^2} d\omega'$	(3.33)
Cauchy	$n = A + \frac{B}{\lambda^2} + \frac{C}{\lambda^4}$	(3.34)
Sellmeier	$n^2 = 1 + \sum_{i=1}^{\infty} \frac{A_i \lambda^2}{\lambda^2 - \lambda_i^2}$	(3.35)
Gladstone-Dale	$\frac{n-1}{\rho} = \sum_{i=1}^{N} p_i k_i = C_{GD}$	(3.36)
Wemple-DiDomenico	$n^2 = 1 + \frac{E_\mathrm{o} E_\mathrm{d}}{E_\mathrm{o}^2 - (h\nu)^2}$	(3.37)
Hervé-Vandamme	$n^2 = 1 + \left(\frac{A}{E_\mathrm{g} + B} \right)$	(3.38)

3.3.3 The Attenuation Coefficient of a Medium

As light propagates through a dielectric medium a certain portion is attenuated by the material. The attenuation may be due to the absorption of light or scattering of light. A fundamental relationship of light intensity to the attenuation coefficient α is defined by Beer-Lambert law in Equation (3.39):

$$I = I_o e^{-\alpha x} \tag{3.39}$$

where the I refers to the light intensity at a point x along the direction of propagation from some arbitrary reference point taken as $x = 0$ on the direction or propagation where the light intensity is I_o, and α is the attenuation coefficient along x. In general, optical attenuation occurs with respect to various mechanisms as a result of light-matter interaction. Such mechanisms may be due to scattering, generation of phonons, photogeneration and free carrier absorption. In thin films, absorption and scattering may be the dominant contributions to attenuation. Equation (3.40) gives an expression for the attenuation coefficient in terms of absorption and scattering contributions:

$$\alpha = \frac{A_a}{h\nu}(h\nu - E_g)^{1/m} + \frac{A_s}{\lambda^p} \tag{3.40}$$

where the first term represents the absorption coefficient that arises from band-to-band (valence band to conduction band) photogeneration and the second term represents the scattering of light. In the first term, α denotes the attenuation coefficient due to band-to-band absorption, A_a represents a constant for the absorption contribution unique to the material and E_g is the optical band gap of the semiconductor medium. The exponent m is either 1/2 or 2 and can be defined for direct and indirect transitions respectively. In the second term, A_s is a constant and p is an index which depends on the nature of scattering. In some cases, the absorption becomes highly dominant so that the scattering contributions may be negligible.

Generally, there are four absorption processes:

1) Band-to-band absorption, which is the first part of Equation (3.40),

2) Impurity or defect absorption, which is due to photogeneration from impurities and/or defects,

3) Lattice absorption, which the absorption of the light by lattice vibrations to generate phonons,

4) Free carrier absorption, electrons in the conduction band and holes in the valence band.

In free carrier absorption, the carriers become accelerated by the applied optical field and then lose the energy by collisions with phonons (lattice vibrations). The classical treatment under the Drude model leads to

$$\alpha = 2k_0 K \approx \frac{2\omega}{c}\left(\frac{\varepsilon_r''}{2n}\right) = \frac{\sigma_0}{n(\lambda)c\varepsilon_0[(\omega\tau)^2 + 1)]} \tag{3.41}$$

where σ_0 is the conductivity of the semiconducting material in Equation (3.41). The quantity ε_r'' represents the imaginary part of the relative (complex) permittivity (ε_r) of the medium. As apparent, this relation is frequency-dependent and can be written in terms of wavelength as well. At high frequencies, Equation (3.41) can be written as

$$\alpha \propto \frac{\sigma_0}{\omega^2} \propto N\lambda^2 \tag{3.42}$$

where N represents the free charge carrier concentration in a semiconductor. At very low frequencies ($\omega < 1/\tau$) where the absorption is controlled by DC conductivity, the relation can be rewritten as:

$$\alpha = \frac{\sigma_0}{n(\lambda)c\varepsilon_0} \tag{3.43}$$

Based on the classical theory (Drude model), ε_r can be expressed as follows:

$$\varepsilon_r = \varepsilon_r' - j\varepsilon_r'' = 1 - \frac{\omega_p^2}{\omega^2 - j\omega/\tau} \tag{3.44}$$

where ω_p describes a plasma frequency and can be defined as:

$$\omega_p^2 = \frac{Ne^2}{\varepsilon_0 m_e} \tag{3.45}$$

At sufficiently low (DC) frequencies, the expression for relative dielectric permittivity can be rewritten as follows:

$$\varepsilon_r = \varepsilon_r' - j\varepsilon_r'' = 1 - \frac{\tau\sigma_0}{\varepsilon_0[(\omega\tau)^2 + 1)]} - j\frac{\sigma_0}{\varepsilon_0\omega[(\omega\tau)^2 + 1)]} \tag{3.46}$$

Lattice (Reststrahlen) absorption appears over wavelengths in the infrared region. This type of absorption is dominant in ionic solids. The light inside the crystal is strongly absorbed. The nature of this absorption relies on the interaction between the EM light and the transverse optical (TO) phonons in the material. According to the Lorentz (dipole) oscillator model, the relation for the complex relative permittivity can be written as:

$$\varepsilon_r = \varepsilon_r' - j\varepsilon_r'' = \varepsilon_r + \frac{\varepsilon_r - \varepsilon_{ro}}{\left(\frac{\omega}{\omega_T}\right)^2 - 1 + j\frac{\gamma_{\text{loss}}}{\omega_T}\left(\frac{\omega}{\omega_T}\right)} \tag{3.47}$$

in which ω_T represents the frequency of transverse optical phonons, where γ_{loss} is the loss coefficient which describes the rate of energy transfer from the EM wave to optical phonons [4].

Band-to-band absorption in a semiconducting material can be classified in terms of direct and indirect bandgap transitions. A direct band gap transition occurs when an electron from the valance band is excited to the conduction band by the absorption of an incoming photon. In this process, the entire energy of the photon is transferred to the electron and there are no phonons involved. In an indirect band gap transition, an electron is excited from the valence band to the conduction band not only by the absorption of a photon but also by the absorption or emission of

phonons, that is lattice vibrations. Figure 3.3 (a) and (b) present direct and indirect absorption in semiconductors, respectively, on the *E*-*k* diagram.

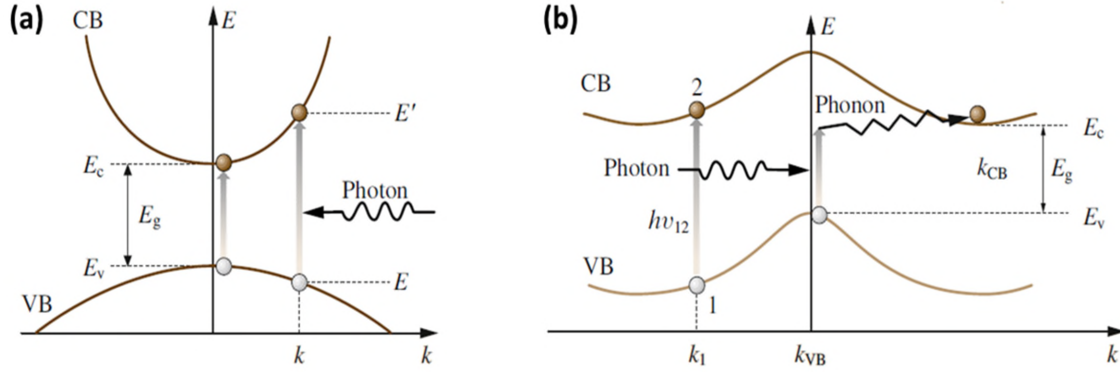

Figure 3.3 (a) Direct band-to-band transition of electron. E_c, E_v, and E_g is the conduction energy, valance energy and energy band gap, respectively. (b) Indirect band-to-band transition with additional energy absorption by phonon through lattice vibration. After Mistrik et al. [5].

In Figure 3.3 (a) an electron absorbs a photon in the valance band (VB) at an energy level E and is excited to the conduction band (CB) at an energy level E'. In Figure 3.3 (b) an electron in the VB absorbs a photon of energy of $h\nu_{12}$ and then it is excited from point 1 in VB to point 2 in the conduction band. The electron then falls down to the bottom of the conduction band by emitting phonons. The absorption of light within a material gives information about the optical band gap, which is explained in the following subsection.

3.3.4 The Optical Band Gap

The optical band gap (E_g) characterizes the minimum amount of photon energy that is able to excite an electron in the VB to the CB and create an electron-hole pair (EHP) in a semiconductor. The optical bandgap of a semiconductor can be obtained for direct and indirect transitions from the photon energy dependence of the optical absorption coefficient,

$$\alpha = \frac{A_a}{h\nu}(h\nu - E_g)^{1/m} \tag{3.48}$$

where the index m is in the range ½ to 2. Equation (3.48) applies in the strong absorption region in which band-to-band transitions are involved. A general method to obtain the optical bandgap is through α vs. photon energy (hv) plot, which is also known as the Tauc plot, as given in Figure 3.4 (a). This approach is applicable for most semiconductors (including amorphous semiconductors) that have a high absorption edge within a certain photon energy range. [5] Figure 3.4 (b) presents the absorption edge of amorphous selenium (a-Se).

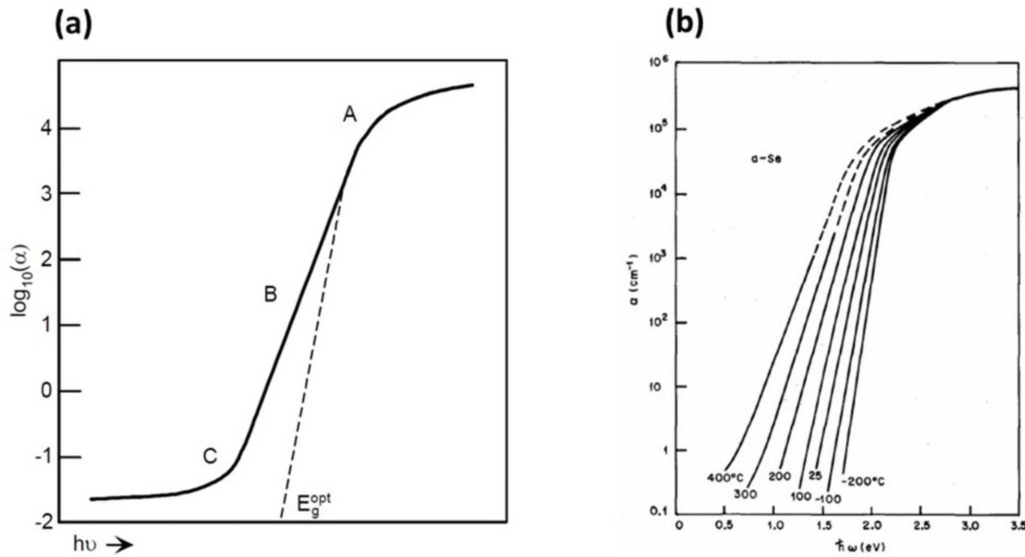

Figure 3.4 (a) Tauc's plot of an amorphous semiconductor which the energy region where the absorption edge is taken into consideration. Region A ($\alpha \geq 10^4$ cm^{-1}) is the fundamental absorption edge. Region B is the Urbach edge, (exponential change in α occurs). Region C represents the weak absorption (Urbach) tail. (b) The absorption edge of a-Se at various temperatures between −200 °C and 400 °C. After Tauc [6] in Ref. [8].

The optical bandgap from direct and indirect transitions can be extracted from $(\alpha hv)^2$ vs. $E(hv)$ and $(\alpha hv)^{1/2}$ vs. hv plots, respectively. Figure 3.5 (a) and (b) provide typical examples that represent the optical bandgap estimation of direct and indirect semiconductors. Note that for direct transitions $m = 2$ and for indirect transitions $m = ½$.

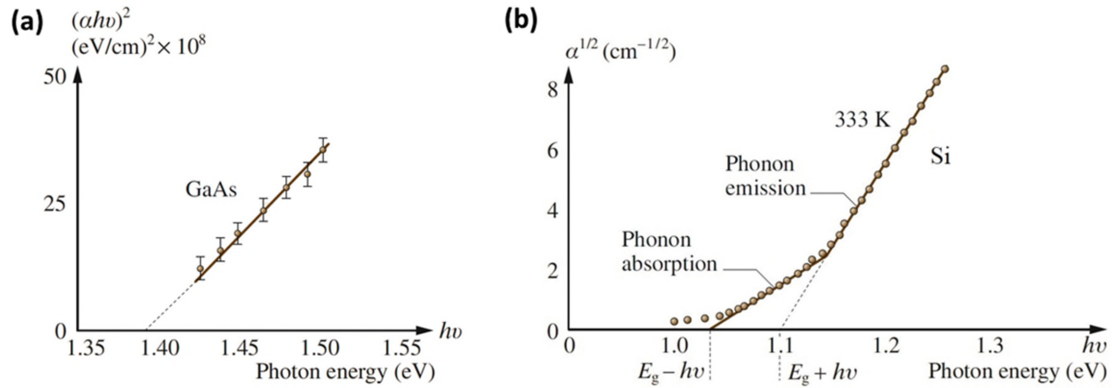

Figure 3.5 Bandgap estimation (a) of single-crystal GaAs, a direct semiconductor, from $(\alpha h\nu)^2$ vs. $h\nu$ (b) Si a well-known indirect semiconductor from $(\alpha h\nu)^{1/2}$ vs. $h\nu$. (a) and (b) are partial extraction from Mistrik et al. [5].

Figure 3.5 (a) shows the estimation of GaAs, a well-known III-V semiconductor. In the $(\alpha h\nu)^2$ vs. $h\nu$ plot, a line drawn through the data is extrapolated onto the $h\nu$-axis. The extrapolated value corresponds to the photon energy at $(\alpha h\nu)^2 = 0$ and is considered to be the optical band gap of the material (approximately 1.38 eV). Figure 3.5 (b) shows the calculation of the optical band gap of Si, an indirect band gap semiconductor. The extrapolated value on the $h\nu$ -axis gives the optical band gap of the semiconductor (approximately 1.06 eV). Notice the curvature in the optical absorption coefficient vs. photon energy plot in the low photon energy range, which represents optical absorption accompanied by photon absorption.

In order to obtain the optical constants and optical bandgap of a thin film medium, certain relations between these quantities and the optical transmission, absorption and reflection spectra must be established. Such relations are available to analyze the transmission and reflection spectra and hence extract the optical constants and the optical gap. In the following sections, the so-called Swanepoel and Manifacier techniques used in this work to calculate optical constants and optical bandgap are introduced and discussed. These two techniques are now widely used to analyze the transmission spectra through thin films.

3.4 Calculation of Optical Constants-Analysis Techniques

Optical constants of a thin film semiconductor can be extracted from the optical transmission spectra obtained from spectrophotometry. The transmission spectrum of thin films may or may not show distinct interference fringes, which depend on the strength of the attenuation (absorption and other mechanisms such as scattering) mechanism in the material. In the case of moderate absorption, the transmission spectrum typically contains two or more interference fringes. On the other hand, in the case of high absorption (which applies to VO_2 thin films), no interference fringes are present in the transmission spectrum. A detailed explanation of the analysis of optical constants using the transmission spectrum of thin films for various film thicknesses and absorption conditions can be found in Refs. [8,9]. The relation of the optical constants of thin films to their optical transmission has a complicated wavelength dependence, which makes the analysis of transmission spectra quite tedious. The section below covers the most common analysis techniques used to extract the optical constants of VO_2 thin films, examined in this work.

3.4.1 The Swanepoel Technique

The Swanepoel technique [10] is widely used to extract the optical constants of semiconductor thin films. Fundamentally, an initial attempt to calculate the optical constants using reflectance and/or transmission spectrum with respect to wavelength has been done by Hall and Ferguson [11]. Subsequently, a model was developed by Lyashenko and Miloslavskii [12] to calculate the complex refractive index and the thickness of thin films. However, the main problem of their technique is impractical due to the complicated approximations used to calculate the optical constants, especially for weakly absorbing thin films. A much more practical technique to determine the optical constants n, K and the thickness (d) of a weakly absorbing thin film has been established by Manifacier et al. [13]. The advantage of the Manifacier technique over Lyashenko and Miloslavskii is that it has straightforward meaningful mathematical equations that give more accurate results for the n, K and d. For materials with high absorption, the extinction coefficient (K) is considered to be negligible. In such cases, the calculation of n and d can be carried out by considering the Swanepoel technique. The basic assumption is that light entering the film at a certain wavelength suffers multiple interferences and, at the same time, experiences attenuation.

The relation between the optical transmittance and the optical constants can be presented through the following equation,

$$\tilde{T}(\lambda) = \frac{A(\lambda)x(\lambda)}{B(\lambda) - C(\lambda)x(\lambda)\cos\phi + D(\lambda)x(\lambda)^2} \tag{3.49}$$

where the parameters in Equation (3.49) are defined in Table 3.6 below. Equation (3.49) applies in the range $0 < x < 1$. The refractive index of the thin film is n and it is wavelength (λ)-dependent. It is the real part of the complex refractive index n^*. The refractive index of the substrate is taken as s and assumed to be independent of the wavelength. x is defined as $\exp(-\alpha d)$ and depends on the wavelength through α. ϕ is the phase change over one round-trip and depends on $n(\lambda)$ and the film thickness d.

Table 3.6 Parameters defined in transmittance ($\tilde{T}$) equation of Swanepoel technique [10].

Parameter	Term
n	Refractive index of the thin film medium
s	refractive index of substrate (independent)
ϕ	$4\pi nd/\lambda$
x	$\exp(-\alpha d)$
α	$C\exp(h\nu / \Delta E)$ or $4\pi K/\lambda$
s	Substrate refractive index
$A(\lambda)$	$16n^2s$
$B(\lambda)$	$(n+1)^3(n+s^2)$
$C(\lambda)$	$2(n^2-1)(n^2-s^2)$
$D(\lambda)$	$(n-1)^3(n-s^2)$

The Swanepoel technique has two versions that depend on the uniformity of the thin film. Essentially, this technique can be applied to uniform and non-uniform thin films separately. In the following the transmittance spectrum of a thin film of a uniform surface is considered for the

Swanepoel analysis. The determination of the refractive index (n) and the absorption coefficient (α) of the thin film requires a sequence of crucial steps in the analysis. The primary step of the analysis is to determine the refractive index of the substrate (s). For a low absorbing substrate, that is a substrate with an extinction coefficient $K \leq 0.1$ and $\alpha \leq 10^{-2}$ cm^{-1}, its refractive index can be calculated from:

$$s = \frac{1}{\tilde{T}} + \sqrt{\left(\frac{1}{\tilde{T}^2} - 1\right)} \tag{3.50}$$

In the second step, the transmittance spectrum of the uniform thin film sample on the substrate is measured. A typical flow chart of the Swanepoel technique used to calculate the optical constants in thin films under weak (but not negligible) absorption is given in Figure 3.6.

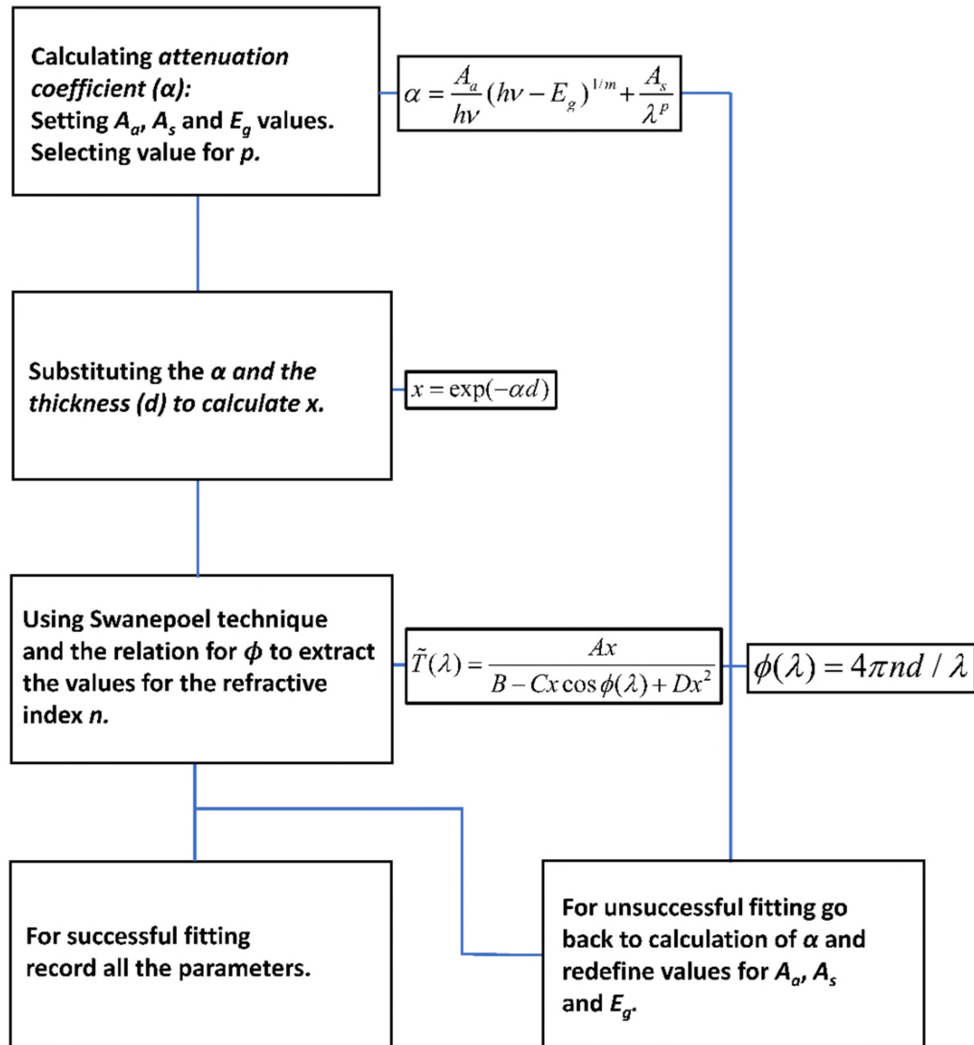

Figure 3.6 Swanepoel technique flow chart for calculating the attenuation coefficient and the optical bandgap.

There are two approaches to applying the Swanepoel technique. If no clear interference fringes are apparent, then the approach is based on varying the optical parameters until the predicted transmittance agrees with the experimental spectrum. The fitting of the transmittance spectrum can be explained as follows. First of all, we begin with Equation (3.49) and the parameters ϕ and x as presented in

Table 3.3. A_a, A_s and E_g values are substituted into Equation (3.40). The index p is chosen with respect to the nature of the scattering. The exponent m is chosen with respect to the type of electron transition (direct or indirect transition). After substituting these numbers, the thickness (d) is used in equations for ϕ and x in Table 3.3. Next, the constants A, B, C and D are substituted into the equation. Multiple attempts are made until the best fit is achieved by adjusting the constants in the Swanepoel model and the constants in the attenuation coefficient. The values that give a near-perfect fitting of the transmittance spectrum are recorded. Consequently, the attenuation coefficient is calculated from the values of A_a, E_g, A_s, m and p that give the best fitting. More explanation regarding the analysis of the attenuation coefficient, optical band gap, m and p exponents can be found in the discussion part of Chapter 4.

If the transmittance spectrum exhibits fringes (at least two), then the analysis becomes more accurate in terms of the dispersion of optical constants and one can also extract the thickness d of the film. A recent description of the Swanepoel technique can be found in Kasap et al. [8], Chapter 1. The procedure can be summarized as follows based on the original description of Swanepoel [10,14].

We begin our explanation of the method to extract the optical constants of the thin films with uniform thickness, deposited on a thick substrate. Figure 3.7 shows a sketch of light transmission through a thin film of uniform thickness.

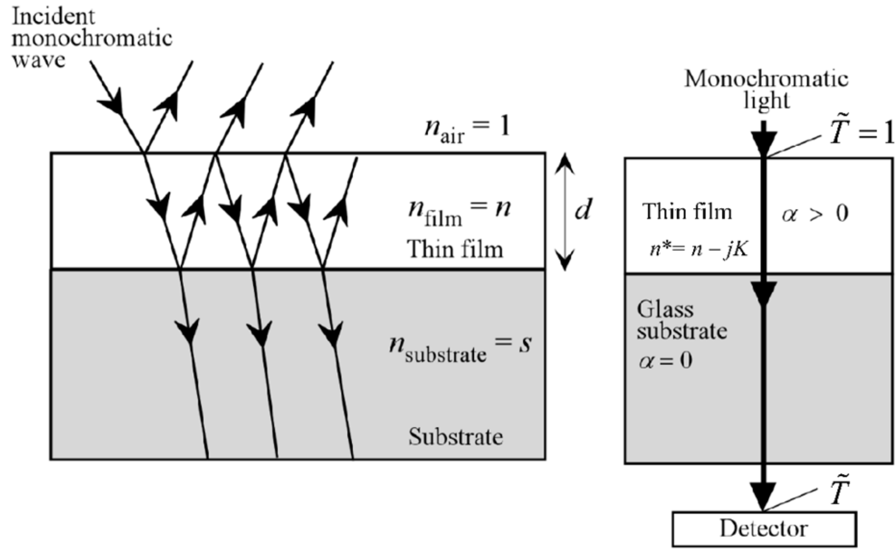

Figure 3.7 Schematic sketch of the typical behavior of light passing through a thin film with uniform thickness on a thick substrate. On the left, the oblique incidence is shown to demonstrate the multiple reflections. In most measurements, the incident beam is nearly normal to the film as shown on the right. After Ref. [8].

Initially, the transmittance spectrum of the thin film is measured in a desired wavelength range. The transmittance spectrum of the substrate is also measured to obtain the wavelength dependence of the substrate. As an initial step, the envelope of tangents at the maxima and minima of the transmittance spectrum of the thin film are constructed. Figure 3.8 shows the construction of envelopes around the transmission spectrum of a uniform a-Se thin film.

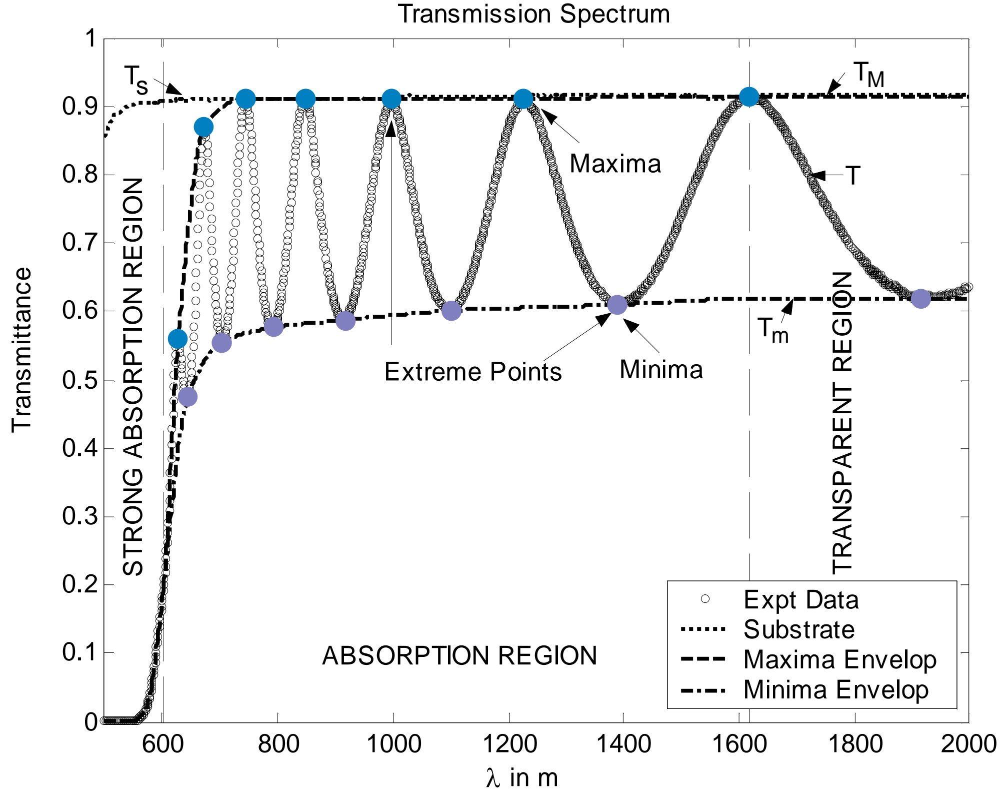

Figure 3.8 The construction of envelopes around the transmission spectrum of a uniform a-Se thin film of 0.9687μm. The extreme points, the maximum transmittance (T_M) and minimum transmittance (T_m) values are indicated with blue and gray dots, respectively. The spectrum consists of strong absorption (λ < 600 nm), absorption (600 nm < λ < 1610 nm) and transparent regions (1610 nm < λ < 2500 nm). After Ref. [8].

After constructing the envelopes, maximum (T_M) and minimum (T_m) transmittance are determined, and the parameter N is calculated using T_M, T_m and $s(\lambda)$ as given below:

$$N = 2s\left[\frac{T_M - T_m}{T_M T_m}\right] + \frac{s^2 + 1}{2} \tag{3.51}$$

Afterwards, using N and $s(\lambda)$ the refractive index of the film $n(\lambda)$ is found for wavelengths at extreme points (λ_{extreme}) using Equation (3.52),

$$n = \left[N + (N^2 - s^2)^{1/2}\right]^{1/2} \tag{3.52}$$

As the next step, at least two adjacent pairs of T_M and T_m are used to calculate a crude thickness (d_{crude}) which can be given below:

$$d_{crude} = \frac{\lambda_1 \lambda_2}{2(\lambda_1 n_2 - \lambda_2 n_1)} \tag{3.53}$$

The d_{crude} values can be recalculated for different pairs of maximum and minimum and averaged to estimate the average thickness (d_{avg}). Afterwards, the absorption coefficient (α) is determined using the relation in Equation (3.54),

$$\alpha = -\frac{\ln(x)}{d_{ave}} \tag{3.54}$$

where the parameter x is defined as:

$$x = \frac{E_M - \sqrt{E_M^2 - (n^2-1)^3(n^2 - s^4)}}{(n-1)^3(n - s^2)} \tag{3.55}$$

and E_M is:

$$E_M = \frac{8n^2 s}{T_M} + (n^2-1)(n^2 - s^2) \tag{3.56}$$

The next step is to find the interference order $m' = 2n_e d_e/\lambda$, where n_e is at $\lambda = \lambda_e$ = extreme point wavelength. Here m' is assigned as an integer for maxima and half integer for minima. Using the integer and half-integer m', the new thickness at each maximum and minimum is calculated

from the relation $d' = m'\lambda_e/2n_e$, where n_e is at $\lambda_e = \lambda$ an extreme point. Then, a new and better average thickness d_{avg} is calculated. Using this new d_{avg} and m' a new n_e at each extreme λ_e is determined. By setting a better dispersion fit $n = f_{new}(\lambda)$ to the new n_e vs. λ_e data is obtained. Using this new data, the x and hence α in the weak absorption region are recalculated. Finally, the calculated parameters are inserted into Equation (3.49) and a transmittance spectrum is generated. The difference between the experimental and the calculated spectra is determined with respect to the experimental thickness (d_{exp}) by minimizing the root-mean-square error given below:

$$\mathrm{RMSE} = \sqrt{\frac{\sum_{i=1}^{q}\left(\tilde{T}_{\mathrm{exp}} - \tilde{T}_{\mathrm{cal}}\right)^2}{q}} \tag{3.57}$$

where $\tilde{T}_{\mathrm{exp}}$ is the experimental transmittance and $\tilde{T}_{\mathrm{cal}}$ is the calculated transmittance and q refers to the range of the experiment.

Figure 3.9 presents the flow chart of the Swanepoel method for films with uniform thickness.

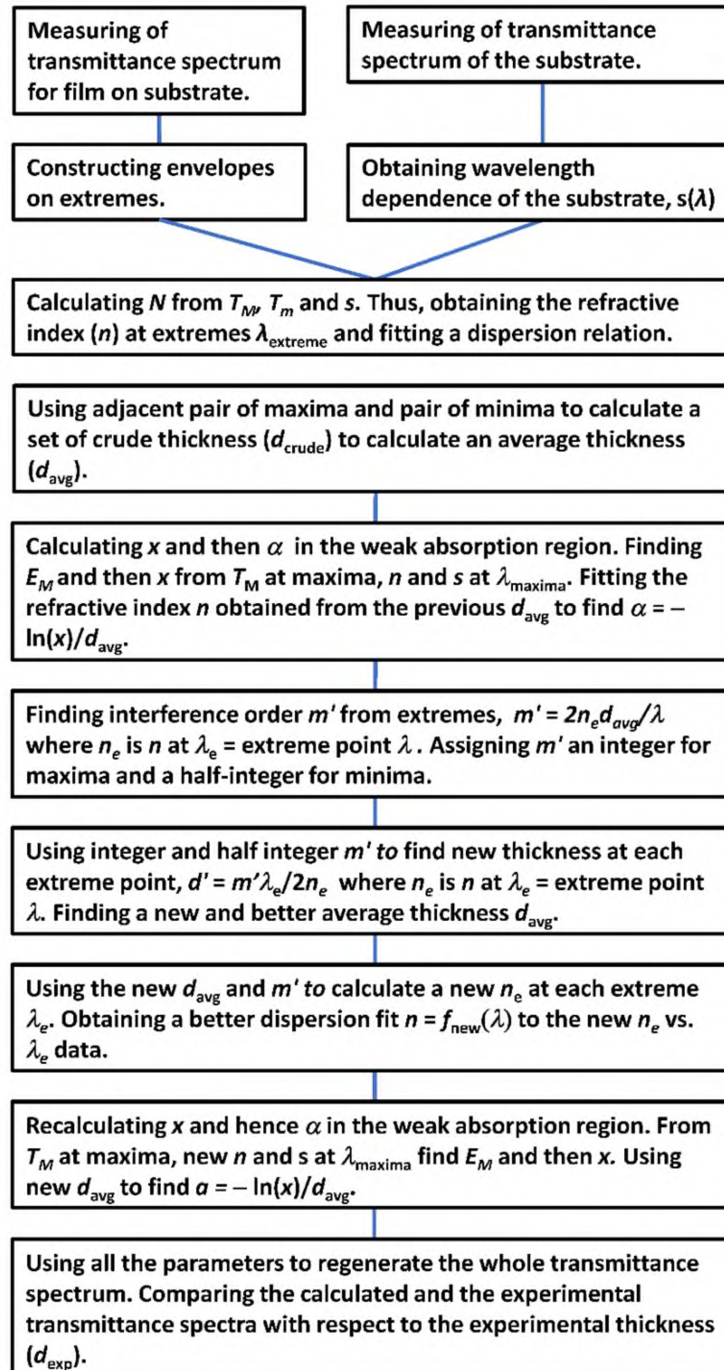

Figure 3.9 The flow chart of the Swanepoel technique applied for a thin film with uniform thickness.

For films with non-uniform thickness, the extraction of the optical constants requires adjustment to the relation presented in Equation (3.49) and several additional steps. First of all, the

transmittance presented in Equation (3.49) can be rewritten for films with non-uniform thickness as:

$$T_{\Delta d} = \frac{1}{\phi_2 - \phi_1} \int_{\phi_1}^{\phi_2} \frac{Ax}{B - Cx\cos\phi + Dx^2} dx \tag{3.58}$$

where the parameters A, B, C and D, x and ϕ are the same as given in Table 3.6. There are two phase constants ϕ_1 and ϕ_2 which are defined below:

$$\phi_1 = \frac{4\pi n(d_{avg} - \Delta d)}{\lambda} \tag{3.59}$$

$$\phi_2 = \frac{4\pi n(d_{avg} + \Delta d)}{\lambda} \tag{3.60}$$

d_{avg} is the average thickness and Δd is the thickness variation. Figure 3.10 shows a sketch of a thin film with non-uniform thickness.

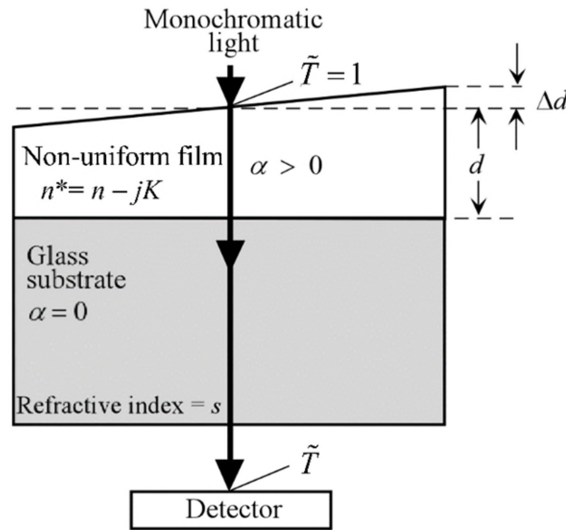

Figure 3.10 Schematic sketch of the typical behavior of light passing through a thin film with a non-uniform thickness on a thick substrate. In most measurements, the incident beam is almost normal to the film. After Ref. [8].

The extraction of the optical constants can be explained as follows. Initially, the transmittance spectrum of the substrate and the thin film are measured. After these measurements, the refractive index n and Δd are obtained from the equations given below:

$$T_{Md} = \frac{\lambda}{2\pi n \Delta d} \frac{a}{\sqrt{1-b^2}} \tan^{-1}\left[\frac{1+b}{\sqrt{1-b^2}} \tan\left(\frac{2\pi n \Delta d}{\lambda} \right) \right] \quad (3.61)$$

$$T_{md} = \frac{\lambda}{2\pi n \Delta d} \frac{a}{\sqrt{1-b^2}} \tan^{-1}\left[\frac{1-b}{\sqrt{1-b^2}} \tan\left(\frac{2\pi n \Delta d}{\lambda} \right) \right] \quad (3.62)$$

where $a = \frac{A}{B+D}$, and $b = \frac{C}{B+D}$. These equations are set for strong absorption, $x = 1$.

Next, n and x are obtained using the maximum and minimum transmittance (T_M and T_m) in the weak to medium absorption region (with noticeable interference fringes) using Δd from the previous step,

$$T_{Mx} = \frac{\lambda}{2\pi n \Delta d} \frac{a_x}{\sqrt{1-b_x^2}} \tan^{-1}\left[\frac{1+b_x}{\sqrt{1-b_x^2}} \tan\left(\frac{2\pi n \Delta d}{\lambda} \right) \right] \quad (3.63)$$

$$T_{mx} = \frac{\lambda}{2\pi n \Delta d} \frac{a_x}{\sqrt{1-b_x^2}} \tan^{-1}\left[\frac{1-b_x}{\sqrt{1-b_x^2}} \tan\left(\frac{2\pi n \Delta d}{\lambda} \right) \right] \quad (3.64)$$

where $a_x = \frac{Ax}{B+Dx^2}$ and $b_x = \frac{Cx}{B+Dx^2}$. As long as the absorbance-type parameter is between $0 < x \le 1$, there is one unique solution to the Equations (3.63) and (3.64). Next, the refractive index n is fitted to a dispersion relation, $n = f(\lambda)$, to get the full spectrum range similar to the measured transmission spectrum. Then, the adjacent pair of maxima and pair of minima in the zero to medium absorption region (where one can still distinguish interference fringes) are used to calculate a set of crude thickness values d_{crude} from Equation (3.53) to find an average thickness (d_{avg}). Afterwards, the calculated x in the weak to medium absorption regions is used to extract α. Also, the α in the strong absorption region can be calculated from the following equation:

$$\alpha_{\text{weak, strong}} = -\frac{\ln(x_{\text{weak, strong}})}{\bar{d}} \tag{3.65}$$

where α_{weak} is the absorption coefficient in the weak and medium absorption region and α_{strong} is the absorption in the strong absorption region. The absorbance-type parameter in the strong absorption region (x_{strong}) can be represented as follows,

$$x_{\text{strong}} = \frac{A - \sqrt{(A^2 - 4T_i^2 BD)}}{2T_i D} \tag{3.66}$$

Further, the interference order m' from extremes, $m' = 2n_e d_{avg}/\lambda$ is found. Here, n_e is the refractive index at an extreme point and λ_{ave} is the wavelength at the extreme point. The m' is assigned an integer for maxima and half-integer for minima. The assigned integer and half-integer of m' is used to calculate a new thickness at each maximum and minimum using $d' = m'\lambda_e/2n_e$. Then, a new and better average thickness d_{avg} is calculated. The new d_{avg} and m' is used to calculate a new n_e at each extreme λ_e. Therefore, a better dispersion fit $n = f_{\text{new}}(\lambda)$ using the new data is established. As a final step, the x is recalculated using Equations (3.65) and (3.66) to calculate a new absorption coefficient (α) in their respective absorption regions. All these parameters are used in Equation (3.58) to regenerate a transmission spectrum. The root mean square error (RMSE) can be determined from the experimental spectrum using Equation (3.57). Figure 3.11 presents a regenerated transmission spectrum of a simulated sample with non-uniform thickness. Figure 3.12 delivers a flow chart of the Swanepoel technique used to extract the optical constants for a thin film with non-uniform thickness.

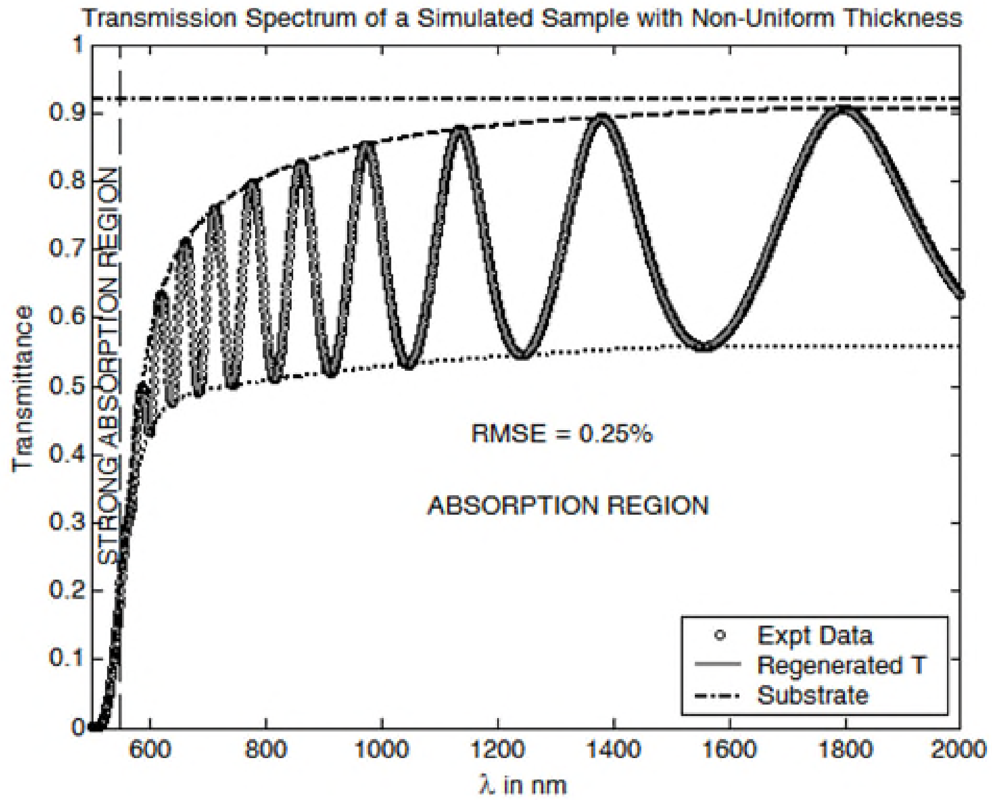

Figure 3.11 A regenerated transmission spectrum of a sample with an average thickness of 1 μm average thickness (d_{avg}) of 30 nm, and a refractive index fitted to a Cauchy equation. After Ref. [8].

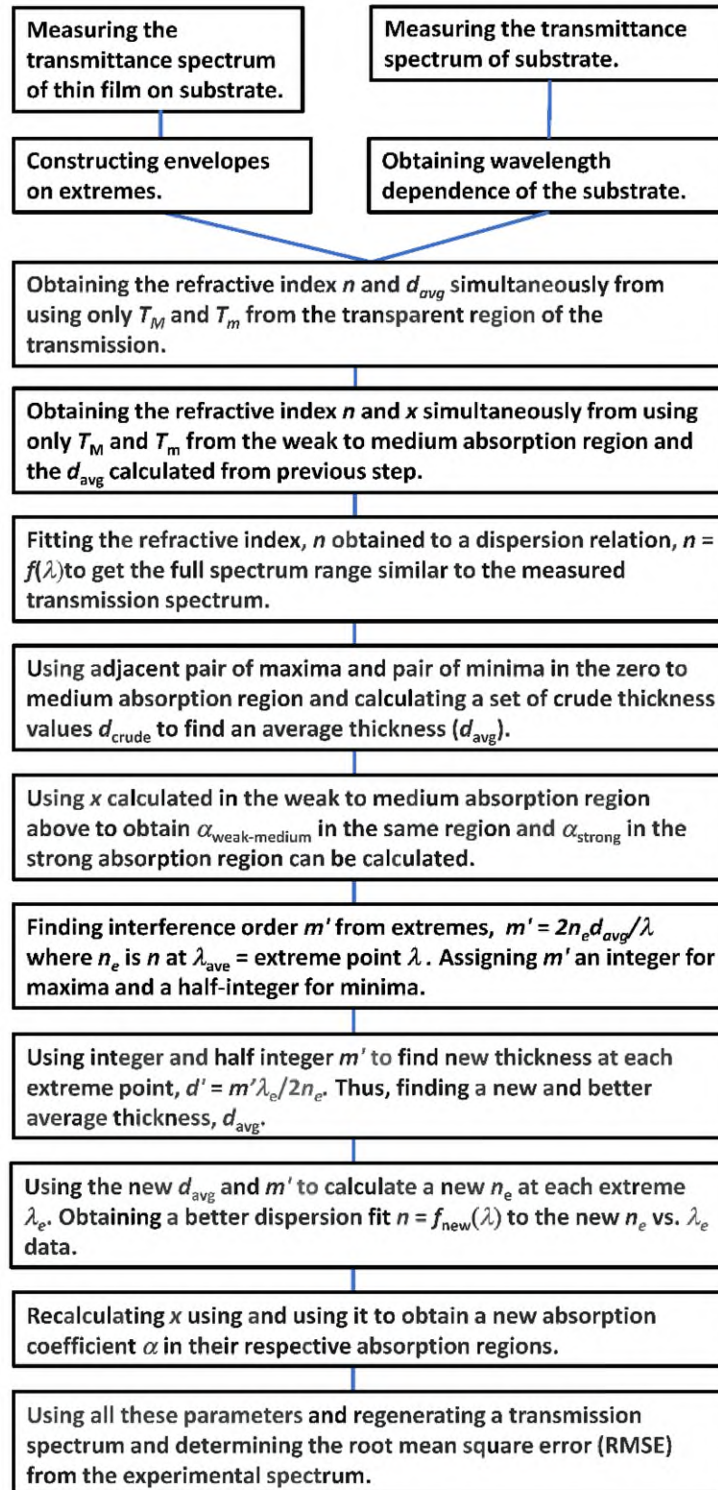

Figure 3.12 The flow chart of Swanepoel technique applied for a thin film with non-uniform thickness.

3.4.2 The Manifacier Technique

As mentioned in the previous subsection, the Manifacier technique offers a more general approach to the calculation of the optical constants where there is strong absorption, and the extinction coefficient (K) is significant. In this technique, the relation of the optical transmittance to the optical constants and thickness (d) is given by Equation (3.67) below and the parameters used therein are introduced in Table 3.7.

$$\tilde{T}(\lambda) = \frac{A(\lambda)x(\lambda)}{B(\lambda) - C(\lambda)x(\lambda) + D(\lambda)x(\lambda)^2} \tag{3.67}$$

This model is particularly useful for extracting the optical constants of a thin film in the strong absorption regime. A good example is the extraction of optical constants of a film on a Si substrate in the wavelength below 1100 nm where absorption is significant. Table 3.7 presents the parameters used in the relation of optical transmittance to the optical constants.

Table 3.7 Parameters defined in transmittance ($\tilde{T}$) equation of the Manifacier technique [13].

Parameter	**Term**
$A(\lambda)$	$16\,s[n^2+K^2]$
$B(\lambda)$	$[(n+1)^2+K^2]\,[(n+1)(n+s^2)+K^2]$
$C(\lambda)$	$C_1\,2\cos(\phi) - C_2\,2\sin(\phi)$
$D(\lambda)$	$[(n-1)^2+K^2]\,[(n-1)\,(n-s^2)+K^2]$
C_1	$[(n^2-1+K^2)\,(n^2s^2+K^2) - 2K^2(s^2+1)]$
C_2	$K[2(n^2-s^2+K^2)+(s^2+1)(n^2-1+K^2)]$
ϕ	$4\pi nd/\lambda$
x	$\exp(-\alpha d)$
α	$4\pi K/\lambda$

The application of the Manifacier technique is given in Chapter 5.

3.5 Summary

This chapter covered light transmission in thin films and the analysis techniques used to calculate the optical constants and optical bandgap. Initially, light transmission in thin films was briefly described. Secondly, the dispersion of light was considered by referring to various dispersion relations. Then, concise information about the optical constants n, K, α and E_g was given. In the fifth section, the calculation of the optical constants was introduced. The Swanepoel technique used to extract the optical constants for films of uniform and non-uniform thicknesses was explained. Moreover, the use of the Swanepoel technique on films that do not display interference fringes was covered. In addition, the Manifacier technique, a more general method to extract the optical constants was presented.

3.6 References

[1] S.O. Kasap, "Wave nature of light," in *Optoelectronics and Photonics: Principles and Practices*, 2nd ed., Upper Saddle River, NJ: Pearson. Education, Inc., 2013, p. 4.

[2] S.O. Kasap. (2019). Optoelectronics and Photonics: Principles and Practices, 2nd ed., for a Complete Course in Power Point [Powerpoint slides]. Available from the author upon request.

[3] E. Hecht, "Electromagnetic theory, photons, and light," in *Optics*, USA: Pearson Education, Inc., 2017, pp. 43-47.

[4] S.O. Kasap, K. Koughia, J. Singh, H. E. Ruda, and A. K. Ray, "Fundamental optical properties of materials II," in *Optical Properties of Materials and Their Applications*, 2nd ed., J. Singh, Ed. West Sussex, UK, John Wiley & Sons Ltd., 2020, p. 40.

[5] J. Mistrik, S. Kasap, H. E. Ruda, C. Koughia and J. Singh, "Optical properties of electronic materials: fundamentals and characterization," in *Handbook of Electronic and Photonic Materials*, 2nd ed., Springer International Publishing, 2017, pp. 47-48.

[6] J. Mistrik, S. Kasap, H. E. Ruda, C. Koughia and J. Singh, "Optical properties of electronic materials: Fundamentals and characterization," in *Handbook of Electronic and Photonic Materials*, 2nd ed., Springer International Publishing, 2017, p. 62.

[7] J. Tauc, *Amorphous and Liquid Semiconductor*, London and New York, Plenum Press, 1974, pp. 177-188.

[8] S.O. Kasap, W. Tan, J. Singh and A. K. Ray, "Fundamental optical properties of materials II," in *Optical Properties of Materials and Their Applications*, 2nd ed., J. Singh, Ed. West Sussex, UK, John Wiley & Sons Ltd., pp. 1-36.

[9] W. C. Tan, "Optical properties of amorphous selenium films," M.Sc. Thesis, Dept. of Elec. & Comp. Eng., Univ. of Saskatchewan, Saskatoon, SK, 2006, pp. 64-91.

[10] R. Swanepoel, "Determination of the thickness and optical constants of amorphous silicon," *Journal of Physics E: Scientific Instruments*, vol. 16, no. 12, p. 1214, 1983.

[11] J. F. Hall and W. F. C. Ferguson, "Optical Properties of Cadmium Sulfide and Zinc Sulfide from 06 Micron to 14 Microns," *Journal of the Optical Society of America A*, vol. 45, no. 9, p. 714, 1955.

[12] S. P. Lyashenko and V. K. Miloslavskii, "A simple method for the determination of the thickness and optical constants of semiconducting and dielectric layers," *Optics and Spectroscopy*, vol. 16, p. 80, 1964.

[13] J. C. Manifacier, J. Gasiot and J. P. Fillard, "A simple method for the determination of the optical constants n, k and the thickness of a weakly absorbing thin film," *Journal of Physics E: Scientific Instruments*, vol. 9, no. 11, p. 1002, 1976.

[14] R. Swanepoel, "Determination of surface roughness and optical constants of inhomogeneous amorphous silicon films," *Journal of Physics E: Scientific Instruments*, vol. 17, no. 10, p. 896, 1984.

4. The Effect of Substrate Biasing During DC Magnetron Sputtering on the Quality of VO_2 Thin Films and their Insulator-Metal Transition Behavior[2]

4.1 Abstract

In this work, VO_2 thin films were deposited on Si wafers (onto (100) surface) by DC magnetron sputtering under different cathode bias voltages. The effects of substrate biasing on the structural and optical properties were investigated. The results show that the metal–insulator transition (MIT) temperature of VO_2 thin films can be increased up to 14 K by applying a cathode bias voltage, compared to deposition conditions without any bias. The decrease in the transition efficiency and increase in the transition temperature are attributed to the enlarged grain size, increased defects, and the residual stress in the VO_2 thin films induced by biasing. The optical transmittance measurements for different thickness films indicate an attenuation coefficient of 3.1×10^7 m^{-1} at 2000 nm or an extinction coefficient (K) of 4.9 in the metal phase. The optical transmittance vs. wavelength characteristics point to an indirect bandgap of 0.6 ± 0.05 eV and significant scattering in the bulk and/or at the interface.

4.2 Introduction

Vanadium dioxide (VO_2) has been widely studied in recent years because of its ability to undergo a reversible metal–insulator transition (MIT) at around 68 °C, from a low-temperature insulating M-phase (monoclinic) to a high-temperature metallic R phase (rutile) [1]. This reversible transition makes VO_2 an excellent material for ultrafast optical switches, smart windows, Mott transistors, strain and gas sensors, actuators, and so forth [2–5]. The bandgap of VO_2 epitaxial films at room temperature have been reported to be about 0.7 eV [6], and would normally classify VO_2 as a semiconductor rather than an insulator, but the term “insulator’ is commonly used to represent the latter semiconducting phase. The properties of VO_2 thin films are

[2] This chapter has been published as Chunzi Zhang, Ozan Gunes, Yuanshi Li, Xiaoyu Cui, Masoud Mohammadtaheri, Shi-JieWen, Rick Wong, Qiaoqin Yang and Safa Kasap, “The effect of substrate biasing during DC magnetron sputtering on the quality of VO2 thin films and their insulator–metal transition behavior,” *Materials*, vol. 12, no. 13, p. 2160, 2019. doi:10.3390/ma12132160.

strongly dependent on deposition processing parameters. The phase inhomogeneity inVO_2 bulk or thin films limits their potential applications by rendering the MIT phase transition broad and diffusive [3,7]. The effects of strain, grain size, stoichiometry, substrate temperature, and substrate material have been extensively studied and optimized to achieve good crystallinity with a higher optical transmittance and a higher near-IR switching contrast [8−15]. In addition to optical transmittance and switching contrast enhancement, extensive efforts have been devoted to modifying the transition temperature (T_t) of VO_2. It was reported that doping and strain control are common methods for T_t modification [16−22]. Doping elements of W, Mo, F usually decrease the T_t [16−19], while doping elements of Al, Cr, Ti can increase the transition temperature [20,21]. The progress on T_t reduction has been successful and the T_t can be brought down by 20 °C [16]. In contrast, the studies on increasing the transition temperature of VO_2 are not many. Nevertheless, the upper bound of working temperatures for most of the electrical devices utilizing optical switches, transistors, sensors, and actuators are possibly higher than 68 °C due to the accumulated heat during service, which would result in a premature MIT of VO_2. So, a higher transition temperature of VO_2 is desirable for these applications.

In previous works, it has been found that the substrate biasing during deposition can change both the microstructure and properties of VO_2 thin films [23−25]. In this work, the effects of substrate biasing are systematically investigated with the goal of increasing the transition temperature of VO_2. We have considered only single-crystal silicon substrates with the view that these VO_2 films would have to be integrated with today's silicon-based microelectronics towards hybrid optoelectronic devices. Results reported in this work show that the substrate biasing during the deposition of VO_2 thin films by DC magnetron sputtering can be effective in increasing the transition temperature.

4.3 Materials and Methods

Si (100) wafer substrates were ultrasonically cleaned in ethanol and dried in air for use in deposition. VO_2 thin films were deposited by DC reactive magnetron sputtering onto Si substrates with substrate biasing (i.e., negative bias is applied to the substrate). A high-purity vanadium target (99.95%) was used and sputtered in an Argon (Ar) (100 SCCM) and oxygen (O_2) (1.3 SCCM) atmosphere at a constant pressure of 1.33 Pa and a constant substrate temperature of 650 °C (923

K). The applied biasing voltage ranged from 89 V to 173 V. The duration of the deposition process was 2 h with a sputtering power of 100 W.

The as-prepared VO_2 thin films were then characterized using scanning electron microscopy (SEM), Raman spectroscopy, and X-ray Photoelectron Spectroscopy (XPS). The Raman spectra were taken at room temperature using a Renishaw Invia Reflex Raman Microscope (Renishaw, Mississauga, ON, Canada). The operating laser wavelength was 514.5 nm. The optical transmission was measured in the wavelength range of 350–2500 nm using a spectrometer. The transmission measurements were carried out at 300 K and 368 K (above the MIT temperature). The thermal hysteresis loops were obtained by collecting transmittance values versus temperature (with 5 K intervals both in the heating and the cooling process) at the wavelength of 2500 nm, corresponding to the largest contract in transmittance. Furthermore, the XPS study was carried out using a synchrotron X-ray radiation source at the Canadian Light Source (Saskatoon, SK, Canada). The X-ray photon energy range used for this study was 5.5–250 eV and the spectra were collected using a Photoemission Scienta 100 analyzer (Scienta Omicron, Uppsala, Sweden) under ultrahigh vacuum (10^{-10} torr). The thickness of the as-deposited VO_2 thin films was measured by a Zygo Optical Profilometer (Zygo, Middlefield, OH, USA) and the grain size was determined on the SEM by using an image processing software SPIP (Version 5.1, Image Metrology, Copenhagen, Denmark).

4.4 Results

4.4.1 Microstructure Characterization by Raman

In order to study the effect of substrate biasing, we have used single-phase VO_2 thin films deposited under different substrate bias voltages. This is because nonstoichiometric VO_x thin films usually have significantly different properties compared with single-phase VO_2 and therefore cannot be used in this work. In our previous work, Raman spectroscopy results have shown to be very useful in studying the stoichiometry of VO_2 thin films [26]. Therefore, Raman measurements were again used in this study. The deposition conditions are listed in Table 4.1. Figure 4.1 shows the Raman spectra of the as-deposited VO_2 thin films. All the films show typical VO_2 with the bias voltage ranging from 89 V to 173 V, suggesting that the films have good stoichiometry. The sharp

Raman peak at 520 cm^{-1} and the broad peak at around 950 cm^{-1} are from the vibrations of the Si substrate [27].

Table 4.1 Grain size and thickness of the as-deposited VO_2 thin films with substrate biasing.

Sample#	Biasing power (W)	Biasing voltage (V)	Average grain size (nm)	Thickness (nm)
A	15	89	58.8 ± 0.6	102 ± 1
B	25	126	67.2 ± 1.0	93 ± 2
C	35	146	88.6 ± 1.2	68 ± 1
D	45	173	75.1 ± 0.5	60 ± 2

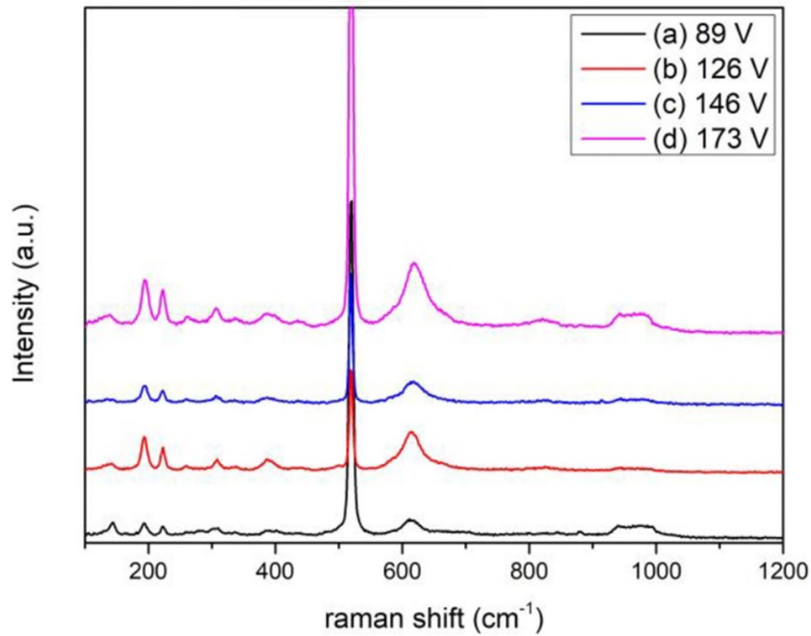

Figure 4.1 Raman spectra of the as-deposited VO_2 thin films with substrate biasing: (a) 89 V; (b) 126 V; (c) 146 V; (d) 173 V.

4.4.2 Surface Morphology Characterization by SEM

The surface morphology of the as-deposited VO_2 thin films was characterized by SEM and the results are shown in Figure 4.2. All the samples show a polycrystalline structure with a few small grains on top of large grains due to secondary nucleation. In our previous work, the average grain size of the VO_2 thin films deposited for 2 h (150 nm thick) without substrate biasing was 55.4 nm as shown in Figure 4.2 (e). However, the grain size of the VO_2 thin films deposited under the same conditions but with substrate biasing for 2 h (68 nm thick) was much higher and reached 88.6 nm, as shown in Table 4.1. Moreover, it can be seen that the deposition rate decreased with increase of substrate bias voltage, which is associated with enhanced ion bombardment. Even with reduced deposition rate and thickness, the grain size was significantly larger. This is due to the competing effects of thickness and substrate biasing. Generally, grain growth increases with increasing film thickness since grains can grow further. However, the substrate bias during deposition increases the kinetic energy of the particles impacting the coating; as a consequence, there is an increase in the surface mobility of the atoms forming the film, leading to larger crystalline grains even in thinner films. These results show that substrate biasing is very effective in grain size enlargement.

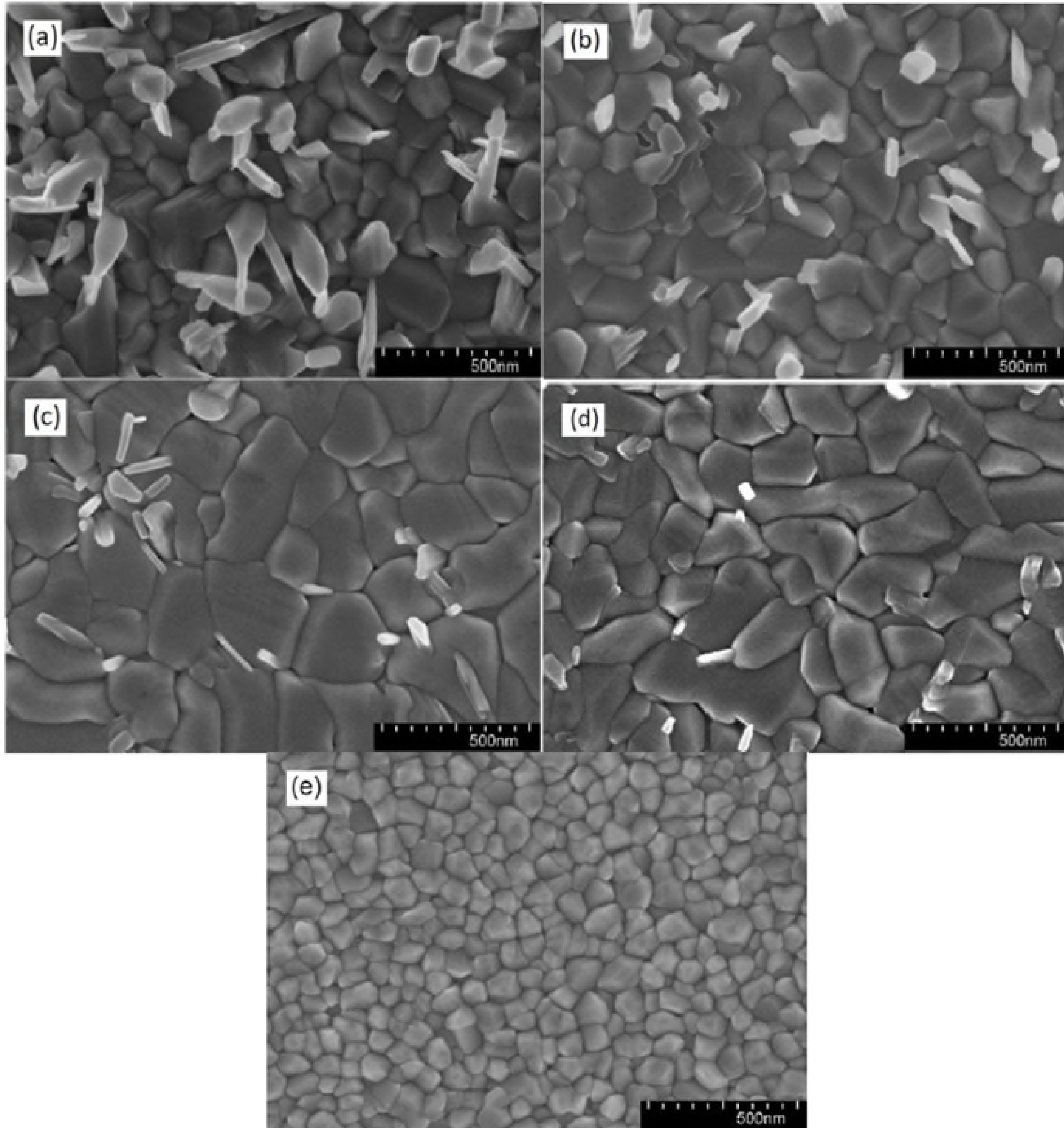

Figure 4.2 SEM images of VO_2 thin films deposited on Si substrates for 2 h with bias voltage of: (a) 89 V; (b) 126 V; (c) 146 V; (d) 173 V; (e) no bias on a sample prepared as in [23].

4.4.3 Chemical States Characterization by XPS

To fully understand the chemical states near the surface area, we have also taken x-ray photoemission spectroscopy on our as-deposited VO_2 thin films as shown in Figure 4.3. The measurement was performed at PGM beamline at the Canadian Light Source, with a beam size of $200 \times 200\ \mu m^2$ at room temperature. We can compare the electron states of V 3d and 3p and O 2s

in the films deposited under different biasing voltage in Figure 4.3. It should be mentioned that due to the sensitivity of this technique and the short escape depth of the electrons, the electrons accounting for the spectra are coming from the very surface, at a depth of a few Angstroms from the surface. Therefore, the spectra give information on how the V–V and V–O bonds can be distinguished from each other on the surface. Based on the XPS spectra shown in Figure 4.3, with all the electronic states considered, it can be concluded that the substrate biasing voltage has little influence on the V–O and V–V bonds at the surface of the thin films.

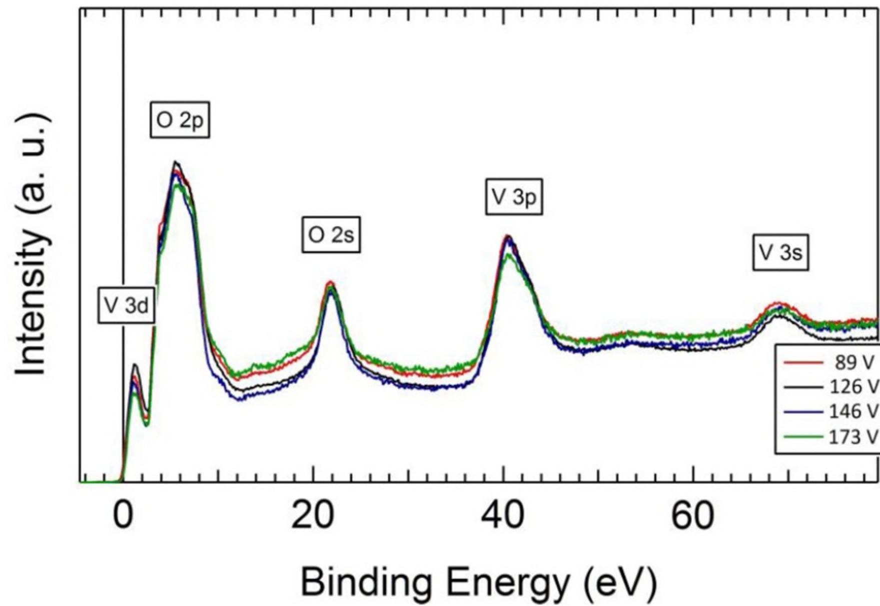

Figure 4.3 XPS spectra of the as-deposited VO_2 thin films with substrate biasing.

4.4.4 Optical Measurements

The transmission spectra of the as-deposited VO_2 thin films under different biasing conditions are shown in Figure 4.4. It should be noted that at wavelengths less than 1100 nm (corresponding to the 1.1 eV bandgap of Si), the Si substrate absorbs all the light as shown in Figure 4.4 (e), so there is no transmittance. The maximum transmittance reaches about 50% at a wavelength of 2500 nm. The optical transmittance of VO_2 thin films deposited under different bias voltage at (a) 300 K and (b) 368 K are shown in Figure 4.5. While in the insulating phase (at 300 K), the transmittance values are very close, in the metal phase (at 368 K), there is distinct dependence on the bias voltage during deposition. However, the actual effect arises from the

difference in the thicknesses. The optical transmittance of a homogeneous medium generally decreases with increasing film thickness as $\tilde{T} = \tilde{T}_0 \exp(-\alpha d)$, where α is the attenuation coefficient, d is the film thickness, and the term $\tilde{T}_0$ is a pre-exponential constant ($\tilde{T}$ as $d \to 0$). Figure 4.6 shows the semilogarithmic plots of the optical transmittance ($\tilde{T}$ as %) vs. the film thickness in the insulating and metal phases. The transmittance contrast $\Delta\tilde{T}$ (transmittance difference between normal and switched phases) vs. film thickness is also shown. First, consider the metal phase at 368 K, and notice the clear reduction in the transmittance as the film thickness increases, following an exponential behavior with an attenuation coefficient $\alpha \approx 3.1 \times 10^7$ m^{-1} at a wavelength of 2000 nm. The reason we can deduce an attenuation coefficient from the ln(T) vs. d plot is that the light intensity is extinguished so much as it passes through the film in this metallic phase that interference phenomena arising from Fresnel reflections are insignificant. This is not the case in the insulating phase.

The transmittance of the VO_2/Si structure in the insulating phase at 300 K shows only a very small decrease with increasing film thickness as apparent in Figure 4.6. The change in $\tilde{T}$ with wavelength and thickness in thin films invariably involves interference in the presence of attenuation, which is analyzed below. It should be emphasized that the attenuation at 2000 nm in this phase -includes some possible band-to-band absorption and losses arises from scattering within the film as well as from any interface roughness, as discussed below. The transmittance contrast $\Delta\tilde{T}$, an important metric for device applications, increases with film thickness because of the steep decline in the transmission through the metallic phase.

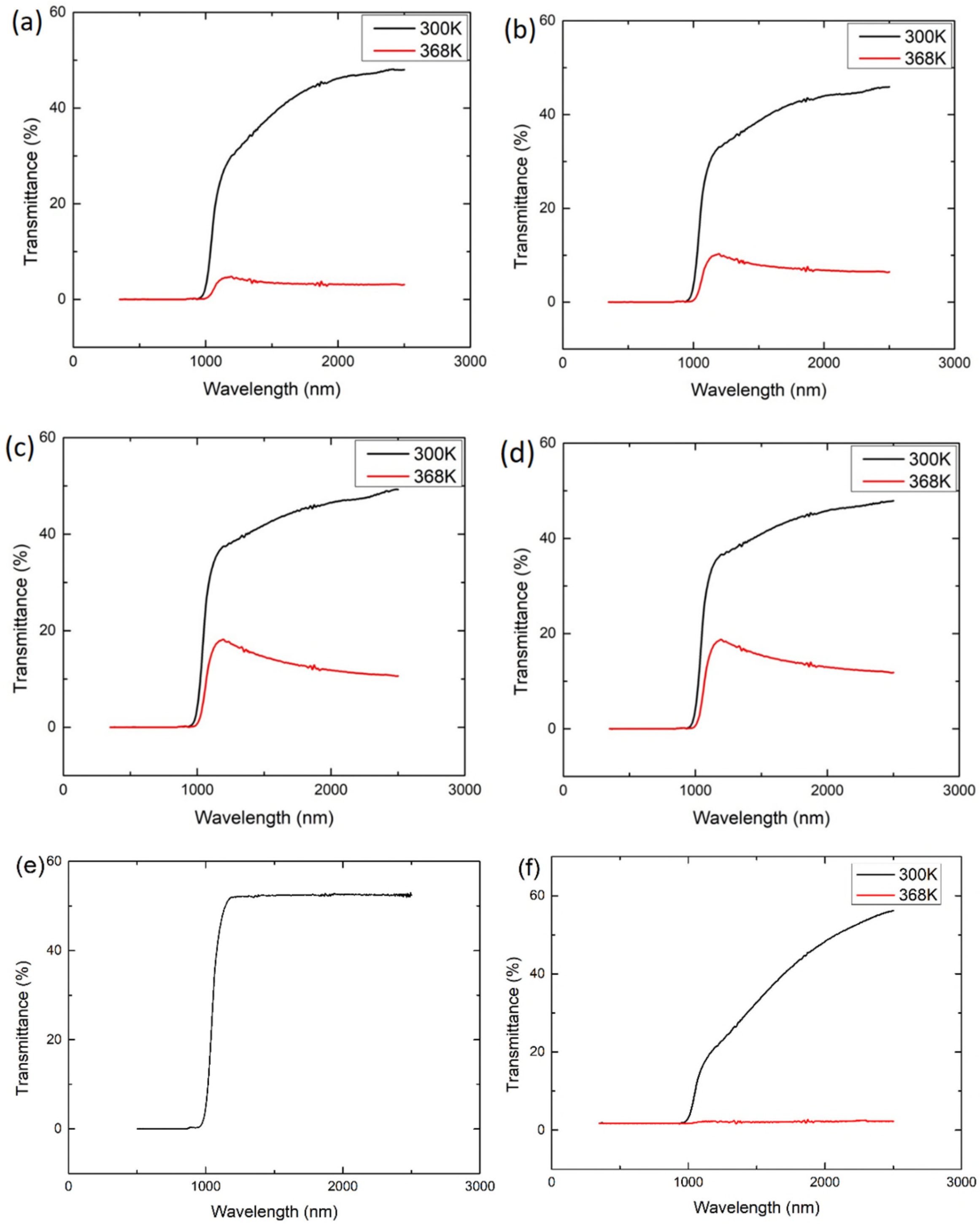

Figure 4.4 Optical transmittance of the as-deposited VO_2 thin films with a substrate bias voltage of: (a) 89 V; (b) 126 V; (c) 146 V; (d) 173 V; (e) bare Si substrate; (f) no bias (data extracted from Ref. [23] and replotted).

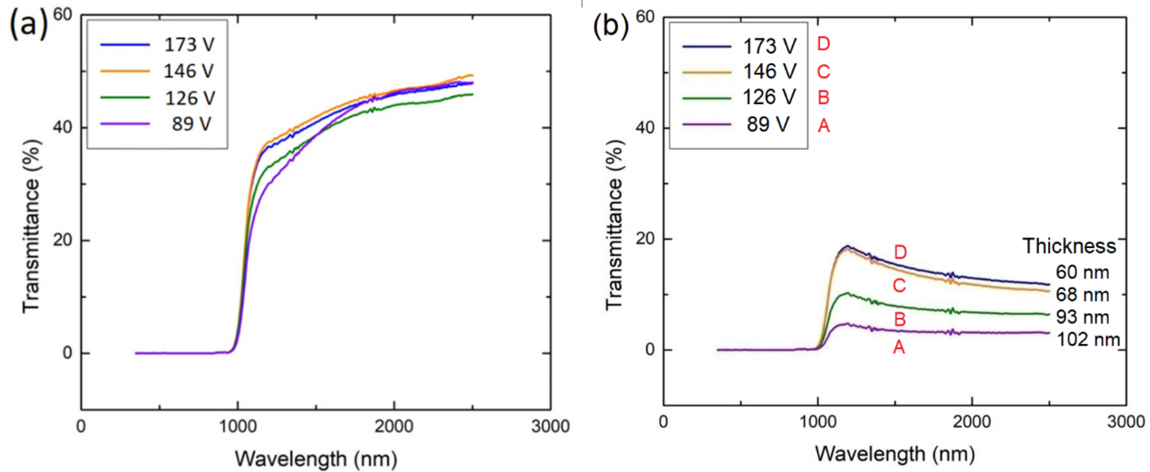

Figure 4.5 Optical transmittance of VO_2 thin films deposited under different bias voltages at (a) 300 K and (b) 368 K.

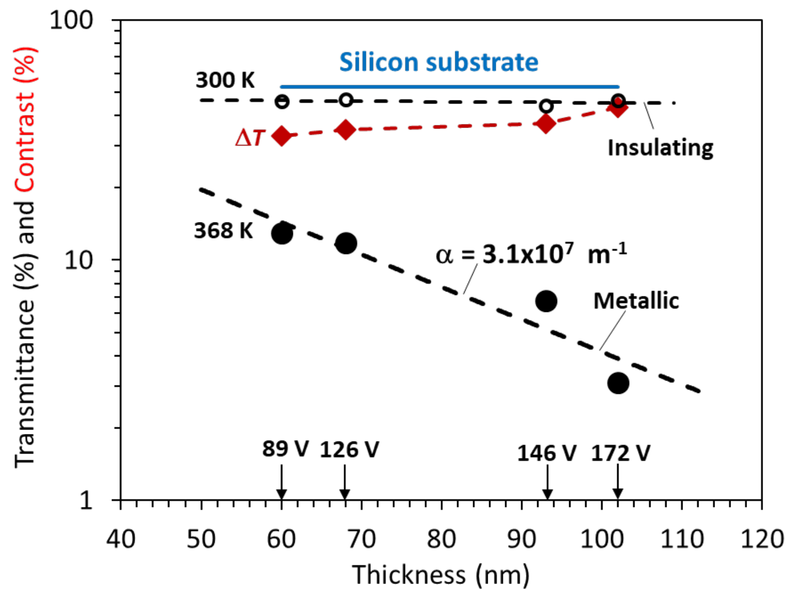

Figure 4.6 Optical transmittance at a wavelength of 2000 nm in the insulator and semiconductor phases (300 and 368 K, respectively) and contrast $\Delta\tilde{T}$ vs. thickness on a semilogarithmic plot. The dashed lines are exponential fits. The attenuation coefficient of the metal phase $\alpha \approx 3.1 \times 10^7$ m^{-1}.

Thermal hysteresis loops of transmittance vs. temperature are shown in Figure 4.7. It can be seen that the VO_2 thin films deposited with a substrate bias voltage from 126 V to 173 V show similar hysteresis with a temperature width (ΔH) of 13 K, while the sample deposited with 89 V

bias shows a wider hysteresis with a width of 20 K. Figure 4.8 provides a summary of transmittance vs. temperature curves under heating and cooling schedules for all the samples; the results are generally consistent with those in Figure 4.4 and Figure 4.5 and the implications in Figure 4.6. The comparison of the hysteresis width (ΔH) of 5 °C in VO_2 thin films deposited without any bias [23], shown in Figure 4.7(e), indicates that the VO_2 thin films deposited with biasing exhibit quite wider hysteresis loops. The ΔH widening can be attributed to grain boundaries and defects induced by the bias, and the enlarged grain size. On the other hand, the transition temperature T_t of VO_2 thin films deposited with bias increases significantly compared with those deposited without biasing. VO_2 thin films deposited without biasing show T_t of 335 K as we reported previously [23], whereas T_t of VO_2 thin films deposited with biasing reaches up to 349 K in this work. Usually, the variation of the transition temperature has been associated with the stress and microstructure of the samples [28]. In this work, it is likely that the increased defect density may also lead to an increase of T_t along the lines in [29]. Another factor is the grain size. The increase of the grain size usually leads to an increase in T_t and also the width of hysteresis ΔH as reported in, which is in accordance with our results. Further, the enhanced ion bombardment by biasing often generates residual stress in the as-deposited films [30]. In Figure 4.9, both the XRD and Raman results of VO_2 thin film deposited with biasing shows a minor shift towards higher angles or wave numbers compared with a VO_2 thin film deposited with no bias, indicating the existence of compressive stress which is induced by biasing during deposition. The significant residual stress in the films may make the phase transition harder, thus stabilizing the semiconductor phase. Therefore, the significant T_t increase (14 K) in this work could be attributed to the combined effect of enlarged grain size, increased defect density, and the residual stress induced by substrate biasing.

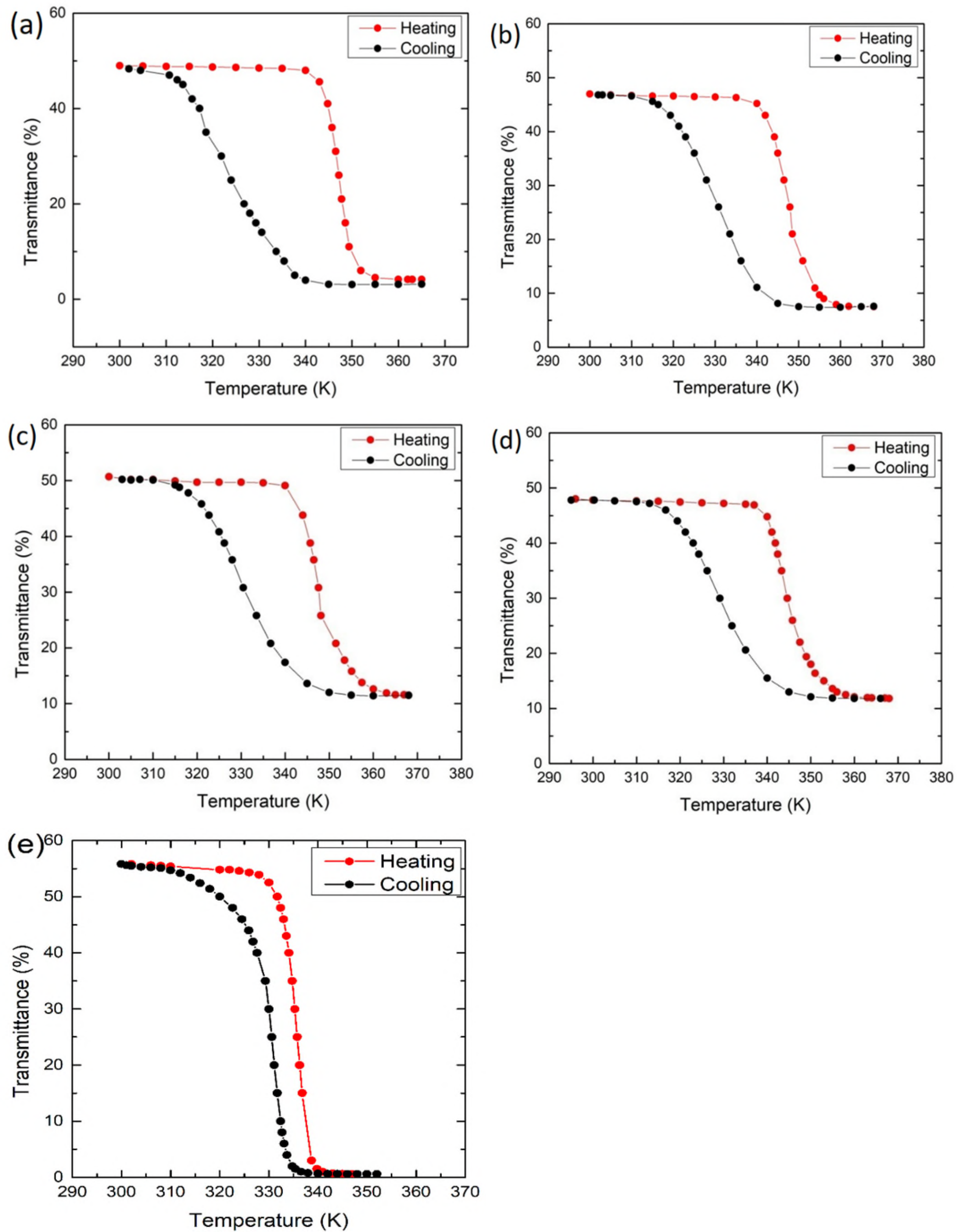

Figure 4.7 Optical transmittance of the as-deposited VO_2 thin films under heating (red) and cooling (black): (a) 89 V; (b) 126 V; (c) 146 V; (d) 173 V; (e) no bias (data extracted from Ref. [23] and replotted).

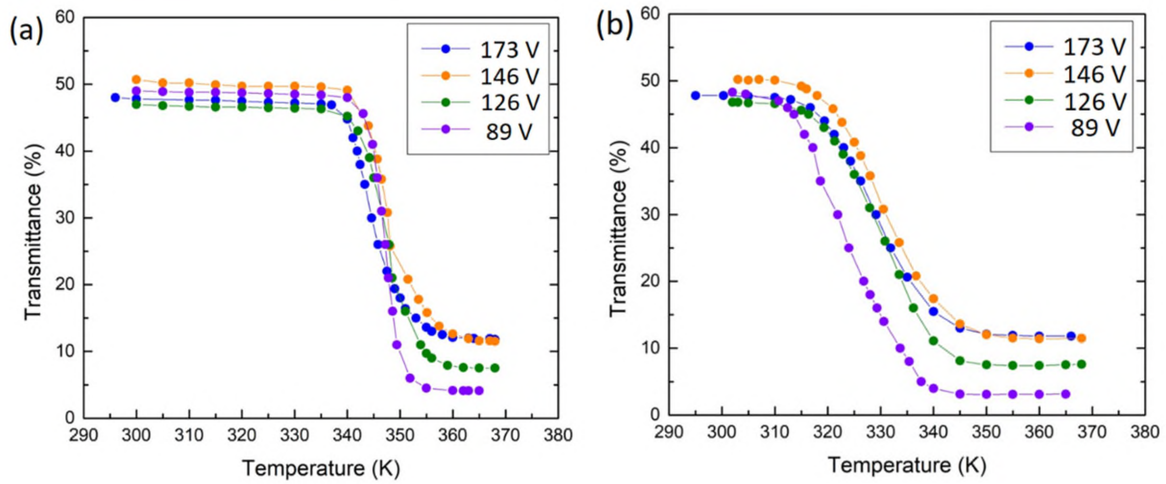

Figure 4.8 Optical transmittance of the as-deposited VO_2 thin films with biasing: (a) under heating and (b) under cooling.

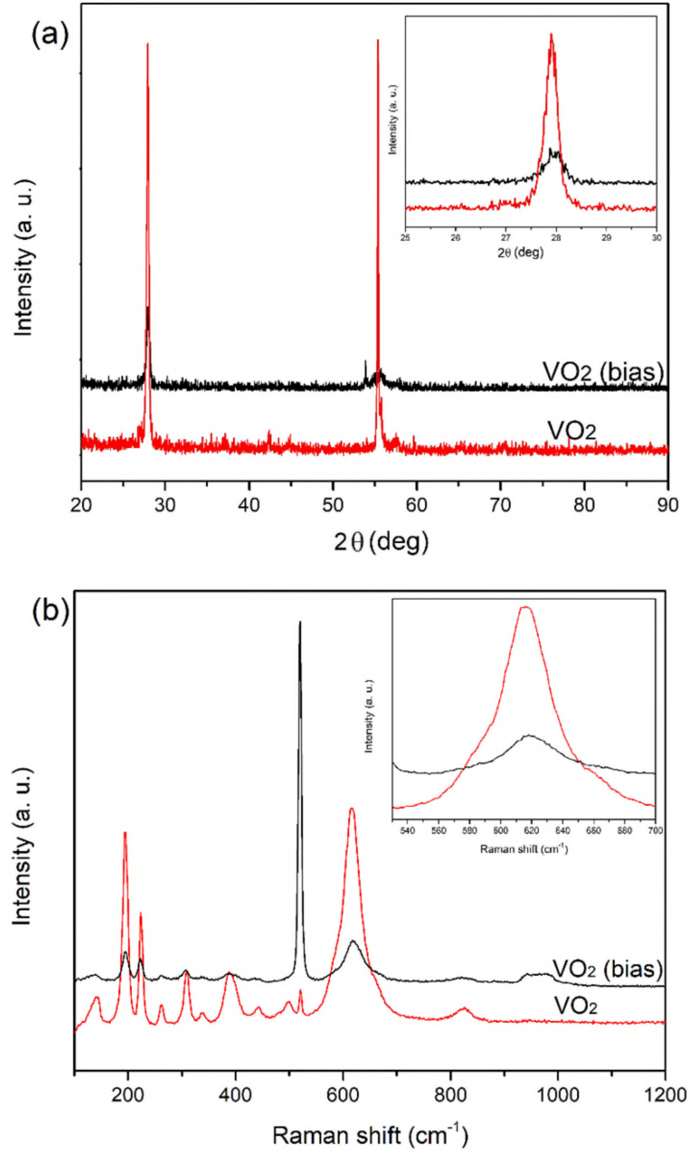

Figure 4.9 (a) X-ray diffraction patterns and (b) Raman spectra of VO_2 thin films (red) and VO_2 thin films deposited with 173 V bias (black).

4.5 Discussion

The present work clearly shows that applying substrate biasing can modify the microstructure and optical properties of VO_2 thin films deposited by magnetron sputtering. By applying substrate biasing, the deposition rate of the as-deposited VO_2 thin films decreases while the grain size increases. The films prepared under a higher bias voltage are thinner and hence show

higher transmission in the metallic phase. The defects induced by the substrate biasing degrade the optical properties of VO_2 in the sense that the hysteresis temperature width ΔH of the transition temperature observed during heating and cooling becomes poor. Applying substrate biasing also alters the characteristics of the phase transition. The transition temperature of VO_2 thin films deposited under bias increases 14 K accompanied by a widened hysteresis curve.

An advantage of the increased transition temperature of VO_2 thin films is the enhancement of thermal stability of VO_2 thin films for various electronic and optoelectronic device applications utilizing optical switches, transistors, sensors, and actuators, in which the working temperatures are possibly higher than 341 K (68 °C) due to the accumulated heat during service. The modification of T_t of VO_2 thin films have been studied previously by others towards reducing T_t. However, studies on increasing T_t of VO_2 have been only limited. In this work, the substrate biasing has been shown to be effective in increasing the T_t of VO_2. In future works, it would be useful to examine the effects of doping and strain control.

The thickness dependence of the transmittance in the metal phase in Figure 4.6 is very clear and leads to an attenuation coefficient of $\alpha \approx 3.1 \times 10^7$ m^{-1}. This high attenuation coefficient represents the absorption of light and can be attributed to free carrier absorption (the Drude model) [31].

$$\alpha \approx \frac{\sigma_o}{cn\varepsilon_o(\omega\tau)^2} \tag{4.1}$$

where σ_o is the real part of the AC conductivity (taken as the DC conductivity), c is the speed of light, n is the refractive index, ε_o is the absolute permittivity, ω is the angular frequency ($2\pi c/\lambda$), and τ is the mean scattering time of free carriers. If μ_d is the drift mobility, then $\mu_d = e\tau/m_e^*$, where e is the elementary charge and m_e^* is the effective mass of the carriers. The measurement of the conductivity in the present case was rendered difficult due to the semiconducting silicon substrate, but typical values in the literature are 3×10^4 $\Omega^{-1}\cdot$m^{-1} for polycrystalline films [32] and 3.8×10^5 $\Omega^{-1}\cdot$m^{-1} for epitaxial films [6]. We can take a typical value of 3×10^4 $\Omega^{-1}\cdot$m^{-1} for polycrystalline films [32], as in this work, but still need τ. The drift mobility in the metallic phase

is roughly 0.1 $cm^2 \cdot V^{-1} \cdot s^{-1}$ [6] and using an effective mass of $7.1m_e$, [33], we can estimate τ to be very roughly 4.0×10^{-16} s, so that with $n \approx 2.2$ in the metal phase [34], we find the expected α to be very approximately 3.5×10^7 m^{-1}. This is very close to the measured value, even though there were four parameters σ_o, μ_d, m_e*, and n used from the literature. If one used an $m_e^* = 3.5m_e$ [35] instead, for example, then α is about 14×10^7 m^{-1}, even higher. Clearly, free carrier absorption can easily account for the observed attenuation coefficient. We can also evaluate the experimental extinction coefficient K at 2000 nm from $\alpha = 2(2\pi/\lambda)K$, which gives $K \approx 4.9$.

The measured transmittance of the VO_2/Si structure in the insulating phase is obviously influenced by the substrate as well as interference of light within the film. As shown in Figure 4.4 (e), for wavelengths greater than about ~ 1150 nm, the Si substrate alone is fully transparent with $\tilde{T} \approx 52.5\%$ with a transmittance that can be shown to be determined by the transmittance through the well-known thick plate equation (with Fresnel reflections) with $n \approx 3.50$ (e.g., [36]). The transmittance of the VO_2/Si structure, on the other hand, over the same wavelength range ($\lambda > 1150$ nm) starts with approximately 30% and rises to about 50% as the wavelength increases from 1150 to 2500 nm. Experiments therefore point to an increase in the attenuation in the VO_2 insulating phase with decreasing wavelength or increasing photon energy $h\nu$. We can explain the change in the transmittance $\tilde{T}$ from around 1200 nm to 2500 nm by considering the transmittance of a thin film on a thick transparent substrate. Over the wavelength region where the extinction coefficient is much less than the refractive index, $\tilde{T}$ can be written in terms of the Swanepoel equation [37]:

$$\tilde{T} = \frac{Ax}{B - Cx\cos\phi + Dx^2} \tag{4.2}$$

Where $A = 16n^2s$, $B = (n+1)^3(n+s^2)$, $C = 2(n^2-1)(n^2-s^2)$, $D = (n-1)^3(n-s^2)$, $\phi = 4\pi nd/\lambda$, $x = \exp(-\alpha d)$ in which s is the refractive index of the substrate and α is the attenuation coefficient in the bulk of the film. We can write α as a sum of absorption and scattering contributions as

$$\alpha = \frac{A_a}{h\nu}(h\nu - E_g)^{1/m} + \frac{A_s}{\lambda^p} \tag{4.3}$$

where A_a a constant, E_g is the optical bandgap, and $m = 2$ for direct and $m = ½$ for indirect optical transition, $h\nu$ is the photon energy ($\nu = c/\lambda$), A_s is a constant, and p is an index that depends on the nature of scattering (e.g., $p = 4$ for Rayleigh scattering). Equations (4.2) and (4.3) were fitted to the data with various choices of parameters.

Figure 4.10 shows the experimental transmittance vs. wavelength behavior from 1200 nm to 2500 nm. The colored lines are $\tilde{T}$ values based on Equations (4.2) and (4.3) with $n \approx 2.8$ [38], [39] and $s = 3.5$. The expected thin film transmittance with no attenuation ($\alpha = 0$) cannot explain the data, and neither can just purely band-to-band absorption with typical bandgaps of $E_g = 0.6$ eV [40,41] and 0.7 eV [6,42] with direct and indirect transitions (not shown), which means that there must be some scattering of light in the film and/or on the surfaces to account for the observed $\tilde{T}$ vs. λ behavior. Theoretical predictions based on Equations (4.2) and (4.3) with $E_g = 0.5$ eV to 0.7 eV and $m = ½$ are shown in Figure 4.10 for the best-fit values of A_a, A_s, and p given in the figure caption. While $E_g = 0.6$ eV appears as a perfect fit, $E_g = 0.55$ eV is also very close. Direct transitions ($m = 2$) could not be fitted at all. Thus, we can conclude that the observed transmittance is in agreement with an indirect bandgap of 0.55 – 0.60 eV. The scattering index p is 2.4 but it should be remembered that any surface scattering in the present analysis based on Equations (4.2) and (4.3) would artificially inflate the scattering term and modify p. Similar good fits were found for the other samples (not shown) with values that are close to those of the best fit.

Table 4.2 summarizes the best-fit parameters for p and A_s for all the films with $E_g = 0.60$ eV and A_a kept the same for all samples; the same absorption coefficient. $A_s d$ represents the total effective scattering in the film. No unambiguous correlation could be established with grain size inasmuch as fitting a multivariable function as in the present case will invariably have uncertainties. Nonetheless, we can conclude that the insulating phase possesses an indirect bandgap of 0.60 eV ± 0.05 eV, and the films exhibit significant scattering of light.

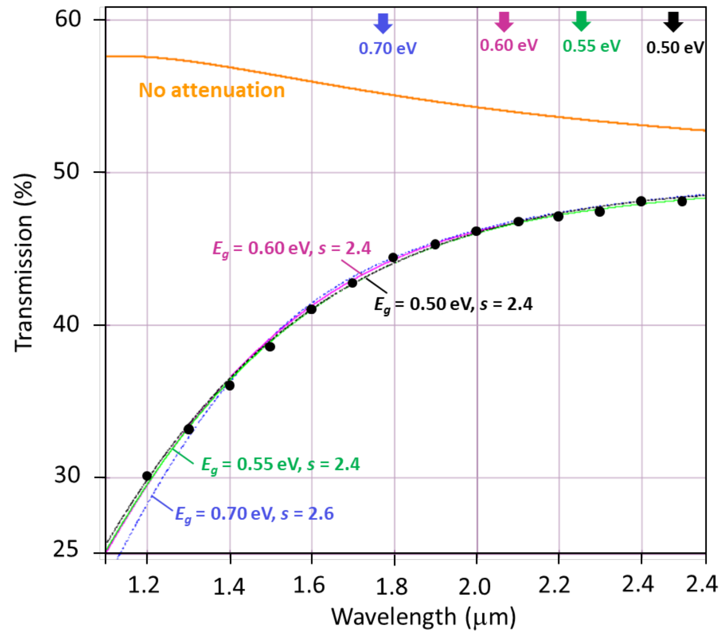

Figure 4.10 The transmittance vs. wavelength for the 102 nm VO_2 thin film with various contributions. The orange curve is the Swanepoel transmittance with no attenuation. Other colored curves are selected fits to the data as follows: blue: $E_g = 0.70$ eV, $A_a = 0.0070$ nm$^{-1}\cdot$eV^{-1}, $p = 2.6$, $A_s = 5.9 \times 10^5$ nm$^{1.6}$**;** magenta: $E_g = 0.60$ eV, $A_a = 0.0048$ nm$^{-1}\cdot$eV^{-1}, $p = 2.4$, $A_s = 1.3 \times 10^5$ nm$^{1.4}$; green: $E_g = 0.55$ eV, $A_a = 0.0038$ nm$^{-1}\cdot$eV^{-1}, $p = 2.4$, $A_s = 1.30 \times 10^5$ nm$^{1.4}$; black: $E_g = 0.50$ eV, $A_a = 0.0035$ nm$^{-1}\cdot$eV^{-1}, $p = 2.4$, $A_s = 1.25 \times 10^5$ nm$^{1.4}$.

Table 4.2 The scattering contribution to attenuation in VO_2 films on Si, given $E_g = 0.60$ eV and $A_a = 0.0048$ nm^{-1}·eV^{-1}.

Sample #	Thickness (nm)	Average grain size (nm)	p	A_s (nm^{s-1})	$A_s d$ at 2000 nm
A	102 ± 1	58.8 ± 0.6	2.4	1.30×10^5	0.16
B	93 ± 2	67.2 ± 1.0	1.6	4.05×10^2	0.20
C	68 ± 1	88.6 ± 1.2	2.0	6.70×10^3	0.11
D	60 ± 2	75.1 ± 0.5	2.2	3.65×10^4	0.12

Finally, we can check the validity of the above arguments by noting that the strongest attenuation occurs at 1200 nm, where, using the best-fit values, the highest extinction coefficient (K) is 0.57. This is still smaller than $n = 2.8$ by a factor of 5, which provides support for the use of Equation (4.2) [37].

4.6 Conclusions

This work clearly shows that applying substrate biasing can modify the microstructure and optical properties of VO_2 thin films deposited by magnetron sputtering. By applying substrate biasing, the deposition rate of the as-deposited VO_2 thin films decreases while the grain size increases. The films prepared under a higher bias voltage are thinner and hence show higher transmission in the metallic phase. The defects induced by the substrate biasing degrade the optical properties of VO_2 in the sense that the hysteresis temperature width ΔH of the transition temperature observed during heating and cooling becomes poor. Applying substrate biasing also alters the characteristics of the phase transition. The transition temperature of VO_2 thin films deposited under bias increases 14 K accompanied by a widened hysteresis curve.

An advantage of the increased transition temperature of VO_2 thin films is the enhancement of thermal stability of VO_2 thin films for various electronic and optoelectronic device applications utilizing optical switches, transistors, sensors, and actuators, in which the working temperatures are possibly higher than 341 K due to the accumulated heat during service.

4.7 References

[1] F. J. Morin, "Oxides Which Show a Metal-to-Insulator Transition at the Neel Temperature," *Physical Review Letters*, vol. 3, pp. 34-36, 1959.

[2] S. Chen, H. Ma, X. Yi, H. Wang, X. Tao, M. Chen, X. Li and C. Ke, "Optical switch based on vanadium dioxide," *Infrared Physics and Technology*, vol. 45, pp. 239–242, 2004.

[3] C. Cheng, H. Guo, A. Amini, K. Liu, D. Fu, J. Zou and H. Song, "Self-assembly and horizontal orientation growth of VO2 nanowires," *Scientific Reports*, vol. 4, no. 1, pp. 1-5, 2014.

[4] L. Pellegrino, N. Manca, T. Kanki, H. Tanaka, M. Biasotti, E. Bellingeri, A. Siri and D. Marré, "Multistate memory devices based on free-standing VO2/TiO2 microstructures driven by Joule self-heating," *Advanced Materials*, vol. 24, pp. 2929–2934, 2012.

[5] O. Srirodpai, J. Wootthikanokkhan, S. Nawalertpanya, K. Yuwawech and V. Meeyoo, "Preparation, Characterization and Thermo-Chromic Properties of EVA/VO2 Laminate Films for Smart Window Applications and Energy Effciency in Building," *Materials*, vol. 10, p. 53, 2017.

[6] D. Fu, K. Liu, T. Tao, K. Lo, C. Cheng, B. Liu, R. Zhang, H. Bechtel and J. Wu, "Comprehensive study of the metal-insulator transition in pulsed laser deposited epitaxial VO2 thin films," *Journal of Applied Physics*, vol. 113, p. 043707, 2013.

[7] I. Kim and L. Lauhon, "Increased yield and uniformity of vanadium dioxide nanobeam growth via two-step physical vapor transport process," *Crystal Growth & Design*, vol. 12, pp. 1383–1387, 2012.

[8] L. Fan, S. Chen, Z. Luo, Q. Liu, Y. Wu, L. Song, D. Ji, P. Wang, W. Chu, C. Gao, C. W. Zou and Z. Y. Wu, "Strain dynamics of ultrathin VO2 film grown on TiO2(001) and the associated phase transition modulation," *Nano Letters*, vol. 14, pp. 4036–4043, 2004.

[9] M. Miller and J. Wang, "Influence of grain size on transition temperature of thermochromic VO2," *Journal of Applied Physics*, vol. 117, p. 034307, 2015.

[10] Z. Luo, Z. Wu, T. Wang, X. Xu, W. Li, W. Li and Y. Jiang, "Comparison of the optical responses of O-poor and O-rich thermochromic VOX films during semiconductor-to-metal transition," *Journal of Physics and Chemistry of Solids*, vol. 73, pp. 1122–1126, 2012.

[11] C. Drosos and D. Vernardou, "Advancements, Challenges and Prospects of Chemical Vapour Pressure at Atmospheric Pressure on Vanadium Dioxide Structures," *Materials*, vol. 11, p. 384, 2018.

[12] E. Chen, "The influence of deposition temperature on the structure and optical properties of vanadium oxide films," *Journal of Vacuum Science & Technology A: Vacuum, Surfaces, and Films*, vol. A4, pp. 432–435, 1986.

[13] Y. Yang, Y. Yao, B. Zhang, H. Lin, Z. Luo, C. Gao, C. Zhang and C. Kang, "Investigating Metal–Insulator Transition and Structural Phase Transformation in the (010)-VO2/(001)-YSZ Epitaxial Thin Films," *Materials*, vol. 11, p. 1713, 2018.

[14] Y. Zhou and S. Ramanathan, "Heteroepitaxial VO2 thin films on GaN: Structure and metal-insulator transition characteristics," *Journal of Applied Physics*, vol. 112, p. 74114, 2012.

[15] D. Zhang, H.-J. Sun, M.-H. Wang, L.-H. Miao, H.-Z. Liu, Y.-Z. Zhang and J.-M. Bian, "VO2 Thermochromic Films on Quartz Glass Substrate Grown by RF-Plasma-Assisted Oxide Molecular Beam Epitaxy," *Materials*, vol. 10, p. 314, 2017.

[16] G. Fu, A. Polity, N. Volbers and B. Meyer, "Annealing effect on VO2 thin films deposited by reactive sputtering," *Thin Solid Films*, vol. 515, pp. 2519–2522, 2006.

[17] M.-D. Zhu, C. Shan, C. Li, H. Wang, H.-J. Qi, D.-P. Zhang and W. Lv, "Thermochromic and Femtosecond-Laser-Induced Damage Performance of Tungsten-Doped Vanadium Dioxide Films Prepared Using an Alloy Target," *Materials*, vol. 11, p. 1724, 2018.

[18] L. Mai, B. Hu, T. Hu, W. Chen, E. Gu and L. Mai, "Electrical property of Mo-doped VO2 nanowire array film by melting− quenching sol− gel method," *The Journal of Physical Chemistry B*, vol. 110, pp. 19083–19086, 2006.

[19] W. Burkhardt, T. Christmann, S. Franke, W. Kriegseis, D. Meister, B. Meyer, W. Niessner, D. Schalch and A. Scharmann, "Tungsten and fluorine co-doping of VO2 films," *Thin Solid Films*, vol. 402, pp. 226–231, 2002.

[20] F. Béteille and J. Livage, "Optical Switching in VO2 Thin Films," *Journal of Sol-Gel Science and Technology*, vol. 13, pp. 915–921, 1998.

[21] J. Du, Y. Gao, H. Luo, L. Kang, Z. Zhang, Z. Chen and C. Cao, "Significant changes in phase-transition hysteresis for Ti-doped VO2 films prepared by polymer-assisted deposition," *Solar Energy Materials and Solar Cells*, vol. 95, pp. 469–475, 2011.

[22] M. Liu, M. Wagner, E. Abreu, S. Kittiwatanakul, A. McLeod, Z. Fei, M. Goldflam, S. Dai, M. Fogler, J. Lu, S. A. Wolf, R. D. Averitt and D. N. Basov, "Anisotropic Electronic

State via Spontaneous Phase Separation in Strained Vanadium Dioxide Films," *Physical Review Letters*, vol. 111, p. 096602, 2013.

[23] C. Zhang, C. Koughia, Y. Li, X. Cui, F. Ye, S. Shiri, M. Sanayei, S. Wen, Q. Yang and S. Kasap, "Near-zero IR transmission of VO2 thin films deposited on Si substrate," *Applied Surface Science*, vol. 440, pp. 415-420, 2018.

[24] L. Bobyak, P. Fallon and A. Razavi, "The effects of biasing and annealing on the optical properties of radio-frequency sputtered VO2," *Journal of Vacuum Science & Technology A: Vacuum, Surfaces, and Films*, vol. 8, pp. 1391–1394, 1990.

[25] N. Azhan, K. Okimura, Y. Ohtsubo, S.-I. Kimura, M. Zaghrioui and J. Sakai, "Large modification in insulator-metal transition of VO2 films grown on Al2O3 (001) by high energy ion irradiation in biased reactive sputtering," *Journal of Applied Physics*, vol. 119, p. 055308, 2016.

[26] C. Zhang, Q. Yang, C. Koughia, F. Ye, M. Sanayei, S. Wen and S. Kasap, "Characterization of vanadium oxide thin films with different stoichiometry using Raman spectroscopy," *Thin Solid Films*, vol. 620, pp. 64-69, 2016.

[27] B. Li, D. Yu and S.-L. Zhang, "Raman spectral study of silicon nanowires," *Physical Review B*, vol. 59, pp. 1645–1648, 1999.

[28] J. De Natale, P. Hood and A. Harker, "Formation and characterization of grain-oriented VO2 thin films.," *Journal of Applied Physics*, vol. 66, pp. 5844–5850, 1989.

[29] C. Mihailescu, E. Symeou, E. Svoukis, R. Negrea, C. Ghica, V. Teodorescu, L. Tanase, C. Negrila and J. Giapintzakis, "Ambiguous Role of Growth-Induced Defects on the Semiconductor-to-Metal Characteristics in Epitaxial VO2/TiO2 Thin Films," *ACS Applied Materials & Interfaces*, vol. 10, pp. 14132–14144, 2018.

[30] S. Bull, A. Jones and A. MacCabe, "Residual stress in ion-assisted coatings," *Surface and Coatings Technology*, vol. 54/55, p. 173–179, 1992.

[31] S. Kasap, *Principles of Electronic Materials and Devices*, 4th ed., New York, NY: McGraw-Hill, 2018, p. 896.

[32] E. Chain, "Optical properties of vanadium dioxide and vanadium pentoxide thin films," *Applied Optics*, vol. 30, p. 2782, 1991.

[33] W. Rosevear and W. Paul, "Hall effect in VO2 near the Semiconductor-To-Metal transition," *Physical Review B*, vol. 7, p. 2109, 1973.

[34] R. Kivaisi and M. Samiji, "Optical and electrical properties of vanadium dioxide films prepared under optimized RF sputtering conditions," *Solar Energy Materials and Solar Cells*, vol. 57, pp. 141–152, 1999.

[35] D. Hensler, "Transport Properties of Sputtered Vanadium Dioxide Thin Films," *Journal of Applied Physics*, vol. 39, p. 2354, 1968.

[36] S. O. Kasap, *Optoelectronics and Photonics: Principles and Practices*, 2nd ed., Upper Saddle River, NJ: Pearson, 2013, p. 73.

[37] R. Swanepoel, "Determination of the thickness and optical constants of amorphous silicon," *Measurement Science and Technology*, vol. 16, pp. 1214–1222, 1983.

[38] C. Wan, Z. Zhang, D. Woolf, C. Hessel, J. Rensber, J. Hensley, Y. Xiao, A. Shahsafi, J. Salman, S. Richter, Y. Sun, M. Qazilbash, R. Schmidt-Grund, C. Ronning, S. Ramanathan and M. Kats, "Optical properties of thin-film vanadium oxide from the visible," *Annalen der Physik*, vol. 531, no. 10, p. 1900188, 2019.

[39] J. T. Swann and D. J. De Smet, "Ellipsometric investigation of vanadium dioxide films.," *Journal of Applied Physics*, vol. 58, pp. 335–1338, 1985.

[40] J. C. Parker, U. W. Geiser, D. J. lam, Y. Xu and W. Y. Ching, "Optical properties of the vanadium oxides VO2 and V2O5," *Journal of the American Ceramic Society*, vol. 73, pp. 3206–3208, 1990.

[41] T. Lin, J. Wang, G. Liu, L. Wang, X. Wang and Y. Zhang, "Influence of Discharge Current on Phase Transition Properties of High-quality Polycrystalline VO2 Thin Film Fabricated by HiPIMS," *Materials*, vol. 10, p. 633, 2017.

[42] S. Shin, S. Suga, M. Taniguchi, M. Fujisawa, H. Kanzaki, A. Fujimori, H. Daimon, Y. Ueda, K. Kosuge and S. Kachi, "Vacuum-ultraviolet reflectance and photoemission study of the metal-insulator phase transitions in VO2, V6O13, and V2O3.," *Physical Review B*, vol. 41, pp. 4993–5009, 1990.

5. Effect of Substrate Temperature on the Structural, Optical and Electrical Properties of DC Magnetron Sputtered VO_2 Thin Films[3]

5.1 Abstract

This study focuses on the effect of the substrate temperature (T_S) on the quality of VO_2 thin films prepared by DC magnetron sputtering. T_S was varied from 350 to 600 °C and the effects on the surface morphology, microstructure, optical and electrical properties of the films were investigated. Results show that T_S below 500 °C favors the growth of V_2O_5 phase, whereas higher T_S (≥ 500 °C) facilitates the formation of the VO_2 phase. Optical characterization of the as-prepared VO_2 films displayed a reduced optical transmittance ($\tilde{T}$) across the near-infrared region (NIR), reduced phase transition temperature (T_t), and broadened hysteresis width (ΔH) through the phase transition region. Also, a decline of the luminous modulation ($\Delta\tilde{T}_{\text{lum}}$) and solar modulation ($\Delta\tilde{T}_{\text{sol}}$) efficiencies of the as-prepared films have been determined. Furthermore, compared with the high-quality films reported previously, the electrical conductivity (σ) as a function of temperature (T) reveals reduced conductivity contrast ($\Delta\sigma$) between the insulating and metallic phases of the VO_2 films, which was of the order of 2. These outcomes indicated the presence of defects and unrelaxed lattice strain in the films. Further, the comparison of present results with those in the literature from similar works show that the preparation of high-quality films at T_S lower than 650 °C presents significant challenges.

5.2 Introduction

Vanadium dioxide (VO_2) has been widely studied for applications such as optical switches, sensors, smart windows, and optical memory devices [1–4]. Currently, potential applications can also be found in neuromorphic computing materials and metamaterials [5–8]. The primary reason

---

[3] This paper was published as: Chunzi Zhang, Ozan Gunes, Shi-JieWen, Qiaoqin Yang and Safa Kasap, “Effect of Substrate Temperature on the Structural, Optical and Electrical Properties of DC Magnetron Sputtered VO2 Thin Films,” *Materials*, vol. 15, no. 21, p. 7849, 2022. doi.org/10.3390/ma15217849.

for its importance in electronics, photonics and optical switching applications is the fast metal-to-insulator phase transition (MIT) between the semiconductor and metallic phases. During the MIT, the VO_2 crystal undergoes an abrupt phase transformation from high-temperature tetragonal phase to a low-temperature monoclinic phase at around 68 °C [9]. Up to now, a variety of deposition methods (e.g., magnetron sputtering, pulsed laser deposition, chemical vapor deposition, electron beam evaporation etc.) have been employed to prepare VO_2 thin films [10–15]. Regardless of the method, high growth temperatures (450–800 °C) are employed to assure its stoichiometry [16–19], which is crucial in the synthesis of VO_2 thin films that display a sharp phase transition. However, instrumentation that delivers high substrate temperatures (T_S) is costly and not industry-friendly [20]. For this reason, there have been numerous efforts to bring the T_S down to more practical temperatures [21–27]. A few studies have already reported the fabrication of the VO_2 thin films at low T_S (down to around 300 °C) by applying a buffer layer such as ZnO, AZO, TiO_2, SnO_2 or VO [21-23]. Other pronounced efforts typically include substrate biasing, applying high power pulse, and post-annealing [24–27]. In order to reduce the T_S, a clear understanding of the effect of the synthesis (substrate) temperature on the stoichiometry, structure and phase transition properties is critical. Some previous works have already revealed the effects of T_S on the microstructure, stress state, and transition temperatures of VO_2 thin films [16,28–31]. Nevertheless, these works are not comprehensive and do not necessarily signify a clear relation of the underlying mechanism related to physical changes due to the T_S.

In our earlier works [17,32], we have reported the preparation of stoichiometric, near-epitaxial VO_2 thin films at T_S of 650 °C by DC reactive magnetron sputtering, where the films showed highly discernable optical and electrical phase transition properties (i.e. high optical transmittance ($\Delta\tilde{T}$) and electrical conductivity ($\Delta\sigma$) contrasts, sharp transitions and near-zero optical transmission in the metallic phase). We have also investigated the effect of substrate biasing on the quality of VO_2 thin films [33]. In the present work, we have undertaken the deposition of VO_2 films at T_S varying from 350 to 600 °C and examined the effects on the microstructure, surface morphology, roughness, optical and electrical phase transition properties. We compared these results with the films deposited at 650 °C in our previous works [17,32]. Also, we extracted and analyzed the $\Delta\tilde{T}$ along with the luminous ($\Delta\tilde{T}_{lum}$) and solar ($\Delta\tilde{T}_{sol}$) optical modulation efficiencies. Furthermore, we estimated the electrical bandgap of the films and compared the results with those

of high-quality VO_2 thin films prepared at 650 °C reported previously [32]. Additionally, we compared our results with other works that studied the effect of T_S on the properties of VO_2 thin films.

5.3 Materials and Methods

Single-crystal p-Si (100) and r-cut sapphire were used as substrates for the thin film preparation. Prior to the deposition, the substrates were ultrasonically cleaned in ethanol and dried in air. After the cleaning process, the substrates were placed in a sputtering chamber. DC reactive magnetron sputtering was utilized to prepare VO_2 thin films. For this purpose, a high-purity vanadium target (99.95%, Plasmionique, Inc.) was used. During every deposition, stable argon (Ar) and oxygen (O_2) flow with constant rates of 100 and 1.3 SCCM were maintained, respectively. The selected Ar and O_2 flow rates facilitate the growth of pure VO_2 films using the above-mentioned deposition process which has been also reported in Ref. [17]. All depositions were performed under a constant pressure of 1.3 Pa for a duration of 2 hours. The thin films were prepared at six different T_S values. The deposition conditions for each T_S are summarized in Table 5.1.

Table 5.1 Deposition conditions of the as-prepared thin films on Si and sapphire substrates.

Substrate temperature (T_S) (°C)	**Oxygen flow rate (SCCM)**	**Sputtering power (W)**	**Pressure (Pa)**	**Duration (Hour)**	**Phase**
350	1.3	100	1.33	2	V_2O_5
400	1.3	100	1.33	2	V_2O_5
450	1.3	100	1.33	2	V_2O_5
500	1.3	100	1.33	2	VO_2
550	1.3	100	1.33	2	VO_2
600	1.3	100	1.33	2	VO_2
650 [17]	1.3	100	1.33	2	VO_2

After deposition, the structural properties of the as-prepared thin films were examined at room temperature using Raman spectroscopy (Renishaw Invia Reflex Raman Microscope), scanning electron microscopy (Hitachi HT-7700 SEM), and X-ray diffractometry (Rigaku Ultima IV XRD). The average crystalline grain size was estimated using ImageJ (a software program developed by NIH, USA [34]) on SEM images. Surface profilometry was used to examine the surface roughness of the films using a profilometer (Zygo OMP-0592). The optical transmission spectrum was measured using a Lambda 900 UV-Vis-NIR Perkin-Elmer spectrophotometer in the wavelength (λ) range of 300 – 2500 nm. During the optical measurements, VO_2-film/substrate sample was mounted on a purpose-built sample heating platform connected to a DC power supply (similar to the one in Ref. [32]). An Omega ® CN-16Pt-330 PID temperature controller was used to control the sample holder temperature and monitor the sample temperature during the heating and cooling processes. The temperature (T) dependence of the optical transmittance ($\tilde{T}$) measurements were conducted at a heating rate of ~ 0.5 °C/min. The T-dependence of the conductivity (σ) of the as-prepared films on sapphire substrates were carried out by depositing gold (Au) contacts at room temperature with the size of (1 mm × 2 mm) using a radio frequency (RF) sputtering system. These measurements were carried out in a cryostat where the samples were placed on a copper (Cu) block which was connected to a DC power supply. The supply was used to heat the block. The temperature of the samples was measured by the use of a thermocouple which was mounted in close proximity to the sample. During these measurements, the heating of the sample was specifically kept at a low rate (~ 0.5 °C/min) to prevent a lag between the temperature reading and the actual temperature of the sample.

5.4 Results

5.4.1 Microstructural Characterization by Raman Spectroscopy and XRD

The microstructural characterization of the vanadium oxide thin films prepared at different T_S was carried out using Raman spectroscopy and x-ray diffraction (XRD) for which the results can be found in Figure 5.1 and Figure 5.2, respectively. These figures show that the pure monoclinic VO_2 phase is achieved only for samples deposited at T_S = 500 °C and higher temperatures. In Figure 5.1, the Raman peaks at 144, 193, 223, 260, 308, 334, 389, 497 and 613

cm^{-1} represent the pure monoclinic phase of VO_2 [15]. In Figure 5.2, the diffraction peaks at 2θ = 28°, 56°, and 58° correspond to the (011), (220), and (022) of pure monoclinic phase of VO_2 [35]. For T_S = 450 °C, the Raman peaks of pure VO_2 are not observed in Figure 5.1 and a small diffraction peak at 2θ = 20° appears in Figure 5.2, which corresponds to the (001) peak of V_2O_5. As the T_S is further decreased down to 350 °C, the (001) peak of V_2O_5 dominates the XRD spectrum as can be seen in Figure 5.2 (a) and (b). The Raman peaks at 145, 195, 284, 303, 405, 483, 528, 701, and 996 cm^{-1} in Figure 5.1 (a) and (b), signify the presence of V_2O_5 phase to be the dominant in the thin film [15] below a T_S of 450 °C. It can be seen that both Raman and XRD peaks of V_2O_5 become the strongest when the T_S reaches 350 °C. It is worth mentioning that the sharp Raman peak around 520 cm^{-1} for the film deposited T_S = 350 °C on a Si substrate arises from the Si substrate itself and is absent in films deposited on sapphire substrates.

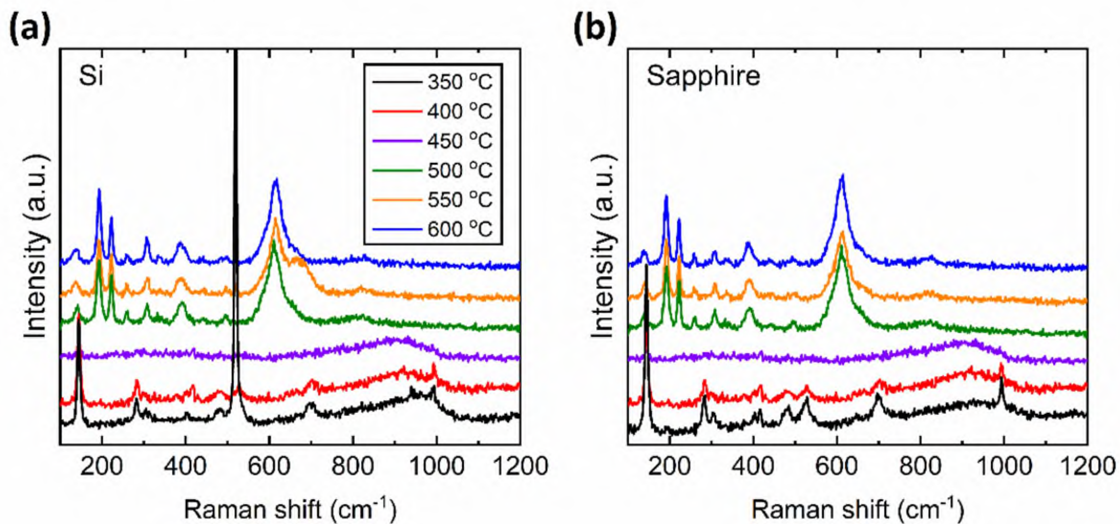

Figure 5.1 Raman spectra of VO_2 and V_2O_5 thin films prepared at various substrate temperatures (T_S) on (a) Si and (b) sapphire substrates. Note that the vertical axes are in arbitrary units (a.u.), so the relative magnitudes of the spectra cannot be compared.

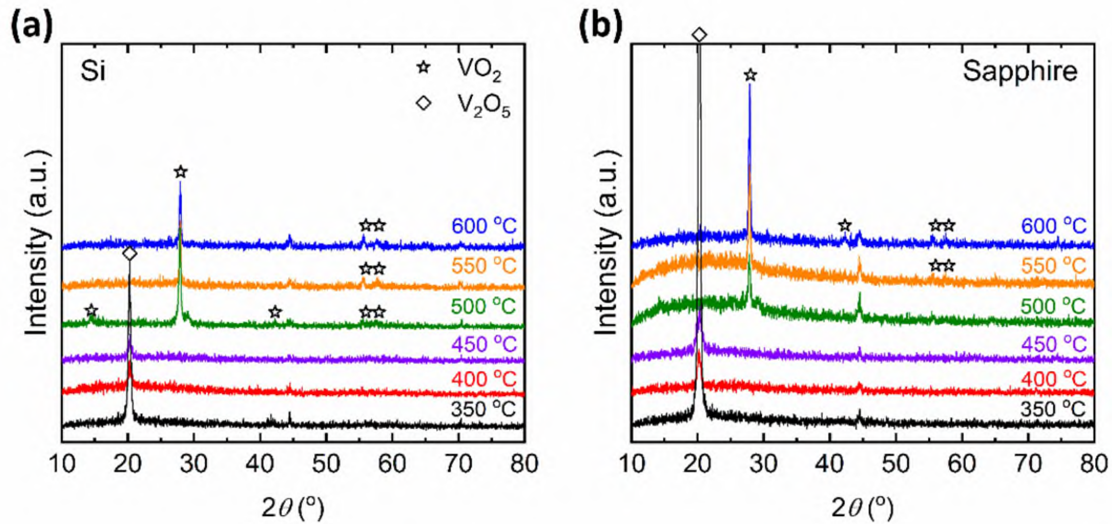

Figure 5.2 XRD spectra of VO_2 and V_2O_5 thin films prepared at various substrate temperatures (T_S) on (a) Si and (b) sapphire substrates. Note that the vertical axes are in arbitrary units (a.u.).

5.4.2 Surface Morphology and Roughness Characterization by SEM and Profilometry

Figure 5.3 presents the SEM surface images of the as-prepared VO_2 thin films. It can be observed that the T_S affects the surface morphology of the thin films. As observed from (a) to (b) to (c) the films show a misoriented crystalline structure with grain sizes ranging between around 100 and 150 nm. The substrate temperatures of 450 and 400 °C produce V_2O_5 nanostructured films with smooth surfaces. When the T_S is lowered to 350 °C the V_2O_5 grains become clearly discernable in the films. Surface profilometry shows that T_S also affects the surface roughness of VO_2 films. Figure 5.4 shows the surface profile images of the VO_2 films deposited at various T_S-values. These images are taken at a surface area of approximately 0.6×0.6 mm^2 of each film. Roughness measurements show that the root-mean-square (R_q) roughness of films on both Si and sapphire substrates increases as T_S is lowered. The maximum R_q measured was obtained for VO_2 films deposited at 500 °C, with 10 nm for films on Si and 8 nm for films on sapphire substrates. The minimum R_q is measured for films deposited at 600 °C as 4 nm on Si and 3 nm on sapphire substrates. Yet, these films show increased roughness compared to the films prepared at 650 °C (Ref. [17]). The R_q is measured as 3 nm on Si and 2 nm on sapphire substrates for films prepared at 650 °C. These in fact, manifest properties associated with high-quality VO_2 films as investigated

previously [36]. Nevertheless, the average roughness (R_a) does not exhibit a strong variation with respect to T_S, in contrast to the clear trend exhibited by R_q.

Table 5.2 and Figure 5.5 present the average grain size (GS_{avg}), R_a and R_q of the VO_2 thin films prepared on Si and sapphire substrates. The grain size in the films on sapphire substrates decreases from 153 nm to 108 nm as T_S is lowered from 600 to 500 °C. Indeed, near-epitaxial growth on sapphire films has been reported in the literature [37]. On the other hand, the grain size of the films prepared on Si substrates, within experimental uncertainties, does not exhibit any compelling dependence on T_S, even though there is seemingly a maximum average grain size at T_S = 600 °C. Films on Si substrates prepared at 600 °C show grains with largely varying size (large standard deviation) and orientation. Even though the grain size is reduced for films prepared at 550 and 500 °C the misorientation of grains is still evident. The thickness of the VO_2 films prepared at T_S = 600, 550 and 500 °C are measured by using cross-section SEM images as 210 ± 8, 230 ± 14, and 289 ± 15 nm, respectively.

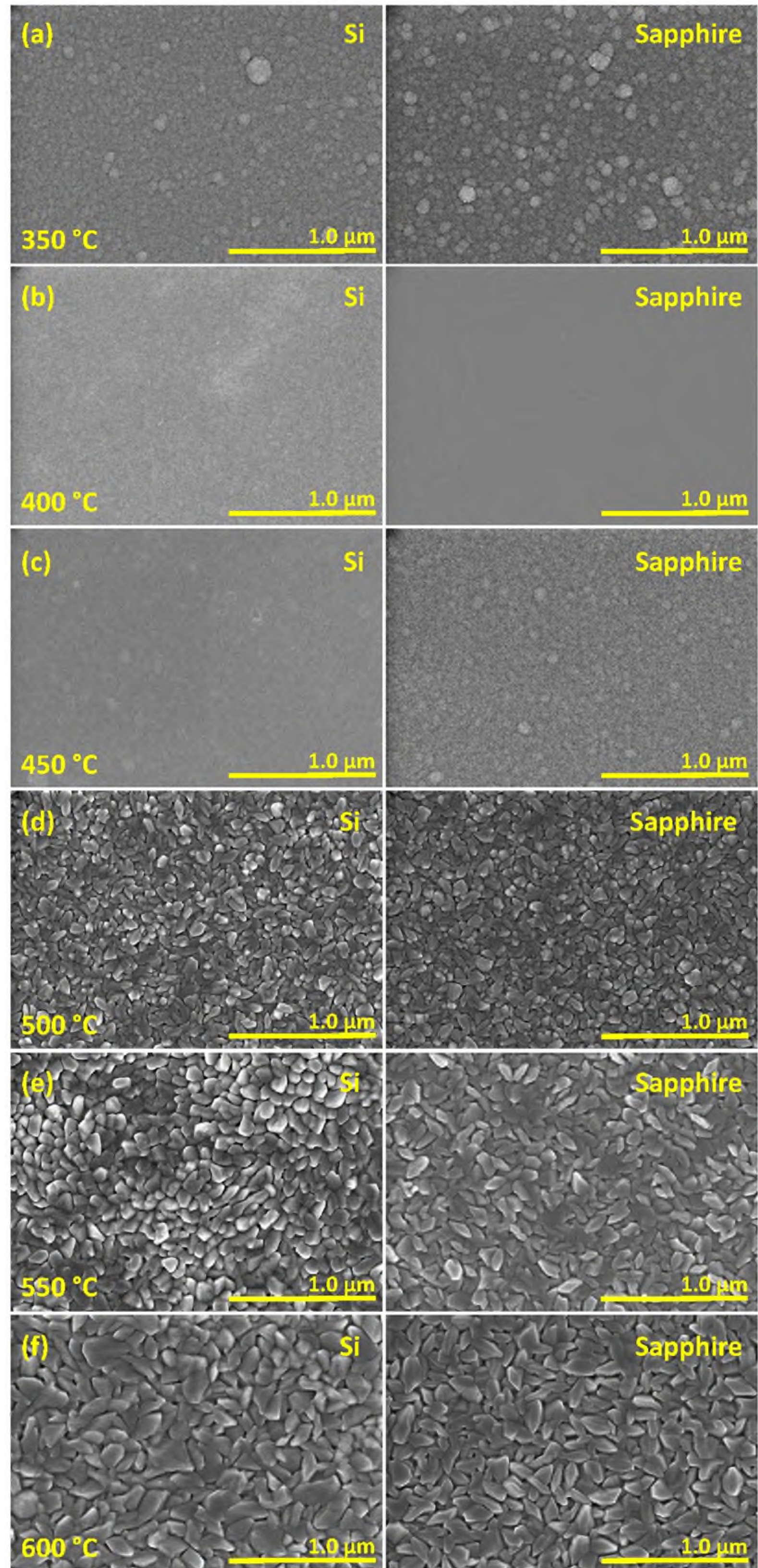
(a)
Si
Sapphire
350 °C
1.0 µm
1.0 µm
(b)
Si
Sapphire
400 °C
1.0 µm
1.0 µm
(c)
Si
Sapphire
450 °C
1.0 µm
1.0 µm
(d)
Si
Sapphire
500 °C
1.0 µm
1.0 µm
(e)
Si
Sapphire
550 °C
1.0 µm
1.0 µm
(f)
Si
Sapphire
600 °C
1.0 µm
1.0 µm

Figure 5.3 Surface images of VO_2 and V_2O_5 thin films prepared at various substrate temperatures (T_S) (a) 350 °C, (b) 400 °C, (c) 450 °C, (d) 500 °C, (e) 550 °C, and (f) 600 °C obtained by SEM.

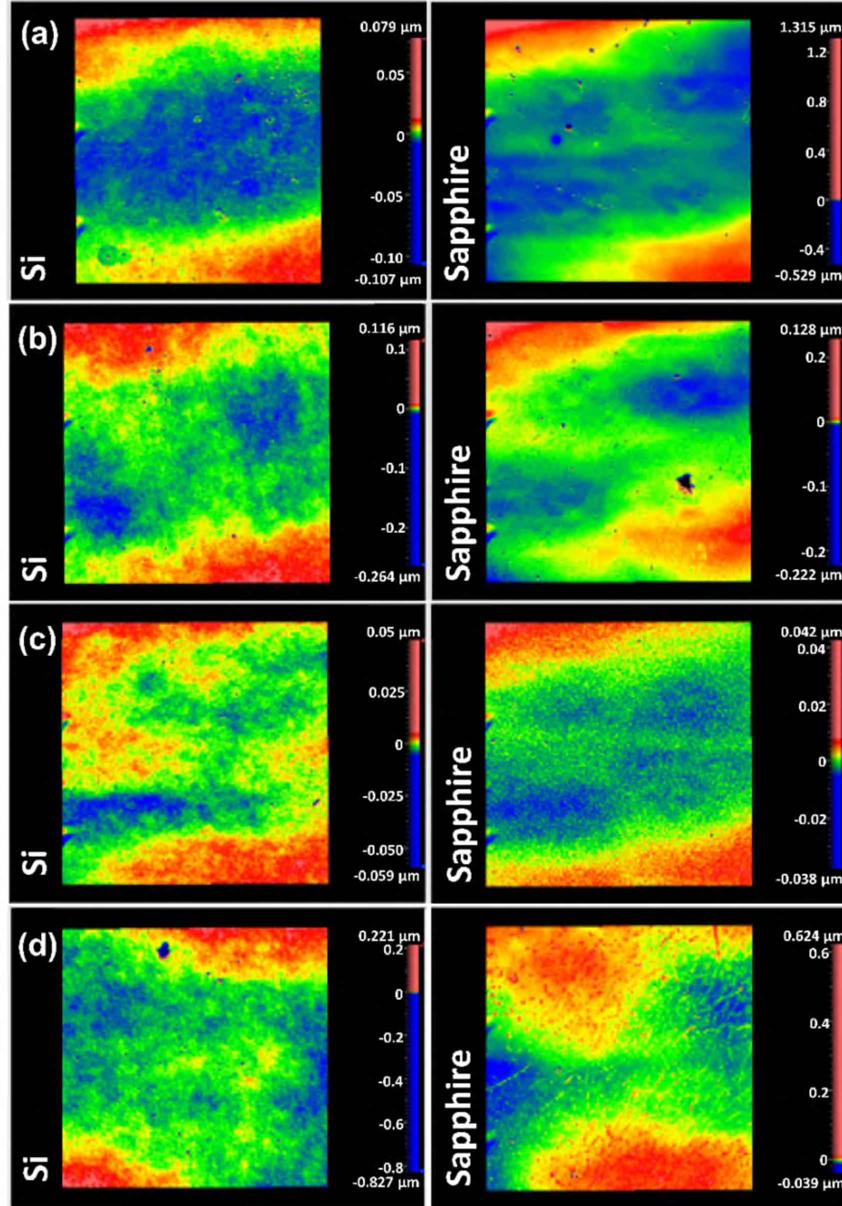

Figure 5.4 Surface profile images of VO_2 thin films deposited on Si and sapphire substrates at (a) 500 °C, (b) 550 °C, (c) 600 °C and (d) 650 °C [17]. The roughness of the surface is indicated by color mapping, where the maximum (peak), median and minimum (depth) points on the surface are indicated in red, green and blue, respectively. The scale bars are used as a measure of the peaks and depths on the surface of the films.

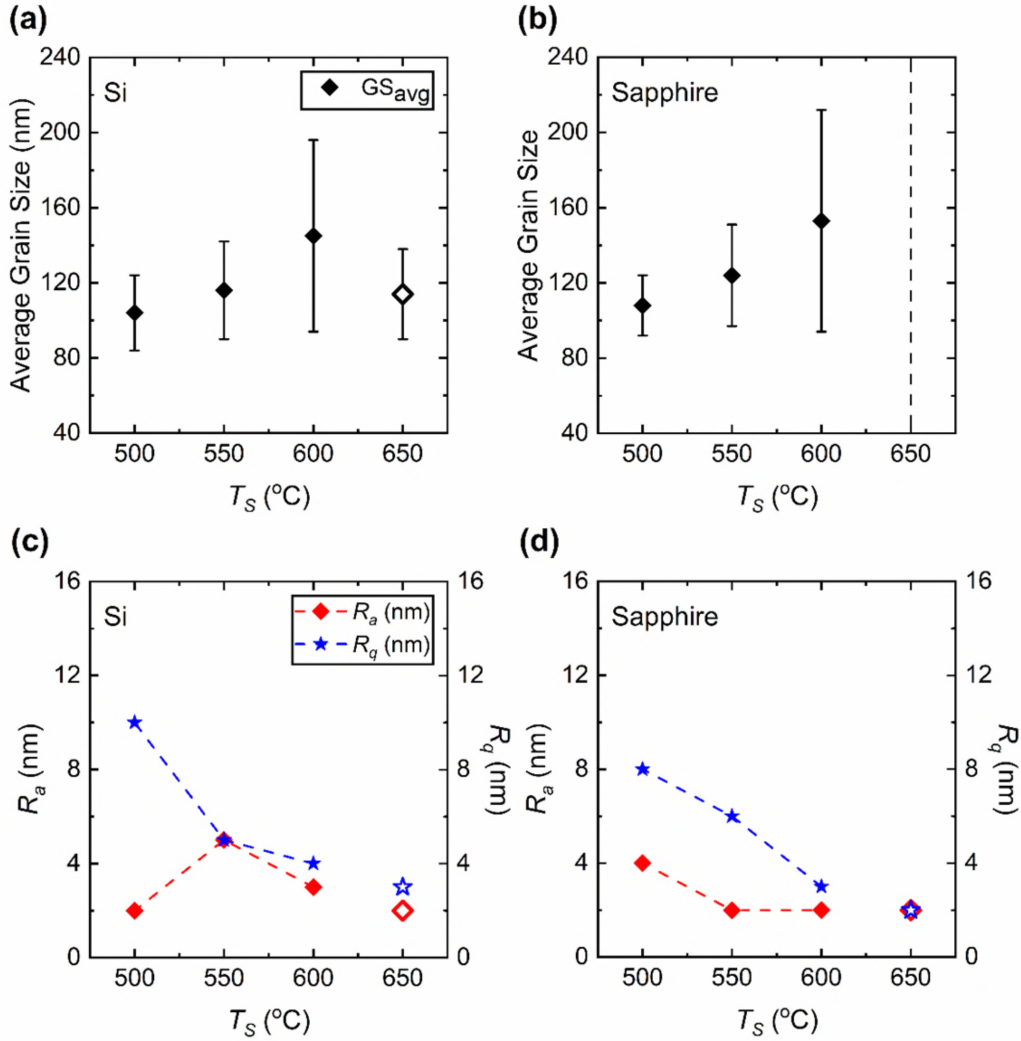

Figure 5.5 Average grain size (GS_{avg}) of VO_2 thin films prepared on (a) Si and (b) sapphire substrates. In (b) the dashed vertical line is an asymptote that indicates the near-epitaxial almost flat surface of the film prepared at 650 °C [17]. (c,d) present the average (R_a) and root-mean-square (R_q) roughness of films prepared on Si and sapphire substrates, respectively. The dashed lines between the data points are guides to the eye. The data points shown in hollow symbols belong to the films pre-pared at 650 °C (prepared as described in Ref. [17] but not reported therein).

Table 5.2 Average grain size (GS_{avg}), average (R_a) and root-mean square (R_q) roughness of VO_2 thin films prepared at various substrate temperatures (T_S).

Substrate temperature (T_S) (°C)	**GS_{avg} (nm)**	**R_a (nm)**	**R_q (nm)**	**GS_{avg} (nm)**	**R_a (nm)**	**R_q (nm)**
	Si			Sapphire		
500	104 ± 20	2	10	108 ± 16	4	8
550	116 ± 26	5	5	124 ± 27	2	6
600	145 ± 51	3	4	153 ± 59	2	3
650 [17]	114 ± 24	2	3	~Flat	2	2

5.4.3 Optical Characterization by Spectrophotometry

To understand the effect of T_S on the structural VO_2 phase transition properties, the optical transmission ($\tilde{T}$) spectrum of VO_2 thin films was measured at 300 K (27 °C) (in the insulating phase) and at 368 K (95 °C) (in the metallic phase) in a wavelength range between 300 and 2500 nm. Figure 5.6 presents the $\tilde{T}$ spectra of these VO_2 thin films. In practical terms, no notable difference can be found in the trend of the $\tilde{T}$ spectra for samples prepared at T_S = 600 and 550 °C. In Figure 5.6 (a), for the film prepared at T_S = 500 °C, $\tilde{T}_{2500nm}$ is observed to be lowest among other examined films, which is around 34% in the insulating phase. In Figure 5.6 (b) and (c) the $\tilde{T}$ of films deposited at T_S = 550 and 600 °C on sapphire are observed to be very close. The drop of the $\tilde{T}$ for films prepared at 500 °C can be related to the increased defects and the inferior crystal quality of VO_2 thin films, which can be clearly observed in Figure 5.3 (d). At 368 K, all the VO_2 films on both Si and sapphire substrates transition into a near-zero transmittance in the metallic phase. Table 5.3 presents the details of $\tilde{T}$ values at 300 K and 368 K along with the optical transmittance contrast ($\Delta\tilde{T}$) of the as-prepared VO_2 films obtained at NIR wavelengths of 1500, 2000 and 2500 nm. $\Delta\tilde{T}$ is defined as the difference in the optical transmittance of the insulating and metallic phases.

(a)

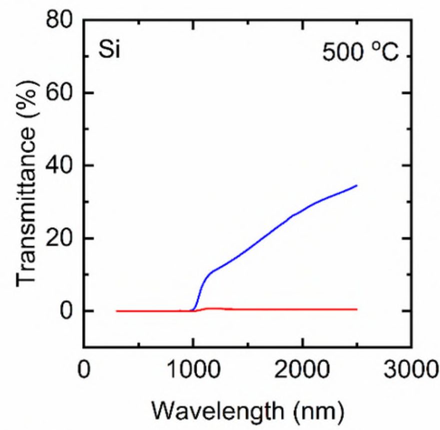

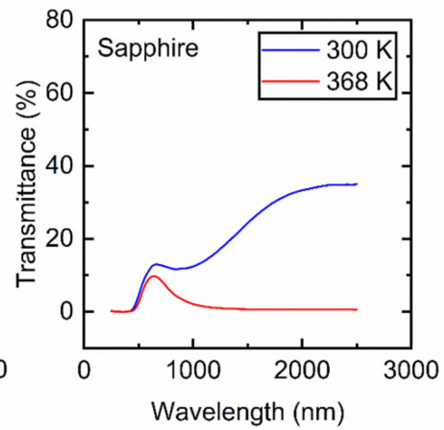

(b)

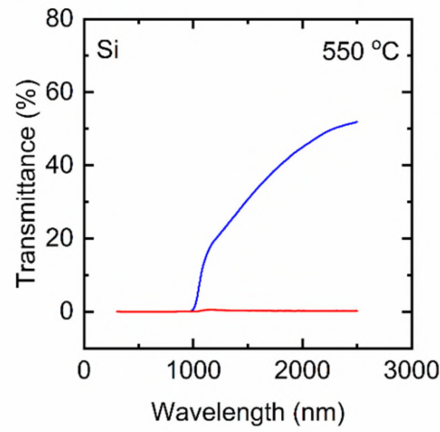

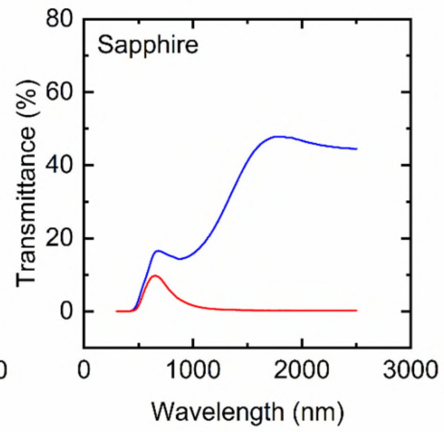

(c)

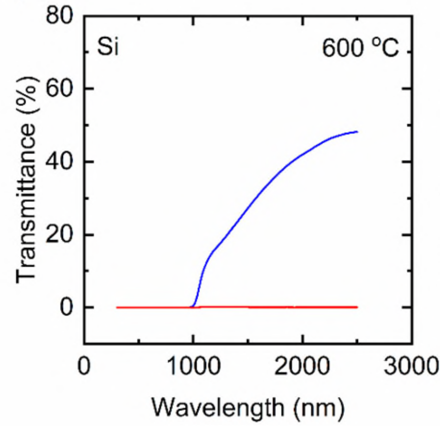

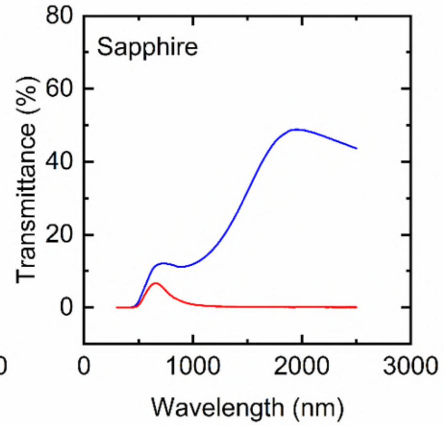

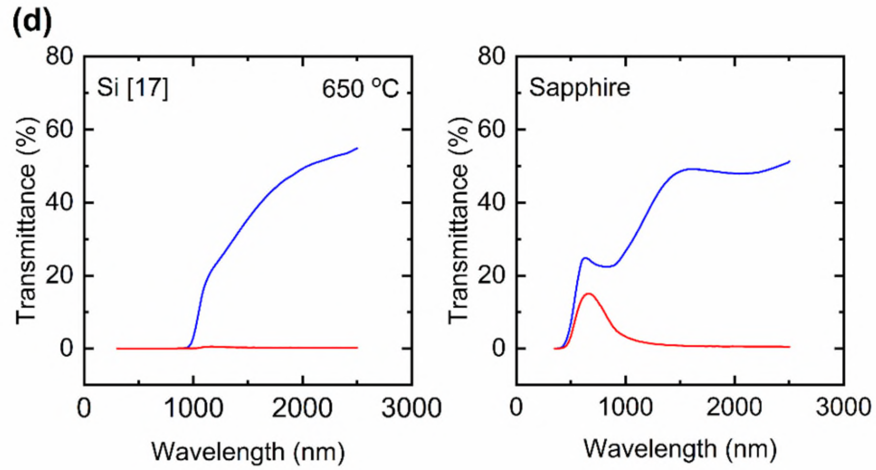

Figure 5.6 Optical transmittance ($\tilde{T}$) spectra of VO_2 thin films deposited at (a) 500 °C, (b) 550 °C, and (c) 600 °C and (d) 650 °C [17] on Si and sapphire substrates at 300 K (insulating phase) and 368 K (metallic phase).

Table 5.3 Optical transmittance ($\tilde{T}$) and transmittance contrast ($\Delta\tilde{T}$) values of VO_2 films prepared at different substrate temperatures (T_S) obtained at 300 K (insulating) and 368 K (metallic) for λ = 1500 nm, 2000 nm and 2500 nm.

Substrate temperature (T_S) (°C)	**λ (nm)**	**$\tilde{T}_{300K}$ (%)**	**$\tilde{T}_{368K}$ (%)**	**$\Delta\tilde{T}$ (%)**	**$\tilde{T}_{300K}$ (%)**	**$\tilde{T}_{368K}$ (%)**	**$\Delta\tilde{T}$ (%)**
	Si				Sapphire		
500	2500	34.5	0.5	34.0	35.0	0.6	34.4
	2000	27.6	0.5	27.1	33.3	0.7	32.6
	1500	16.9	0.5	16.4	24.4	0.7	23.5
550	2500	51.9	0.2	51.7	44.5	0.2	44.3
	2000	45.0	0.2	44.8	46.7	0.3	46.4
	1500	30.7	0.3	30.4	41.1	0.3	40.8
600	2500	48.2	0.1	48.1	43.7	0.1	43.6
	2000	42.0	0.1	41.9	48.7	0.1	48.6
	1500	27.3	0.1	27.2	31.8	0.2	31.6
650 [17]	2500	54.9	0.3	54.6	51.3	0.5	50.8
	2000	49.3	0.4	48.9	45.2	0.5	44.7
	1500	35.5	0.5	35.0	39.9	0.8	39.1

Figure 5.7 (a) gives the temperature dependence of $\tilde{T}_{2500nm}$. Figure 5.7 (b) to (e) show the $d\tilde{T}/dT$ vs. T plots which give the critical temperatures (T_{IMT} and T_{MIT}) and sharpness (full width at half maximum, FWHM) of the IM and MI phase transitions. It is important to emphasize that the narrow and sharp hysteresis of IM and MI transitions in VO_2 films deposited at 650 °C on sapphire substrate in Ref. [17] is not observed in the thin films deposited at T_S = 600 °C and below. The hysteresis width (ΔH) of the films deposited on both Si and sapphire substrates become broader as the T_S is lowered. The broadening appears to be about 14 –16 K for films on Si and 13 – 21 K for films on sapphire.

Figure 5.8 presents the comparison of phase transition properties obtained at $\lambda = 2500$ nm. In Figure 5.8 (a) the insulator-to-metal (T_{IMT}), metal-to-insulator (T_{MIT}) and the phase transition (T_t) temperatures are presented. The T_t is calculated as the mean of the T_{IMT} and T_{MIT} and is given in Equation (5.1) below:

$$T_t = \frac{T_{\mathrm{IMT}} + T_{\mathrm{MIT}}}{2} \tag{5.1}$$

By definition, T_t depends on the hysteresis width (ΔH). It is observed that the critical temperatures on silicon substrates are relatively the same as T_S is lowered from 650 (Ref. [17]) to 550 °C, but eventually decrease sharply for films prepared at 500 °C. For films on Si, as the T_t stays approximately constant for T_S = 650, 600 and 550 °C at about 340 K but falls to 320 K for T_S = 500 °C. On the other hand, the T_t of the films on sapphire appear to be lower compared to that for the film prepared at 650 °C in Ref. [17], displaying the lowest T_t around 322 K at 500 °C. There is no clear dependence of T_t on T_S for films prepared on sapphire substrates. This change in T_t indicates increased defects in the VO_2 films. Also, the change may be attributed to the spatial variation of local T_{IMT} and T_{MIT} due to increased number of coexisting metallic and insulating phases within the volume of the films as pointed out elsewhere [38]. Figure 5.8 (b) presents the ΔH and the full width half maximum (FWHM) of the IM and MI transitions of the as-prepared VO_2 thin films. The increasing FWHM can be interpreted as the degrading sharpness of the phase transitions. Figure 5.8 (c) introduces the comparison of transmittance contrast ($\Delta\tilde{T}$) of the as-prepared films at λ = 1500, 2000, and 2500 nm which are commonly considered in NIR applications [39,43]. At lower T_S, the ΔH becomes broader. The luminous (visible) and solar transmission characteristics of the as-prepared VO_2 films deposited on sapphire substrates are also analyzed. The luminous transmittance ($\tilde{T}_{\mathrm{lum}}$), solar transmittance ($\tilde{T}_{\mathrm{sol}}$), the luminous modulation ($\Delta\tilde{T}_{\mathrm{lum}}$) and solar modulation ($\Delta\tilde{T}_{\mathrm{sol}}$) efficiencies are commonly considered properties for smart window applications [44,50]. $\tilde{T}_{\mathrm{lum}}$ measures the amount of visible light passing through a semi-transparent material. $\tilde{T}_{\mathrm{sol}}$ is considered as an index that characterizes the transmission of sunlight within the visible and near-infrared spectrum. $\tilde{T}_{\mathrm{lum}}$ and $\tilde{T}_{\mathrm{sol}}$ can be determined from Equation (5.2) below:

$$\tilde{T}_{\text{lum,sol}} = \frac{\int \varphi_{\text{lum,sol}}(\lambda)\tilde{T}(\lambda)d\lambda}{\int \varphi_{\text{lum,sol}}(\lambda)d\lambda} \quad (5.2)$$

$\tilde{T}_{\text{lum}}$ is obtained for wavelengths between 380 and 780 nm and $\tilde{T}_{\text{sol}}$ is obtained for a wavelength range between 300 and 2500 nm. $\varphi_{\text{lum}}(\lambda)$ is the spectral sensitivity of the light adapted human eye [51], $\varphi_{\text{sol}}(\lambda)$ is the solar irradiance spectrum for air mass of 1.5 (37° sunlight above the horizon of earth) [52], and $\tilde{T}(\lambda)$ is acquired from the transmittance spectrum of the as-prepared films. $\Delta\tilde{T}_{\text{lum}}$ and $\Delta\tilde{T}_{\text{sol}}$ are calculated from the Equation (5.3) given below:

$$\Delta\tilde{T}_{\text{lum, sol}} = \tilde{T}_{\text{lum, sol}}(300\text{ K}) - \tilde{T}_{\text{lum, sol}}(368\text{ K}) \quad (5.3)$$

The results of the calculations of $\tilde{T}_{\text{lum, sol}}$ and $\Delta\tilde{T}_{\text{lum, sol}}$ values are summarized in Table 5.4. Figure 5.9 gives the distribution of the data presented in Table 5.4. In Figure 5.9 (a), $\tilde{T}_{\text{lum}}$ values obtained for VO_2 thin films prepared at T_S = 500, 550 and 600 °C in the insulating phase (300 K) appear to be smaller from that obtained for films prepared at T_S = 650 °C. The $\tilde{T}_{\text{lum}}$ values in the metallic phase (368 K) show a similar characteristic. Because the difference between $\tilde{T}_{\text{lum}}$ values obtained at 300 and 368 K is not large due to the high optical transmittance between 450 and 700 nm, the $\Delta\tilde{T}_{\text{lum}}$ values are small. Figure 5.9 (b) presents $\tilde{T}_{\text{sol}}$ and $\Delta\tilde{T}_{\text{sol}}$ values of the as-prepared VO_2 films which are also lower than those obtained for the film prepared at 650 °C [17]. However, the $\tilde{T}_{\text{sol}}$ values at 368 K are indeed much lower compared to the ones at 300 K, due to the near-zero transmission in the NIR region integrated in Equation (5.2). This large difference between the $\tilde{T}_{\text{sol}}$ values at 300 and 368 K is reflected on the large values of $\Delta\tilde{T}_{\text{sol}}$.

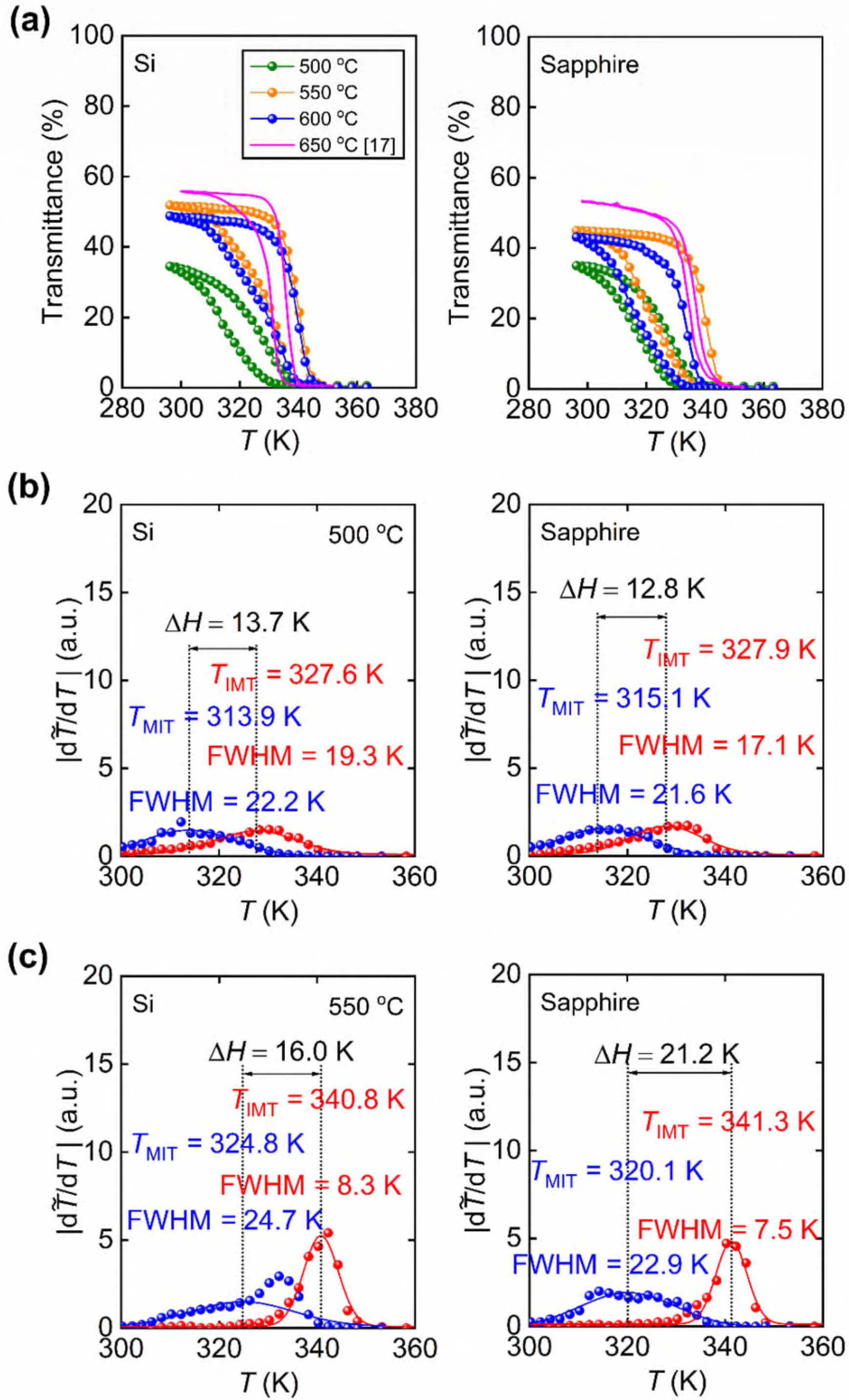
(a)
Si
500 °C
550 °C
600 °C
650 °C [17]
Transmittance (%)
T (K)
Sapphire
(b)
Si
500 °C
ΔH = 13.7 K
T_IMT = 327.6 K
T_MIT = 313.9 K
FWHM = 19.3 K
FWHM = 22.2 K
|dT̃/dT| (a.u.)
Sapphire
ΔH = 12.8 K
T_IMT = 327.9 K
T_MIT = 315.1 K
FWHM = 17.1 K
FWHM = 21.6 K
(c)
Si
550 °C
ΔH = 16.0 K
T_IMT = 340.8 K
T_MIT = 324.8 K
FWHM = 8.3 K
FWHM = 24.7 K
Sapphire
ΔH = 21.2 K
T_IMT = 341.3 K
T_MIT = 320.1 K
FWHM = 7.5 K
FWHM = 22.9 K

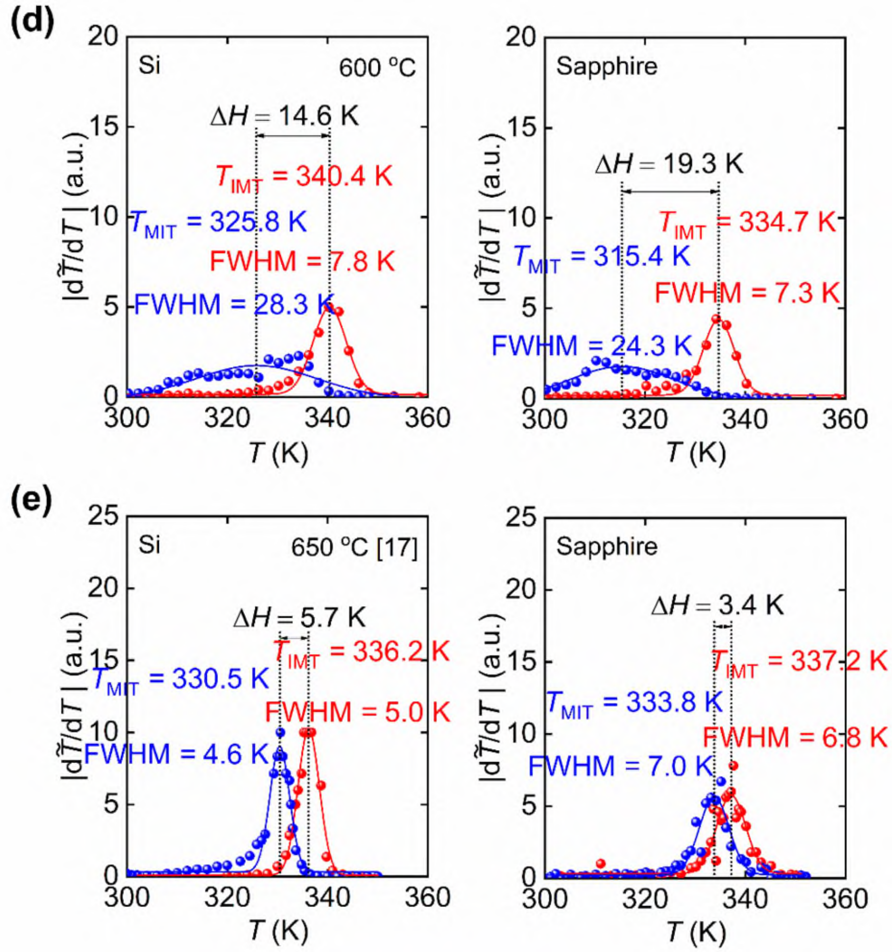

Figure 5.7 (a) Temperature dependence (T) of optical transmittance ($\tilde{T}$) obtained at a light wavelength of λ = 2500 nm for VO_2 thin films deposited at 500, 550, 600 and 650 °C [17]. The phase transition characteristics for heating and cooling cycles for films prepared at (b) 500 °C, (c) 550 °C, (d) 600 °C, and (e) 650 °C [17] on Si and sapphire substrates at 300 K (insulating phase) and 368 K (metallic phase).

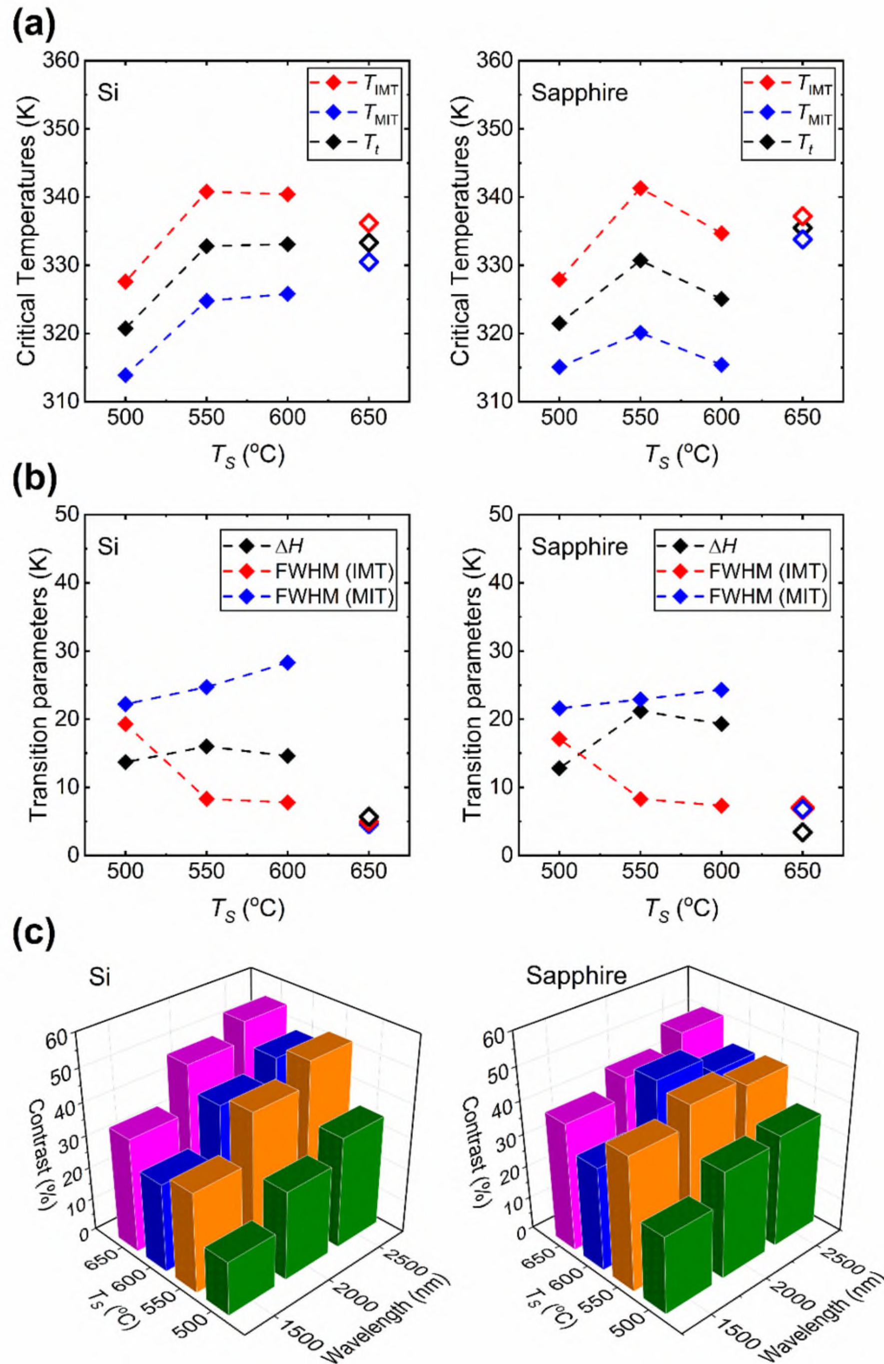

Figure 5.8 (a) Critical temperatures (T_{IMT}, T_{MIT} and T_t) of the VO_2 films on Si and sapphire prepared at various substrate temperatures (T_S) obtained at a light wavelength of $\lambda = 2500$ nm. (b) Hysteresis (ΔH) and sharpness (FWHM) of the Gaussian curves obtained from $\mathrm{d}\tilde{T} / \mathrm{d}T$ vs. T plots in Figure 5.7. In (a) and (b) the data points for films prepared at 650 °C [17] are shown in hollow

symbols. (c) Comparison of optical transmittance contrast, $\Delta\tilde{T} = \tilde{T}(300\text{ K}) - \tilde{T}(368\text{ K})$, obtained at NIR wavelengths λ = 1500 nm, 2000 nm and 2500 nm for films prepared at T_S = 500 (olive), 550 (orange), 600 (navy) and 650 [17] (magenta) °C.

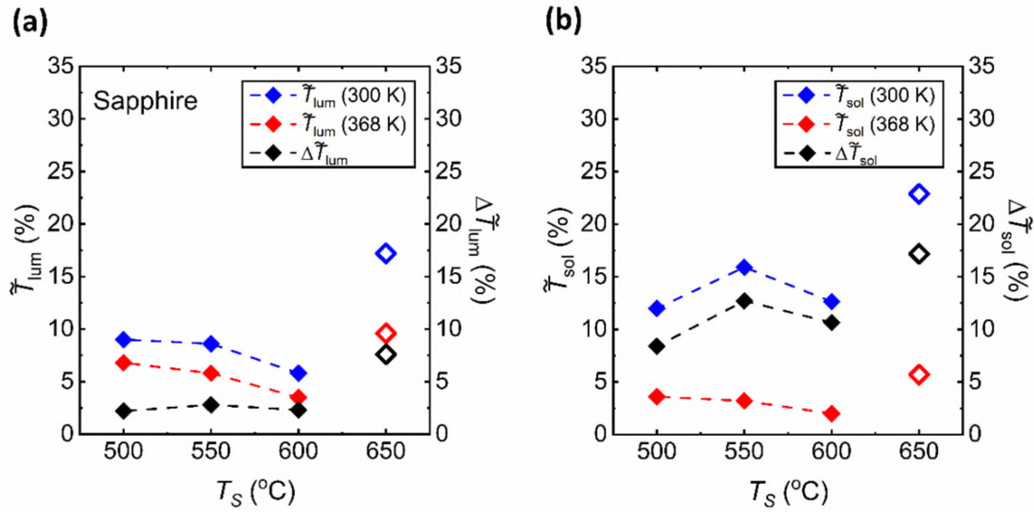

Figure 5.9 (a) Luminous transmittance ($\tilde{T}_{\text{lum}}$) at 300 K and 368 K and luminous modulation efficiency ($\Delta\tilde{T}_{\text{lum}}$) obtained for films deposited at various substrates temperatures (T_S). (b) Solar transmittance ($\tilde{T}_{\text{sol}}$) at 300 K and 368 K and solar modulation efficiency ($\Delta\tilde{T}_{\text{sol}}$) obtained for films deposited at various substrates temperatures (T_S). Data for the substrate temperature (T_S) of 650 °C [17] are presented in hollow symbols.

Table 5.4 Luminous and solar modulation efficiencies of VO_2 films prepared on sapphire substrates at various T_S.

Substrate temperature (T_S) (°C)	**$\tilde{T}_{\text{lum}}$ (%) (300 K)**	**$\tilde{T}_{\text{lum}}$ (%) (368 K)**	**$\Delta\tilde{T}_{\text{lum}}$ (%)**	**$\tilde{T}_{\text{sol}}$ (%) (300 K)**	**$\tilde{T}_{\text{sol}}$ (%) (368 K)**	**$\Delta\tilde{T}_{\text{sol}}$ (%)**
500	9	6.8	2.2	12	3.6	8.4
550	8.6	5.8	2.8	15.91	3.2	12.71
600	5.8	3.5	2.3	12.64	2	10.64
650 [17]	17.2	9.6	7.6	22.88	5.7	17.18

5.4.4 Electrical MIT Characterization

Figure 5.10 shows the temperature (T) dependence of the electrical conductivity (σ) of the VO_2 films prepared at T_S = 500, 550, 600 and 650 °C (Ref. [32]), and their phase transition properties. The critical temperatures T_{IMT}, T_{MIT} and the sharpness (FWHM) are obtained from the d(log(σ))/dT vs. T. plots as shown in Figure 5.10 (b) to (e). Here, it can be seen that there is only a slight broadening of the ΔH. On the other hand, the electrical phase transition properties of VO_2 thin films studied in this work show a prominent difference compared to the film prepared at T_S = 650 °C in Ref. [32]. The difference between the hysteresis properties of the samples is due to the difference in the nature of electrical and structural (observed optically) MIT [33,53]. Figure 5.11 gives the critical temperatures and phase transition parameters of VO_2 films deposited on sapphire substrates obtained in σ vs. T measurements. As it is clear from the Figure 5.11 (a), the transition temperatures (T_{IMT}, T_{MIT} and T_t) drop with decreasing T_S. In Figure 5.11 (b), the ΔH does not seem to be greatly affected from T_S. As the T_S is lowered from 650 to 550 °C, the ΔH broadens from 9 to 11 K, respectively. However, for T_S = 500 °C, the ΔH drops to 8.4 K which shows narrower ΔH compared to the other VO_2 films. On the other hand, the effect of T_S appears to be prominent on the sharpness of both IM and MI transitions and the conductivity contrast ($\Delta\sigma$). The FWHM of the films prepared between 500 and 600 °C are larger compared with those of the film prepared at 650 °C in both IM and MI transitions. The increase of FWHM, or loss of sharpness, in films between 500 and 600 °C indicates degradation of the abrupt phase transition. Also, compared to the high-quality VO_2 films prepared at 650 °C (Ref. [32]), the $\Delta\sigma$ of the films prepared at T_S = 600 °C and below displays a substantial drop from the order of 4 to 2.

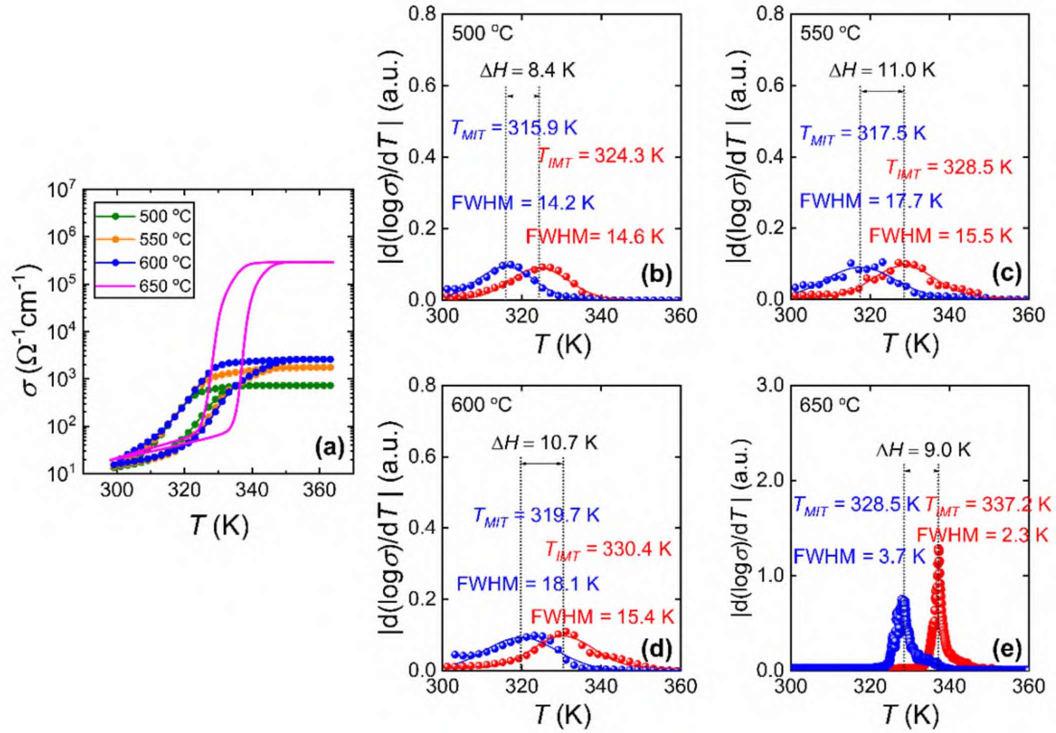

Figure 5.10 Temperature (T) dependence of electrical conductivity (σ) of VO_2 films prepared at various substrate temperatures (T_S). (a) Comparison of T dependence of σ of films prepared at T_S = 500 °C, 550 °C, 600 °C, and 650 °C [32]. The phase transition characteristics for heating and cooling cycles for films prepared at T_S = (b) 500 °C, (c) 550 °C, (d) 600 °C and (e) 650 °C [32].

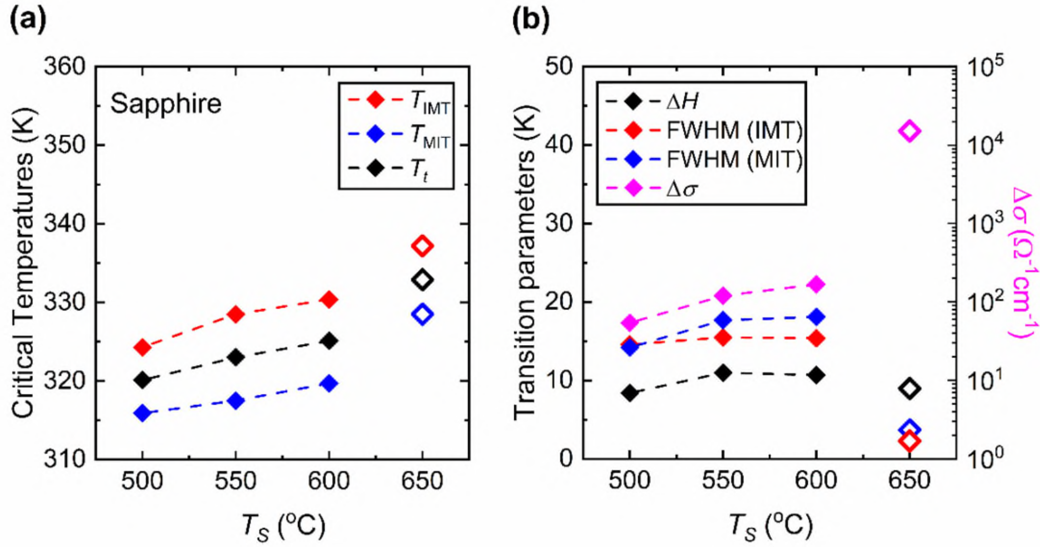

Figure 5.11 Electrical conductivity phase transition properties of VO_2 films prepared on sapphire substrates at various substrate temperatures (T_S). (a) Critical temperatures of the phase transition (T_{IMT}, T_{MIT} and T_t). (b) Phase transition parameters (ΔH, FWHM (IMT), and FWHM (MIT)) and the contrast of conductivity, $\Delta\sigma = \sigma(368\text{ K})/\sigma(300\text{ K})$. The data points for the substrate temperature 650 °C are from Ref. [32] and displayed in hollow symbols.

5.5 Discussion

We begin our discussion by considering the structural investigation of VO_2 thin films. The results presented in Figure 5.1–Figure 5.4 clearly show that the T_S has a considerable effect on the film structure, including both the crystallinity and surface roughness. For T_S between 600 and 500 °C, both the XRD diffractograms and the Raman spectra show VO_2 peaks, which disappear for $T_S \leq 450$ °C. From this observation, it can be understood that higher T_S (≥ 500 °C) facilitates the formation of the VO_2 phase, whereas lower temperature growth favors the formation of the V_2O_5 phase as can be referred to in Table 5.1. Since the V_2O_5 phase appears at lower T_S and the root mean square roughness (R_q) increases with lower T_S, one may argue that there may a correlation between the two observations. Nonetheless, we do not have any further experimental evidence to validate the latter. Yet, it is apparent from Figure 5.3 that low T_S leads to a polycrystalline structure of misoriented grains with dissimilar geometries. Thus, not only the smaller grain size but also the increased defects in the films at low T_S (e.g., 500 °C) may explain

the drop in the $\tilde{T}$ spectrum. Secondly, the drop in the transition temperature (T_t) can be related to the significance of unrelaxed lattice strain [54,55]. The degradation of the crystalline quality can be seen in the worsening of the phase transition properties given in Figure 5.7. Moreover, considering the electrical characterization, the degradation of contrast in the conductivity between the insulator and metallic phases ($\Delta\sigma$) may be a result of the reduction of the current path due to increased oxygen vacancies and surface roughness [56]. We also examined the conductivity activation energy of the as-prepared VO_2 films. The Arrhenius plot of $\ln(\sigma)$ vs. $1000/T$ is presented in Figure 5.12 where it is apparent that the conductivity (σ) of VO_2 is thermally activated. We can represent the thermally activated behavior by[4]

$$\sigma = \sigma_o \exp\left(-\frac{\Delta E}{2k_B T}\right) \tag{5.4}$$

where $\Delta E = E_g$ if we assume the sample is intrinsic. Equation (5.4) yields ΔE of the VO_2 films as 0.53 ± 0.02, 0.52 ± 0.01 and 0.49 ± 0.01 eV corresponding to prepared at $T_S = 600$, 550 and 500 °C respectively. The thermally activated conductivity can arise either from intrinsic conductivity (thermal generation across the bandgap) with $\Delta E = E_g$ as in Equation (5.4) or from the ionization of defects or impurities in the film, in which case ΔE is not the bandgap but the magnitude of the energy difference between the transport band and the defect or impurity level. The ΔE values appear to be lower than that of high-quality VO_2 films, which is 0.64 ± 0.01 eV from Ref. [36]. The ΔE values seem to follow a similar trend to that of $\Delta\sigma$ with respect to T_S in Figure 5.11 (b). The drop in $\Delta\sigma$ and the apparent narrowing of ΔE may too be related to the increased density of grain boundaries and defects of oxygen vacancies due to low T_S which as pointed out in Ref. [57]. In addition, Figure 5.13 presents the shifting of the amplified XRD peak of VO_2 (011) at ~28 ° to a lower angle as T_S decreases. This signifies an enlarged lattice parameter of VO_2 due to defects and lattice strain, which is also suggested in Ref. [56]. It is worth comparing $\Delta E = 0.49 - 0.64$ eV for these VO_2 films with the indirect (smallest) optical bandgap reported for VO_2 films deposited

[4] The journal paper has an obvious typo in Equation (5.4) in which the negative sign is missing. The typo does not affect any of the calculations or discussions. Further, the usual thermally activated conductivity equation is written without the factor 2 in the denominator of the argument. In this paper a factor of 2 was used so that ΔE would be simply E_g for the intrinsic case. [For an n-type semiconductor, $\Delta E = 2(E_c - E_{Fn})$ and $\Delta E = 2(E_{Fp} - E_v)$ for a p-type.]

at 650 °C, which is 0.52 eV [17]. The work in Ref. [33] puts the optical bandgap between in the range 0.55–0.60 eV; again ΔE is very close to these values.

Finally, we compare our results with other works [21,28,30,57] in which the effect of T_S on the phase transition properties of VO_2 thin films have been studied. These studies have employed RF reactive inverted cylindrical magnetron sputtering [21], RF magnetron sputtering [28], inductively coupled plasma (ICP)-assisted sputtering [30] and pulsed-laser deposition (PLD) [57] for thin film preparation. We also consider selected works [26,36] which have reported the production of high-quality VO_2 thin films at low substrate temperatures. Figure 5.14 presents the phase transition properties of VO_2 thin films obtained by means of optical transmittance ($\tilde{T}$) and electrical conductivity (σ) measurements. Figure 5.14 (a) and (b) show the comparison of the T_t and ΔH characteristics of the films on sapphire substrates from the present work with the films prepared in Refs. [21,30]. It should be noted that the optical transmittance has been measured at different wavelengths. VO_2 films reported in Ref. [26] were prepared at T_S = 200 °C by reactive magnetron sputtering with a post-deposition annealing treatment at 300 °C, and the transition properties were obtained at λ = 2000 nm. The present work has used λ = 2500 nm, whereas λ = 1450 nm for Ref. [21] and 1100 nm for Ref. [30] were used. In Figure 5.14 (a), the films in Ref. [21] have a constant T_t around 340 K, whereas the T_t of films in Ref. [30] decreases from T_S = 600 to 500 °C and stays constant around 343 K until T_S = 450 °C. In contrast, the T_t of the VO_2 films on sapphire substrates presented in this work drops down to 323 K as the T_S is lowered to 500 °C. As can be observed in Figure 5.14 (b), reducing the T_S has a significant impact on the ΔH of the films prepared in the present work which can be related to the polycrystallinity as well as increased compressive and tensile strain in the films [28, 32]. Figure 5.14 (c) and (d) present the comparison of electrical phase transition properties obtained from Refs. [28,57]. Moreover, VO_2 films reported in Ref. [36] were prepared by molecular beam epitaxy (MBE) at T_S = 350 °C. In Figure 5.14 (c), the T_t of the films of Ref. [28] increases from a low T_S = 450 to 550 °C and then drops at high T_S = 700 and 720 °C. On the contrary, in Figure 5.14 (d), the ΔH values appear to be relatively unaffected by T_S, and they seem to be mostly constant around 5.5 K, only films prepared at 450 °C have a large ΔH around 10 K. The T_t values obtained from Ref. [57] are constant around 343 K. Also, the ΔH drops with decreasing T_S from 13 K and 5 K. However, if the phase transition sharpness and $\Delta\sigma$ are taken into consideration, these films in Refs. [28,57] do not display attributes

associated with high-quality films with decreasing T_S. Overall, according to these comparisons, the preparation of high-quality VO_2 films at low temperatures appear to be a challenge even though different deposition techniques and deposition parameters are applied. The degradation of the film properties may essentially rise from loss of crystalline quality, the degradation of stoichiometry (e.g., if there is an interface film between VO_2 and the substrate) and the presence of defects and lattice strain that arise from film-substrate mismatch.

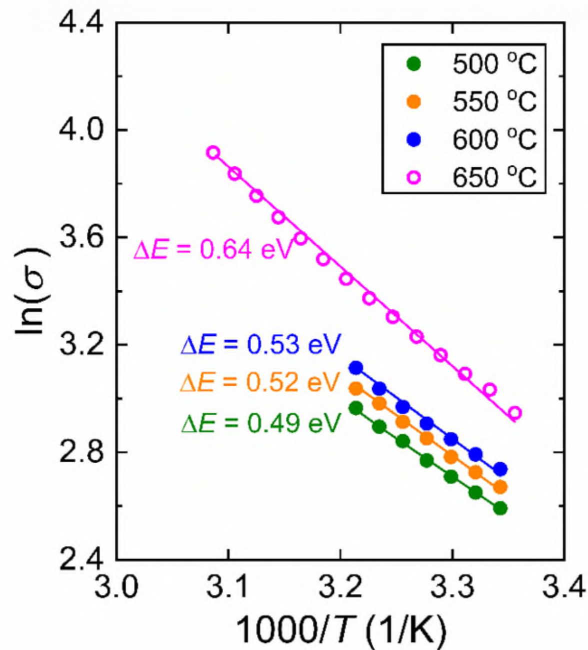

Figure 5.12 Arrhenius plot of conductivity (σ) data obtained from VO_2 films in their insulating phases. Data set for VO_2 film prepared at 650 °C is extracted from the σ vs. T plot in Ref. [32].

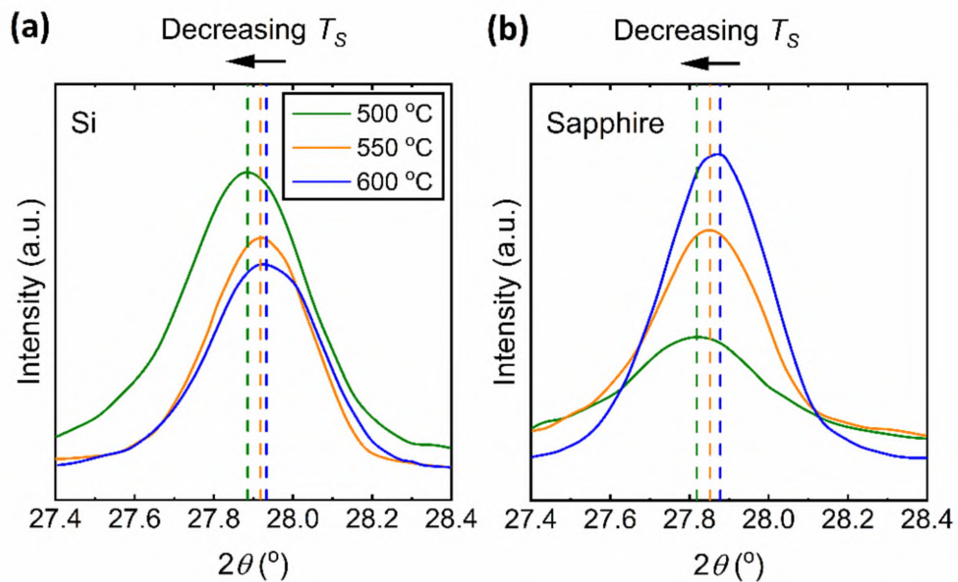

Figure 5.13 X-ray diffraction of (011) planes of VO_2 thin films deposited at T_S = 500, 550, and 600 °C on (a) Si and (b) sapphire substrates.

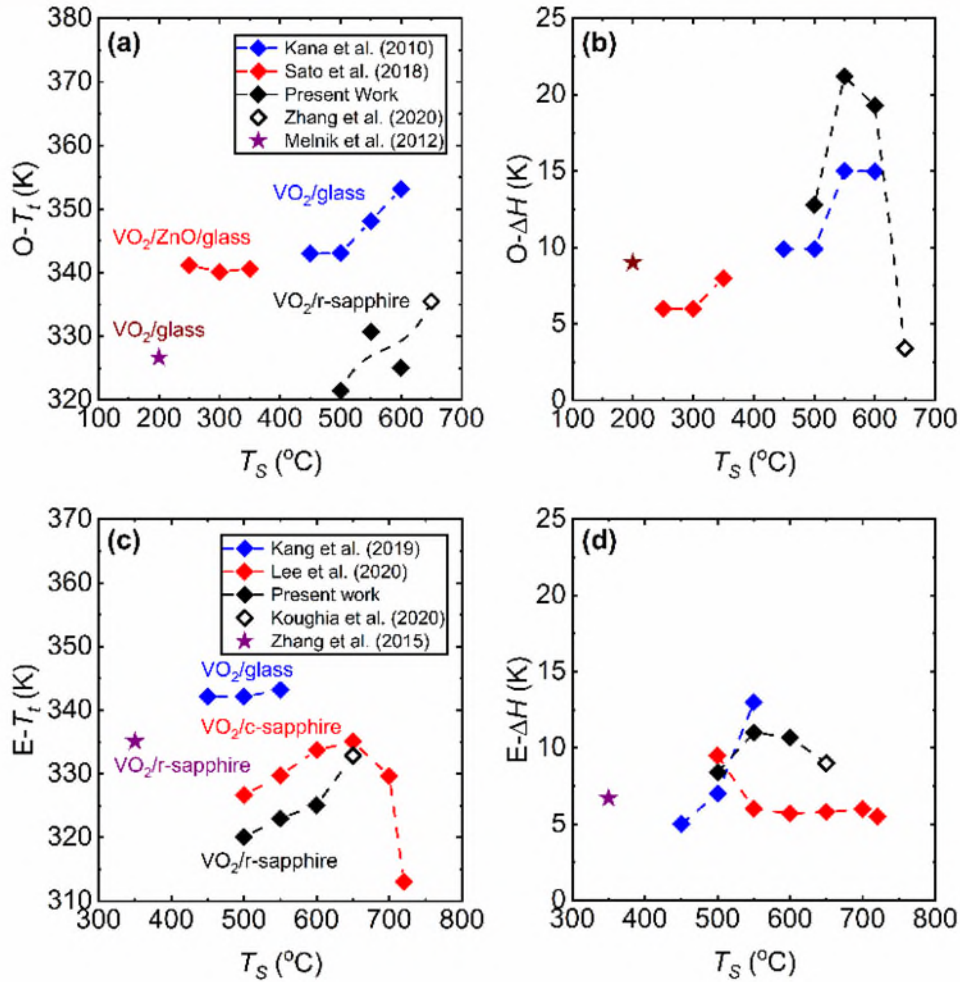

Figure 5.14 Comparison of VO_2 thin films deposited at various temperatures studied in different works. (a) Comparison of T_t obtained from optical (O-) switching measurements. (b) Hysteresis width (ΔH) of the films that are obtained from the temperature (T) dependence of optical transmittance ($\tilde{T}$). (c) Comparison of phase transition temperature (T_t) obtained from electrical (E-) switching. (d) Hysteresis width (ΔH) of the films that are obtained from the T-dependence of electrical conductivity or resistance. Note that Kana et al. (2010) is [30]; Kang et al. (2019) is [57]; Koughia et al. (2020) is [32]; Lee et al. (2020) is [28]; Melnik et al. (2012) is [26]; Sato et al. (2012) is [21]; Zhang et al. (2015) is [36]; Zhang et al. (2020) is [17].

5.6 Conclusion

The effect of substrate temperature (T_S) on the structural, optical and electrical properties of VO_2 thin films during DC magnetron sputtering have been investigated. The results showed that the T_S plays a crucial role on the microstructure and hence the optical and electrical phase transition properties of the VO_2 films. It is found that T_S below 500 °C favors the growth of the V_2O_5 phase where T_S of 500 °C and higher facilitate the growth of stoichiometric VO_2 films. The lowering of T_S from 600 to 500 °C have shown reduced transmittance ($\tilde{T}$) and modulation efficiencies, broadened hysteresis width (ΔH), and decreased transition temperature, which suggests the presence of defects and unrelaxed lattice strain in the films. The comparison of the present results with those published on similar VO_2 samples where the effect of T_S has been examined indicates significant challenges remain in the fabrication of high-quality VO_2 films below a T_S of 650 °C.

5.7 References

[1] H. Zhou, J. Li, Y. Xin, G. Sun, S. Bao and P. Jin, "Optical and electrical switching properties of VO2 thin film on MgF2 (111) substrate," *Ceramics International*, vol. 42, p. 7655, 2016.

[2] A. Simo, K. Kaviyarasu, B. Mwakikunga, R. Madjoe, A. Gibaud and M. Maaza, "Phase transition study in strongly correlated VO2 based sensing systems," *Journal of Electron Spectroscopy and Related Phenomena*, vol. 216, p. 23, 2017.

[3] D. Malarde, M. J. Powell, R. Quesada-Cabrera, R. L. Wilson, C. J. Carmalt, G. Sankar, I. P. Parkin and R. G. Palgrave, "Optimized Atmospheric-Pressure Chemical Vapor Deposition Thermochromic VO2 Thin Films for Intelligent Window Applications," *ACS Omega*, vol. 2, p. 1040, 2017.

[4] H. Coy, R. Cabrera, N. Sepulveda and F. E. Fernandez, "Optoelectronic and all-optical multiple memory states in vanadium dioxide," *Journal of Applied Physics*, vol. 108, p. 113115, 2010.

[5] X. Hong, D. J. Loy, P. A. Dananjaya, F. Tan, C. Ng and W. Lew, "Oxide-based RRAM materials for neuromorphic computing," *Journal of Materials Science*, vol. 53, p. 8720, 2018.

[6] Z. Yang, C. Ko and S. Ramanathan, "Oxide electronics utilizing ultrafast metal-insulator transitions," *Annual Review of Materials Research*, vol. 1, pp. 337-367, 2011.

[7] J. Jeong, Y. Jung, Z. Qu, B. Cui, A. Khanda, A. Sharma, S. S. P. Parkin and J. K. S. Poon, "VO2 electro-optic memory and oscillator for neuromorphic computing," *CLEO: Science and Innovations*, pp. STh3R-2, 2020.

[8] H. Liu, J. Lu and X. R. Wang, "Metamaterials based on the phase transition of VO2," *Nanotechnology*, vol. 29, no. 2, p. 024002, 2017.

[9] J. B. Goodenough, "The two components of the crystallographic transition in VO2," *Journal of Solid State Chemistry*, vol. 3, no. 4, pp. 490-500, 1971.

[10] T. Hajlaoui, N. Émond, C. Quirouette, B. L. Drogoff, J. Margot and M. Chaker, "Metal–insulator transition temperature of boron-doped VO2 thin films grown by reactive pulsed laser deposition," *Scripta Materialia*, vol. 177, p. 32, 2020.

[11] B. Rajeswaran and A. M. Umarji, "Defect engineering of VO2 thin films synthesized by Chemical Vapor Deposition," *Materials Chemistry and Physics*, vol. 245, p. 122230, 2020.

[12] J. Leroy, A. Bessaudou, F. Cosset and A. Crunteanu, "Structural, electrical and optical properties of thermochromic VO2 thin films obtained by reactive electron beam evaporation," *Thin Solid Films*, vol. 520, p. 4823, 2012.

[13] E. Gagaoudakis, E. Aperathitis, G. Michail, M. Panagopoulou, D. Katerinopoulou, V. Binas and... and G. Kiriakidis, "Low-temperature rf sputtered VO2 thin films as thermochromic coatings for smart glazing systems," *Solar Energy*, vol. 165, pp. 115-121, 2018.

[14] M. Li, S. Magdassi, Y. Gao and Y. Long, "Hydrothermal synthesis of VO2 polymorphs: advantages, challenges and prospects for the application of energy efficient smart windows," *Small*, vol. 13, no. 36, p. 1701147, 2017.

[15] C. Zhang, Q. Yang, C. Koughia, F. Ye, M. Sanayei, S. Wen and S. Kasap, "Characterization of vanadium oxide thin films with different stoichiometry using Raman spectroscopy," *Thin Solid Films*, vol. 620, pp. 64-69, 2016.

[16] S. Lafane, S. Abdelli-Messaci, M. Kechouane, S. Malek, B. Guedouar, J. Lappalainen, ... and T. Kerdja, "Direct growth of VO2 nanoplatelets on glass and silicon by pulsed laser deposition through substrate temperature control," *Thin Solid Films*, vol. 632, pp. 119-127, 2017.

[17] C. Zhang, C. Koughia, O. Güneş, J. Luo, N.Hossain, Y. Li, X. Cui, S.-J. Wen, R. Wong, Q. Yang and S. Kasap, "Synthesis, structure and optical properties of high-quality VO2 thin films grown on silicon, quartz and sapphire substrates by high temperature magnetron sputtering: Properties through the transition temperature," *Journal of Alloys and Compounds*, vol. 848, p. 156323, 2020.

[18] Z. A. Umar, N. Ahmed, R. Ahmed, M. Arshad, M. Anwar-Ul-Haq, T. Hussain and M. A. Baig, "Substrate temperature effects on the structural, compositional, and electrical properties of VO2 thin films deposited by pulsed laser deposition," *Surface and Interface Analysis*, vol. 50, no. 3, pp. 297-303, 2018.

[19] A. Diallo, N. M. Ndiaye, B. D. Ngom, S. Khamlich, K. Talla, S. Ndiaye and ... and M. Maaza, "Effect of substrate temperature on the structure and the metal insulator transition in pulsed laser deposed V02\films on soda lime glass," *Journal of Optics*, vol. 44, no. 1, pp. 36-44, 2015.

[20] J. Houska, "Design and reactive magnetron sputtering of thermochromic coatings," *Journal of Applied Physics*, vol. 131, no. 11, p. 110901, 2022.

[21] K. Sato, H. Hoshino, M. S. Mian and K. Okimura, "Low-temperature growth of VO2 films on transparent ZnO/glass and Al-doped ZnO/glass and their optical transition properties," *Thin Solid Films*, vol. 651, pp. 91-96, 2018.

[22] G. Sun, X. Cao, X. Li, S. Bao, N. Li, M. Liang, ... and P. Jin, "Low-temperature deposition of VO2 films with high crystalline degree by embedding multilayered structure," *Solar Energy Materials and Solar Cells*, vol. 161, pp. 70-76, 2017.

[23] Z. Xiang, Z. Wu, C. Ji, Y. Shi, J. Dai, Z. Huang, ... and Y. Jiang, "Low temperature fabrication of high-performance VO2 film via embedding low vanadium buffer layer," *Applied Surface Science*, vol. 517, p. 146101, 2020.

[24] M. Zhu, H. Qi, C. Li, B. Wang, H. Wang, T. Guan and D. Zhang, "VO2 thin films with low phase transition temperature grown on ZnO/glass by applying substrate DC bias at low temperature of 250° C," *Applied Surface Science*, vol. 453, pp. 23-30, 2018.

[25] J. Houska, D. Kolenaty, J. Vlcek and R. Cerstvy, " Properties of thermochromic VO2 films prepared by HiPIMS onto unbiased amorphous glass substrates at a low temperature of 300° C," *Thin Solid Films*, vol. 660, pp. 463-470, 2018.

[26] V. Melnik, I. Khatsevych, V. Kladko, A. Kuchuk, V. Nikirin and B. Romanyuk, "Low-temperature method for thermochromic high ordered VO2 phase formation," *Materials Letters*, vol. 68, pp. 215-217, 2012.

[27] B. Guo, L. Chen, S. Shi, A. Ishaq, D. Wan, Z. Chen, ... and Y. Gao, "Low temperature fabrication of thermochromic VO 2 thin films by low-pressure chemical vapor deposition," *RSC Advances*, vol. 7, no. 18, pp. 10798-10805, 2017.

[28] D. Lee, D. Yang, H. Kim, J. Kim, S. Song, K. S. Choi, ... and S. Park, "Deposition-temperature-mediated selective phase transition mechanism of VO2 films," *The Journal of Physical Chemistry C*, vol. 124, no. 31, pp. 17282-17289, 2020.

[29] R. McGee, A. Goswami, B. Khorshidi, K. McGuire, K. Schofield and T. Thundat, "Effect of process parameters on phase stability and metal-insulator transition of vanadium dioxide (VO2) thin films by pulsed laser deposition," *Acta Materialia*, vol. 137, pp. 12-21, 2017.

[30] J. K. Kana, J. M. Ndjaka, B. D. Ngom, A. Y. Fasasi, O. Nemraoui, R. Nemutudi, ... and M. Maaza, "High substrate temperature induced anomalous phase transition temperature shift in sputtered VO2 thin films," *Optical Materials*, vol. 32, no. 7, pp. 739-742, 2010.

[31] J. K. Kana, J. M. Ndjaka, B. D. Ngom, N. Manyala, O. Nemraoui, A. Y. Fasasi, ... and M. Maaza, "Thermochromic nanocrystalline Au–VO2 composite thin films prepared by radiofrequency inverted cylindrical magnetron sputtering," *Thin Solid Films*, vol. 518, no. 6, pp. 1641-1647, 2010.

[32] C. Koughia, O. Gunes, C. Zhang, S. J. Wen, R. Wong, Q. Yang and S. O. Kasap, "Topology of conductive clusters in sputtered high-quality VO2 thin films on the brink of percolation threshold during insulator-to-metal and metal-to-insulator transitions," *Journal*

of Vacuum Science & Technology A: Vacuum, Surfaces, and Films, vol. 38, no. 6, p. 063401, 2020.

[33] C. Zhang, O. Gunes, Y. Li, X. Cui, M. Mohammadtaheri, S. Wen, R. Wong, Q. Yang and S. Kasap, "The effect of substrate biasing during DC magnetron sputtering on the quality of VO2 thin films and their insulator-metal transition behavior," *Materials*, vol. 12, p. 2160, 2019.

[34] ImageJ. *Image processing and Analysis in Java* [Online]. Available: https://imagej.nih.gov /ij/. [Accessed 5 February 2023].

[35] S. S. Majid, D. K. Shukla, F. Rahman, S. Khan, K. Gautam, A. Ahad, ... and J. Strempfer, "Insulator-metal transitions in the T phase Cr-doped and M 1 phase undoped VO 2 thin films," *Physical Review B*, vol. 98, no. 7, p. 075152, 2018.

[36] H. T. Zhang, L. Zhang, D. Mukherjee, Y. X. Zheng, R. C. Haislmaier, N. Alem and R. Engel-Herbert, "Wafer-scale growth of VO2 thin films using a combinatorial approach," *Nature Communications*, vol. 6, no. 1, pp. 1-8, 2015.

[37] J. A. Creeden, S. E. Madaras, D. B. Beringer, M. R. Beebe, I. Novikova and R. Lukaszew, "Structural and photoelectric properties of epitaxially grown vanadium dioxide thin films on c-plane sapphire and titanium dioxide," *Scientific Reports*, vol. 9, no. 1, pp. 1-9, 2019.

[38] K. Miyazaki, K. Shibuya, M. Suzuki, H. Wado and A. Sawa, "Correlation between thermal hysteresis width and broadening of metal–insulator transition in Cr-and Nb-doped VO2 films," *Japanese Journal of Applied Physics*, vol. 53, no. 7, p. 071102, 2014.

[39] J. Liang, P. Li, L. Zhou, J. Guo and Y. Zhao, "Near-infrared tunable multiple broadband perfect absorber base on VO2 semi-shell arrays photonic microstructure and gold reflector," *Materials Research Express*, vol. 5, no. 1, p. 015802, 2018.

[40] X. Chu, Q. Xie, X. Zhang, B. Guo, J. Liao and X. Zhao, "Fabrication and Optical Characterization of VO2-Based Thin Films Deposited on Practical Float Glass by Magnetron Sputtering and Professional Annealing," *Materials*, vol. 15, no. 9, p. 2990, 2022.

[41] D. P. Zhang, M. D. Zhu, Y. Liu, K. Yang, G. X. Liang, Z. H. Zheng, ... and P. Fan, "High performance VO2 thin films growth by DC magnetron sputtering at low temperature for smart energy efficient window application.," *Journal of Alloys and Compounds*, vol. 659, pp. 198-202, 2016.

[42] B. Ko, T. Badloe, S. J. Kim, S. H. Hong and J. Rho, "Employing vanadium dioxide nanoparticles for flexible metasurfaces with switchable absorption properties at near-infrared frequencies," *Journal of Optics*, vol. 22, no. 11, p. 114002, 2020.

[43] S. B. Son, J. W. Youn, K. S. Kim and D. U. Kim, "Optical properties of periodic micropatterned VO2 thermochromic films prepared by thermal and intense pulsed light sintering," *Materials & Design*, vol. 182, p. 107970, 2019.

[44] T. D. Vu, S. Liu, X. Zeng, C. Li and Y. Long, "High-power impulse magnetron sputtering deposition of high crystallinity vanadium dioxide for thermochromic smart windows applications," *Ceramics International*, vol. 46, no. 6, pp. 8145-8153, 2020.

[45] S. Wang, W. Wei, T. Huang, M. Yuan, Y. Yang, W. Yang, ... and N. Dai, "Al-Doping-Induced VO2 (B) Phase in VO2 (M) Toward Smart Optical Thin Films with Modulated ΔTvis and ΔTc.," *Advanced Engineering Materials*, vol. 21, no. 12, p. 1900947, 2019.

[46] C. Ji, Z. Wu, X. Wu, J. Wang, J. Gou, Z. Huang, H. Zhou, W. Yao and Y. Jiang, "Al-doped VO2 films as smart window coatings: reduced phase transition temperature and improved thermochromic performance," *Solar Energy Materials and Solar Cells*, vol. 176, pp. 174-180, 2018.

[47] X. Zhao, X. Hu, J. Sun, Q. You, H. Xu, W. Liu, ... and X. Jiang, "VO2-based composite films with exemplary thermochromic and photochromic performance," *Journal of Applied Physics*, vol. 128, no. 18, p. 185107, 2020.

[48] X. P. Zhao, S. A. Mofid, T. Gao, G. Tan, B. P. Jelle, X. B. Yin and R. G. Yang, "Durability-enhanced vanadium dioxide thermochromic film for smart windows," *Materials Today Physics*, vol. 13, p. 100205, 2020.

[49] Y. Cui, Y. Ke, C. Liu, Z. Chen, N. Wang, L. Zhang, ... and Y. Long, "Thermochromic VO2 for energy-efficient smart windows," *Joule*, vol. 2, no. 9, pp. 1707-1746, 2018.

[50] B. Li, S. Tian, Z. Wang, B. Liu, X. Gong and X. Zhao, "Thermochromic Ta Doped VO2 Films: Enhanced Luminous Transmittance, Significantly Depressed Phase Transition Temperature and Hysteresis Width," *Applied Surface Science*, vol. 568, p. 150959, 2021.

[51] R. W. G. Hunt, *The reproduction of colour*, 6 ed., M. A. Kriss, Ed. West Sussex: John Wiley & Sons, 2004, pp. 678, 679.

[52] National Renewable Energy Laboratory. *Reference air mass 1.5 spectra* [Online]. Available: https://www.nrel.gov/grid/solar-resource/spectra-am1.5.html. [Accessed 5 February 2023].

[53] O. Gunes, C. Koughia, C. Zhang, G. Belev, S. J. Wen, Q. Yang and S. O. Kasap, "Self-heating-induced electrical and optical switching in high-quality VO2 films controlled with current pulses," *Journal of Materials Science: Materials in Electronics*, vol. 32, no. 19, pp. 24285-24295, 2021.

[54] J. Sang, T. Zheng, L. Xu, X. Zhou, S. Tian, J. Sun, ... and Y. Liu, "Modulating the metal-insulator transition in VO2/Al2O3 (001) thin films by grain size and lattice strain," *Journal of Alloys and Compounds*, vol. 876, p. 160208, 2021.

[55] T. H. Yang, R. Aggarwal, A. Gupta, H. Zhou, R. J. Narayan and J. Narayan, "Semiconductor-metal transition characteristics of VO 2 thin films grown on c-and r-sapphire substrates," *Journal of Applied Physics*, vol. 107, no. 5, p. 053514, 2010.

[56] J. Yoon, C. Park, S. Park, B. S. Mun and H. Ju, "Correlation between surface morphology and electrical properties of VO2 films grown by direct thermal oxidation method," *Applied Surface Science*, vol. 353, pp. 1082-1086, 2015.

[57] C. Y. Kang, Z. F. Wei, C. Zhang, S. S. Liang, C. C. Geng, J. B. Wu, ... and M. Li, "Evolution of polymorph and photoelectric properties of VO2 thin films with substrate temperature," *Journal of Alloys and Compounds*, vol. 803, pp. 394-400, 2019.

6. Synthesis, Structure and Optical Properties of High-Quality VO_2 Thin Films Grown on Silicon, Quartz and Sapphire Substrates by High Temperature Magnetron Sputtering: Properties Through the Transition Temperature[5]

6.1 Abstract

VO_2 thin films were deposited on silicon (100), quartz, and r-cut sapphire substrates by DC reactive magnetron sputtering at 650 °C. The thin films were characterized by Raman spectroscopy and imaging, scanning electron microscopy (SEM), x-ray photoelectron spectroscopy (XPS), x-ray diffraction (XRD), energy dispersive x-ray spectroscopy (EDS), and transmission electron microscopy (TEM). The optical transmittance and hence the insulator-to-metal transition (IMT) and metal-to-insulator transition (MIT) were characterized as a function of temperature. The effects of substrate material on VO_2 thin film's growth, microstructure, stoichiometry and optical properties were investigated. The results show that the as-deposited VO_2 thin films on Si, quartz, and sapphire all show a near-zero IR transmission in switched metallic phase; especially VO_2 thin film grown on sapphire shows superior IMT characteristics compared with previously published works on thin VO_2 films, and very close to its bulk single-crystal form, which is probably due to the significantly reduced imperfections in the film and the interface, and especially the highly preferred growth with similar paralleled grain orientation of VO_2 on sapphire arising from both the high deposition temperature and epitaxial growth. The spectral transmittance of the films on quartz and sapphire substrates was analyzed to extract the optical constants n and K as a function of wavelength. No significant difference between optical properties could be observed for films deposited on quartz and sapphire substrates indicating that the differences in microstructure of these films play a minor role in their optical properties. n and K spectra are, in general, in agreement with previously reported works. The absorption coefficient versus photon energy characteristics indicate that VO_2 in the insulating phase possesses a direct bandgap at 2.6 eV and an indirect

[5] This paper was published as: Chunzi Zhang, Cyril Koughia, Ozan Güneş¸ Jun Luo, Nazmul Hossain, Yuanshi Li, Xiaoyu Cui, Shi-Jie Wen, Rick Wong, Qiaoqin Yang, Safa Kasap, "Synthesis, structure and optical properties of high-quality VO2 thin films grown on silicon, quartz and sapphire substrates by high temperature magnetron sputtering: Properties through the transition temperature," *Journal of Alloys and Compounds*, vol. 848, 156323, 2020. doi.org/10.1016/j.jallcom.2020.156323.

bandgap of 0.52 eV. Raman imaging was used to map the phase mixture of various regions of the film at micron scale (1.2 mm × 1.2 mm) during heating and cooling scans through the IMT and MIT. The dependence of the integrated Raman intensities at 220 cm^{-1} and 600 cm^{-1} on the temperature shows an excellent correlation with the optical transmittance through the IMT and MIT, both during heating and cooling scans. It is shown that the transformation occurs by the growth of one phase at the expense of the other and, in the IMT/MIT region, both phases coexist.

6.2 Introduction

Vanadium dioxide (VO_2) has been widely studied for applications in optical switches, sensors, smart windows, and optical memory devices [1–4]. Potential applications could be also found in neuromorphic computing materials and metamaterials [5,6]. The primary reason for its importance in electronics and photonics is its pronounced insulator-to-metal transition (IMT) (or MIT, metal-to-insulator transition) between the insulator (semiconductor) and metallic phases, which is around 67 °C (340 K), and easily accessible. For example, recently very fast RF switches have been demonstrated in which fast and local resistive microheaters embedded in the device have enabled switching speeds in the gigahertz range (up to 20 GHz) [7]. During IMT, the crystal undergoes an abrupt phase transformation from a low temperature monoclinic phase to a high-temperature tetragonal phase. Up to now, a variety of methods have been employed to prepare VO_2 thin films [8–15]. Many applications require a sharp hysteresis loop, large transition contrast and large resistance drop, all of which are considered to be desirable characteristics for an MIT material. However, the issue of phase inhomogeneity induced by non-stoichiometry and interfacial mismatch with the substrate material have significantly limited their potential applications by rendering a broad hysteresis loop and low transition contrast, which are found to be strongly dependent on the deposition process parameters and the substrate material [16]. There has been a considerable amount of research performed to date to improve both the stoichiometry and crystallinity by studying the effects of substrate temperature, pressure, doping elements, co-sputtering, thickness and substrate material [17–30]. Various substrate materials such as silicon (Si), quartz (SiO_2), sapphire (Al_2O_3), titanium dioxide (TiO_2), and magnesium fluoride (MgF_2) have been explored to control both of the interfacial strain and transition temperature [27,31–38]; even lithographic effects have been studied [39]. Of particular interest is the recent work by Huang

et al. [30] where the authors prepared W-doped VO_2 thin films on quartz substrates by magnetron sputtering (and post annealing at a high temperature) and demonstrated that they could lower the IMT temperature down to 39.6 °C (on heating), and at the same time obtain a temperature hysteresis width ΔH of 4.3 °C. ΔH is usually defined as the observed temperature difference in the phase transformation during cooling and heating scans, where the temperature of the transformation is the half point in the optical transmittance; one of the most commonly measured properties in studying the VO_2 phase transformation. Creeden et al. [40] have recently been able to grow high-quality epitaxial films by DC pulsed magnetron sputtering on c-cut sapphire and titanium dioxide. The reflectance of the film was studied and heating and cooling curves through the insulator-metal-insulator (IMI) transitions almost overlap, indicating negligible ΔH. The film exhibited near-single-crystal characteristics. In another recent study, B-doping has lowered the transition temperature of pulsed-laser-deposited VO_2 films at a rate 31.5 C/at. % B, the highest rate reported [41]. While the modification of the transition temperature is of interest, there is also much interest in obtaining a very narrow transition hysteresis ΔH.

This work focuses on the growth and characteristics of VO_2 thin films on three different substrates of interest, silicon, quartz and sapphire crystalline substrates, by magnetron sputtering at a high deposition temperature of 650 °C, which have not been fully addressed in the literature. Comprehensive studies of their structural and optical properties (dispersion characteristics of optical properties n, K) have not yet been reported [42–45]. Although high-temperature depositions have been reported using different vacuum deposition techniques such as pulsed laser deposition (PLD), metal-organic chemical vapor deposition (MOCVD) or ion beam assisted deposition [28,46–49], their structural and optical properties are very limited in the published literature. The work done by Kovacs [28] on the other hand is encouraging in that the films deposited by PLD at 630 °C were not only epitaxial but exhibited a sharp IMI in the electrical conductivity (the optical properties were not reported). In this work, we have examined the structural and optical properties of a range of VO_2 thin films deposited by DC reactive magnetron sputtering onto crystalline silicon, quartz and sapphire substrates at 650 °C towards obtaining a sharp IMT transition with narrow hysteresis in the optical transmission characteristics, that is, towards enhancing the optical properties. We have also extracted the dispersion of the optical constants of these films. The study of the characteristics of VO_2 thin films on Si is due to the

interest in integrating VO_2 with Si-based microelectronics for various device applications. The structural studies involved Raman scattering, scanning electron microscopy (SEM), x-ray diffraction (XRD), energy dispersive x-ray spectroscopy (EDS), X-ray photoelectron spectroscopy (XPS), high resolution transmission electron microscopy (HRTEM) and selected area electron diffraction (SAED). The results clearly show that the r-cut sapphire substrate is very effective in facilitating near-epitaxial growth of VO_2 as it reduces the structural mismatch at the sapphire-VO_2 interface, and the thin films grown on sapphire have near-epitaxial structure. Further, VO_2 thin films grown on sapphire substrates exhibit superior IMT characteristics compared with previous published work on sputtered VO_2 thin films on sapphire, and very close to that for VO_2 single-crystals. Interfacial characterization and optical property characterization have been conducted to elucidate the mechanism. Our results in this work clearly show that it is possible to use magnetron sputtering at a high substrate temperature of 650 °C and other appropriate deposition parameters to achieve near epitaxial growth of VO_2 thin films on r-cut sapphire with a very sharp IMI transition characteristic.

6.3 Experimental Procedure

Substrates of Si (100), quartz, and r-cut sapphire were first ultrasonically cleaned in ethanol. After cleaning, VO_2 thin films were deposited on the Si, quartz, and r-cut sapphire substrates by DC reactive magnetron sputtering. A high purity vanadium target (99.95%) was used. During deposition, the argon (Ar) and oxygen (O_2) gas flow rates were kept at 100 and 1.3 SCCM, respectively. The deposition conditions are listed in Table 6.1. The thickness of the VO_2 thin films as measured on the SEM are in the approximately range 140-185 nm. After deposition, the structural properties of these films were investigated by Raman spectroscopy (Renishaw Invia™ Reflex Raman Microscope), scanning electron microscopy (Hitachi SU-8010 SEM), X-ray photoelectron spectroscopy (XPS), and X-ray diffraction (Rigaku Ultima IV XRD), energy dispersive X-ray spectroscopy (EDS), and transmission electron microscopy (TEM). The optical transmission was measured using a Lambda 900 Perkin-Elmer spectrophotometer in the wavelength range of 350-2500 nm. The VO_2-film/substrate sample was stationed on a custom designed heating platform (with an Omega® CN16Pt-330 PID temperature controller), the temperature of which could be controlled to within 0.3 °C. The spectral transmittance $\tilde{T}(\lambda)$ of

films on quartz and sapphire substrates was analyzed by using the transmittance equation as a function of wavelength that accounts for light interference and absorption in a thin film on a thick transparent substrate as formulated by Manifacier et al. [50]. The results of the latter analysis lead to the optical constant $n = n(\lambda)$ and $K = K(\lambda)$, which were then compared with those values in the literature. The wavelength dependence of the extinction coefficient $K(\lambda)$was used to obtain the absorption coefficient $\alpha(h\nu)$.

For Raman imaging studies, Renishaw Invia™ Reflex Raman Microscope was used. The sample was mounted on a temperature-controlled platform whose temperature could be controlled to within ± 0.3 °C, and it could be heated or cooled (with a user defined *T*-*t* profile, e.g., ramp or hold or other *T*-*t* profile) as desired with the temperature controller. The Raman excitation was at 514.5 nm. The present system allowed pixelated Raman imaging from an area consisting of a square of 30 mm × 30 mm onto 25 × 25 pixels with each pixel being 1.2 mm × 1.2 mm. Thus, we could map various regions of the VO_2 film by following the evolution of the Raman spectra from a given region of the film at the micron scale. The extraction of the Raman images is described in Appendix B.

Table 6.1 Deposition conditions of VO_2 thin films on Si, quartz and sapphire.

Deposition process	**Temperature (°C)**	**Oxygen flow rate (SCCM)**	**Sputtering power (W)**	**Pressure (Pa)**	**Duration (h)**
A	650	1.33	90	1.33	2
B	650	1.33	95	1.33	2
C	650	1.33	100	1.33	2

6.4 Results and Discussion

6.4.1 Microstructure Characterization by Raman

In order to investigate the effect of the substrate material on the stoichiometry of VO_2, a vanadium deficient/oxygen rich environment was firstly used for deposition, then gradually decreased to regular level, as shown in Table 6.1. The microstructure is characterized by Raman

spectroscopy and the results are shown in Figure 6.1. It can be found that under oxygen rich conditions (deposition A), mixed phases of V_2O_5 and V_6O_{13} were developed on Si and quartz substrates, as shown in Figure 6.1 (a). The Raman peaks at 145, 195, 284, 303, 405, 483, 702 and 992 cm^{-1} and Raman peaks at 167, 845, 880, 936 and 1033 cm^{-1} signify the presence of V_2O_5 and V_6O_{13}, respectively [14]. In contrast, typical Raman peaks of VO_2 [14] can be observed on a film deposited on the sapphire substrate under the same conditions, in which peaks from impurity phases are not significant. With the sputtering power increased to the level indicated in the deposition B in Table 6.1, stoichiometric VO_2 can be found on both the Si and sapphire substrates, as shown in Figure 6.1 (b). VO_2 phase can also be observed in films on quartz substrates under the same conditions, however with minor second-phase peaks of V_6O_{13}. In Figure 6.1 (c), under the conditions of deposition C in Table 6.1, stoichiometric VO_2 thin films were achieved on all the Si, quartz and sapphire substrates. As such, it can be seen that the substrate material plays an important role in the microstructure development, thus affecting the resulting stoichiometry. The substrate effect arises mainly from the epitaxial relationships across the interface. In this work, sapphire is demonstrated to be favourable for VO_2 nucleation, followed by Si, and then quartz.

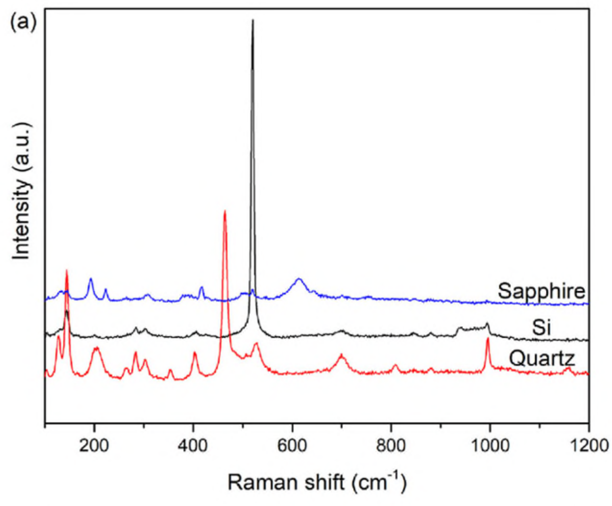
(a)
Intensity (a.u.)
Sapphire
Si
Quartz
200
400
600
800
1000
1200
Raman shift (cm-1)

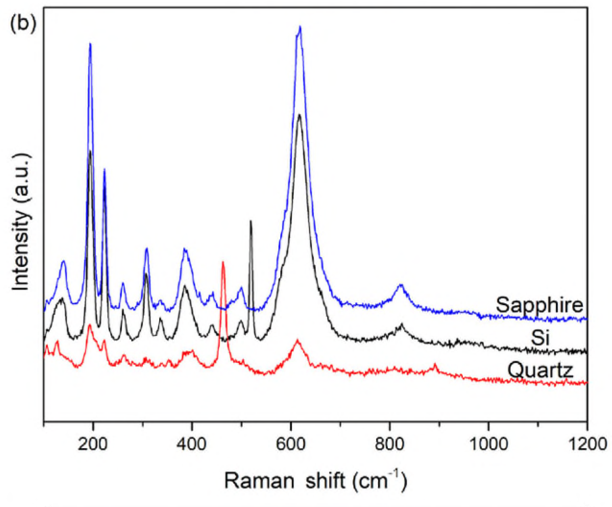
(b)
Intensity (a.u.)
Sapphire
Si
Quartz
200
400
600
800
1000
1200
Raman shift (cm-1)

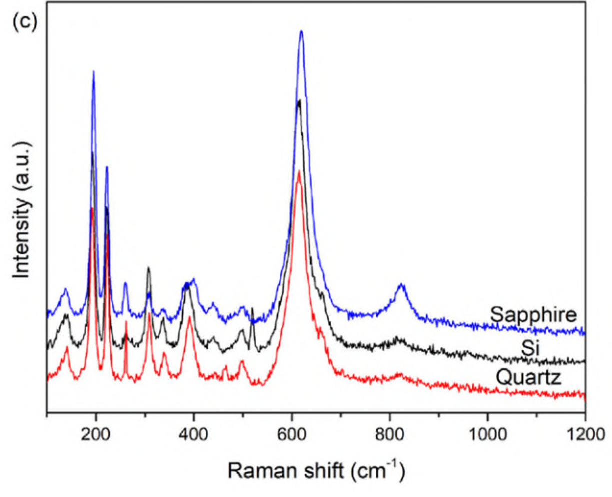
(c)
Intensity (a.u.)
Sapphire
Si
Quartz
200
400
600
800
1000
1200
Raman shift (cm-1)

Figure 6.1 Raman spectra of the as-deposited VO_2 thin films on Si, quartz and sapphire substrates with sputtering power of (a) 90 W, (b) 95 W, (c) 100 W.

6.4.2 Surface Morphology Characterization by SEM

The surface topography of these VO_2 thin films are shown in Figure 6.2. The VO_2 thin films grown on Si and quartz substrates show a typical polycrystalline structure with grain-like surface topography. The grain shape and size are quite similar for films on both Si and quartz. In contrast, the VO_2 thin film grown on sapphire surprisingly shows a flat surface, which is significantly different from the other two samples deposited under the same conditions. Significantly reduced roughness of VO_2 grown on sapphire can be also found in Kovacs's work [28]. This kind of structure is expected at high deposition temperature ($T_s/T_m > 0.4$), at Zone II growth [51]. For thin film materials, the melting temperature could be much lower than its bulk due to the large surface area and defects, so a substrate temperature of 650 °C might reach Zone II for producing thin films with significantly reduced roughness. Another explanation could be epitaxial growth of VO_2 on sapphire substrates [38], called (tri-) epitaxy-stabilized columnar growth as discussed in Kovacs's work [28].

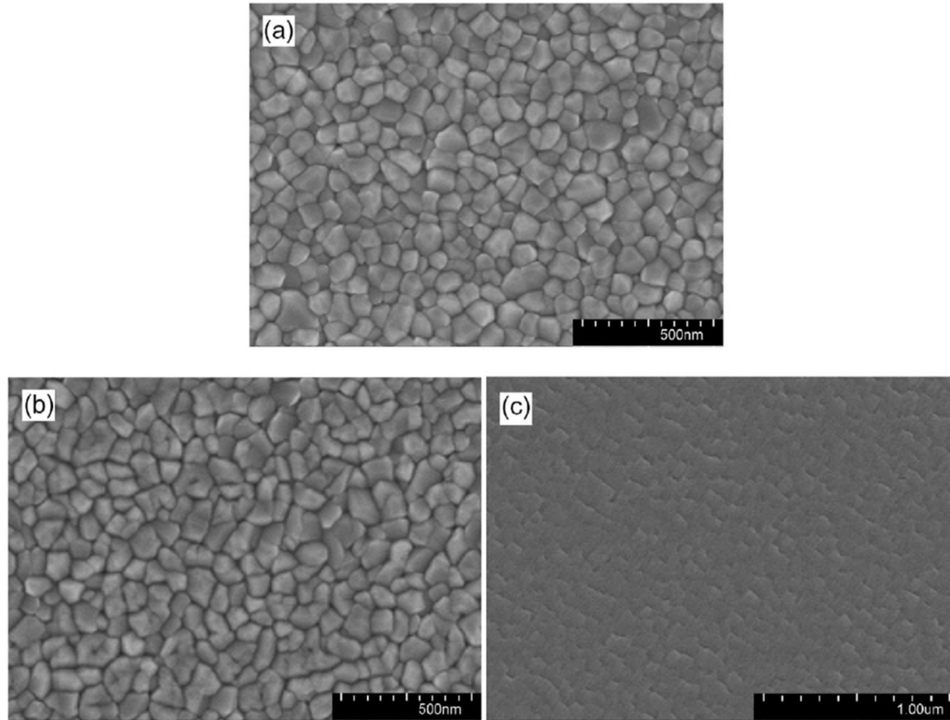

Figure 6.2 SEM images of VO_2 thin films deposited on (a) Si, (b) quartz, and (c) sapphire.

6.4.3 Chemical State Characterization by XPS

Figure 6.3 shows the x-ray photoemission data on as-deposited VO_2 thin films. These experiments have been done at the PGM beamline at the Canadian Light Source (the Canadian synchrotron) with a photon energy of 150 eV at room temperature. As shown in Figure 6.3, the samples prepared on different substrates are nearly stoichiometric. We cannot see a clear difference between the V (3d; 3p and 3s) and O (2p and 2s) states of VO_2 thin films deposited on Si (red curve), quartz (blue curve), and sapphire (black curve). One can conclude that the VO_2 deposition procedure on different substrates may cause a change of structures at the interface but not at the very surface.

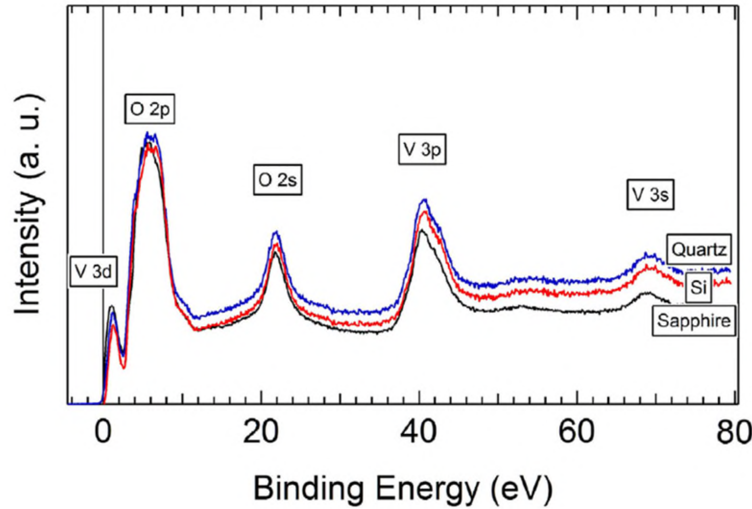

Figure 6.3 XPS spectra of the as-deposited VO_2 thin films on Si (red), quartz (blue), and sapphire (black). (For interpretation of the references to color in this figure legend, the reader is referred to the Web version of this article.)

6.4.4 Optical Properties Through Insulator-Metal-Insulator Transition

The transmission spectra of the as-deposited VO_2 thin films on different substrates are shown in Figure 6.4 (a) to (c) and (d) shows only the substrates. One can see that the transmission spectra of the VO_2 thin films on quartz and sapphire show similar features, which are different from the transmission spectra of VO_2 thin film on Si. As shown in Figure 6.4 (a), at room temperature (300 K), the transmittance of VO_2 thin film on Si increases with increasing wavelength and reaches 55% at the wavelength of 2500 nm. At a high temperature of 368 K (after MIT switching to the metal phase), the VO_2 thin film on Si shows a near-zero transmittance, comparable with our previous work [16]. However, as can be seen in Figure 6.4 (b) and (c), at the room temperature, the transmittances of VO_2 thin films on quartz and sapphire increase and then decrease over the visible range and increase again with wavelength up to 1500 nm. Beyond 1500 nm the transmittances slightly decrease and then increase again until they reach 45% and 52% for VO_2 thin films on quartz and sapphire, respectively, at a wavelength of 2500 nm.

The comparison of the transmittances of these VO_2 thin films on different substrates, as shown in Figure 6.5, suggests that, at the room temperature, the transmittance of VO_2 thin film on

sapphire is always higher than those for films on quartz and Si for wavelengths less than 1600 nm. Over wavelengths beyond 1600 nm, the increases in the transmittance of VO_2 thin films on quartz and sapphire are not significant, while beyond 1000 nm the transmittance of the VO_2 thin film on Si continues to increase with wavelength and becomes the greatest at the wavelength of 2500 nm. At wavelengths less than 1000 nm, the Si substrate absorbs light as shown in Figure 6.4 (d), so there is no transmittance. In the switched metallic phase (368 K), the transmittance of the VO_2 thin film on sapphire is always higher than those of films on quartz and Si in the visible range and becomes near-zero for all thereafter. Further, it can be seen that the optical transition efficiency in the IR range for all reaches 40% due to the near-zero transmittance in the metallic phase. Among them, the transition efficiency of VO_2 thin film on sapphire reaches 50%, which is very promising for practical applications.

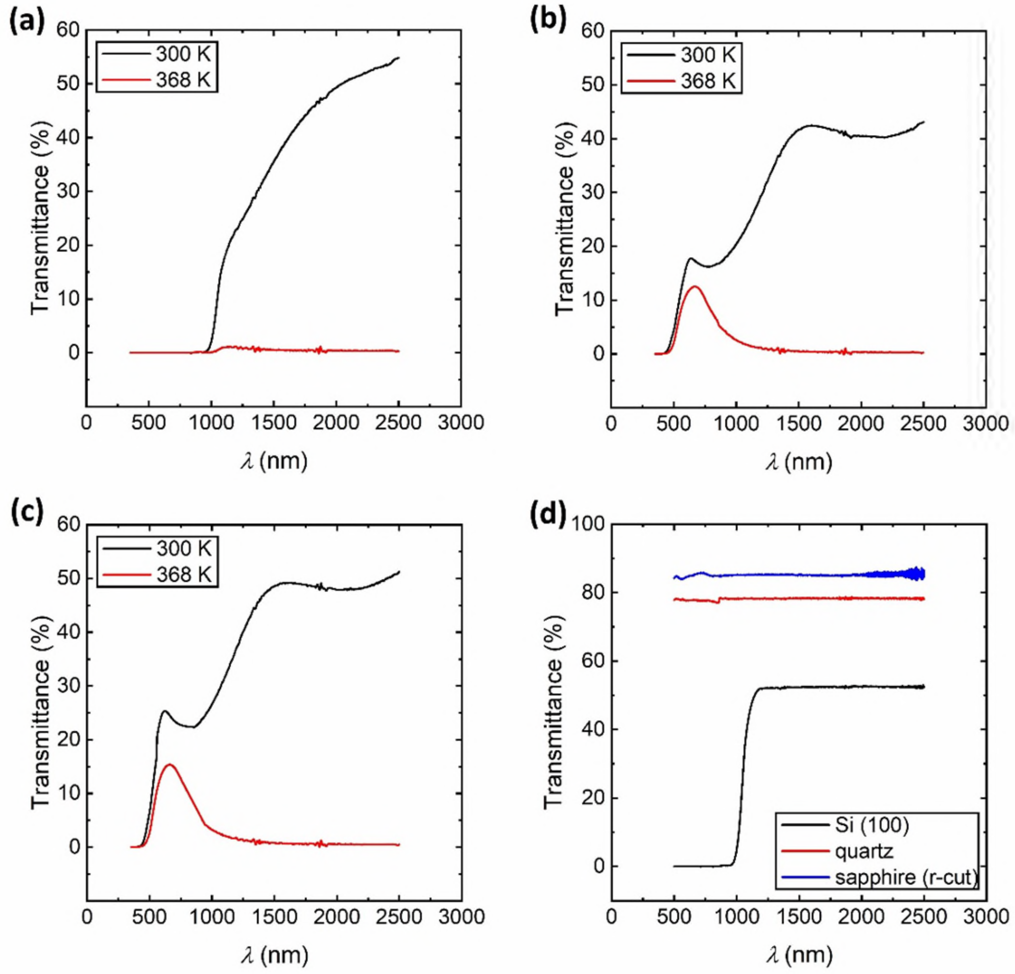

Figure 6.4 Optical transmittance of the as-deposited VO_2 thin films on (a) Si, (b) quartz, (c) sapphire, (d) optical transmittance of substrates.

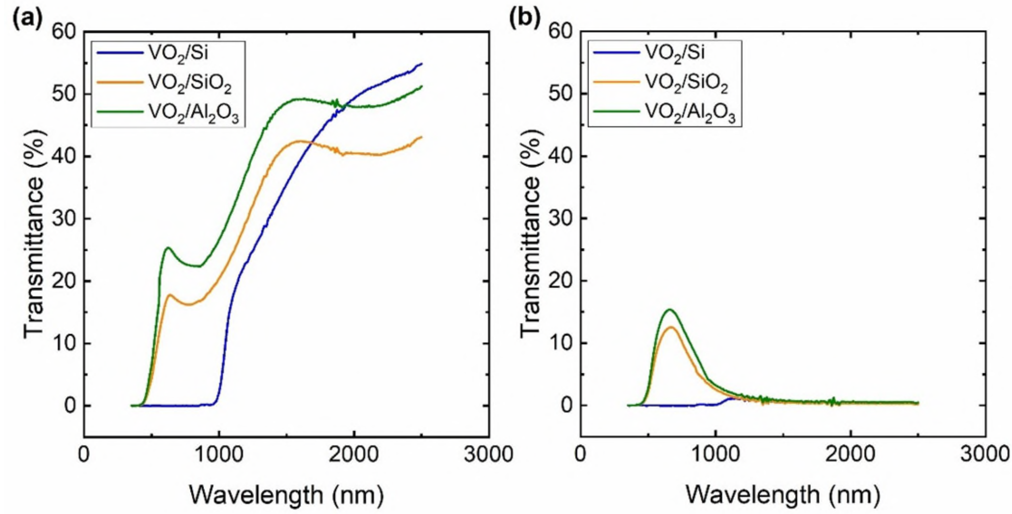

Figure 6.5 Optical transmittance of the as-deposited VO_2 thin films on Si, quartz and sapphire at (a) 300 K, (b) 368 K.

Thermal hysteresis loops in the transmittance of the thin films are shown in Figure 6.6, the experimental details can be found in our previous work [16]. It can be seen that the VO_2 thin films deposited on Si shows the highest transition efficiency of 56%, the ones on sapphire shows transition efficiency of 52%, and the ones on quartz shows the lowest value of 43%. Another important property is the width of the hysteresis (ΔH), which is defined as the temperature difference between the points corresponding to half the maximum transmittance during heating and cooling scans. It can be seen that the VO_2 thin films deposited on both Si and quartz exhibits quite similar hysteresis with a width of 6.5 K. In contrast, the VO_2 thin film on sapphire surprisingly shows a narrow hysteresis with ΔH of 2.1 K, as shown in Figure 6.6 (c). In addition to the high transition efficiency and low ΔH, the VO_2 thin film on sapphire also shows a transition temperature (T_t) of around 340 K, almost identical with its bulk material, suggesting that the film is structurally relaxed [36]. Similar thermal hysteresis loop at the wavelength of 1500 nm (IR range) is shown in Figure 6.6 (d) with narrow ΔH and T_t of around 340 K. On the other hand, VO_2 thin films deposited on Si and quartz show a depressed T_t of 335 K. The optical transmittance hysteresis of the VO_2 thin film on sapphire of this work is compared with published works with same VO_2 thin film- sapphire materials system, as shown in Figure 6.6 (e). It is worth to be noticed that compared with optical transmittance hysteresis through MIT published in Refs. [19,27,34], VO_2 thin film of this work shows near zero transmittance at the switched state and right at 340 K

transition temperature indicating better crystalline quality. Usually, the deviations of the transition temperature correlate with changes in the c-axis length (V-V distance), which have been associated with imperfection in the samples, such as strain, grain boundary states, defects, and non-stoichiometry. Therefore, in summary, the high transition efficiency, low ΔH and right T_t of VO_2 thin films on sapphire are all comparable to VO_2 single-crystals, indicating significantly reduced imperfections in both stoichiometry and microstructure in VO_2 thin films on sapphire.

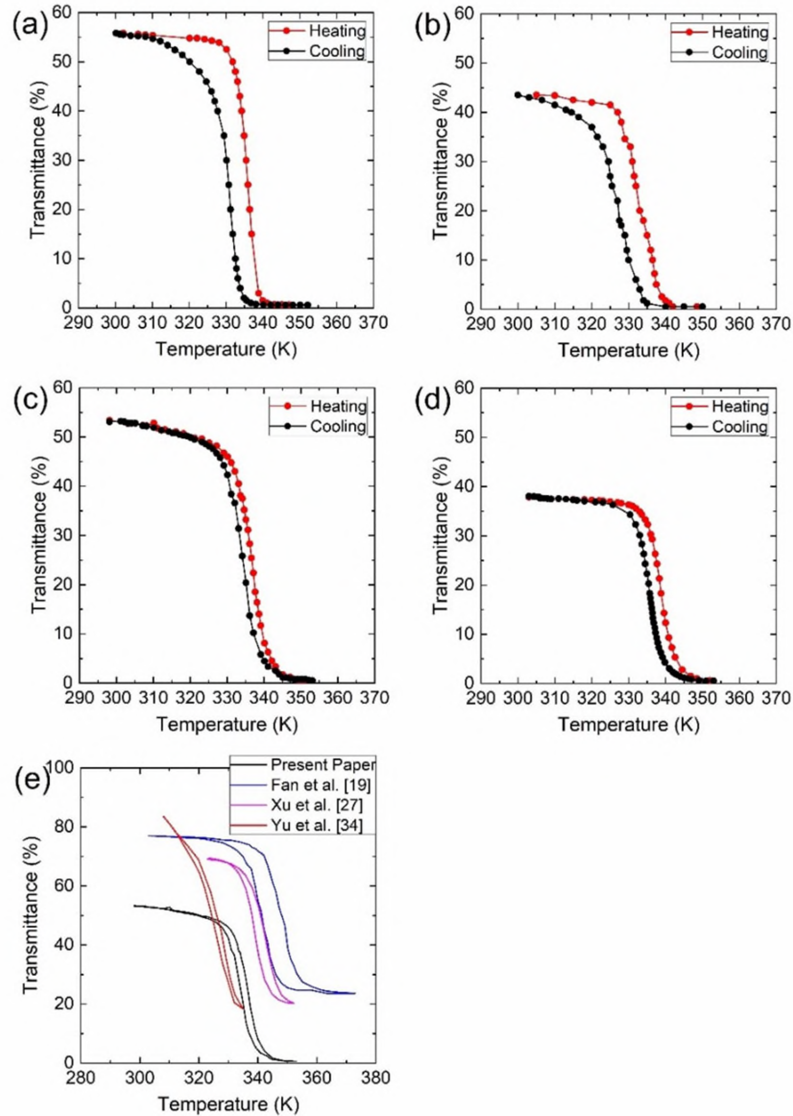

Figure 6.6 Optical transmittance of the as-deposited VO_2 thin films on (a) Si, (b) quartz, and (c) sapphire at a wavelength of 2500 nm, (d) on sapphire at a wavelength of 1500 nm under heating (red) and cooling (black), (e) optical transmittance hysteresis of the VO_2 thin film on sapphire

compared with reproduced results from published works [19,27,34] (Optical transmittance hysteresis of this work, [19] and [34] were taken at wavelength of 2500 nm, [27] was taken at 2000 nm.)

6.4.5 Optical Constants *n*, *K* and Bandgap

The transmittance spectra $\tilde{T}(\lambda)$ through thin films on thick transparent substrates in the presence of interference and extinction have been well-described in the literature as reviewed in by a number of authors [52,53] Most analyses involve the Swanepoel technique [1] but in the presence of strong absorption, the resulting transmittance is given by [50].

$$\tilde{T}(\lambda) = \frac{A(\lambda)x(\lambda)}{B(\lambda) - C(\lambda)x(\lambda) + D(\lambda)x(\lambda)^2} \tag{6.1}$$

Where,

$A(\lambda) = 16s[n^2+K^2]$

$B(\lambda) = [(n+1)^2+K^2]\,[(n+1)(n + s^2+K^2]$

$C(\lambda) = [(n^2-1 + K^2)\,(n^2s^2+K^2) - 2\,K^2(s^2+1)]2\cos(\phi) - K[2(n^2-s^2+K) + (s^2+1)(n^2-1+K^2)]2\sin(\phi)$

$D(\lambda) = [(n-1)^2+K^2]\,[(n-1)(n-s^2)+K^2]$;

$\phi = 4\pi nd/\lambda$;

$x = \exp(-\alpha d)$

$\alpha = 4\pi K/\lambda$

Figure 6.7 shows the experimental and calculated transmittance spectra for the VO_2 films on quartz and sapphire substrates in the semiconductor and metal phases. The calculations are based on bringing Equation (6.1) to match the experimental transmittance spectra by finding the best $n = n(\lambda)$, $K = K(\lambda)$ and d. The substrate refractive index $s = s(\lambda)$ was taken as constant and set to 1.77 for sapphire and 1.45 for quartz (slight variations do not significantly affect the calculations). In fact, as can be seen from Figure 6.7, the model and experimental transmittance can be made to agree over the whole wavelength range accessed by optimizing $n = n(\lambda)$, $K = K(\lambda)$ and d. (Reducing the root mean square deviation between measured and calculated transmittance.)

Figure 6.8 compares the real n and imaginary K part of the complex refractive index n^* as a function of wavelength with the published optical constant for VO_2. Further, we can use the extinction coefficient $K(\lambda)$ to calculate the absorption coefficient $\alpha(\lambda)$ as a function of photon energy $h\nu$ as shown in Figure 6.9 for both the semiconducting and metallic phases. One can clearly identify a direct and an indirect bandgap at ~ 2.6 and ~ 0.52 eV respectively. The absorption coefficient of the metallic phase at a wavelength of 2000 nm was previously determined from different thickness films as 3.1×10^7 m^{-1}. It can be seen that the present results in Figure 6.9, extracted from $\tilde{T}(\lambda)$ vs. λ data, point to an almost identical value.

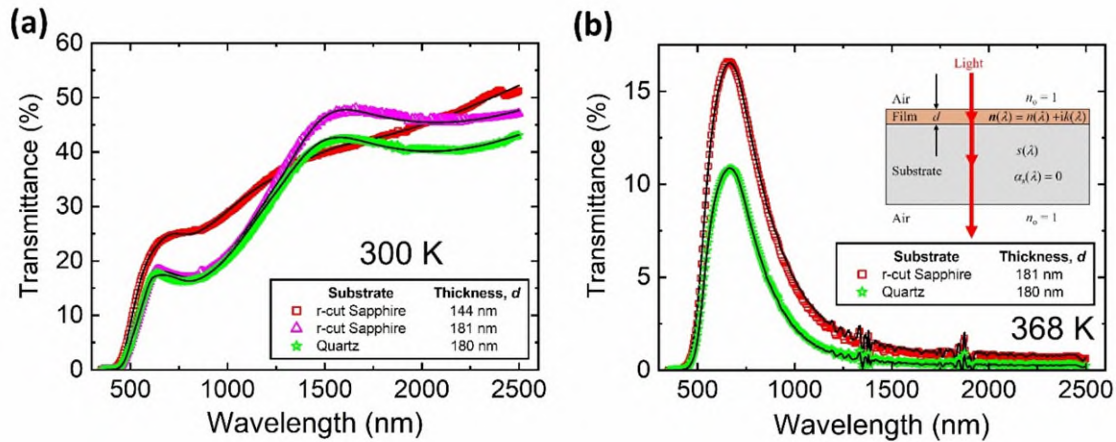

Figure 6.7 Comparison of model predictions with experimental data collected for VO_2 films of varying thicknesses on different substrates in the semiconducting (300 K) and metallic (368 K) phases. The inset to Figure 6.7 (a) shows the schematic of measurements. The film with thickness d has complex refractive index $n^*(\lambda) = n(\lambda) + jK(\lambda)$ where λ is the wavelength light and the absorption in the substrate is negligible ($\alpha_s(\lambda) = 0$). The reader should not be confused by the "noise" around 1380 nm, 1870 nm and 2700 nm, which is an artifact appearing most likely from IR absorption of water vapor.

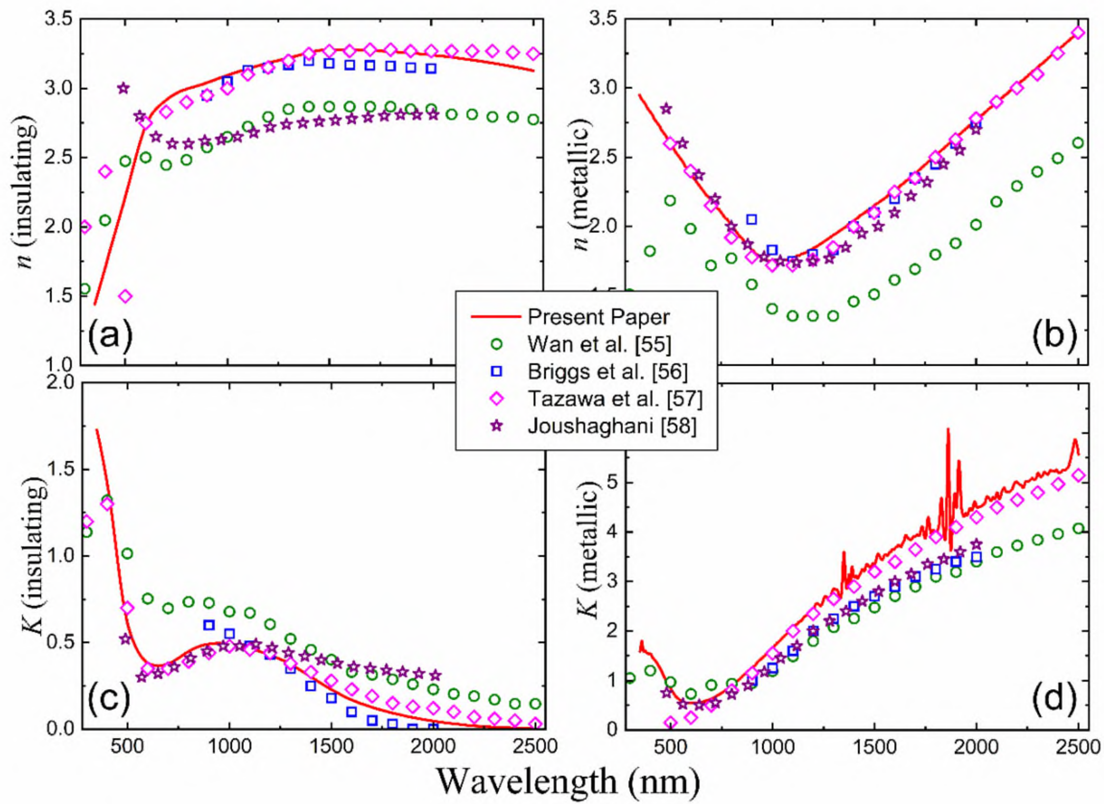

Figure 6.8 Real (n) and imaginary (K) parts of complex refractive index n^* of VO_2 measured in the semiconducting phase (at 300 K) and metallic phase at (368 K). The plots compare present data with previously data extracted from Refs. [55,58].

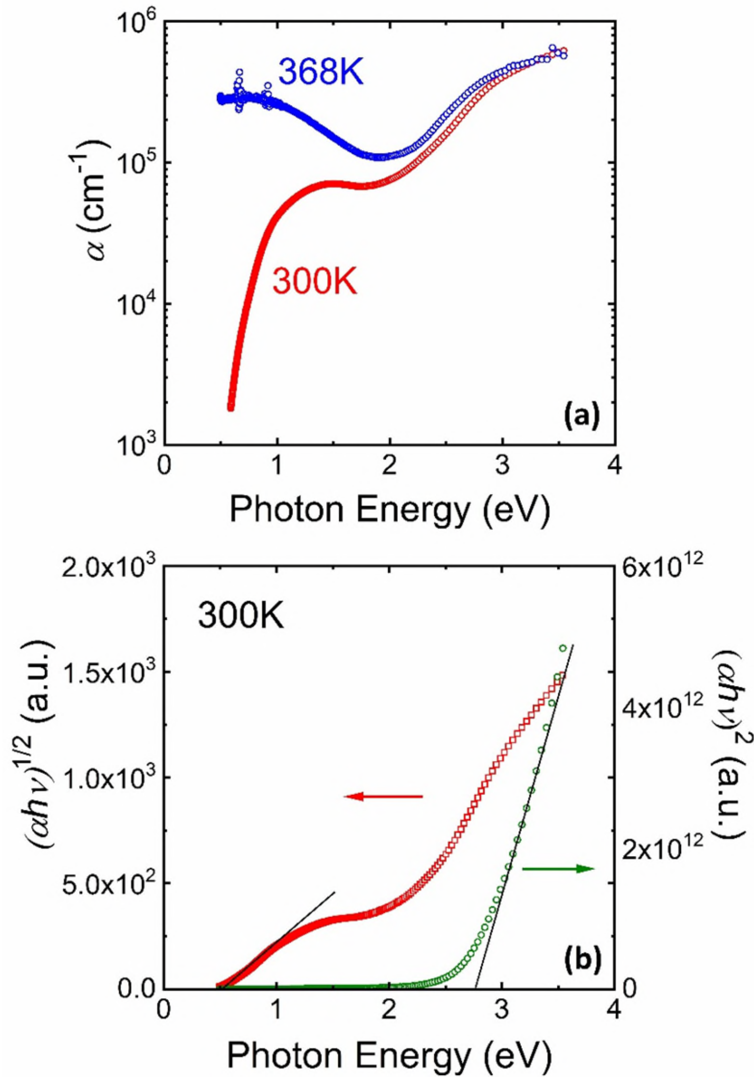

Figure 6.9 (a) Comparison of optical absorption coefficients of VO_2 films measured in semiconducting (300 K) and metallic (368 K) phases. (b) The corresponding plots for indirect ($\alpha(h\nu)^{1/2}$) and direct ($\alpha(h\nu)^2$) optical band gaps for semiconducting state[6]. One indirect optical bandgap at ~ 0.52 eV and one direct bandgap at ~ 2.6 eV is observed. Straight lines are guides to the eye to illustrate the direct and indirect theoretical predictions.

[6] In the published paper, Figure 6.9 (b) is plotted as $\alpha^{1/2}$ and α^2 vs. photon energy to obtain indirect and direct bandgaps, respectively. However, this does not affect the prediction of the bandgaps. The uncertainty of the bandgap values may be considered within ± 0.05 eV.

The optical properties of the films on quartz and sapphire substrates were extracted from the transmittance spectra as described in this section. The theoretical model based on Equation (6.1) as three variables to optimize, n, K and d to match the equation to the experimental data. There are several facts that provide further confirmation of the analysis. First is that the thickness d of each film was very close to that determined from SEM images. Secondly, the same optical constants are generated with different thickness films. Third, the values are in general agreement with those reported for VO_2 films in the literature. Because of its insulator-metal phase transition, its optical properties have been studied previously and there is noticeable scatter between the data of different researchers. More detailed analysis of refractive index n in Figure 6.8 (a) shows quite high values compared to those published in [57], for films deposited using magnetron sputtering and [56] employing pulsed laser deposition. Our values of n exceeds those from [55] for magnetron sputtering and [58] for RF sputtering implying higher optical and probably physical density of material. The latter conclusion on the high-quality VO_2 films in this work is supported by Figure 6.8 (c) demonstrating low values of extinction coefficient K. For metallic phase we have used the values of n close to those published in [57] to extract K, which again lie on the high-end of the published data (Figure 6.8 (c)).

Figure 6.9 shows the absorption coefficient as a function of photon energy in both phases. We notice the comparable magnitudes of α for the metallic and semiconducting phases at high photon energies. This is due to the strong interband absorption in the semiconducting phase. According to Refs. [59,60], the absorption in this spectral range is connected with transitions between 2p oxygen and 3d vanadium states which are virtually not affected by MIT. Figure 6.9 (b) shows that this absorption in semiconducting phase may be interpreted in terms of a direct bandgap absorption ($\alpha^2 \propto (h\nu - E_g)$) at 2.6 eV correlating well with the results of [59,60]. Second, in the semiconducting phase we observe an indirect optical bandgap ($\alpha(h\nu)^{1/2} \propto (h\nu - E_g)$) at 0.52 eV. This lower energy bandgap has been reported previously and is usually connected with the splitting of 3d vanadium states.

6.4.6 Interface Characterization by XRD, EDS, and HRTEM

To better understand the relationship between the phase transition characteristic and microstructure, EDS, XRD and HRTEM were used to analyze the structural details. The XRD

result is shown in Figure 6.10, in which only VO_2 (011) peak can be found without any impurity peaks (the Al_2O_3 (400) peak is from the substrate). These structural and property enhancements probably arise from the epitaxial growth of VO_2 on sapphire. Figure 6.11 shows the EDS mapping and depth profile of the VO_2 film deposited on the sapphire substrate. It can be seen that the thickness of VO_2 film is 150 nm. The vanadium to oxygen ratio is quite constant in the film, indicating good stoichiometry, which confirms the previous hypothesis. At the top surface, there is a slight decrease in the vanadium to oxygen ratio, probably due to surface oxidation. TEM images taken from different locations of the VO_2 film grown on sapphire are shown in Figure 6.12 (a). It can be seen that at the VO_2/sapphire interface, only $1-2$ atomic layers can be found, indicating significantly reduced imperfections in the interface. In addition, these three images taken at different locations show the same crystal orientation, indicating highly paralleled growth with similar grain orientation in the VO_2 film along the film growth direction, which again confirms the hypothesis of the epitaxial growth of VO_2 on sapphire. Figure 6.12 (b) shows the SAED patterns taken from the VO_2 film, the interfacial area, and the sapphire substrate. Indexing of the SAED patterns show that the diffraction spots of VO_2 are from $[00\bar{2}]$, and the diffraction spots from the substrate correspond to $[\bar{1}101]$ of Al_2O_3, which indicates the epitaxial growth of VO_2. At the interface, the pattern shows two sets of lattices, representing single-crystal VO_2 and single-crystal Al_2O_3, respectively. So, we can conclude that the significantly enhanced phase transition property of the VO_2 film on sapphire substrate arises from reduced imperfections in the film/ substrate interface and film structure, which is due to the epitaxial growth of VO_2 on sapphire.

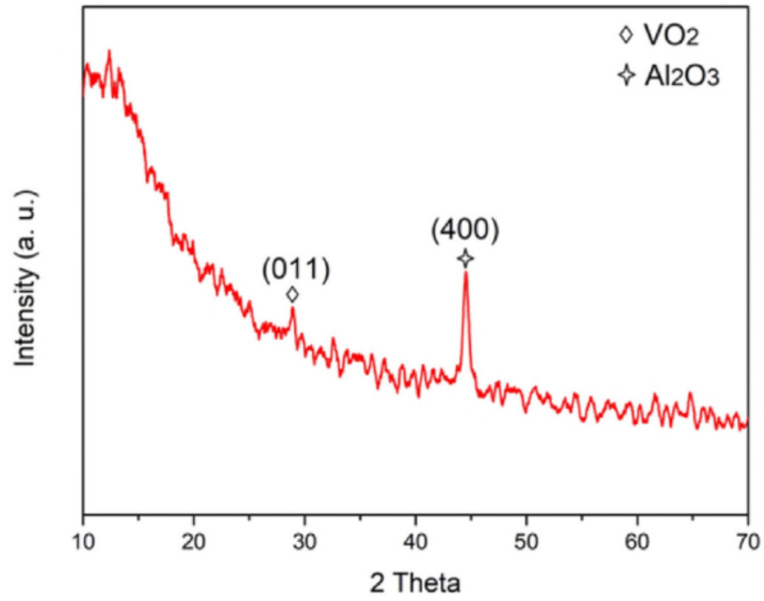

Figure 6.10 X-ray diffraction pattern of VO_2 thin film on sapphire.

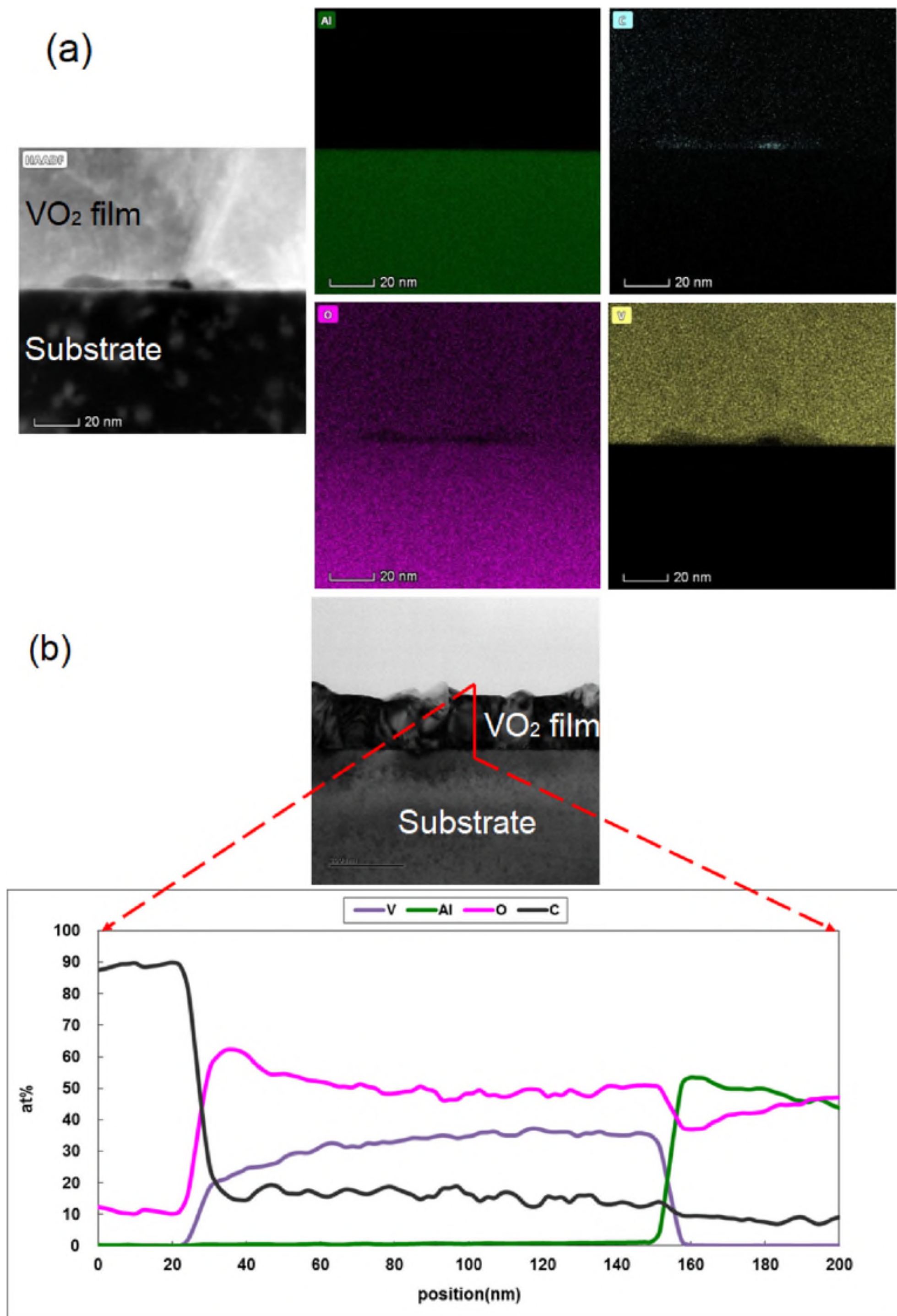

Figure 6.11 EDS (a) mapping and (b) depth profile of VO_2 thin film on sapphire substrate.

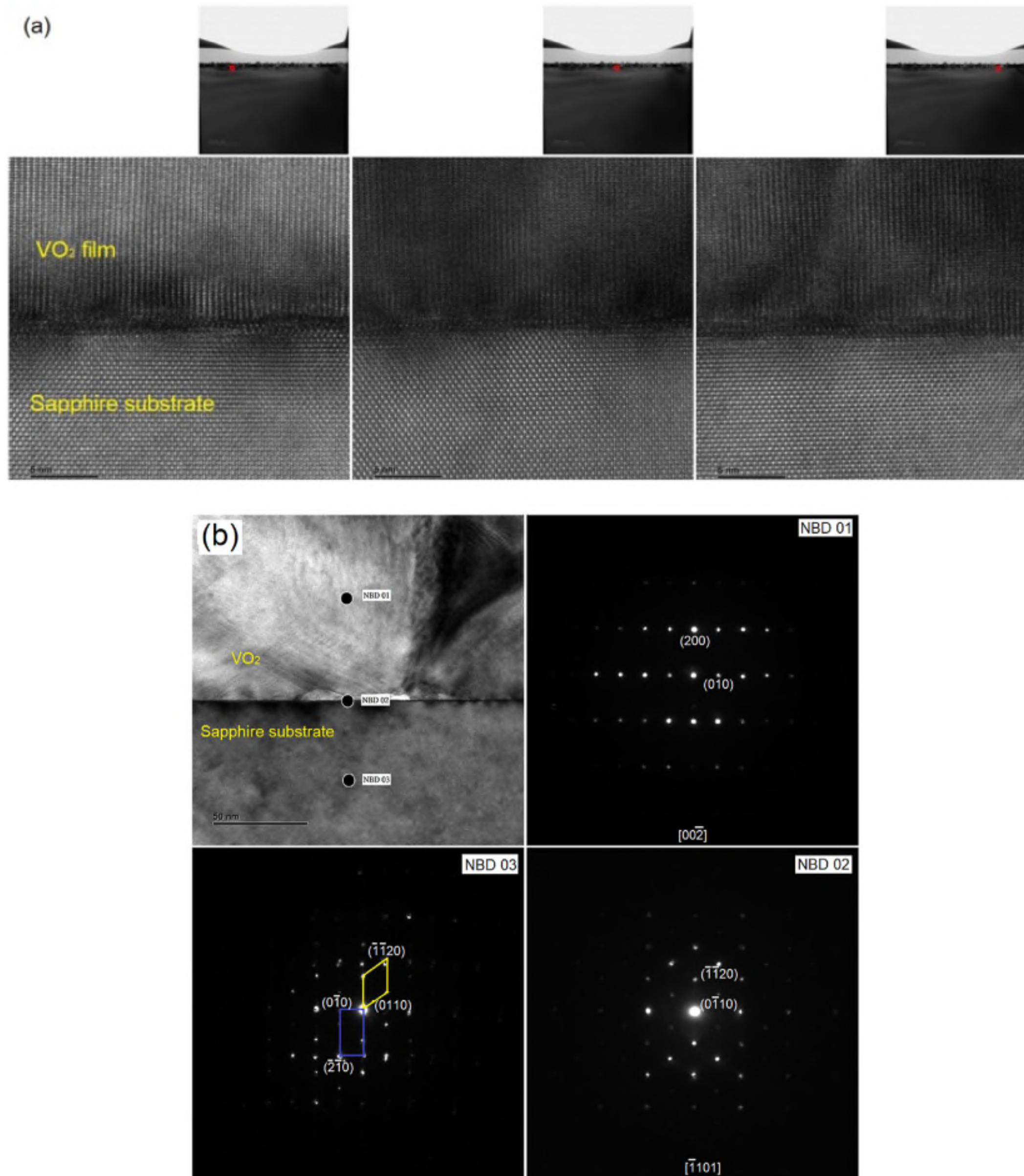

Figure 6.12 (a) HRTEM and (b) SAED patterns of VO_2 thin film on sapphire substrate.

6.4.7 Mapping of Phase Transition of VO_2 by Raman Spectroscopy

Figure 6.13 (a) and (b) show the results of the Raman spectra (around 613 $cm^{-1}$and 223 cm^{-1}) at different temperatures on the near-epitaxial VO_2 thin film. Figure 6.14 compares the temperature dependence of two dominant peaks in the Raman spectrum with the temperature dependence of optical transmittance; Figure 6.14 (a) is the optical transmittance and (b) and (c) are the integral Raman peaks at around 613 cm^{-1} and 223 cm^{-1}. The integral Raman signal

corresponds to the integration of the Raman peaks (as shown in Figure 6.13) from 525 to 750 cm^{-1} and from 210 to 245 cm^{-1} at corresponding temperatures. A good correlation can be seen between the optical transmittance and Raman integral peaks with obvious temperature hysteresis, as is typical for MIT in VO_2. Within this hysteresis, VO_2 is partially in insulating (semiconducting) and partially metallic states. Figure 6.13 and Figure 6.14 clearly demonstrate that these states may be identified by the presence or absence of a Raman signal and give rise to the possible mapping of VO_2 phase whose results are shown in Figure 6.15. The detailed procedure of mapping is explained in Appendix B. Figure 6.15 shows that the structure of VO_2 during IMT is very non-uniform, which agrees well with the results obtained by different methods [61,62]. This mapping also confirms the presence of a temperature hysteresis, which leads to the observation of distinct difference in the sample structure under heating and cooling, particularly striking at 338 K (65 °C).

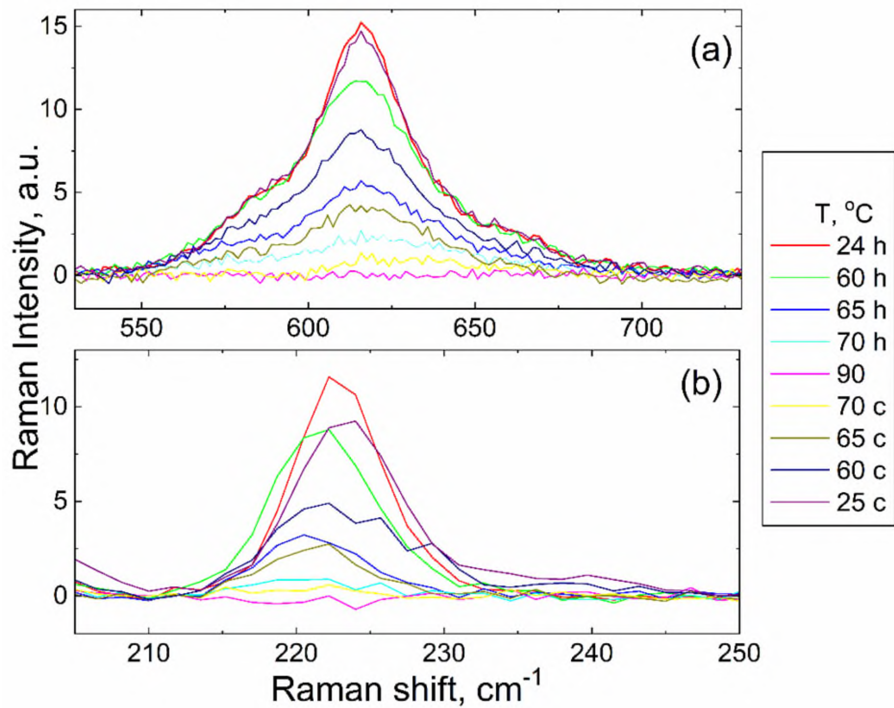

Figure 6.13 Raman spectra in the region of the peaks at around (a) 600 cm^{-1} and (b) 220 cm^{-1} at different temperatures under heating (marked "h" in the legend) and cooling (marked "c" in legend). The data collected over a square area of 25 × 25 pixels. The size of every pixel is 1.2 μm × 1.2 μm.

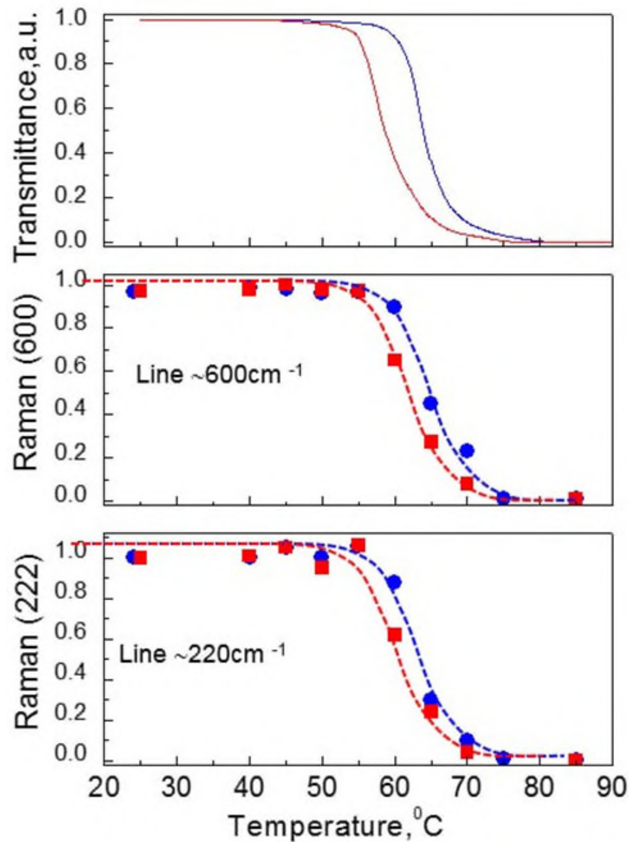

Figure 6.14 Temperature dependences of optical transmittance (a) and integral Raman intensities of peaks at around 600 cm^{-1} (b) and 220 cm^{-1} (c). Heating curves are in blue. Cooling curves are in red. Integral Raman intensities are found by the integration of Raman signal (as shown in Figure 6.13) from 525 to 750 cm^{-1} and from 210 to 245 cm^{-1} at corresponding temperatures, respectively. Dashed lines in (b) and (c) are guides to eye.

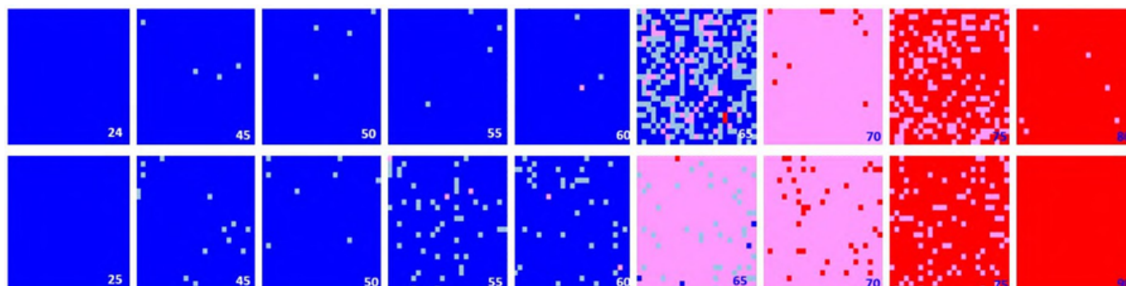

Figure 6.15 Maps of VO_2 conversion from the semiconducting to metallic phase under heating (upper row) and under cooling (lower row) derived from Raman scattering as explained in

Appendix B. The temperature increases from left to right (upper row) and decreases from right to left (lower row). The values of temperature are shown inside of the large image squares (bottom right corner). The size of every big square is 25 × 25 pixels. The size of every pixel is 1.2 mm × 1.2 mm. Blue color marks the pixels showing semiconducting properties. Red color marks the pixels with metallic properties. Pink and greyish colors mark mixed metal/semiconductor pixels with the dominance of metal or semiconductor, respectively. See Appendix B for the criteria used to identify the phase composition of the imaged VO_2 region. (For interpretation of the references to color in this figure legend, the reader is referred to the Web version of this article.)

6.5 Conclusions

In this work, VO_2 thin films have been successfully deposited on Si, quartz and sapphire substrates. The sapphire substrate has been demonstrated to be favorable for the nucleation and growth of high-quality, near-single-crystal VO_2 films, which show sharp insulator-metal transition characteristics. The as-deposited VO_2 thin films all show a near- zero IR transmission in the switched metallic phase and high transition efficiency. In particular, the VO_2 thin film grown on sapphire shows optical properties very close to its single-crystal form, with a transition efficiency of 52% at a wavelength of 2500 nm, a hysteresis width ΔH of 2.1 K (°C), and a MIT temperature of T_t of 340 K. SEM, TEM, XPS, XRD and EDS studies of the VO_2 films indicate significantly reduced imperfections in this film's stoichiometry, interface, and structure, which arises from the near-epitaxial growth of VO_2 on sapphire. The optical transmittance spectra were analyzed using the thin film transmittance equation of Manifacier and optimizing the complex refractive index $n^*(\lambda) = n(\lambda) + jK(\lambda)$ and the thickness d (three parameters only) to extract the optical constants $n(\lambda)$ and $K(\lambda)$ of the films on quartz and sapphire substrates both in the insulator (semiconductor) and metallic phases. These films on quartz and sapphire substrates have almost indistinguishable constants. The extinction coefficient was used to extract the absorption coefficient as a function of photon energy, α vs. $h\nu$, in both phases. In the semiconductor phase, the absorption coefficient clearly indicates features that correspond a direct bandgap at 2.6 eV and an indirect bandgap at 0.52 eV. Mapping of phase transition by Raman demonstrates non-uniform structural domains during the IMT and MIT.

6.6 References

[1] H. Zhou, J. Li, Y. Xin, G. Sun, S. Bao and P. Jin, "Optical and electrical switching properties of VO2 thin film on MgF2 (111) substrate," *Ceramics International*, vol. 42, pp. 7655-7663, 2016.

[2] A. Simo, K. Kaviyarasu, B. Mwakikunga, R. Madjoe, A. Gibaud and M. Maaza, "Phase transition study in strongly correlated VO2 based sensing systems," *Journal of Electron Spectroscopy and Related Phenomena*, vol. 216, pp. 23-32, 2017.

[3] D. Malarde, M. Powell, R. Quesada-Cabrera, R. Wilson, C. Carmalt, G. Sankar, I. Parkin and R. Palgrave, "Optimized Atmospheric-Pressure Chemical Vapor Deposition Thermochromic VO2 Thin Films for Intelligent Window Applications," *ACS Omega*, vol. 2, pp. 1040-1046, 2017.

[4] H. Coy, R. Cabrera, N. Sepulveda and F. Fernandez, "Optoelectronic and all-optical multiple memory states in vanadium dioxide," *Journal of Applied Physics*, vol. 108, p. 113115, 2010.

[5] X. Hong, D. Loy, P. Dananjaya, F. Tan, C. Ng and W. Lew, "Oxide-based RRAM Materials for Neuromorphic Computing," *Journal of Materials Science*, vol. 53, pp. 8720-8746, 2018.

[6] Z. Yang, C. Ko and S. Ramanathan, "Oxide electronics utilizing ultrafast metal-insulator transitions," *Annual Review of Materials Research*, vol. 1, pp. 337-367, 2011.

[7] J. Jiang, G. Chugunov and R. R. Mansour, "Fabrication and characterization of VO2-based series and parallel RF switches," in *2017 IEEE MTT-S International Microwave Symposium (IMS)*, 2017.

[8] H. Kim, H. You, R. Chiarello, H. Chang, T. Zhang and D. Lam, "Finite-size effect on the first-order metal-insulator transition in VO2 films grown by metal-organic chemical-vapor deposition," *Physical Review B*, vol. 47, pp. 12900-12907, 1993.

[9] D. Kim and H. Kwok, "Pulsed laser deposition of VO2 thin films," *Applied Physics Letters*, vol. 65, pp. 3188-3190, 1994.

[10] R. R. Kumar, B. Karunagaran, D. Mangalaraj, S. Narayandass, P. Manoravi and M. Joseph, "Characteristics of amorphous VO2 thin films prepared by pulsed laser deposition," *Journal of Materials Science*, vol. 39, pp. 2869-2871, 2004.

[11] M. Pan, H. Zhong, S. Wang, J. Liu, Z. Li, X. Chen and W. Lu, "Properties of VO2 thin film prepared with precursor VO(acac)2," *Journal of Crystal Growth*, vol. 265, pp. 121-126, 2004.

[12] S. Lu, L. Hou and F. Gan, "Preparation and optical properties of phase-change VO2 thin films," *Journal of Materials Science*, vol. 28, pp. 2169-2177, 1993.

[13] J. Leroy, A. Bessaudou, F. Cosset and A. Crunteanu, "Structural, electrical and optical properties of thermochromic VO2 thin films obtained by reactive electron beam evaporation," *Thin Solid Films*, vol. 520, pp. 4823-4825, 2012.

[14] C. Zhang, Q. Yang, C. Koughia, F. Ye, M. Sanayei, S. Wen and S. Kasap, "Characterization of vanadium oxide thin films with different stoichiometry using Raman spectroscopy," *Thin Solid Films*, vol. 620, pp. 64-69, 2016.

[15] M. Soltani, S. Bah, R. Karmouch, M. Gaidai and R. Vallee, "Phase transition in thermochromic VO2 coatings grown by ac dual magnetron cathode sputtering," *Journal of Materials Science: Materials in Electronics*, vol. 30, pp. 20043-20049, 2019.

[16] C. Zhang, C. Koughia, Y. Li, X. Cui, F. Ye, S. Shiri, M. Sanayei, S. Wen, Q. Yang and S. Kasap, "Near-zero IR transmission of VO2 thin films deposited on Si substrate," *Applied Surface Science*, vol. 440, pp. 415-420, 2018.

[17] D. Zhang, M. Zhu, Y. Liu, K. Yang, G. Liang, Z. Zheng, X. Cai and P. Fan, "High performance VO2 thin films growth by DC magnetron sputtering at low temperature for smart energy efficient window application," *Journal of Alloys and Compounds*, vol. 659, pp. 198-202, 2016.

[18] Y. Luo, F. Su, S. Pan, S. Xu, C. Zhang, J. Pan, J. Dai, P. Li and G. Li, "Terahertz conductivities of VO2 thin films grown under different sputtering gas pressures," *Journal of Alloys and Compounds*, vol. 655, pp. 442-447, 2016.

[19] L. Fan, Y. Wu, C. Si, C. Zou, Z. Qi, L. Li, G. Pan and Z. Wu, "Oxygen pressure dependent VO2 crystal film preparation and the interfacial epitaxial growth study," *Thin Solid Films*, vol. 520, pp. 6124-6129, 2012.

[20] N. Wang, M. Duchamp, R. Dunin-Borkowski, S. Liu, X. Zeng, X. Cao and Y. Long, "Terbium-doped VO2 thin films: Reduced phase transition temperature and largely enhanced luminous transmittance," *Langmuir*, vol. 32, pp. 759-764, 2016.

[21] D. Liu, H. Cheng, X. Xing, C. Zhang and W. Zheng, "Thermochromic properties of W-doped VO2 thin films deposited by aqueous sol-gel method for adaptive infrared stealth application," *Infrared Physics and Technology*, vol. 77, pp. 339-343, 2016.

[22] M. Wan, M. Xiong, N. Li, B. Liu, S. Wang, W. Ching and X. Zhao, "Observation of reduced phase transition temperature in N-doped thermochromic film of monoclinic VO2," *Applied Surface Science*, vol. 410, pp. 363-372, 2017.

[23] D. Gu, Z. Sun, X. Zhou, R. Guo, T. Wang and Y. Jiang, "Effect of yttrium-doping on the microstructures and semiconductor-metal phase transition characteristics of polycrystalline VO2 thin films," *Applied Surface Science*, vol. 359, pp. 819-825, 2015.

[24] S. Xu, H. Ma, S. Dai and Z. Jiang, "Study on optical and electrical switching properties and phase transition mechanism of Mo6+-doped vanadium dioxide thin films," *Journal of Materials Science*, vol. 39, pp. 489-493, 2004.

[25] C. Zhang, O. Gunes, Y. Li, X. Cui, M. Mohammadtaheri, S. Wen, R. Wong, Q. Yang and S. Kasap, "The effect of substrate biasing during DC magnetron sputtering on the quality of VO2 thin films and their insulator-metal transition behavior," *Materials*, vol. 12, p. 2160, 2019.

[26] J. Choi, H. Lee and K. Ko, "Oxidation potential control of VO2 thin films by metal oxide co-sputtering," *Journal of Materials Science*, vol. 49, pp. 5087-5092, 2014.

[27] G. Xu, P. Jin, M. Tazawa and K. Yoshimura, "Thickness dependence of optical properties of VO2 thin films epitaxially grown on sapphire (0001)," *Applied Surface Science*, vol. 244, pp. 449-452, 2005.

[28] G. Kovacs, D. Burger, I. Skorupa, H. Reuther, R. Heller and H. Schmidt, "Effect of the substrate on the insulator-metal transition of vanadium dioxide films," *Journal of Applied Physics*, vol. 109, p. 063708, 2011.

[29] A. Petraru, R. Droopad and H. Kohlstedt, "Characterization of VO2/ferroelectric thin film heterostructures deposited on various complex oxide single crystal substrates," *Journal of Vacuum Science & Technology A: Vacuum, Surfaces, and Films*, vol. 37, p. 021514, 2019.

[30] Z. Huang, Z. Wu, C. Ji, J. Dai, Z. Xiang, D. Wang, X. Dong and Y. Jiang, "Improvement of phase transition properties of magnetron sputtered W-doped VO2 films by post-annealing approach," *Journal of Materials Science: Materials in Electronics*, vol. 31, p. 4150, 2020.

[31] E. Radue, E. Crisman, L. Wang, S. Kittiwatanakul, J. Lu, S. Wolf, R. Wincheski, R. Lukaszew and I. Novikova, "Effect of a substrate-induced microstructure on the optical properties of the insulator-metal transition temperature in VO2 thin films," *Journal of Applied Physics*, vol. 113, p. 233104, 2013.

[32] Y. Cui and S. Ramanathan, "Substrate effects on metal-insulator transition characteristics of rf-sputtered epitaxial VO2 thin films," *Journal of Vacuum Science & Technology A: Vacuum, Surfaces, and Films*, vol. 29, p. 041502, 2011.

[33] Y. Zhao, J. Lee, Y. Zhu, M. Nazari, C. Chen, H. Wang, A. Bernussi, M. Holtz and Z. Fan, "Structural, electrical, and terahertz transmission properties of VO2 thin films grown on c-, r-, and m-plane sapphire substrates," *Journal of Applied Physics*, vol. 111, p. 053533, 2012.

[34] S. Yu, S. Wang, M. Lu and L. Zuo, "A metal-insulator transition study of VO2 thin films grown on sapphire substrates," *Journal of Applied Physics*, vol. 122, p. 235102, 2017.

[35] Y. Guo, Y. Zhang, L. Zhang, X. Lv, L. Wu, Y. Cao and L. Song, "Study of the phase transition properties and electronic band structures of VO2 thin films grown on different substrates," *Materials Research Express*, vol. 6, p. 026409, 2019.

[36] Y. Muraoka, Y. Ueda and Z. Hiroi, "Large modification of the metal–insulator transition temperature in strained VO2 films grown on TiO2 substrates," *Journal of Physics and Chemistry of Solids*, vol. 63, p. 965, 2002.

[37] K. Shibuya, J. Y. Tsutsumi, T. Hasegawa and A. Sawa, "Fabrication and Raman scattering study of epitaxial VO2 films on MgF2 (001) substrates," *Applied Physics Letters*, vol. 103, no. 2, p. 021604, 2013.

[38] T. H. Yang, R. Aggarwal, A. Gupta, H. Zhou, R. J. Narayan and J. Narayan, "Semiconductor-metal transition characteristics of VO 2 thin films grown on c-and r-sapphire substrates," *Journal of Applied Physics*, vol. 107, no. 5, p. 053514, 2010.

[39] H. Yuce, H. Alaboz, Y. Demirhan, M. Ozdemir, L. Ozyuzer and G. Aygun, "Investigation of electron beam lithography effects on metal–insulator transition behavior of vanadium dioxide," *Physica Scripta*, vol. 92, no. 11, p. 114007, 2017.

[40] J. A. Creeden, S. E. Madaras, D. B. Beringer, M. R. Beebe, I. Novikova and R. Lukaszew, "Structural and photoelectric properties of epitaxially grown vanadium dioxide thin films on c-plane sapphire and titanium dioxide," *Scientific Reports*, vol. 9, no. 1, pp. 1-9, 2019.

[41] T. Hajlaoui, N. Émond, C. Quirouette, B. L. Drogoff, J. Margot and M. Chaker, "Metal–insulator transition temperature of boron-doped VO2 thin films grown by reactive pulsed laser deposition," *Scripta Materialia*, vol. 177, p. 32, 2020.

[42] R. O. Dillon, K. Le and N. Ianno, "Thermochromic VO2 sputtered by control of a vanadium-oxygen emission ratio," *Thin Solid Films*, vol. 398, pp. 10-16, 2001.

[43] V. Sanphuang, N. Ghalichechian, N. K. Nahar and J. L. Volakis, "Reconfigurable THz filters with integrated micro-heater," in *2014 IEEE Antennas and Propagation Society International Symposium (APSURSI)*, 2014.

[44] I. G. Madiba, L. Kotsedi, B. D. Ngom, B. S. Khanyile and M. Maaza, "Effect of substrate temperature on thermochromic vanadium dioxide thin films sputtered from vanadium target," in *AIP Conference Proceedings*, 2018.

[45] J. K. Kana, J. M. Ndjaka, B. D. Ngom, A. Y. Fasasi, O. Nemraoui, R. Nemutudi, ... and M. Maaza, "High substrate temperature induced anomalous phase transition temperature shift in sputtered VO2 thin films," *Optical Materials*, vol. 32, no. 7, pp. 739-742, 2010.

[46] Z. A. Umar, N. Ahmed, R. Ahmed, M. Arshad, M. Anwar-Ul-Haq, T. Hussain and M. A. Baig, "Substrate temperature effects on the structural, compositional, and electrical properties of VO2 thin films deposited by pulsed laser deposition," *Surface and Interface Analysis*, vol. 50, no. 3, pp. 297-303, 2018.

[47] H. L. M. Chang, H. You, J. Guo and D. J. Lam, "Epitaxial TiO2 and VO2 films prepared by MOCVD," *Applied Surface Science*, vol. 48, pp. 12-18, 1991.

[48] E. E. Chain, "The influence of deposition temperature on the structure and optical properties of vanadium oxide films," *Journal of Vacuum Science & Technology A: Vacuum, Surfaces, and Films*, vol. 4, no. 3, pp. 432-435, 1986.

[49] A. Diallo, N. M. Ndiaye, B. D. Ngom, S. Khamlich, K. Talla, S. Ndiaye, ... and M. Maaza, "Effect of substrate temperature on the structure and the metal insulator transition in pulsed laser deposed V02\films on soda lime glass," *Journal of Optics*, vol. 44, no. 1, pp. 36-44, 2015.

[50] J. C. Manifacier, J. Gasiot and J. P. Fillard, "A simple method for the determination of the optical constants n, k and the thickness of a weakly absorbing thin film," *Journal of Physics E: Scientific Instruments*, vol. 9, no. 11, p. 1002, 1976.

[51] I. Petrov, P. B. Barna, L. Hultman and J. E. Greene, "Microstructural evolution during film growth," *Journal of Vacuum Science & Technology A: Vacuum, Surfaces, and Films*, vol. 21, no. 5, pp. S117-S128, 2003.

[52] J. Mistrik, S. Kasap, H. E. Ruda, C. Koughia and J. Singh, "Optical properties of electronic materials: fundamentals and characterization," in *Springer Handbook of Electronic and Photonic Materials, Springer Handbooks*, S. Kasap and P. Capper, Eds., Cham (Switzerland).

[53] S. Kasap, W. Tan, J. Singh and A. K. Ray, "Fundamental optical properties of materials," in *Optical Properties of Materials and Their Applications*, 2nd ed., J. Singh, Ed. West Sussex, UK, John Wiley & Sons Ltd., 2020.

[54] R. Swanepoel, "Determination of the thickness and optical constants of amorphous silicon," *Journal of Physics E: Scientific Instruments*, vol. 16, no. 12, p. 1214, 1983.

[55] C. Wan, Z. Zhang, D. Woolf, C. M. Hessel, J. Rensberg, J. M. Hensley, ... and M. A. Kats, "Optical properties of thin-film vanadium oxide from the visible," *Annalen der Physik*, vol. 531, no. 10, p. 1900188, 2019.

[56] R. M. Briggs, I. M. Pryce and H. A. Atwater, "Compact silicon photonic waveguide modulator based on the vanadium dioxide metal-insulator phase transition," *Optics Express*, vol. 18, no. 11, pp. 11192-11201, 2010.

[57] M. Tazawa, P. Jin and S. Tanemura, "Optical constants of V 1-x W x O 2 films," *Applied Optics*, vol. 37, no. 10, pp. 1858-1861, 1998.

[58] A. Joushaghani, "Micro- and Nano-Scale Optoelectronic Devices Using Vanadium Dioxide", Ph. D. Dissertation, Grad. Dept. Elect. & Comp. Eng., Univ. of Toronto, Toronto, ON, 2014.

[59] J. B. Goodenough, "The two components of the crystallographic transition in VO2," *Journal of Solid State Chemistry*, vol. 3, no. 4, pp. 490-500, 1971.

[60] H. W. Verleur, A. S. Barker Jr. and C. N. Berglund, "Optical properties of V O 2 between 0.25 and 5 eV," *Physical Review*, vol. 172, no. 3, p. 788, 1968.

[61] H. Asayesh-Ardakani, A. Nie, P. M. Marley, Y. Zhu, P. J. Phillips, S. Singh, ... and R. Shahbazian-Yassar, "Atomic origins of monoclinic-tetragonal (rutile) phase transition in doped VO2 nanowires," *Nano Letters*, vol. 15, no. 11, pp. 7179-7188, 2015.

[62] S. Zhang, J. Y. Chou and L. J. Lauhon, "Direct correlation of structural domain formation with the metal insulator transition in a VO2 nanobeam," *Nano Letters*, vol. 9, no. 12, pp. 4527-4532, 2009.

7. Topology of Conductive Clusters in Sputtered High-Quality VO_2 Thin Films on the Brink of Percolation Threshold During Insulator-to-Metal and Metal-to-Insulator Transitions[7]

7.1 Abstract

Electrical conductivity (σ) and optical transmittance of high-quality VO_2 thin films deposited by DC reactive magnetron sputtering on r-cut sapphire substrates (at 650 °C) have been measured simultaneously as a function of temperature by heating and cooling scans through the phase transition region. The partial concentration of the metallic phase (X_m) has been calculated from the optical transmittance, and the $\sigma(X_m)$ dependence has been analyzed through an insulator-to-metal transition (IMT) during heating and through a metal-to-insulator transition (MIT) during cooling. The results have shown to be consistent with the Efros–Shklovskii percolation theory, predicting the formation of two-dimensional infinite conductive cluster (ICC) during IMT and the preservation of three-dimensional ICC during MIT. The critical concentrations (X_c) corresponding to the appearance of ICC at IMT and the disappearance of ICC at MIT were found to be very different, 0.57 and 0.06, respectively. A mathematical model explaining very small X_c at MIT was developed. The dissimilarity of the ICC topology during IMT and MIT is connected with the appearance and disappearance of local mechanical stresses imminent in VO_2 phase transitions.

7.2 Introduction

In chemically pure stoichiometric monocrystalline vanadium dioxide (VO_2), a sharp insulator-to-metal transition (IMT) occurs close to a critical temperature (T_t) around 340 K. The high-temperature metallic phase has a tetragonal rutile structure with a symmetry space group P42/mnm (No. 136). During a metal-to-insulator transition (MIT), VO_2 is converted to a low-temperature insulator (more precisely, a semiconducting) phase, which leads to the monoclinic

[7] This paper was published as: Cyril Koughia, Ozan Gunes, Chunzi Zhang, Shi-Jie Wen, Rick Wong, Qiaoqin Yang, and Safa O. Kasap. Topology of conductive clusters in sputtered high-quality VO2 thin films on the brink of percolation threshold during insulator-to-metal and metal-to-insulator transitions. *Journal of Vacuum Science & Technology A: Vacuum, Surfaces, and Films*, vol. 38, no. 6, p. 063401, 2020. doi.org/10.1116/6.0000443.

distortion of the rutile structure. The unit cell doubles in size with the conversion of space symmetry to P21/c (No. 14). Subsequently, the electrical conductivity drops ~10^5 times. There are also dramatic changes in light absorption and refraction characteristics.

Unlike sharp IMT transitions in single-crystals, transitions in thin films spread over a certain temperature range, which depends on film deposition conditions. The backward MIT observed during cooling occurs at substantially lower temperatures. In some pioneering papers, the dispersion of IMT/MIT over temperatures, also known as the hysteresis of the IM/MI transition, was connected with the coexistence of metallic and semiconducting phases, where every phase could exist independently above and below $T_t = 340$ K. [1] A few years later, this coexistence of two phases was tentatively explained by the presence of mechanical strains between the film and the substrate and structural nonuniformities. [2] Recently, the investigations of the influence of strain on IMT and MIT in VO_2 has become a topical research and discussion forum. The strain is mostly induced by the choice of the substrate material, such as TiO_2 [3,4] or RuO_2 (to induce particularly massive strain) [5], as well as the thickness of the film and other factors. In one recent study, the IMT and MIT in VO_2 thin films sputtered on sapphire substrates were investigated by ellipsometry and AFM. [6] The film thickness was varied to modify the strain in the film to understand the interplay between electronic and structural changes through the IMT/MIT. In another recent study, different thickness VO_2 thin films were grown on a variety of substrates, and the IMT/MIT temperature was correlated with the strain along the c axis. [3,7] It is important to emphasize that experimental work to date shows that the single-crystal sapphire substrate is very effective in reducing the structural mismatch at the sapphire–VO_2 interface, thereby facilitating near-epitaxial VO_2 nucleation and growth leading to a near epitaxial VO_2 structure. There are various papers covering different aspects of VO_2 deposition on sapphire, some of which include near epitaxial growth as discussed in Refs. [8−16]. The VO_2 films reported in this work have been grown as near-epitaxial films on a sapphire substrate. Another common way to influence IMT and MIT is by doping. There are various papers in the literature dealing with a large variety of dopants; for example, most recently, it was shown that B-doping could be used to lower IMT significantly, approximately 31.5 °C per at. %B doping. [17]

It is well known that the IMT in VO_2 is an extremely fast process (with a transition time well below 10−12 s) which may be induced by temperature and/or electric field. [18] It is,

therefore, not surprising that today the IMT transition, especially in VO_2, is a flourishing field of applied research with a large number of publications. This material has been tested in smart windows, [19] optical memory devices [20], optical [21] and microwave switches [22], and sensors [23]. Other applications which are worth mentioning are in metamaterials, [24] neuromorphic computing materials [25], and oscillatory neural networks [26–30].

There are numerous methods of VO_2 deposition and here we mention just some of these, such as magnetron cathode sputtering reactive electron beam evaporation, [31] pulsed laser deposition, [32,33] metal-organic chemical-vapor deposition, [34] aqueous solgel method, [35] and many others [36–38]. Within these methods, there have been significant efforts to improve the VO_2 quality by studying the effects of substrate temperature, pressure, thickness, substrate bias, co-sputtering, and post-annealing with some recent examples in Refs. [39–43].

In the present paper, we simultaneously investigate electrical and optical properties of quasi epitaxial VO_2 thin films deposited onto r-cut sapphire substrates. On the same sample, we measure simultaneously the electrical conductivity and transmittance as a function of temperature from room temperature to above the IMT. We extract the partial concentration of the metallic phase (X_m) from experimental data of transmittance, and we investigate the dependence of electrical conductivity on X_m through IMT during heating and MIT during cooling. We show that the results are consistent with the Efros–Shklovskii (ES) percolation theory that predicts the formation of highly conductive clusters at IMT and the preservation of these clusters during MIT. We also show that the topology of the highly conductive clusters at IMT and MIT is strikingly dissimilar: the IMT-cluster has a massive 2D structure, while the MIT-cluster has a fine 3D structure.

7.3 Experimental Procedure

In this work, the electrical and optical properties of VO_2 thin films deposited on an r-cut sapphire at a high substrate temperature were examined simultaneously. The films are of high-quality and grown quasi epitaxially with a near-single-crystal structure at the sapphire/VO_2 interface as apparent under transmission electron microscope studies as we have recently reported in Ref. [16]. As mentioned in the latter reference, high-temperature deposition on the r-cut sapphire leads to a highly preferred growth with nearly parallel grain orientations of VO_2 similar to that

reported in Ref. [14]. The sample was prepared by DC reactive magnetron sputtering. A high purity vanadium target (99.95%) was used for the deposition process. VO_2 was sputtered on the r-cut sapphire substrate at a constant pressure of 1.33 Pa and a substrate temperature of 650 °C for a duration of 2 h. During thin film deposition, constant flow argon (Ar) and oxygen (O_2) flow rates were sustained at 100 and 1.3 SCCM, respectively. Film characterization was done using Raman spectroscopy (Renishaw Invia™ Reflex Raman Microscope), optical spectrophotometry (Perkin-Elmer Lambda 900 spectrophotometer) and scanning electron microscopy (Hitachi HT-7700 SEM). The thickness of the VO_2 film as measured in SEM was ~240 nm.

The simultaneous measurements of electrical conductivity (σ) and optical transmittance ($\tilde{T}$) of the VO_2 film under heating and cooling scans were done using a purpose-built experimental setup. The simplified schematic of the setup is shown in Figure 7.1 (a). A laser diode (Thorlabs) operating at 1550 nm was used for the transmittance measurements. Figure 7.1 (b) shows the schematic geometry of the sample used in our experiments. Two coplanar gold contacts separated by 0.5 mm were deposited on top of the VO_2 film using RF magnetron sputtering to measure the conductivity. The light used for measuring the optical transmittance was passed through the gap between the electrodes exactly in the same area that is used to measure the electrical conductivity. To achieve this, the area of illumination was limited by the optically thick electrodes and additional black masks. The transmitted light was collected by an InGaAs (Thorlabs, SM05PD2A) photodiode. The heating and cooling scans were performed using a Labview program communicating with a PID controller (Omega® CN16Pt-330). The temperature of the sample was controlled with a precision of ± 0.1 °C. The film structure through the insulator-metal-insulator transition during heating and cooling scans were studied by Raman imaging using a Renishaw Invia™ Reflex Raman microscope as described in Ref. [16].

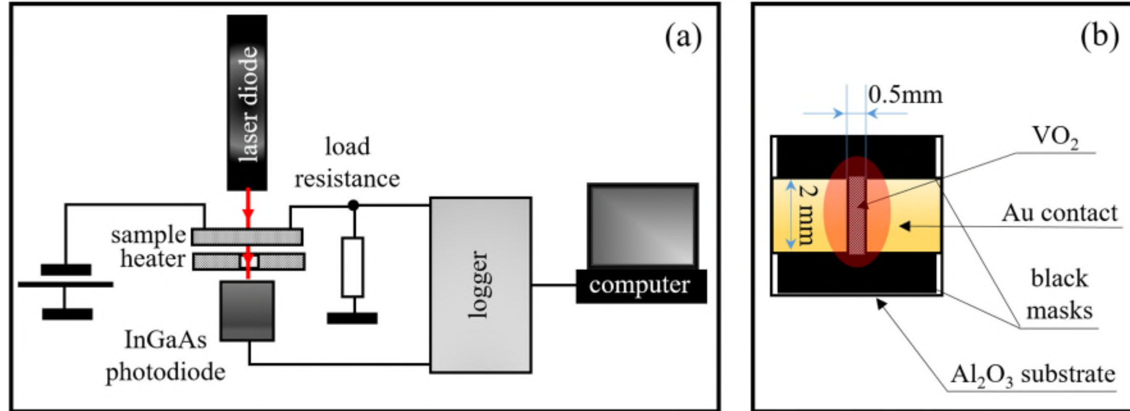

Figure 7.1 (a) Simplified schematic diagram of the experimental setup used for simultaneous measurements of electrical conductivity (σ) and optical transmittance ($\tilde{T}$). Operational wavelength of the laser diode is 1550 nm. (b) A schematic geometry of the sample used in our experiments. The black masks limit the passage of light. Au contacts are sufficiently thick (~54 nm) to be optically non-transparent. The red spot shows the illumination region.

7.3 Results

Figure 7.2 summarizes the main experimental results. Figure 7.2 (a) shows the hysteresis for conductivity which changes from ~19 Ω^{-1}cm^{-1} at room temperature to ~ 2.9×10^5 Ω^{-1} cm^{-1} at elevated temperatures above the IMT. The poorly conductive low temperature state shows a strong temperature dependence. This dependence can be approximated by an Arrhenius equation (2.0×10^6 Ω^{-1} cm^{-1})exp[−(0.3 eV)/$k_B T$], which is also shown in Figure 7.2 (a). The Arrhenius-type dependence of conductivity to temperature agrees well with the published results. [44–46] The conductivity in the highly conductive (metallic) phase seems to be temperature independent. Figure 7.2 (b) shows the temperature dependences of transmittance upon heating and cooling. Within 320–350 K, the transmittance changes from ~49% to ~0% upon heating and restores back to the maximum value upon cooling. The halfwidth of thermal hysteresis is ~5 K. These electrical and optical properties are typical for a high-quality VO_2 exhibiting IMT and MIT at heating and cooling, respectively.

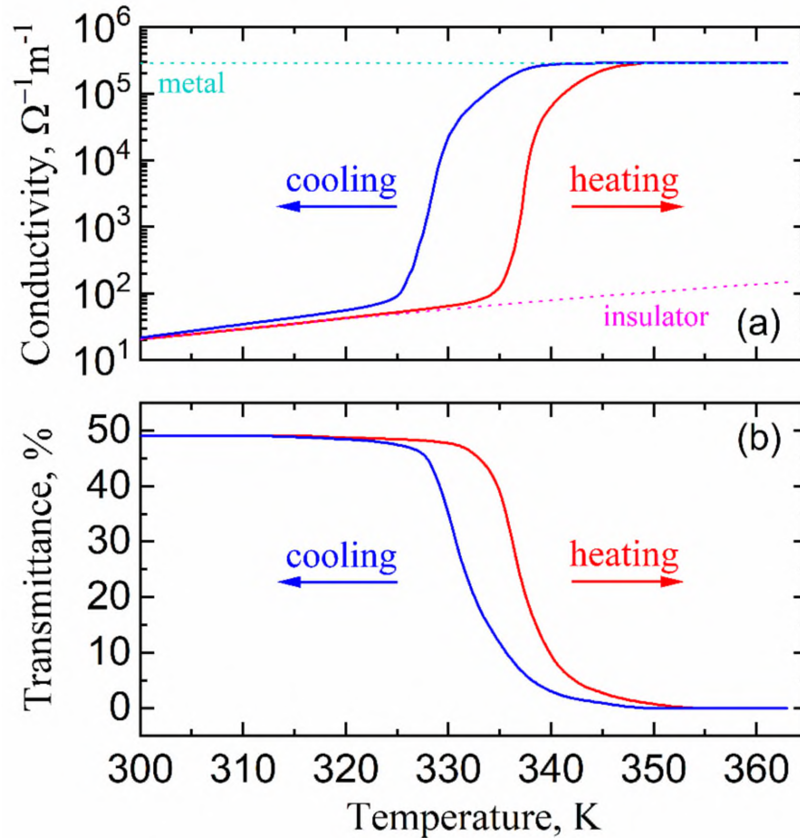

Figure 7.2 Experimental results of (a) conductivity and (b) optical transmittance as a function of temperature during heating (red curves) and cooling (blue curve). Magenta dotted curve is the best fit approximation to the conductivity of VO_2 in the insulating (semiconducting) state by the equation $(2.0 \times 10^6\ \Omega^{-1}\ \text{cm}^{-1})\exp[-(0.3\ \text{eV})/k_BT]$. The horizontal cyan dotted curve is the approximation for the relatively temperature independent conductivity of VO_2 in the metallic state.

Figure 7.3 (a) shows the dependence of conductivity (σ) of VO_2 versus partial concentration of metallic phase (X_m) during IMT and MIT. X_m values have been extracted from the optical transmittance data of both heating and cooling scans, by assuming that the metal fraction of the film is opaque and the insulating fraction is transparent [see Equation (7.1) in Section 7.4.1]. Figure 7.3 (a) also shows the results of calculations using different models of the effective medium approximation (EMA) which are described later in Section 7.4.2. Figure 7.3 (b) shows the derivative of the conductivity of VO_2 over the fraction of the metallic phase (X_m) normalized to values of conductivity and X_m. Despite unavoidable noise due to numerical differentiation, there

are clear maxima at around $X_m \approx 0.57$ on the heating curve and at around $X_m \approx 0.06$ on the cooling one.

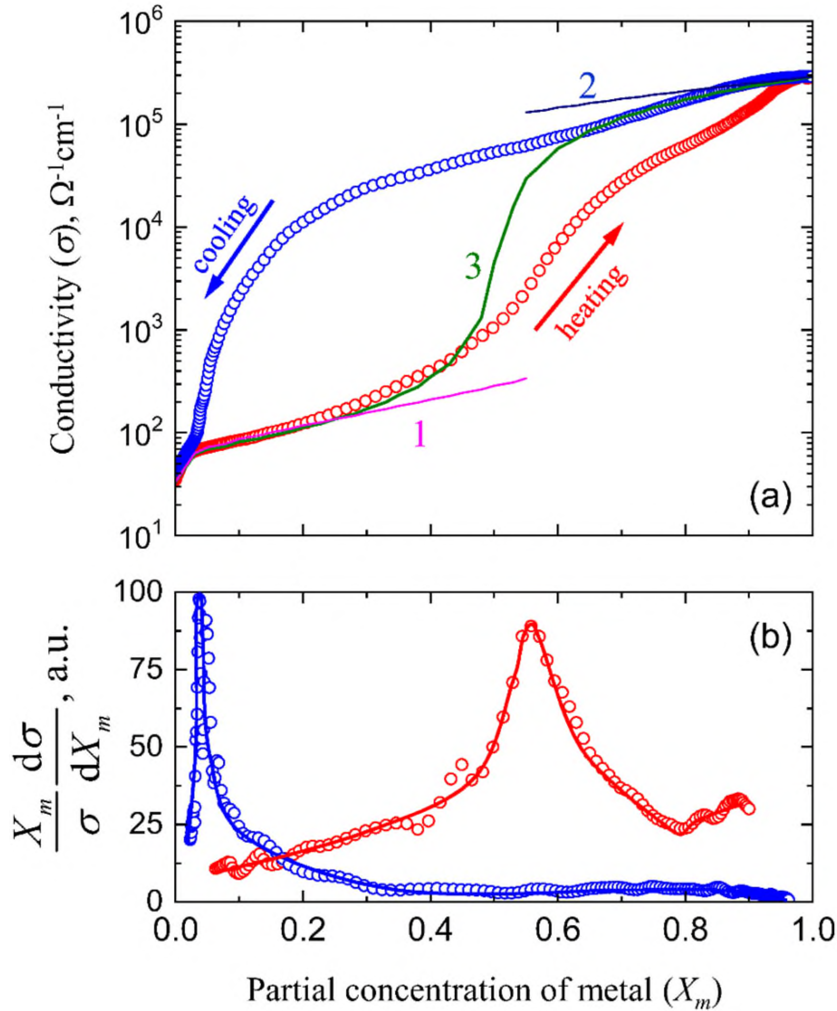

Figure 7.3 (a) Dependence of conductivity (σ) on the partial concentration of metal (X_m) in a VO_2 film under heating (red symbols) and cooling (blue symbols). Estimations of conductivity using the effective medium approximations (EMAs). The curves 1, 2, and 3 are obtained using Equations (7.3), (7.4), and (7.6), respectively. (b) The derivatives of conductivity vs. metallic phase content for heating (red) and cooling (blue). Symbols are the results of numerical differentiation. The curves are guides to the eye. The maxima indicate the percolation thresholds (X_c) of heating and cooling scans (a.u. represents arbitrary units with the maximum set to 100).

Figure 7.4 (a) and (b) show the derivatives of electrical conductivity of VO_2 and optical transmittance, respectively, as a function of temperature. The derivatives are normalized to

conductivity and transmittance, respectively, to amplify the importance of relative changes. It is clearly seen that the maxima in the optical transmittance precedes the maxima in the conductivity. The difference between the critical temperatures of heating ($T_c^{(h)}$) and cooling ($T_c^{(c)}$) scans and the hysteresis ($\Delta T_c = T_c^{(h)} - T_c^{(c)}$) of conductivity and transmittance is explained in Section 7.4.2.

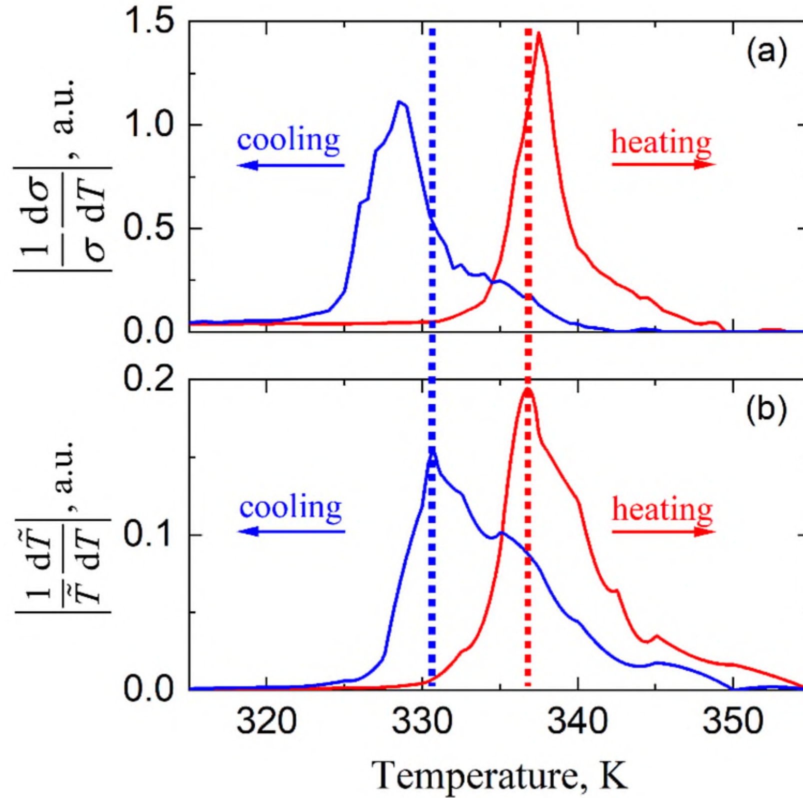

Figure 7.4 Normalized derivatives of conductivity (σ) in (a) and transmittance ($\tilde{T}$) in (b) as a function of temperature (T) during heating (red) and cooling (blue). Vertical lines mark the positions of maxima in the optical transmittance related curves in (b) (a.u. represents arbitrary units).

Figure 7.5 reproduces the dependence of the electrical conductivity of VO_2 versus fraction of the metallic phase X_m during IMT and MIT from Figure 7.3 (a). Additionally, it shows the positions of critical concentrations corresponding to maxima in Figure 7.3 (b). It also shows the functions drawn in accordance with the ES percolation theory [47], which are discussed in Section 7.4.

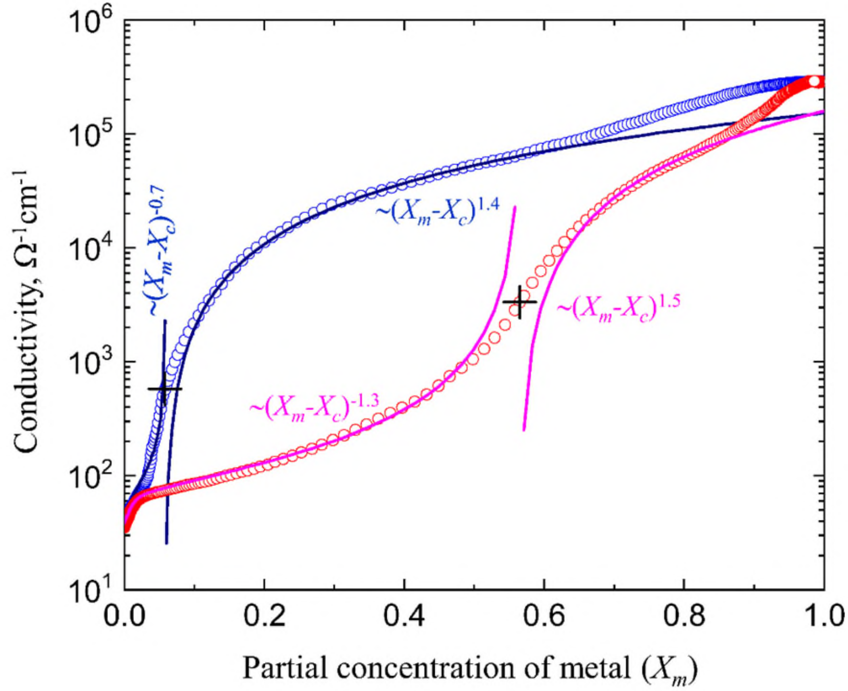

Figure 7.5 Dependence of conductivity vs. partial content of metallic phase (X_m) under heating (red symbols) and cooling (blue symbols) scans. The crosses mark the critical concentrations corresponding to the appearance (upon heating) and disappearance (upon cooling) of the infinite conductive cluster. Magenta and navy curves show the approximation functions explained in the text and defined in accordance with Efros–Shklovskii (ES) percolation theory (Ref. [47]).

Figure 7.6 shows a Raman map of the VO_2 phase structure during thermal cycling. The results are obtained using Raman spectroscopy, and data are extracted from Ref. [16] where one can find a detailed explanation of the procedure. The Raman mapping clearly shows the coexistence of the insulating and metallic phases during the IMT and MIT intervals and the hysteresis between the two transition temperatures. The importance of this figure is discussed later in Section 7.4.

7.4 Physical Model and Discussion

7.4.1 Metallic Content

Figure 7.2 shows that, as the temperature increases, the transparency of VO_2 decreases and finally disappears due to the formation of the new metallic phase. This effect may be interpreted as simple shadowing of light by optically non-transparent metallic phase given that during the IMT and MIT, the semiconductor and metal phases coexist. References [46] and [48] offer a straightforward method to quantify the partial volume content of the metallic phase (X_m) by assuming that the observed optical transmittance ($\tilde{T}$) is proportional to X_m in as much as the measured transmittance is over the whole film area (see Figure 7.1). Transformed regions of the film, being opaque, simply remove optical power from the through-beam. Using this method, X_m may be calculated from

$$X_m = \frac{\tilde{T}_M - \widehat{T}}{\tilde{T}_M - \tilde{T}_m} \tag{7.1}$$

where $\tilde{T}_M$ is the maximum transmittance and $\tilde{T}_m$ is the minimum transmittance, before and after the phase transition, respectively.

7.4.2 Conductivity of VO_2 and Effective Medium Approximation

Figure 7.3 (a) shows the dependence of the electrical conductivity of VO_2 versus the metallic phase content [X_m calculated using Equation (7.1)] during IMT at heating and MIT at cooling. Within these transitions, the material is an inhomogeneous mixture of coexisting semiconducting and metallic phases. Recently, this inhomogeneity has been demonstrated directly by different experimental methods [48–51].

EMA is widely used to establish the relation between the mixture composition and dielectric constant and/or conductivity. This theory substitutes the dielectric constant of an inhomogeneous material with some effective dielectric constant. Some examples of EMA applications with respect to VO_2 may be found in Refs. [46] and [52–54]. There are many well-

known theories for EMA aimed to predict the conductivity of a medium with dispersed second phase particles. Mostly, they are based on two assumptions: (1) the shape of particles is close to spherical and (2) the spatial distribution of particles is random but without clusterization. In the present paper, we mention two popular models among a number of effective media approaches. [55] The first one has been developed in early classical papers and produces the Maxwell–Garnet equation,

$$\frac{\varepsilon_{\text{eff}} - \varepsilon_{\beta}}{\varepsilon_{\text{eff}} + 2\varepsilon_{\beta}} = \chi_{\alpha} \frac{\varepsilon_{\alpha} - \varepsilon_{\beta}}{\varepsilon_{\alpha} + 2\varepsilon_{\beta}} \tag{7.2}$$

where ε_{eff} is the effective dielectric permittivity of the inhomogeneous medium, ε_{β} is the dielectric permittivity of the host medium, εα is the dielectric permittivity of the second phase dispersed medium, and χ_{α} is the volume fraction of dispersed media. As VO_2 is being heated and dispersed metallic phase starts to appear within the semiconducting medium, Equation (7.2) may be rewritten as

$$\frac{\sigma - \sigma_s}{\sigma + 2\sigma_s} = X_m \frac{\sigma_m - \sigma_s}{\sigma_m + 2\sigma_s} \tag{7.3}$$

where σ is the effective conductivity of VO_2, σ_s is the conductivity of VO_2 in the semiconducting phase, σ_m is the conductivity of VO_2 in the metallic phase, and X_m is the partial concentration of VO_2 in the metallic phase. On the other hand, upon cooling, the metallic phase is dominant and Equation (7.2) may be transformed to

$$\frac{\sigma - \sigma_m}{\sigma + 2\sigma_m} = X_s \frac{\sigma_s - \sigma_m}{\sigma_s + 2\sigma_m} \tag{7.4}$$

where X_s is the volume fraction of VO_2 in the semiconducting phase and obviously $X_s = (1-X_m)$. Figure 7.3 (a) shows the results from Equations (7.3) and (7.4). One can see that this EMA model works reasonably well for $X_m < 0.12$ and $0.86 < X_m$ and fails completely in between.

The second model to be mentioned in the present paper is a symmetrical effective medium theory for the second phase inclusions in a two-dimensional system, known as the Bruggeman mixture rule, [56,57].

$$\sum_k \delta_k \frac{\sigma_k - \sigma_{\text{eff}}}{\sigma_k + \sigma_{\text{eff}}} = 0 \tag{7.5}$$

where σ_k and X_k are the conductivity and fraction of kth inclusion, respectively. Specifically for VO_2, this gives

$$X_m \frac{\sigma_m - \sigma}{\sigma_m + \sigma} + (1 - X_m)\frac{\sigma_s - \sigma}{\sigma_s + \sigma} = 0 \tag{7.6}$$

The results of calculations using Equation (7.6) are shown Figure 7.3 (a). It is clear that this model works well at $X_m < 0.18$ and $0.66 < X_m$ and fails in between. Therefore, based on the results from Figure 7.3 (a), two tentative conclusions can be drawn:

1. Initially ($X_m < 0.12$ during heating and $0.86 < X_m$ during cooling), both EMA theories seem to work well. It implies the validity of two general assumptions about (1) spheroid shape of dispersed particles and (2) their random spatial distribution without clusterization. Schematic presentations of such distributions are shown in Figure 7.7 (a) and (c).

2. At intermediate values of X_m ($0.18 < X_m < 0.66$), the EMA approach seems to fail. We believe that when the growing dispersed particles become so numerous and big they begin to coalesce and form some types of clusters similar to that shown in Figure 7.7 (b) and (d).

Figure 7.4 (a) shows the derivative of the electrical conductivity of VO_2 and Figure 7.4 (b) shows the derivative of the optical transmittance as a function of temperature. The derivatives are normalized to conductivity and optical transmittance, respectively, to highlight the importance of relative changes. It is apparent that the maxima in conductivity are delayed with respect to maxima in the optical transmittance, i.e., the fastest changes in the conductivity start happening only when the fastest changes in the concentration of metallic fraction are already over. It implies the connection of conductivity with the topology of the spatial distribution of dispersed particles and control of conductivity by a percolation path through clusters with dominant metallic conductivity.

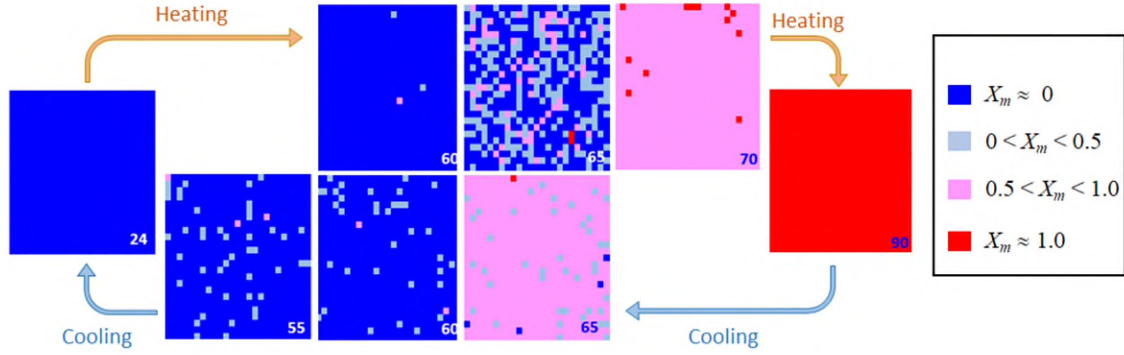

Figure 7.6 Map of the VO_2 phase structure during thermal cycling. The results are obtained using Raman spectroscopy. The data have been extracted from our previous paper (Ref. [16]) where one can find a detailed explanation of the mapping procedure. Every large square is 25 × 25 pixels with each pixel having a size of 1.2 × 1.2 μm^2. The numbers in the maps refer to the substrate temperature in degrees Celsius (°C).

7.4.3 Conductivity in VO_2 and Percolation Theory

For the general aspects of percolation theory applications to a variety of physical phenomena, we refer to the review in Ref. [58]. Recently, the importance of the percolative characteristic of MIT in VO_2 films has been recognized and corresponding theories have been created. [46,59−63] Here, we refer to the ES percolation theory, [47] because it discusses the percolation in a system composed of a good conductor/poor conductor mixture, which seems to be the most appropriate in the case of VO_2. In addition, it gives very clear recommendations on the identifications of percolation thresholds and the topology of infinite percolation clusters. Figure 7.3 (b) shows the derivatives of conductivity against the fractional metallic phase content X_m for IMT during heating and MIT during cooling. Despite the inevitable noise imminent in numerical differentiation, clear maxima may be identified at around $X_m \approx 0.57$ on the heating curve and at around $X_m \approx 0.06$ on the cooling one. According to the ES theoretical model, [47] these points may be identified as percolation thresholds corresponding to the appearance ($X_c^{(h)} \approx 0.57$) and disappearance ($X_c^{(c)} \approx 0.06$) of infinite conductive clusters. Surprisingly, this striking asymmetry of IMT and MIT in VO_2 is confirmed by chemical etching in acid which shifts T_t for IMT but leaving MIT intact. [64] Clearly, there is a pronounced difference between $X_c^{(h)} \approx 0.57$ and $X_c^{(c)} \approx 0.06$. Thus, we intend to discuss the values of $X_c^{(h)} \approx 0.57$ and $X_c^{(c)} \approx 0.06$ in detail. The ES

theoretical model predicts that, in the range $X_c << X_m << 1$, the conductivity is supposed to increase with the metallic phase content (X_m) as

$$\sigma(X_m) \sim \sigma_m (X_m - X_c)^r \tag{7.7}$$

where X_m is the fraction of the metallic phase, σ_m is the conductivity of a fully metallic lattice and r is the first critical index. Meanwhile, below X_c in the range $0 << X_m << X_c$, the conductivity follows

$$\sigma(X_m) \sim \sigma_s (X_c - X)^q \tag{7.8}$$

where σ_s is the conductivity of the fully semiconductive (poorly conductive) lattice and q is the second critical index. Figure 7.5 shows that these predictions work reasonably well for VO_2 with percolation thresholds being at $X_c^{(h)} \approx 0.57$ and at $X_c^{(c)} \approx 0.06$ with values of r and q shown in Figure 7.5 and in Table 7.1. The theory also predicts that the conductivity at the percolation threshold must follow the rule

$$\sigma(X_c) = \sigma_m \left(\frac{\sigma_s}{\sigma_m} \right)^s \quad \text{or} \quad s = \ln\left(\frac{\sigma(X_c)}{\sigma_m} \right) \Big/ \ln\left(\frac{\sigma_s}{\sigma_m} \right) \tag{7.9}$$

where s is the third and the last critical index. Furthermore, all three indices must be related through

$$q = r\left(\frac{1}{s} - 1 \right) \quad \text{or} \quad \frac{1}{s} - \frac{q}{r} = 1 \tag{7.10}$$

Table 7.1 shows the critical indices for both percolation thresholds in the case of VO_2 films of this work. It should be noted that the thresholds are reached at different temperatures. Therefore, temperature changes in the conductivities must be taken into account, while calculating the critical indices. As given in Table 7.1, the critical indices calculated for IMT in VO_2 during heating are in good agreement with a two-dimensional structure of metallic conductive clusters appearing in initially semiconducting VO_2.

Table 7.1 Comparison of experimental results with theoretical predictions of paper [47]. X_c is percolation threshold, T_c is temperature corresponding to percolation threshold, $\sigma(X_c)$ is the conductivity at percolation threshold, σ_s is the conductivity of VO_2 in semiconducting phase at temperature T, σ_m is the conductivity of VO_2 in metallic phase. The values marked with asterisk (*) are the published results of computer simulations and may be considered as approximate (for details see Refs. [47,65] and references herein]).

	Experimental data		**ES percolation theory [47]**	
Cluster dimension temperature scan	**Heating**	**Cooling**	**2D**	**3D**
X_c	0.57	0.06	0.5	-
r[8]	1.50	1.50	1.3*	1.6*
q	1.30	0.70	1.3*	1.0*
s	0.54	0.72	0.50	0.62*
Rule check Equation (7.10)	0.99	0.91	1.00	1.00
T_c , K	337.3	327.2	-	-
$\sigma(X_c)$, $\Omega^{-1}cm^{-1}$	3300	565	-	-
σ_s , $\Omega^{-1}cm^{-1}$	72.5	52.8	-	-
σ_m , $\Omega^{-1}cm^{-1}$	2.89×10^5	2.89×10^5	-	-

Consequently, we come to the model of metallic volcanic islands [Figure 7.7 (b)] which appear as small spheroidal dispersed inclusions [Figure 7.7 (a) in accordance with EMA theories], and then grow and overlap forming a mountain chain—infinite conductive cluster. It is interesting that the value of $X_c^{(h)} \approx 0.57$ lays close to 0.5 which is predicted for an ideal 2D percolation model. (The derivation may be found in Refs. [66] and [67].) There is further experimental evidence on the existence of a 2D infinite conductive cluster in these varying films from Raman imaging. Figure 7.6 shows a Raman map of the phase structure of the film at different temperatures during thermal cycling. Indeed, the percolation threshold of $X_c^{(h)} \approx 0.57$ is achieved at 337.3 K (≈ 64 °C). Meanwhile, at around 338 K (65 °C), Figure 7.6 clearly shows the appearance of extended 2D structures consisting of pixels with dominant metal composition.

[8] In the published paper, there exists a typo where t should be r. Also, the critical indices in the published version of the table are printed in uppercase, which in fact should be lowercase.

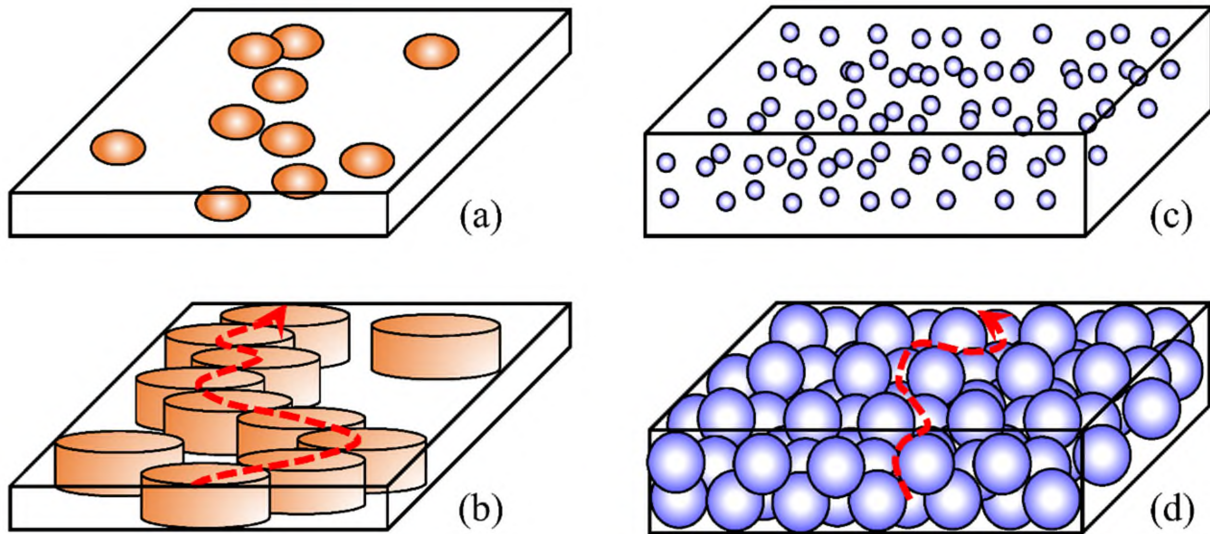

Figure 7.7 Simplified views of the appearance of 2D infinite conductive cluster at heating (a), (b) and disappearance of 3D infinite conductive cluster at cooling (c), (d). In (a) and (b), brownish color marks the appearance and disappearance of the metallic phase respectively. White shows the initial insulating phase. In (c) and (d), violet spheres show the appearance and disappearance of the insulating phase, respectively. White shows the remaining metallic phase. The red arrows show possible current paths in 2D (b) and 3D (d) infinite conductive clusters.

7.4.4 Percolation Threshold in Metal-to-Insulator Transition

Now, we turn our attention to MIT occurring during cooling and to the second surprisingly small percolation threshold observed at $X_c^{(c)} \approx 0.06$. The MIT starts with the purely metallic (highly conductive) phase and ends up with the semiconducting phase with a much poorer conductivity. A structural model of poorly conducting bubbles spread throughout the volume of the film in a highly conductive phase is sketched in Figure 7.7 (c). The conductivity starts to decrease with the formation of the poorly conductive bubbles. With increasing bubble size, the conductivity grows poorer. The initial decrease in the conductivity agrees well not only with the predictions of EMA theories, as in Figure 7.3 (a), but also with the structural model of the poorly conducting bubbles spread throughout a highly conductive phase, as sketched in Figure 7.7 (c). The percolation threshold is reached when the bubbles are so big and numerous that they nearly block the last remaining metallic path through the sample as illustrated in Figure 7.7 (d). Overall, the structure

resembles Swiss cheese where semiconducting pores are embedded in a metallic medium. Percolation cluster in this case is obviously three dimensional and Table 7.1 seems to support this conclusion.

The Swiss cheese model has proved to be effective in the percolation research. [68,69] However, the question remains on "Is it possible to achieve the percolation limit as small as $X_c^{(c)} \approx 0.06$ within the framework of this model?" To prove the point, we created our own numerical model of Swiss cheese and briefly discuss it below step by step.

7.4.4.1 Generation of the Network

We start by generating the cubic network of sites. It is generated at positions (n_1, n_2, n_3) where integers n_1, n_2, and n_3 vary from 1 to N, that is, sites occupy evenly spaced positions inside the cube $N \times N \times N$. Initially, all sites are considered to be metallic and they are assigned the same value 1 (indication of metallicity). We tested cubes of different sizes of $50 \times 50 \times 50$, $70 \times 70 \times 70$, and $100 \times 100 \times 100$. According to our results, cubes of $50 \times 50 \times 50$ give too much scattering from one attempt to another and produce statistically unreliable data. On the other hand, cubes of $100 \times 100 \times 100$ are much better but require too much computational time. Accordingly, cubes of $70 \times 70 \times 70$ have been found to be a good compromise combining reasonable computational time with statistically stable results.

7.4.4.2 Generation of spherical voids inside the cube

On the next step, spherical voids are generated in random positions inside the cube. The positions of centers of spherical voids (total number M) are generated as combinations of (x_m, y_m, z_m) where $m = 1, 2\ldots M$ and x_m, y_m, and z_m are random numbers which are uniformly distributed between 0 and N. All voids are considered to have the same radius R. The proximity of the sites (n_1, n_2, n_3) to the centers of voids (x_m, y_m, z_m) is tested for all sites and all centers of voids. If the proximity is close, i.e., $(n_1 - x_m)^2 + (n_2 - y_m)^2 + (n_3 - z_m)^2 \leq R^2$ this site is converted to the insulating phase (or a pore) by assigning it the value of 0 in place of 1. An example of the appearance of that a very porous and highly irregular structure is shown in Figure 7.8 (a)–(c). It is worth noting here that, in our experience, the appearing structure is already so complicated that the use of random R_m (where $m = 1,2\ldots M$) instead of an identical R does not make any substantial difference.

7.4.4.3 Percolation Through the System or "Wetting" The Sites

As the next step, we identify the nearest neighbors forming conductivity clusters [Figure 7.8(d) – (f)] and we calculate the cross-sectional area of the cluster which may be presented graphically as in Figure 7.8 (d) – (f) or numerically as in Figure 7.9. To achieve this goal, in the first layer, for all sites (except on the very border to exclude uncertainties), we change 1 to 2 [compare Figure 7.8 (a) and (d)]. Having 2 for a site means that it is wet, i.e., it belongs to a conductive cluster. In the second layer, we check all sites containing 1 and change 1 to 2 if the site has a wet neighbor in the first layer. We repeat this procedure consecutively for next layers for wetting (changing 1 to 2) sites, which have the wet neighbor/ neighbors in the preceding layer. Eventually, we arrive at two possible outcomes.

(a) No wet sites appear in a current layer which means that, in this system, the percolation is impossible. Accordingly, the calculations are terminated, and a new system of spherical voids is generated and tested.
(b) Wet sites appear in the last (N^{th}) layer. It means that the percolation is successful, and the results are saved for future analysis.

Wet sites form an infinite percolation cluster. An example of an infinite percolation cluster and its cross section are shown in Figure 7.8 (d) – (f) and Figure 7.9.

7.4.4.4 Identification of the "Gorge" of the Cluster and Calculation of Conductivity

Next, we identify the gorge [the narrowest cross-sectional area of the infinite conductive cluster as seen in Figure 7.8 (e)]. It should be noted here that the cluster shown in Figure 7.8 is the only one of infinite amount of possibilities produced by our model. In fact, it is quite unique because at the gorge its cross section is just only one pixel [Figure 7.8 (e) and Figure 7.9]. In the next step, we calculate the dependence of gorge area as a function of partial metal concentration (X_m) as shown in Figure 7.10. Close to the percolation threshold, most computational attempts give no percolation at all, and they are rejected. As X_m decreases, the scattering of results increases. Eventually, we interpolate the results using the equation.

$$W_g(X_m) \sim (X_m - X_{\text{crit}})^{\gamma} \tag{7.11}$$

where W_g is the width of the gorge, X_m is the fraction of the metallic phase content, γ is a power index (a coefficient), and X_c is the percolation threshold. The best fit using the least-square procedure gives

$$W_g(X_m) \sim (X_m - 0.058)^{1.6} \tag{7.12}$$

with $X_c = 0.058$ which is in nearly perfect agreement with the experimental value of $X_c^{(c)} \approx 0.06$. This result confirms the achievability of very low percolation threshold values in systems with high porosity. In addition, this simple model allows us to calculate the conductivity versus X_m. Assuming that right above the percolation threshold the conductivity is limited by the width of the gorge, we can approximately calculate the conductivity through

$$\sigma(X_m) \approx \sigma_m W_g(X_m) + \sigma_s(1 - W_g(X_m)) \tag{7.13}$$

where σ_m is the conductivity of the metallic phase and σ_s is the conductivity of the semiconductive phase. The results are presented in Figure 7.10 (b), where it can be seen that there is a surprisingly good agreement with experimental data for such a basic model.

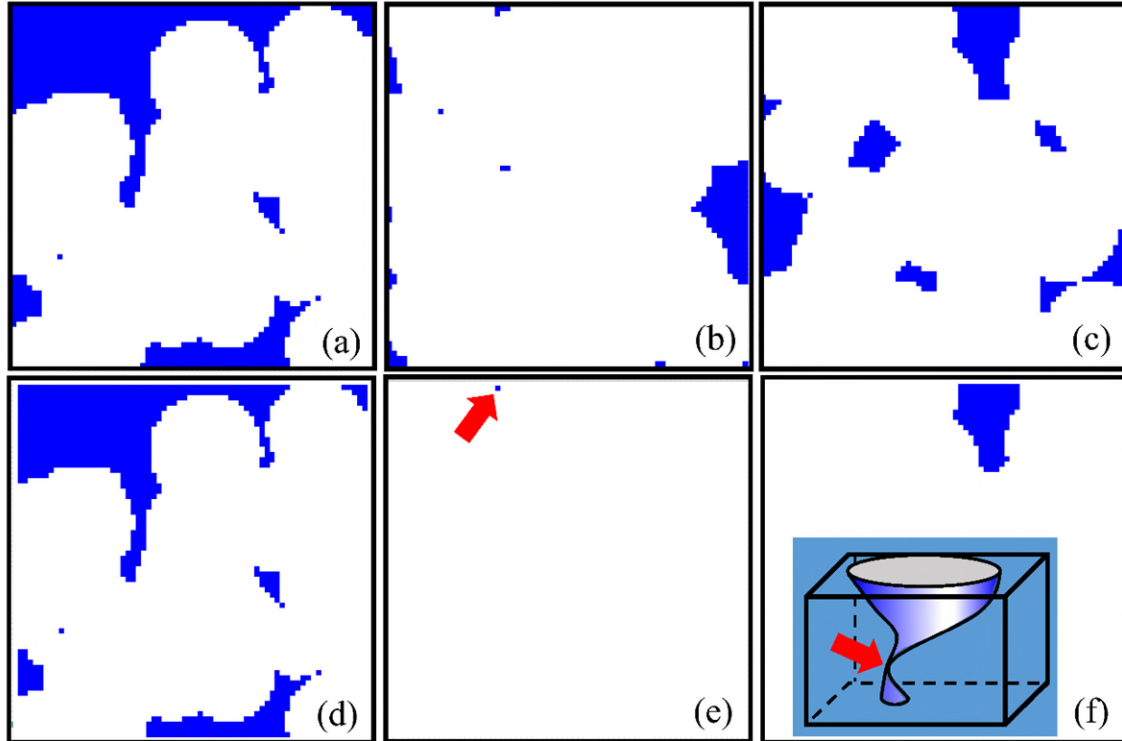

Figure 7.8 Cross sections of the cube of 70 × 70 × 70 used in modeling where (a) and (d) are the first layer; (b) and (e) are the 28th; (c) and (f) are the 70th layer. The first row (a)–(c) shows the metallic sites (i.e., containing 1 in computations) in blue. The second row (d)–(f) shows the wet sites (i.e., containing 2) in blue color. Figure (e) shows the gorge (the narrowest cross section) of the conductive cluster. The red arrow in figure (e) enables the reader to see the position of the gorge which is only one pixel. In all figures, white pixels denote voids, i.e., insulating sites (containing 0). The inset to figure (f) schematically shows the infinite percolation cluster as two vortexes with common gorge marked with a red arrow. No information is blocked by the inset: all pixels behind the inset are white. The results shown here represent one of the possible outcomes of the numerical simulations.

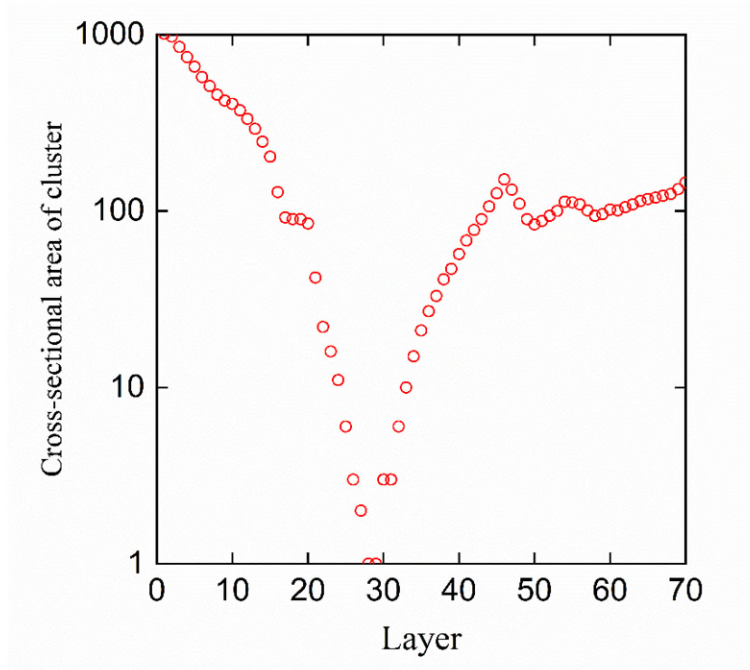

Figure 7.9 Cross-sectional area of the critical infinite conductive percolation cluster presented in Figure 7.8. Cross section is a number of wet sites, i.e., belonging to the conductive cluster. The size of the model is $70 \times 70 \times 70$. The gorge (with a width of one site) is on 28th and 29th layers.

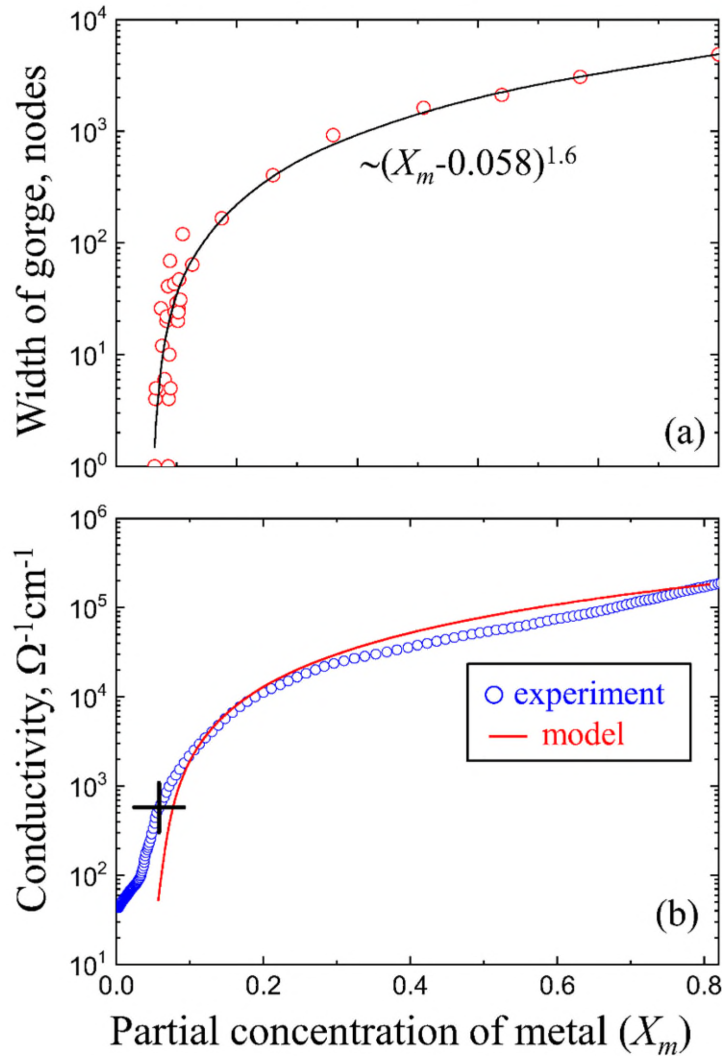

Figure 7.10 (a) Width of the gorge (the narrowest cross-sectional area) of the infinite conductive cluster [schematically shown in the inset of Figure 7.8 (f) and in Figure 7.7 (d)] as a function of partial concentration of remaining metal. The results of the Swiss cheese model where the initial metal is substituted by spherical nonconductive voids. (b) The comparison of the Swiss cheese numerical model predictions with the measured VO_2 conductivity during sample cooling. The details of model are explained in the text.

7.4.5 Difference in the Topology of the ICCs in IMT and MIT of VO_2

We need to address the basic question on why the topology of the conductive cluster is so different at IMT and MIT? Consider the basics of the VO_2 phase transformation. At temperatures

below T_c = 340 K, single-crystal VO_2 resides in the semiconducting phase and has a monoclinic crystal structure of a distorted rutile. [70] In this semiconducting monoclinic phase, the V^{4+} ions form pairs along the c axis, leading to alternate short and long V-V distances of 0.265 Å and 0.312 nm. Above T_c, the structure becomes tetragonal, like rutile TiO_2, and the material transitions into the metallic phase. In this new metallic rutile phase, the V^{4+} ions are separated by a fixed distance of 0.296 nm. In other words, the essence of this transition is a small shift of vanadium atoms to and from each other. This type of transition is clearly non-diffusional because the atoms are moved to distances smaller than the interatomic distances, without changing or switching the closest neighbors. Phase transformations in VO_2 are known to be of martensitic-type which is one of the possible cases of non-diffusional transformations. [71–73] The key to martensitic phase transformations is the formation of interphase boundaries, which become the sources of internal stresses and strains caused by the difference between the specific volumes of the initial and new phases. The dynamic balance between free energy reduction due to the formation of a new phase and energy gain due to internal strain energy determines the IMT and MIT in VO_2.

It is appropriate to recall here that the densities of VO_2 below and above T_c are substantially different. In the monoclinic semiconducting phase, VO_2 has a density of 4.571 g/cm^3, while the density of the tetragonal metallic phase is substantially larger than 4.653 g/cm^3. This means that while VO_2 undergoes a local insulator-to-metal transition, the local density increases creating local tensile stresses surrounding the appearing metallic phase (see Figure 7.11). Obviously, for a metal-to-insulator transition, the outcome is the opposite and a new semiconducting phase becomes surrounded by local compressive stresses. The next question is to quantify the effect of these stresses and induced mechanical strains. There are evidences to a strong influence of mechanical strains on the IMT in VO_2. A detailed review of the subject may be found in Ref. [74] and references therein. It seems established that one directional strains may substantially shift the transition temperature T_c and may even lead to total IMT suppression. [75–77] Very supportive results have been obtained in VO_2 nanobeams and nanobelts. [78–80] However, the closest analogy to the stresses appearing in our case would be hydrostatic pressure on which we could identify only two systematic papers dealing with this subject. [81,82] These papers give positive values for (dT_c/dP) in the range $(6 - 7) \times 10^{-5}$ K/bar, i.e., pressure application tends to increase transition temperature T_c. Hence, we can attempt to estimate the possible mechanical stresses

appearing during IMT and related shift of T_c. Imagine that a sphere of semiconducting VO_2 with radius R_s undergoes a phase transformation to metallic phase. Suppose that R_m and R_s are the radii of the metallic and semiconductor phases, respectively, then mass conservation requires that

$$\frac{4\pi}{3}R_s^3\rho_s = \frac{4\pi}{3}R_m^3\rho_m \tag{7.14}$$

where ρ_m and ρ_s are densities of the metallic and semiconductor phases, respectively. As mentioned earlier, this transformation would lead to the appearance of a volume strain associated with local stress. The pressure P and volume strain Δ are related through the bulk modulus B.

$$P = -B\Delta \tag{7.15}$$

The first principles calculations of B may be found in Refs. [83] and [84]. They give comparable values of $B \approx 240$ GPa for semiconducting and metallic phases of VO_2 (here, for our rough estimations we do not require any better precision). Using Equation (7.14), we transform Equation (7.15) into

$$P = -\ B\Delta = B\frac{V_m - V_s}{V_s} = B\left(1 - \frac{R_s^3}{R_m^3}\right) = B\left(1 - \frac{\rho_m}{\rho_s}\right) \tag{7.16}$$

Equation (7.16) gives the estimation of the stress produced in constraining media by the deformation/transformation of the sphere. It also allows us to estimate the shift of the transition temperature ΔT_c as

$$\Delta T_t \approx P\left(\frac{dT_c}{dP}\right) \approx B\left(1 - \frac{\rho_m}{\rho_s}\right)\left(\frac{dT_c}{dP}\right) \tag{7.17}$$

$\approx$ (250 GPa)$\times$(1-4.653/4.571)$\times$ (6$\times 10^{-5}$ K/bar) ≈ -2.4 K

Accordingly, local IMT leads to the appearance of local tensile stresses leading to a sizable decrease in the phase transition temperature in a local neighborhood. Therefore, the local IMT facilitates and promotes further IMT in its vicinity. Hence, once initiated, the metallic intrusion

will grow in volume. Schematically, this situation is presented in Figure 7.11 as 1 and 2. The limiting factors of the growth in volume are the surface and interface with the substrate of the film. Once they are reached, further growth becomes two dimensional, similar to islands sketched in Figure 7.7 (b). We refer here again to the results of Raman mapping in Figure 7.6, showing the presence of “big” (1.2 × 1.2 μm) islands, existing close to the percolation threshold.

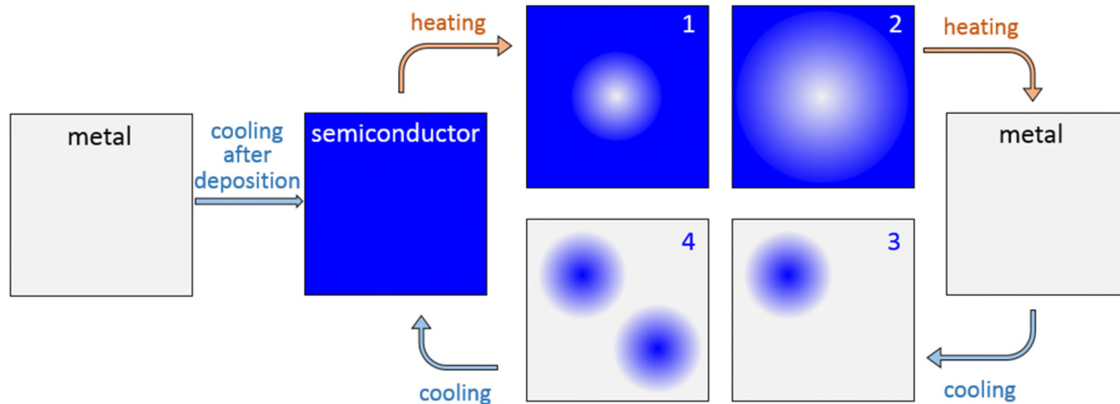

Figure 7.11 Schematic presentation of IMT and MIT.

We anticipate the opposite situation in the case of compressive local stresses appearing around newly transformed semiconducting inclusions during MIT. These stresses would create a protective shell denying further local transformation as schematically shown in Figure 7.11 in 3 and 4. Therefore, the appearance of new semiconductor inclusions would be preferable to the growth of existing inclusions. The small size inclusions would appear throughout the volume of VO_2 forming a sophisticated 3D structure. The examination of Raman mapping shows a much more uniform structure close to the percolation threshold during MIT as in Figure 7.6. In summary, we conclude that during IMT, the growth of relatively big 2D metallic islands seems to control the phase transformation. Conversely, during MIT, the phase transformation seems to be controlled by the appearance of relatively small semiconducting inclusions forming a 3D structure similar to Swiss cheese.

7.5 Conclusions

Electrical conductivity (σ) and optical transmittance ($\tilde{T}$) of quasi epitaxial VO_2 thin films deposited on r-cut sapphire substrates have been measured simultaneously as a function of

temperature. The measurements were done in the same region of the film. The partial concentration of the metallic phase (X_m) has been calculated from the experimental data of $\tilde{T}$ and the σ (X_m) dependence has been analyzed through IMT during heating and MIT during cooling. The results have been shown to be consistent with the Efros–Shklovskii percolation theory predicting the formation of an infinite conductive cluster during IMT and the preservation of clusters during MIT. The topology of clusters during IMT and MIT has been found to be strikingly dissimilar, two- and three dimensional, respectively. During IMT, the growth of relatively big 2D metallic islands seems to control the phase transformation. Conversely, during MIT, the phase transformation seems to be controlled by the appearance of relatively small semiconducting inclusions forming a 3D structure similar to Swiss cheese.

7.6 References

[1] H. W. Verleur, J. A. S. Barker and C. N. Berglund, "Optical properties of VO2 between 0.25 and 5 eV," *Physical Review*, vol. 172, p. 788, 1968.

[2] Y. M. Gerbshtein, T. V. Smirnova, E. I. Terukov and F. A. Chudnovskii, "Features of the optical properties of vanadium dioxide films near the semiconductor-metal phase transition.," *Soviet Physics-Solid State (English Translation)*, vol. 18, p. 503, 1976.

[3] B. Hong, Y. Yang, K. Hu, Y. Dong, J. Zhou, Y. Zhang, W. Zhao, Z. Luo and C. Gao, "Strain engineering on the metal-insulator transition of VO2/TiO2 epitaxial films dependent on the strain state of vanadium dimers," *Applied Physics Letters*, vol. 115, p. 251605, 2019.

[4] Y. Muraoka, Y. Ueda and Z. Hiroi, "Large modification of the metal–insulator transition temperature in strained VO2 films grown on TiO2 substrates," *Journal of Physics and Chemistry of Solids*, vol. 63, p. 965, 2002.

[5] S. Fischer, J.-O. Krisponeit, M. Foerster, L. Aballe, J. Falta and J. I. Flege, "Massively Strained VO2 Thin Film Growth on RuO2," *Crystal Growth & Design*, vol. 20, p. 2734, 2020.

[6] I. Voloshenko, B. Gompf, A. Berrier, G. Schnoering, F. Kuhl, A. Polity and M. Dressel, "Interplay between electronic and structural transitions in VO2 revealed by ellipsometry," *Journal of Vacuum Science & Technology B, Nanotechnology and Microelectronics: Materials, Processing, Measurement, and Phenomena*, vol. 37, p. 061202, 2019.

[7] Z. Yu, Y. Liu, Z. Zhang, M. Cheng, Z. Zou, Z. Lu, D. Wang, J. Shia and R. Xiong, "Controllable phase transition temperature by regulating interfacial strain of epitaxial VO2 films," *Ceramics International*, vol. 46, p. 12393, 2020.

[8] Y. Zhao, J. H. Lee, Y. Zhu, M. Nazari, C. Chen, H. Wang, A. Bernussi, M. Holtz and Z. Fan, "Structural, electrical, and terahertz transmission properties of VO2 thin films grown on c-, r-, and m-plane sapphire substrates," *Journal of Applied Physics*, vol. 111, p. 053533, 2012.

[9] G. Xu, P. Jin, M. Tazawa and K. Yoshimura, "Thickness dependence of optical properties of VO2 thin films epitaxially grown on sapphire (0 0 0 1)," *Applied Surface Science*, vol. 244, p. 449, 2005.

[10] T.-H. Yang, R. Aggarwal, A. Gupta, H. Zhou, R. J. Narayan and J. Narayan, "Semiconductor-metal transition characteristics of VO2 thin films grown on c- and r-sapphire substrates," *Journal of Applied Physics*, vol. 107, p. 053514, 2010.

[11] K. Shibuya, J. Tsutsumi, T. Hasegawa and A. Sawa, "Fabrication and Raman scattering study of epitaxial VO2 films on MgF2 (001) substrates," *Applied Physics Letters*, vol. 103, p. 021604, 2013.

[12] S. Yu, S. Wang, M. Lu and L. Zuo, "A metal-insulator transition study of VO2 thin films grown on sapphire substrates," *Journal of Applied Physics*, vol. 122, p. 235102, 2017.

[13] J. Ma, G. Xu, L. Miao, M. Tazawa and S. Tanemura, "Thickness-Dependent Structural and Optical Properties of VO2 Thin Films," *Japanese Journal of Applied Physics*, vol. 50, p. 020215, 2011.

[14] G. J. Kovâcs, D. Bürger, I. Skorupa, H. Reuther, R. Heller and H. Schmidt, "Effect of the substrate on the insulator–metal transition of vanadium dioxide films," *Journal of Applied Physics*, vol. 109, p. 063708, 2011.

[15] J. A. Creeden, S. E. Madaras, D. B. Beringer, M. R. Beebe, I. Novikova and R. A. Lukaszew, "Structural and Photoelectric Properties of Epitaxially Grown Vanadium Dioxide Thin Films on c-Plane Sapphire and Titanium Dioxide," *Scientific Reports*, vol. 9, p. 9362, 2019.

[16] C. Zhang, C. Koughia, O. Güneş, J. Luo, N.Hossain, Y. Li, X. Cui, R. Wong, Q. Yang, S. Kasap and S.-J. Wen, "Synthesis, structure and optical properties of high-quality VO2 thin films grown on silicon, quartz and sapphire substrates by high temperature magnetron sputtering: Properties through the transition temperature," *Journal of Alloys and Compounds*, vol. 848, p. 156323, 2020.

[17] T. Hajlaoui, N. Émond, C. Quirouette, B. L. Drogoff, J. Margot and M. Chaker, "Metal–insulator transition temperature of boron-doped VO2 thin films grown by reactive pulsed laser deposition," *Scripta Materialia*, vol. 177, p. 32, 2020.

[18] F. Chudnovskiy, S. Luryi and B. Spivak, "Switching device based on first-order metal-insulator transition induced by external electric field," in *Future trends in microelectronics: the nano millennium*, 2002.

[19] D. Malarde, M. J. Powell, R. Quesada-Cabrera, R. L. Wilson, C. J. Carmalt, G. Sankar, I. P. Parkin and R. G. Palgrave, "Optimized Atmospheric-Pressure Chemical Vapor Deposition Thermochromic VO2 Thin Films for Intelligent Window Applications," *ACS Omega*, vol. 2, p. 1040, 2017.

[20] H. Coy, R. Cabrera, N. Sepulveda and F. E. Fernandez, "Optoelectronic and all-optical multiple memory states in vanadium dioxide," *Journal of Applied Physics*, vol. 108, p. 113115, 2010.

[21] H. Zhou, J. Li, Y. Xin, G. Sun, S. Bao and P. Jin, "Optical and electrical switching properties of VO2 thin film on MgF2 (111) substrate," *Ceramics International*, vol. 42, p. 7655, 2016.

[22] J. Jiang, G. Chugunov and R. R. Mansour, "Fabrication and characterization of VO2-based series and parallel RF switches," in *2017 IEEE MTT-S International Microwave Symposium (IMS)*, Honolulu, HW, 4–9 June 2017.

[23] A. Simo, K. Kaviyarasu, B. Mwakikunga, R. Madjoe, A. Gibaud and M. Maaza, "Phase transition study in strongly correlated VO2 based sensing systems," *Journal of Electron Spectroscopy and Related Phenomena*, vol. 216, p. 23, 2017.

[24] Z. Yang, C. Ko and S. Ramanathan, "Oxide Electronics Utilizing Ultrafast Metal-Insulator Transitions," *Annual Review of Materials Research*, vol. 41, p. 337, 2011.

[25] X. Hong, D. J. Loy, P. A. Dananjaya, F. Tan, C. Ng and W. Lew, "Oxide-based RRAM materials for neuromorphic computing," *Journal of Material Science*, vol. 53, p. 8720, 2018.

[26] A. I. Selverston and M. Moulins, "Oscillatory Neural Networks," *Annual Review of Physiology*, vol. 47, p. 29, 1985.

[27] M. Di Ventra and Y. V. Pershin, "Biologically-inspired electronics with memory circuit elements," in *Advances in Neuromorphic Memristor Science and Applications*, R. Kozma, R. Pino, G. E. Pazienza, Eds. Dordrecht: Springer, 2012.

[28] N. Shukla, A. Parihar, E. Freeman, H. Paik, G. Stone, V. Narayanan, H. Wen, Z. Cai, V. Gopalan, R. Engel-Herbert, D. G. Schlom, A. Raychowdhury and S. Datta, "Synchronized charge oscillations in correlated electron systems," *Scientific Reports*, vol. 4, p. 4964, 2015.

[29] H.-T. Kim, B.-J. Kim, S. Choi, B.-G. Chae, Y. W. Lee, T. Driscoll, M. M. Qazilbash and D. N. Basov, "Electrical oscillations induced by the metal-insulator transition in VO2," *Journal of Applied Physics*, vol. 107, p. 023702, 2010.

[30] M. Soltani, S. T. Bah, R. Karmouch, M. Gaidai and R. Vallee, "Phase transition in thermochromic VO2 coatings grown by ac dual magnetron cathode sputtering," *Journal of Materials Science: Materials in Electronics*, vol. 30, p. 20043, 2019.

[31] J. Leroy, A. Bessaudou, F. Cosset and A. Crunteanu, "Structural, electrical and optical properties of thermochromic VO2 thin films obtained by reactive electron beam evaporation," *Thin Solid Films*, vol. 520, p. 4823, 2012.

[32] D. H. Kim and H. S. Kwok, "Pulsed laser deposition of VO2 thin films," *Applied Physics Letters*, vol. 65, p. 3188, 1994.

[33] R. T. R. Kumar, B. Karunagaran, D. Mangalaraj and S. A. K. Narayandass, "Characteristics of amorphous VO2 thin films prepared by pulsed laser deposition," *Journal of Material Science*, vol. 39, p. 2869, 2004.

[34] H. K. Kim, H. You, R. P. Chiarello, H. L. M. Chang, T. J. Zhang and D. J. Lam, "Finite-size effect on the first-order metal-insulator transition in VO 2 films grown by metal-organic chemical-vapor deposition," *Physical Review*, vol. 47, no. 19, p. 12900, 1993.

[35] D. Liu, H. Cheng, X. Xing, C. Zhang and W. Zheng, "Thermochromic properties of W-doped VO2 thin films deposited by aqueous sol-gel method for adaptive infrared stealth application," *Infrared Physics and Technology*, vol. 77, p. 339, 2016.

[36] M. Pan, H. Zhong, S. Wang, J. Liu, Z. Li, X. Chen and W. Lu, "Properties of VO2 thin film prepared with precursor VO(acac)2," *Journal of Crystal Growth*, vol. 265, p. 121, 2004.

[37] S. Lu, L. Hou and F. Gan, "Preparation and optical properties of phase-change VO2 thin films," *Journal of Material Science*, vol. 28, p. 2169, 1993.

[38] C. Z. Zhang, Q. Yang, C. Koughia, F. Ye, M. Sanayei, S. J. Wen and S. Kasap, "Characterization of vanadium oxide thin films with different stoichiometry using Raman spectroscopy," *Thin Solid Films*, vol. 620, p. 64, 2016.

[39] M. Wan, M. Xiong, N. Li, B. Liu, S. Wang, W. Y. Ching and X. Zhao, "Observation of reduced phase transition temperature in N-doped thermochromic film of monoclinic VO2," *Applied Surface Science*, vol. 410, p. 363, 2017.

[40] Y. Y. Luo, F. H. Su, S. S. Pan, S. C. Xu, C. Zhang, J. Pan, J. M. Dai, P. Li and G. H. Li, "Terahertz conductivities of VO2 thin films grown under different sputtering gas pressures," *Journal of Alloys and Compounds*, vol. 655, p. 442, 2016.

[41] C. Zhang, O. Gunes, Y. S. Li, X. Cui, M. Mohammadtaheri, S. J. Wen, R. Wong, Q. Yang and S. Kasap, "The Effect of Substrate Biasing during DC Magnetron Sputtering on the Quality of VO2 Thin Films and Their Insulator–Metal Transition Behavior," *Materials*, vol. 12, p. 2160, 2019.

[42] C. Zhang, C. Koughia, Y. Li, X. Cui, F. Ye, S. Shiri, M. Sanayei, S.-J. Wen, Q. Yang and S. Kasap, "Near-zero IR transmission of VO2 thin films deposited on Si substrate," *Applied Surface Science*, vol. 410, p. 363, 2017.

[43] Z. Huang, Z. Wu, C. Ji, J. Dai, Z. Xiangh, D. Wang, X. Dong and Y. Jiang, "Improvement of phase transition properties of magnetron sputtered W-doped VO2 films by post-annealing approach," *Journal of Materials Science: Materials in Electronics*, vol. 31, p. 4150, 2020.

[44] C. N. Berglund and H. J. Guggenheim, "Electronic Properties of VO2 near the Semiconductor-Metal Transition," *Physical Review*, vol. 185, p. 1022, 1969.

[45] H. Jerominek, F. Picard and D. Vincent, "Vanadium oxide films for optical switching and detection," *Optical Engineering*, vol. 32, p. 2092, 1993.

[46] J. Rozen, R. Lopez, R. F. Haglund Jr. and L. C. Feldman, "Two-dimensional current percolation in nanocrystalline vanadium dioxide films," *Applied Physics Letters*, vol. 88, p. 081902, 2006.

[47] A. L. Efros and B. I. Shklovskii, "Critical behavior of conductivity and dielectric constant near the metal-non-metal transition threshold," *Physics Status Solidi B*, vol. 76, p. 475, 1976.

[48] Y. J. Chang, C. H. Koo, J. S. Yang, Y. S. Kim, D. H. Kim, J. S. Lee, T. W. Noh, H.-T. Kim and B. G. Chae, "Phase coexistence in the metal–insulator transition of a VO2 thin film," *Thin Solid Films*, vol. 486, pp. 46-49, 2005.

[49] M. Liu, A. J. Sternbach, M. Wagner, T. V. Slusar, T. Kong, S. L. Bud'ko, S. Kittiwatanakul, M. M. Qazilbash, A. McLeod, Z. Fei, E. Abreu, J. Zhang, M. Goldflam, S. Dai, G.-X. Ni, J. Lu and H. A. Be, "Phase transition in bulk single crystals and thin films of VO2 by nanoscale infrared spectroscopy and imaging," *Physical Review B*, vol. 91, p. 245155, 2015.

[50] H. Madan, M. Jerry, A. Pogrebnyakov, T. Mayer and S. Datta, "Quantitative Mapping of Phase Coexistence in Mott-Peierls Insulator during Electronic and Thermally Driven Phase Transition," *ACS Nano*, vol. 3, p. 2009, 2015.

[51] H. T. Stinson, A. Sternbach, O. Najera, R. Jing, A. S. Mcleod, T. V. Slusar, A. Mueller, L. Anderegg, H. T. Kim, M. Rozenberg and D. N. Basov, "Imaging the nanoscale phase separation in vanadium dioxide thin films at terahertz frequencies," *Nature Communications*, vol. 9, p. 3604, 2018.

[52] P. J. Hood and J. F. DeNatale, "Millimeter-wave dielectric properties of epitaxial vanadium dioxide thin films," *Journal of Applied Physics*, vol. 70, p. 376, 1991.

[53] H. S. Choi, J. S. Ahn, J. H. Jung and T. W. Noh, "Mid-infrared properties of a VO2 film near the metal-insulator transition," *Physical Review B*, vol. 54, p. 4621, 1996.

[54] L. A. L. de Almeida, G. S. Deep, A. M. N. Lima and H. Neff, "Modeling of the hysteretic metal-insulator transition in a vanadium dioxide infrared detector," *Optical Engineering*, vol. 41, p. 2582, 2002.

[55] S. Kasap, C. Koughia and H. E. Ruda, “Electrical Conduction in Metals and Semiconductors,” in *Springer Handbook of Electronic and Photonic Materials*, S. Kasap and P. Capper, Eds. New York: Springer, 2017.

[56] D. A. G. Bruggeman, "Berechnung verschiedener physikalischer Konstanten von heterogenen Substanzen. I. Dielektrizitätskonstanten und Leitfähigkeiten der Mischkörper aus isotropen Substanzen," *Annalen der Physik*, vol. 24, p. 636, 1935.

[57] R. Landauer, "Electrical conductivity in inhomogeneous media," *AIP Conference Proceedings*, vol. 40, p. 2, 1978.

[58] M. Sahimi, *Applications of Percolation Theory*, London: Taylor and Francis, 1994.

[59] H.-M. Jung, W. Choi, S. Um "Path-percolation modeling of electrical property variations with statistical procedures in spatially disordered inhomogeneous media," *Journal of the Korean Physical Society*, vol. 56, p. 591, 2010.

[60] Y. J. Chang, J. S. Yang, Y. S. Kim, D. H. Kim, T. W. Noh, D.-W. Kim, E. Oh, B. Kahng and J.-S. Chung, "Surface versus bulk characterizations of electronic inhomogeneity in a VO2 thin film," *Physical Review B*, vol. 76, p. 075118, 2007.

[61] D. Ruzmetov, K. T. Zawilski, S. D. Senanayake, V. Narayanamurti and S. Ramanathan, "Infrared reflectance and photoemission spectroscopy studies across the phase transition boundary in thin film vanadium dioxide," *Journal of Physics: Condensed Matter*, vol. 20, p. 465204, 2008.

[62] A. R. Gentle, G. B. Smith and A. I. Maaroof, "Frequency and percolation dependence of the observed phase transition in nanostructured and doped VO2 thin films," *Journal of Nanophotonics*, vol. 3, p. 031505, 2009.

[63] V. S. Aliev, S. G. Bortnikov and I. A. Badmaeva, "Anomalous large electrical capacitance of planar microstructures with vanadium dioxide films near the insulator-metal phase transition," *Applied Physics Letters*, vol. 104, p. 132906, 2014.

[64] L. Kang, L. Xie, Z. Chen, Y. Gaoc, X. Liud, Y. Yanga and W. Lianga, "Asymmetrically modulating the insulator–metal transition of thermochromic VO2 films upon heating and cooling by mild surface-etching," *Applied Surface Science*, vol. 311, p. 676, 2014.

[65] B. I. Shklovskii and A. L. Efros, "Percolation theory and conductivity of strongly inhomogeneous media," *Soviet Physics Uspekhi*, vol. 18, p. 845, 1975.

[66] A. M. Dykhne, "Conductivity of a two-dimensional two-phase system," *Soviet Physics JETP*, vol. 32, no. 1, p. 63, 1971.

[67] R. Zallen and H. Scher, "Percolation on a Continuum and the Localization-Delocalization Transition in Amorphous Semiconductors," *Physical Review B*, vol. 4, p. 4471, 1971.

[68] G. A. Garfunkel and M. B. Weissman, "Noise scaling in continuum percolating films," *Physical Review Letters*, vol. 55, p. 296, 1985.

[69] B. I. Halperin, S. Feng and P. N. Sen, "Differences between Lattice and Continuum Percolation Transport Exponents," *Physical Review Letters*, vol. 54, p. 2391, 1985.

[70] F. J. Morin, "Oxides Which Show a Metal-to-Insulator Transition at the Neel Temperature," *Physical Review Letters*, vol. 3, p. 34, 1959.

[71] Z. Nishiyama, *Martensitic transformation*, M. E. Fine, M. Meshii and C. M. Wayman, Eds., New York: Academic Press, 2012.

[72] A. L. Roitburd, "The theory of the formation of a heterophase structure in phase transformations in solids," *Soviet Physics Uspekhi*, vol. 17, p. 326, 1974.

[73] X. O. Urinov, X. A. Jumanov, A. Amonov, A. M. Xidirov and J. R. Kilichov, "Martensitic transformations in VO2 films," *IOP Conference Series: Materials Science and Engineering*, vol. 665, p. 012013, 2019.

[74] Z. Shao, X. Cao, H. Luo and P. Jin, "Recent progress in the phase-transition mechanism and modulation of vanadium dioxide materials," *NPG Asia Materials*, vol. 10, p. 581, 2018.

[75] N. Sepúlveda, A. Rúa, R. Cabrera and F. Fernández, "Young's modulus of VO2 thin films as a function of temperature including insulator-to-metal transition regime," *Applied Physics Letters*, vol. 92, p. 191913, 2008.

[76] Y. Muraoka and Z. Hiroi, "Metal–insulator transition of VO2 thin films grown on TiO2 (001) and (110) substrates," *Applied Physics Letters*, vol. 80, p. 583, 2002.

[77] M. Yang, Y. Yang, B. Hong, L. Wang, K. Hu, Y. Dong, H. Xu, H. Huang, J. Zhao, H. Chen, L. Song, H. Ju, J. Zhu, J. Bao, X. Li, Y. Gu, T. Yang, X. Gao, Z. Luo and C. Gao, "Suppression of Structural Phase Transition in VO2 by Epitaxial Strain in Vicinity of Metal-insulator Transition," *Nature Nanotechnology*, vol. 4, p. 732, 2009.

[78] J. Wu, Q. Gu, B. S. Guiton, N. P. d. Leon, L. Ouyang and H. Park, "Strain-Induced Self Organization of Metal−Insulator Domains in Single-Crystalline VO2 Nanobeams," *Nano Letters*, vol. 6, p. 2313, 2006.

[79] J. Cao, E. Ertekin, V. Srinivasan, W. Fan, S. Huang, H. Zheng, J. W. L. Yim, D. R. Khanal, D. F. Ogletree, J. C. Grossman and J. Wu, "Strain engineering and one-dimensional

organization of metal–insulator domains in single-crystal vanadium dioxide beams," *Nature nanotechnology*, vol. 4, p. 732, 2009.

[80] B. Hu, Y. Ding, W. Chen, D. Kulkarni, Y. Shen, V. V. Tsukruk and Z. L. Wang, "External-Strain Induced Insulating Phase Transition in VO2 Nanobeam and Its Application as Flexible Strain Sensor," *Advanced Materials*, vol. 22, p. 5134, 2010.

[81] M. A. Ivanov and M. A. Krivoglaz, "Phonon damping in solid solutions," *Fizika Tverdogo Tela*, vol. 6, p. 200, 1964.

[82] L. A. Ladd and W. Paul, "Optical and transport properties of high-quality crystals of V2O4 near the metallic transition temperature," *Solid State Communications*, vol. 7, p. 425, 1969.

[83] C. Sun, L. Yan, B. Yue, H. Liu and Y. Gao, "The modulation of metal–insulator transition temperature of vanadium dioxide: a density functional theory study," *Journal of Materials Chemistry C*, vol. 2, p. 9283, 2014.

[84] H. Dong and H. Liu, "Elastic properties of VO2 from first-principles calculation," *Solid State Communications*, vol. 167, p. 1, 2013.

8. Self-Heating-Induced Electrical and Optical Switching in High-Quality VO_2 Films Controlled with Current Pulses[9]

8.1 Abstract

The time dependences of electrical conductivity (σ), optical transmittance ($\tilde{T}$) at 1550 nm and film temperature (T) of VO_2 films grown on c-cut sapphire substrate were simultaneously monitored during Joule self-heating (SH) caused by passing electrical pulses of constant driving current (I_D) at various magnitudes for a constant duration of five seconds (Δt = 5 s). Prior to the I_D-application, the films were pre-heated to 57 °C which is at the brink of thermochromic insulator-to-metal transition (IMT). Upon the application of I_D, the SH effect leads to a rise in film temperature (T) and, consequently, to the transition of VO_2 from insulator-to-metallic phase (IMT) causing substantial changes in σ and $\tilde{T}$. Depending on the magnitude of I_D, σ and $\tilde{T}$ demonstrate strikingly different temporal behavior during the SH induced IMT and during the recovery to the insulating phase after the removal of I_D. A simple model based on percolation theory was developed to explain the observed phenomena and was compared with the previous results of (structural) IMT obtained by Raman micro-mapping.

[9] This paper was published as: Ozan Gunes, Cyril Koughia, Chunzi Zhang, George Belev, Shi-Jie Wen, Qiaoqin Yang, and Safa O. Kasap, "Self-heating-induced electrical and optical switching in high quality VO2 films controlled with current pulses," *Journal of Materials Science: Materials in Electronics*, vol. 32, no. 19, p. 24285. doi.org/10.1007/s10854-021-06895-2.

8.2 Introduction

The discovery of the insulator-to-metal transition (IMT) during heating at ~ 68 °C and the reverse metal-to-insulator transition (MIT) during cooling in monocrystalline vanadium dioxide (Ref. [1]) has led to much research on the switching properties and possible applications of this material. Recently, much scientific interest has focused on VO_2 of various forms including thin films and micro- and nanostructures. The up-to-date reviews of the subject may be found in Refs. [2–4].

The IMT can be induced by means of applying heat, electrical field, optical excitation and mechanical stress as reviewed in Ref. [5]. However, thermochromic IMT in VO_2 has been the most popular method. In some applications, such as smart windows [6,7] or millimeter- and terahertz-wave imaging [8–10] this approach develops naturally as the heating of VO_2 is done by an electromagnetic field whose intensity must be controlled and/or measured. In contrast, many applications rely on external and built-in-heaters, such as memory elements and electrical switches [11,12]. Specifically, there are some selected applications that rely on the effect of *self-heating* (SH), where a well-known Joule heating is achieved by passing an electric current through the VO_2 itself multistate memory devices [13–16] and neuromorphic networks [17–20] are good examples in which SH of VO_2 is utilized.

In the present paper, we investigate the effect of SH in a macro-scale near epitaxial VO_2 film devices under the application of a constant driving current (I_D). We attempt to give a deeper insight to the dynamics of SH by carrying out simultaneous measurements of electrical conductivity (σ), optical transmittance ($\tilde{T}$) and temperature (T) of VO_2 films. Depending on the value of the driving current (I_D), we observe surprisingly different temporal behavior of the electrical and the optical switching. We finalize our discussion by creating a simple physical model, based on percolation theory, to explain the observed phenomena.

8.3 Experimental Procedure

High-quality VO_2 films were grown on c-cut sapphire substrates (10 mm ×10 mm) from AdValue Technology, using DC magnetron sputtering in reactive environment. The substrates

were ultrasonically cleaned prior to deposition. High purity vanadium target (99.95%) was used as the target for the deposition. Deposition took place in a reactive environment at a substrate temperature of 650 °C. Constant flow of O_2 and Ar was applied during the sputtering process, 1.3 and 100 SCCM respectively. The chamber pressure was kept at 1.33 Pa during the deposition. The thickness of the sample was measured as 240 nm ± 4 nm. The films were characterized by measuring the optical transmittance spectrum using UV-Vis-NIR Lambda 900 Perkin-Elmer spectrophotometer at 27 °C and 95 °C, in the semiconducting and metallic phases respectively. The Raman spectra using Renishaw Invia™ Reflex Raman Microscope. More details on the deposition technique and characterization methods may be found in our previous paper [21,22].

Figure 8.1 (a) and (b) show sketches of the front and back views of the VO_2 device we have used. For measurements of electrical conductivity, two square optically thick co-planar gold contacts with a thickness of 34 nm were deposited on top of the VO_2 films using RF magnetron sputtering at room temperature. The size of the contacts is 2 mm × 2 mm, and they are separated by 0.5 mm. Thin copper wires (diameter: 0.1 mm) were glued by silver conductive epoxy to gold contacts. For temperature measurements two Pt-100 platinum thermistors (PRs) with TCR 3851 ppm/°C were attached to the back of the sapphire substrate by thermally conductive tape (polymer, thermal conductivity of 0.6 W/m °C) which was also glued to the substrate with a thermally conductive glue (with thermal conductivity of 0.7 W/m°C) as shown in Figure 8.1 (b). The sample was fixed on a square PVC platform with the abovementioned wires being fixed to the sides of the platform. This setup minimized the thermal mass of the sample and made the temperature changes during the SH fast and reliable. The investigation on SH was conducted using a purpose-built bench-top system sketched in Figure 8.1 (c), where the film temperature (T), optical transmittance ($\tilde{T}$) and electrical resistance (R) were recorded simultaneously. The temperature of the substrate was measured and stabilized using thermistors PR1 and PR2. The PR1 was used as a heater which was regulated by a DC power supply that was controlled by a PID software program. The second thermistor (PR2) was used to measure the "temperature of the film" which was recorded by Logger 3 built in the Digilent® Analog Discovery 2 (schematically sketched in Figure 8.1 (c)), a multipurpose digital device. The reason of stating "the temperature of the film" is discussed in the next section to justify the use of this term.

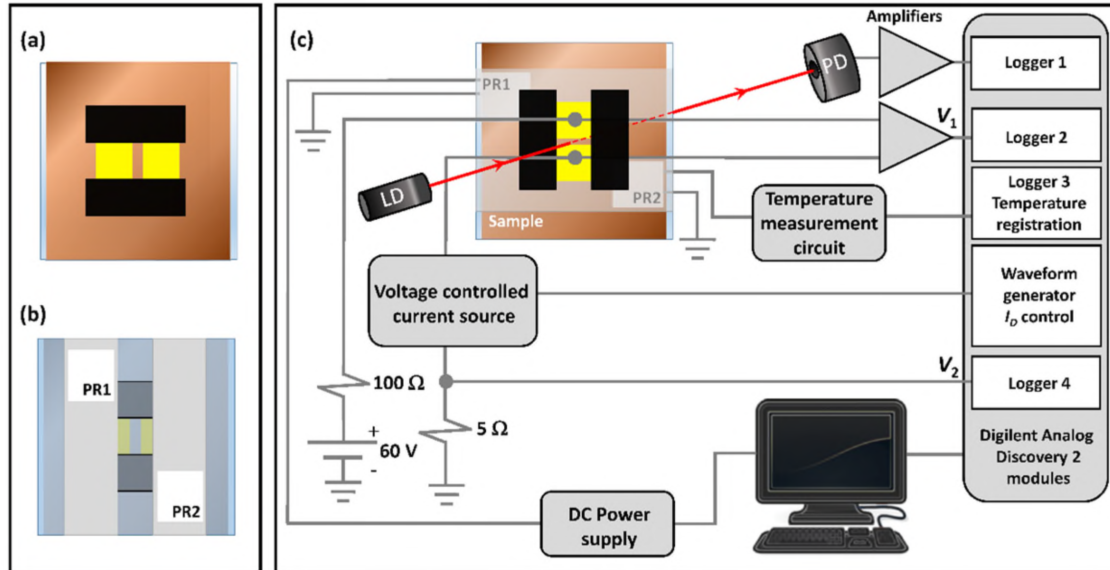

Figure 8.1 (a). Front view of VO_2 film on c-cut sapphire. 2 mm × 2mm gold contacts separated by 0.5 mm are covered by black non-conductive opaque tapes, above and below, to limit the light passing through the gap. (b) Rear view of VO_2 film on c-cut sapphire. Two platinum Pt-100 thermistors (PR1 and PR2) are attached on thermally conductive tapes which are also attached to the sapphire substrate. The PR1 thermistor is used simultaneously as a heater to pre-heat the sample and as a thermometer to stabilize the substrate temperature. The PR2 thermistor is used to measure the temperature of the sample. (c) Outline of the experimental setup. The size of the sample is grossly exaggerated. LD is laser diode operating at 1550 nm, PD is the photodiode sensitive at 1550 nm, PR1 and PR2 are platinum thermistors shown in (b).

The relative optical transmittance ($\tilde{T}_r$) at 1550 nm was measured by passing a continuous light beam from a laser diode (Thorlabs, LDM1550) through the gap between gold contacts as sketched in Figure 8.1 (c). The intensity of the light was detected by an InGaAs photodiode (Thorlabs, SM05PD2A), amplified and registered by Logger 1 built into the Agilent Discovery module. The $\tilde{T}_r$ was calculated by taking into account the maximum and minimum detector voltage readings, V_M and V_m, respectively. The maximum detector voltage reading V_M represents the light transmitted on the photodiode at room temperature (fully semiconducting phase of VO_2) and the minimum voltage V_m is the voltage reading corresponding to the fully metallic phase of VO_2. To ensure that only light passing through the gap was monitored, the unused surface of the sample

outside the gap was covered by black non-conductive, opaque tapes as shown in Figure 8.1 (a). The Au contacts were sufficiently thick to block the light without additional screening. The detector and the laser were first aligned. Next, the sample was placed at a location that corresponded to the maximum transmitted intensity. The detector voltage reading of transmitted light during measurements was recorded as V_{trans}, and using the latter $\tilde{T}_r$ was determined through

$$\tilde{T}_r = \frac{V_{\text{trans}} - V_m}{V_M - V_m} \times 100\% \tag{8.1}$$

Two independent electrical circuits were connected with the Au contacts deposited on the top of the VO_2 film. The first circuit was aimed to measure the VO_2 resistance. The first circuit was used to measure the VO_2 resistance (R) by recording the voltage drop across the film (V_1) and the voltage drop across the 5 Ω sampling resistor (V_2) with data loggers 2 and 4, respectively (see Figure 8.1 c). The voltage V_2 was also used to calculate the current I_D passing through the film and the R of the film calculated from the ratio V_1/I_D. The σ of the sample was extracted from the R reading. The voltage controlled current source circuit was used to pass square pulses of constant current (I_D) through the sample. The constant I_D driven through the sample was independent of the sample resistance. The pulse duration and the current magnitude were controlled by the waveform generator (see Figure 8.1). In the experiments, the value of the constant current was regulated between 100 and 500 mA, and the pulse duration was kept constant at 5 s. The 100 Ω protection resistor (see Figure 8.1 (c)) was used to limit the current trough the sample thus protecting the sample from destruction in case of a failure in the electronic circuit controlling the current.

8.4 Results

Figure 8.2 (a) shows the optical transmission spectrum of VO_2 grown on c-cut sapphire in the semiconductor (27 °C) and metallic phases (95 °C). At 1550 nm, the optical transmittance of the VO_2 film is around 45% at 27 °C and approximately 0% at 95 °C. Figure 8.2 (b) shows the Raman spectrum of the VO_2 film. The Raman peaks at 140, 193, 223, 303, 393, and 613 cm^{-1} are clear indicators of VO_2 similar to those reported in earlier works [21,23–26]. Figure 8.2 (c) – (d) show the surface and cross-sectional images of the VO_2 films. The SEM surface images obtained from the VO_2 films show polycrystalline structure comparable to the films investigated in Refs.

[27,28]. The structure consists of mostly irregularly structured grains with significant grain boundaries. The average grain size was determined through the ImageJ program (developed at NIH, USA) to be 180 nm ± 29 nm. From cross-sectional imaging as in Figure 8.2 (d), the thickness of the sample was determined to be 191 nm ± 8 nm. The optical transmission spectra given in Figure 8.2 (a) were used to calculate the optical constants in semiconducting and metallic phases. The Manifacier model [29] was applied to the transmission spectra in both semiconducting and metallic phases and the results were quite similar to those obtained in our previous work (Ref. [21]) and therefore not reproduced here. Good fits of the Manifacier model to the experimental spectra yielded an average film thickness of 183 nm ± 16 nm, which is close to the thickness that is obtained from SEM measurements.

Figure 8.2 (e), (f) show the temperature dependence of the electrical conductivity (σ) and relative optical transmittance ($\tilde{T}_r$) of VO_2 under constant heat/cool rate of 0.4 °C/min, where red curves indicate heating and blue curves indicate cooling process. The vertical lines in the insets show the critical temperatures obtained for heating (red) and cooling (blue) curves. The difference between $\tilde{T}$ at 1550 nm and electrical conductivity in semiconducting and metallic phases are $\Delta\tilde{T}_{1550nm} = 42\%$ and $\Delta\sigma = 2.3 \times 10^3\ \Omega^{-1}cm^{-1}$, respectively. These values are slightly less than those obtained for high-quality VO_2 films grown on r-cut sapphire substrates investigated in Ref [30].

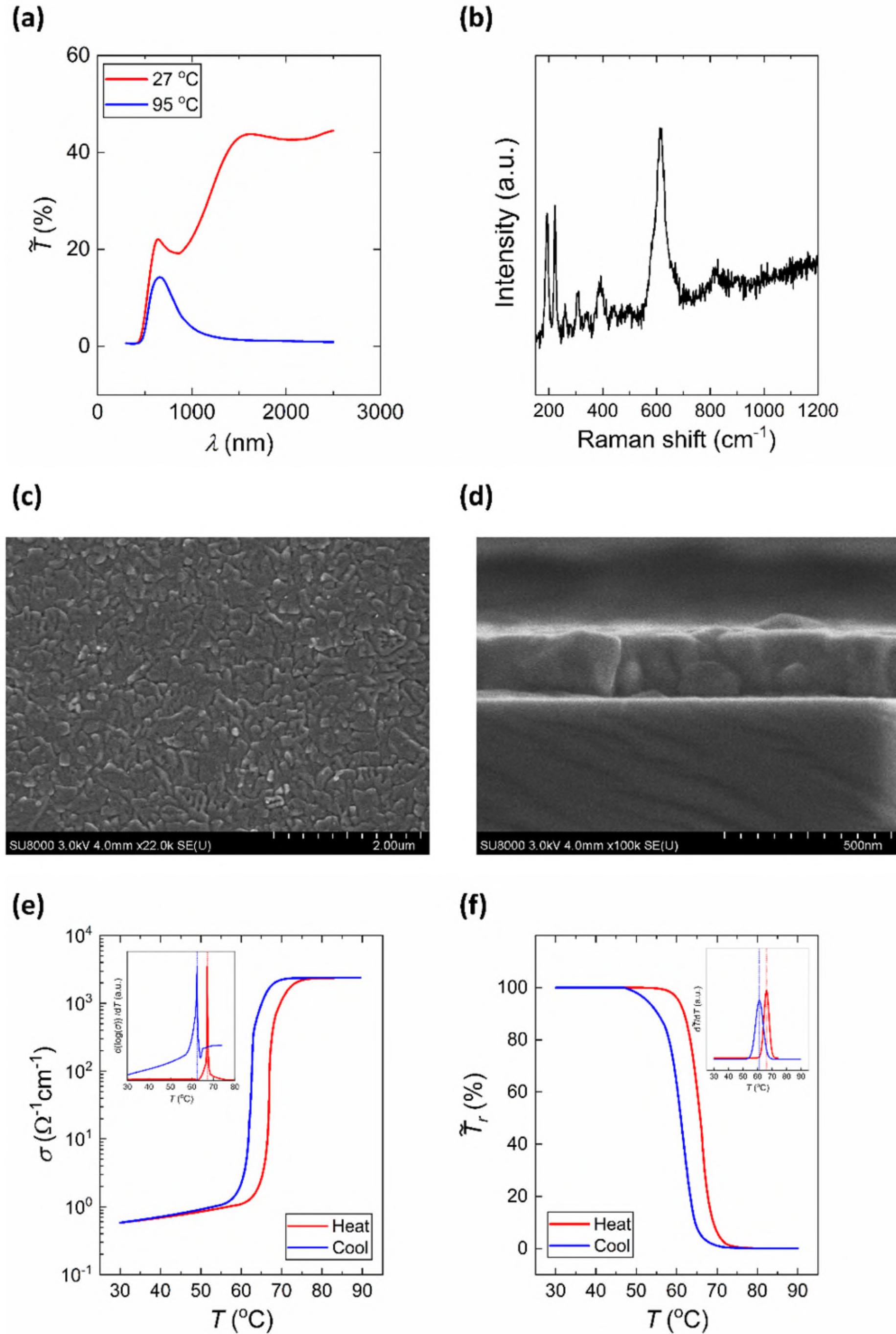

Figure 8.2 (a) Optical transmission spectrum of VO_2 films grown on c-cut sapphire at 27 °C and 95 °C. (b) Raman spectrum of VO_2 film taken at room temperature. (c) SEM surface image of the VO_2 film under 3 kV operation. (d) Cross sectional SEM image of VO_2 film under 3 kV operation. The thickness of the sample is measured as 190 nm ± 10 nm. (e) The temperature dependence of electrical conductivity at heating and cooling cycles. The inset shows the calculated T_{IMT} and T_{MIT}

which are 67.2 °C and 62.5 °C, respectively. The hysteresis width (ΔH_{elec}) is 4.7 °C. (f) The temperature dependence of relative optical transmittance ($\tilde{T}_r$) at heating and cooling cycles. The T_{IMT} and T_{MIT} are calculated as 66.2 °C and 61.3 °C. The hysteresis width (ΔH_{opt}) is approximately 4.9 °C.

Figure 8.3 summarizes the main results of the present work, given in linear axes as a function of time (t) before, during and after the application of an I_D-pulse with a duration of five seconds (Δt = 5 s). The base temperature of the sample was always kept at 57 °C during the measurements. Figure 8.3 (a) shows the σ vs. T behavior. From the behavior of σ during and after the application of the I_D-pulse, four distinctive time intervals were considered. These time intervals are analyzed in detail in Figure 8.4. During the first interval, σ remains low (typical for the VO_2 in the semiconducting phase at 57 °C). During the second short time interval, there is a sudden jump of σ. Depending on the magnitude of I_D this jump reaches up to 20–90 % of the conductivity in the metallic phase (σ_m). It is observed that the delay between the application of I_D and the burst (sudden jump) of σ decreases with increasing I_D. During the third time interval, σ gradually increases, reaching maximum conductivity (σ_m) for higher I_D (275–400 mA). Finally, during the fourth time interval when I_D is turned off, σ decreases with the rate of change from fast for small I_D (100 – 150 mA) to slow for high I_D (275 – 400 mA).

Figure 8.3 (b) shows the time dependence of the $\tilde{T}_r$. It shows that at small I_D (100–150 mA) the changes in the optical transmittance are so small that they could not be seen using the vertical scale in Figure 8.3 (b) and may be revealed only by using a special approach as given in Figure 8.4. Starting with I_D = 175 mA, the modulation of transmittance becomes clearly visible. In similarity with the conductivity, there is a clear delay between the application of I_D and the sudden drop of the transmittance. Again, the value of the delay decreases with increasing I_D. However, the values of the delay for optical transmittance are substantially larger than those for the conductivity. Overall, there is a startling dissimilarity in the temporal behavior of σ and $\tilde{T}_r$.

Figure 8.3 (c) shows the time dependence of "the temperature of the VO_2 film" on time. The results are straightforward but have one feature that specifically requires some explanation. One could anticipate an immediate increase of the film temperature as an I_D-pulse is applied and

an immediate decrease when the I_D is cut-off. However, it can be seen that there is a regular and systematic time delay of ~ 0.8 s between the I_D application and the temperature readings. Moreover, this delay seems to not depend on the value of the I_D. The possible origin of this delay as well as the reason of quoting "the temperature of the film" is straightforward and is rooted in the details of measurements. In non-steady-state conditions such as during the application of current pulses, the temperature of the Pt film may lag behind the temperature of VO_2 film as it is spatially separated by the sapphire substrate, the thermally conductive tape and the ceramic body of the thermistor. In our opinion, this may explain the systematic time delay as seen in Figure 8.3 (c). Overall, in the following discussion the time scale for "the temperature of the film" is shifted (normalized) by 0.8 s with respect to the time scale of the σ and the partial fractional volume content of the metallic phase (X_m) extracted from the optical transmittance data in Figure 8.3 (b) using Equation (8.2).

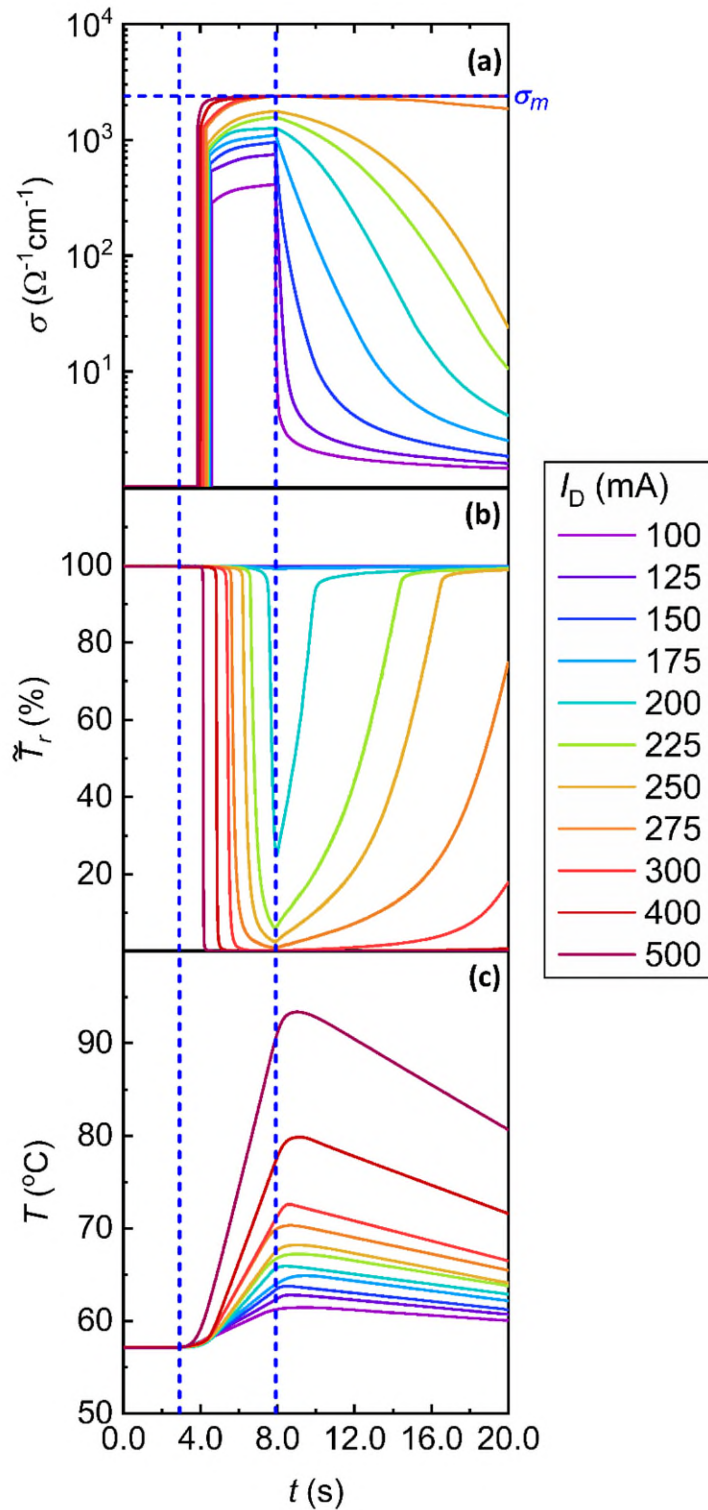

Figure 8.3 The conductivity (a), the optical transmittance (normalized to that of the film in semiconducting phase) (b) and the temperature (c) of the VO_2 film sample sketched in Figure 8.1 (a) in function of time before, during and after application of driving pulses with varying value of

electrical current passed through the VO_2 and fixed duration of 5 seconds. The sample was kept at 57 °C before and after application of the pulse. The time discretization of the experiments was 2.5 ms and therefore all faster processes appear on graphs as vertical lines. The σ_m value shows fully metallic conductivity. The optical transmittance of the VO_2 in metallic phase is zero and in semiconducting phase is taken to be 100%.

Figure 8.4 (a) and (b) show the temporal dependences of conductivity (normalized to the conductivity of the metallic phase) and the partial fractional volume content of the metallic phase (X_m) for two values of I_D (125 and 175 mA). The X_m may be related directly to optical transmittance assuming that the reduction of transmittance is due to the shadowing of light by the non-transparent metallic phase appearing during the IMT. Refs. [30–32], offer a simple way to calculate X_m as

$$X_m = \frac{\tilde{T}_M - \tilde{T}}{\tilde{T}_M - \tilde{T}_m} \tag{8.2}$$

where $\tilde{T}_M$ and $\tilde{T}_m$ are the maximal and the minimal optical transmittance of the VO_2 film in the semiconducting or in the metallic phase, respectively. Figure 8.4 (c) – (d) present the temporal dependences of the temperature of the sample. The time scale in Figure 8.4 (a) is split into time intervals from A to E to facilitate the description and discussion, which the four time intervals from (A–D) are during the application of I_D and one time interval (E) is the recovery period after the applicationof the I_D pulses.

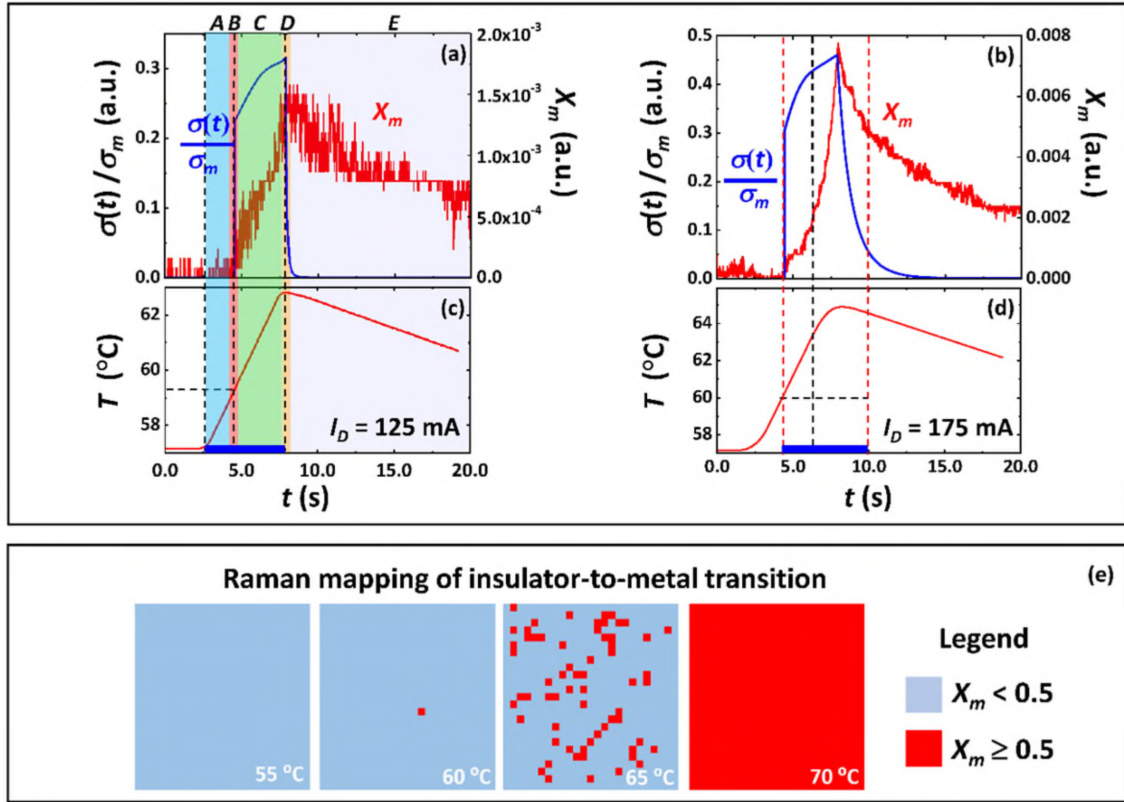

Figure 8.4 (a), (b) The dynamics of conductivity normalized to that of VO_2 in metallic phase ($\sigma(t)/\sigma_m$) and partial concentration of the metallic phase (X_m) before, during and after application of I_D pulses with electrical current of 125 mA (a), (c) and 175 mA (b), (d). The pulse duration is 5 seconds and the time position is marked by the blue rectangular on the lower time axis. (b), (d) The corresponding dynamics of VO_2 temperature. All data are re-calculated from Figure 8.3. The time scale in (a) and (c) is split into time intervals $A - E$ with varying highlighting. The meaning of the intervals $A - E$ is explained in the text. The size of big squares is 25×25 pixels. The size of single pixel is 1.2×1.2 μm. The legend shows the color coding of the partial concentration of the metallic phase (X_m) in single pixel. The numbers in the maps refer to the substrate temperature (°C).

Within the first time interval A, the constant current I_D is on, and the T slowly rises but σ and X_m remain zero. With the beginning of the second time interval B, the T reaches around 59

– 60 °C and within a very short period, the σ experiences a sudden and very sharp, burst-like initial rise. The burst in σ reaches up to ~ 22% of σ_m for I_D = 125 mA and ~ 30% of σ_m for I_D = 175 mA. This sudden burst is faster than the time resolution of the apparatus (2.5 ms) and the change of σ is presented in the graph by the vertical line (within *B*). Meanwhile, X_m remains close to zero. During the third time interval *C*, the σ continues to rise. By the end of the I_D pulse, it reaches ~33% σ_m for I_D = 125 mA and ~47% σ_m for I_D = 175 mA. There is also a gradual increase of X_m reaching quite small values of ~1.5×10^{-3} for I_D =125 mA and ~8×10^{-3} for I_D = 175 mA. In the interval *C,* the *T* keeps rising as well. Within the short time interval *D,* the pulse duration ends and the I_D is off. This results in a sharp drop of σ for I_D = 125 mA and slower drop for I_D = 175 mA. In the last time interval *E,* the I_D is off and the sample cools down back to the base temperature of 57 °C. The σ gradually drops to zero with the rate of drop depending on the value of the I_D. Hence, the X_m and *T* gradually decrease. What is intriguing is that at longer observation times (> 15 s), the σ reaches its minimum ($\sigma \approx 10^0$ Ω^{-1}cm^{-1}) while X_m is small but still measurable. Figure 8.4 (e) shows the phase map of VO_2 film undergoing the IMT. The phase map was collected by measuring the Raman spectra at certain temperatures under steady-state conditions. The map shows that at 55 °C, the VO_2 is in the semiconducting phase and the first predominantly metallic nucleus appears at 60 °C. At 65 °C, metallic clusters may be detected while at 70 °C and above, the domination of metallic phase becomes obvious.

Figure 8.5 shows the model of the events happening within time intervals marked as *A* – *E* in Figure 8.4 and *A* – *C*, *D′* – *F′* in Figure 8.6. The detailed explanations are given in the Discussion section. Figure 8.6 shows the temporal dynamics of σ, X_m and the *T* for larger I_D. The presentation of time intervals *A* – *C*, *D′* – *F′* is given in Figure 8.6 (c). In general, Figure 8.6 is similar to Figure 8.4 with one strikingly different feature: a sudden and fast increase of X_m within short time interval *D′*. Here the sequence of events happening within defined time intervals may be explained one by one. Within the time interval *A*, the current I_D is on, the *T* is slowly rising but the σ remains small (typical for the semiconductor phase) and the X_m remains zero. Similarly, in Figure 8.4, with the beginning of time interval *B,* the *T* reaches 59 – 60 °C, and within a very short time interval *B*, the σ experiences a sudden and sharp burst to ~ 35 – 60 % of σ_m. Within time interval *C*, the σ grows steadily up to ~ 55 – 100% of σ_m as the *T* reaches 63 – 65 °C. Concurrently, the X_m grows slowly,

and this growth may only be detected only using × 20 magnification shown by broken magenta lines in Figure 8.6 (a) – (c). By the time interval *D′* the *T* reaches 65 – 66 °C and during this very short time interval the X_m experiences sharp burst and reaches the values 0.3 – 0.9 which show a substantial presence of metallic phase. Meanwhile, no sharp changes in σ is detected. Within time interval *E′* the σ, the X_m and *T* keeps growing steadily. At I_D = 275 mA σ reaches σ_m as well as X_m reaches 1.0, pointing to full conversion of VO_2 into metallic phase, and the *T* reaches 70 °C. During time interval *E′* the current I_D is off and the *T*, σ and X_m are decreasing. The interesting observation about this time interval is that the X_m decreases faster than the σ in sharp contrast to the small I_D case (Figure 8.4 (a)).

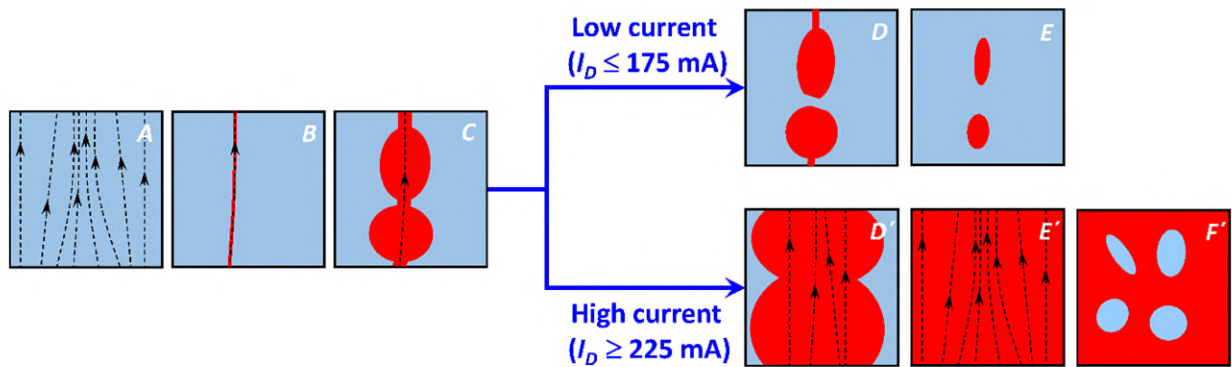

Figure 8.5 The simplified model of the events happening during the time intervals *A* – *E* in Figure 8.4 and time intervals *A* – *C* and *D′* – *F′* in Figure 8.6. Blue color corresponds to the semiconducting phase and the red color to the metallic one. Broken arrows schematically show the flow and the spatial distribution of the driving electrical current I_D. All other necessary explanations are given in the text.

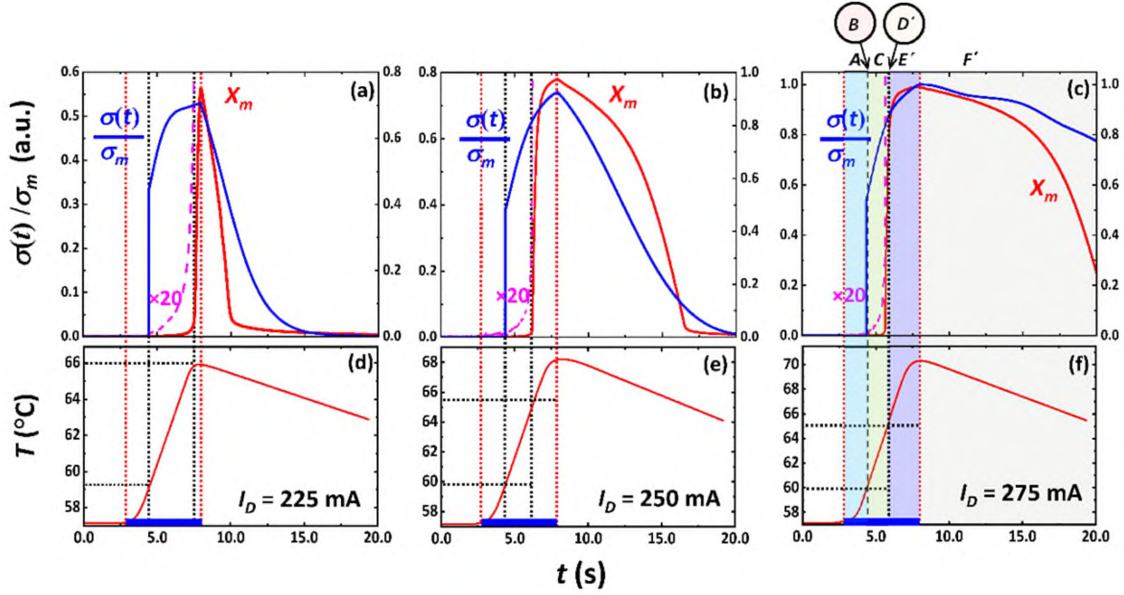

Figure 8.6 (a) – (c) The dynamics of conductivity normalized to that of VO_2 in metallic phase ($\sigma(t)/\sigma_m$) and partial concentration of the metallic phase (X_m) before, during and after application of driving pulses with electrical current of 225 mA in (a) and (d), 250 mA in (b) and (e), and 275 mA in (c) and (f). The pulse duration is 5 seconds. Broken magenta lines present the same data as thick red lines but with (× 20) magnification. (d) – (f) show the corresponding dynamics of VO_2 temperature. The pulse duration is 5 seconds, and the time position is marked by the blue rectangular on the lower time axis. All data are re-calculated from Figure 8.1. The time scale in (c) and (f) is split into time intervals *A*, *B, D'– F'* with varying highlighting. The meaning of the intervals *A*, *B, D'– F'* is explained in the text.

Figure 8.7 shows the dependences of relative conductivity (σ/σ_m) on X_m for different I_Ds. The dependences are recalculated from Figure 8.6 (a) – (c) using the decaying part of the curves after switching of the I_D. The sharp kink in the σ (X_m) slope takes place at $X_m = 0.02 – 0.05$ and it is highlighted.

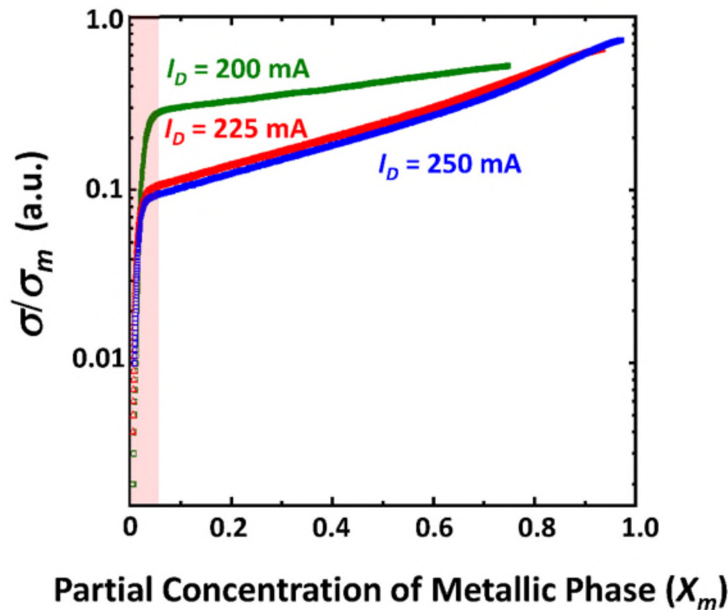

Figure 8.7 The conductivity versus partial concentration of metallic phase (X_m). The data are taken from Figure 8.6 (a) – (c) when σ and X_m are relaxing when I_D is off. Note that both X_m and σ/σ_m are measured in non-steady-state conditions while the sample, previously heated by the driving pulse, is uncontrollably cooling down to 57 °C.

8.5 Discussion

In this study, we have examined the self-heating effect caused by DC current pulses (I_D) that were passed through VO_2 films grown on c-cut sapphire between two coplanar Au electrodes. As indicated in the previous section, before applying the I_Ds the T was stabilized at 57 °C which is at the brink of IMT. At this temperature, the VO_2 was in the purely semiconducting phase, as confirmed by the micro-Raman mapping given in Figure 8.4. Experimental data in Figure 8.3 show that passing I_D leads to a rise of the T and, consequently, the appearance of the metallic phase in the film. In other words, passing I_D through the VO_2 film leads to the appearance and ensuing growth of the metallic content (X_m) with a related increase in the conductivity (σ). We start the discussion of the experimental data for I_D = 125 mA shown in Figure 8.5 and we go through the time intervals $(A) - (E)$ (highlighted in Figure 8.4 (a) – (c)) while developing the model which is schematically presented in Figure 8.5 $(A) - (E)$. As the next step, we analyze the data for larger

current I_D = 275 mA shown in Figure 8.6 (c) – (f) and discuss the corresponding model presented in Figure 8.5 (A) – (C) and (D') – (F'). Then, we go through time intervals $A - E$ from Figure 8.4 (a), (c) one by one.

As mentioned earlier, within the first time interval A, the current I_D is already causing a gradual rise in the T while the σ remains small, typical for a semiconductor, and X_m remains zero. A in Figure 8.5 represents this process of the initial SH of the sample. The next very short time interval B presents the most fascinating result of the present research. This interval shows the sudden growth of the σ surprisingly preceding the appearance of any measurable amount of X_m. Here, it is useful to mention that the electrically driven IMT, more precisely the voltage induced IMT, in VO_2 has already been proposed for utilization in new generation memory devices [33–35]. Also, the mechanism of the IMT has been investigated in a series of papers, [36–38] and it is agreed that the IMT is based on local formation of a hot ultra-thin channel (filament) with metallic conductivity. Moreover, another interesting observation is the spontaneous and gradual constriction of the electric current in the semiconducting phase of VO_2 which precedes the local IMT. [39] As summarized in Ref. [40] "in the blow-up regime, the IMT occurs locally even in uniform films: a narrow 'hot' metallic channel along the current direction arises in the insulating 'cool' environment". All these considerations are schematically reflected in Figure 8.5. A in Figure 8.5 shows the current flow in semiconducting VO_2 on the brink of IMT. The non-uniformity of the flow may be connected with the polycrystallinity of VO_2. However, the non-uniformity may not be necessary as the IMT occurs locally even in uniform films. [40] B in Figure 8.5 illustrates the current constriction leading to local IMT with the formation of an ultra-thin conductive channel with metallic conductivity. C and D in Figure 8.5 show that this process takes place when the T_s reach 59 – 60 °C. Meanwhile, the Raman experiments carried out in steady-state conditions and presented in Figure 8.4 (e) also show the appearance of first metallic inclusions at around 60 °C [21].

During the time interval C in Figure 8.4 (a), (c), the σ and X_m gradually rise. Noticeably, that how small X_m is very small: even by the end of the driving pulse it does not reach 1%. The T also rises and reaches 63 – 65 °C by the end of the pulse. The possible explanation is given in C in Figure 8.5, which suggests the widening of a conductive channel with metallic conductivity.

Such scenario is supported by the Raman data in Figure 8.4 which show the active formation of linear and isolated metallic clusters at 65 °C in steady-state condition. Here it is appropriate to mention an interesting method of cluster visualization of the insulator-insulator and the insulator-mixed-metal-insulator-transitions in self-heated $Al_xV_{1-x}O_2$ single-crystals reported in Ref. [41].

Within the short time interval *D,* the I_D is cut-off and the σ rapidly decreases. The smaller the I_D, the faster the σ recovers back to its minimum. In contrast, the decrease rate of X_m is much smaller. Figure 8.5 (*D*) gives a possible explanation of the situation. The conductive channel, which was initially over-heated by passing constant current, releases heat to the ambient. As a result, the conductive channel narrows and eventually loses continuity. The duration to full discontinuity depends on the initial width of the conductive channel and is longer for larger I_Ds (compare Figure 8.6 (a) and (b)). The metallic phase remains in a form of dead pools as shown in *D* and *E* in Figure 8.5. Within the last time interval *E*, the I_D is off, and the metallic dead pools slowly disappear giving rise to a gradual decrease of X_m (see the model in *E* in Figure 8.5).

As the I_D exceeds 225 mA, a new feature appears: a sudden burst of X_m within a short time interval D' as shown in Figure 8.6 (c). The previous stages $A - C$ are similar to what was discussed earlier. However, the initial growth of X_m during $A - C$ may be detected only under proper (×20) magnification (broken magenta lines in Figure 8.6 (a) to (c)). Figure 8.6 (d) – (f) show that the burst in X_m happens when the T reaches 65 − 66 °C. According to the Raman data in Figure 8.4 (e), 65 °C is the beginning of a massive transition to the metallic phase, while at 70 °C the VO_2 film is already fully metallic. The latter is reflected in the model of the stage D' in Figure 8.5. The heat produced by a conduction channel is sufficient for the large part of the film to reach the IMT temperature. As a result, there is an intensive conversion of the semiconducting phase into the metallic one. In the next time interval E', σ and X_m gradually increase. By the end of E', at maximal I_D = 275 mA, the T reaches 70 °C, and as a result the X_m finally reaches 1.0. The IMT is complete and the entire film resides in the metallic phase.

During the time interval F', the driving current is cut-off and the sample cools down (back to 57 °C). The σ and X_m gradually decrease but the X_m decreases faster unlike the small current case (i.e., Figure 8.4 (a)). The model of the cooling events during F' in Figure 8.6 is given by F' in Figure 8.5. In our previous paper [30] we have shown that the MIT happens through the formation

of semiconducting bubbles in the metallic matrix. The appearing structure is sometimes referred to as "Swiss cheese" structure, with the "cheese" being highly conductive metallic phase and the "pores" being poorly conductive semiconducting phase. An interesting feature of Swiss cheese structure is a very low percolation limit ($X_c^{(c)}$), where 6% of the X_m is needed to sustain the metallic conductivity. Figure 8.7 shows the dependence of σ versus X_m derived from the data in Figure 8.6 (a) – (c) taken during the time interval E'. Despite some differences in the curves corresponding to different I_Ds there is one common feature: A kink at $X_m \approx 3 - 5\%$. By analogy to our previous paper [30], this kink may be interpreted as a sign of a transition from the metallic (larger X_m) to semiconducting (smaller X_m) conductivity. The small value of the critical X_m ($X_c^{(c)} = 6\%$) agrees well with the Swiss cheese model, which explains the faster decrease of X_m compared to σ.

8.6 Summary

The time dependences of the electrical conductivity (σ), optical transmittance at 1550 nm ($\tilde{T}$) and film temperature (T) of VO_2 films grown on c-cut sapphire have been measured during the Joule self-heating (SH) caused by passing a constant current along the film as rectangular current pulses with varying magnitude (I_D) and constant duration of 5 seconds. Prior to I_D-pulse application, the films were maintained at 57 °C in the semiconducting phase. The SH leads to a rise in T and, consequently, to a transition of VO_2 from the insulating-to-metallic phase (IMT) causing substantial changes in σ and $\tilde{T}$. The value of optical transmittance $\tilde{T}$ was used to calculate the partial concentration of the metallic phase X_m. For all I_D we observe a sudden burst-like growth of σ preceding the appearance of any measurable amount of X_m. Using the percolation model presented in Ref. [30], this effect is explained by local IMT and the formation of an ultra-thin hot highly conductive metallic channel within a cool semiconducting VO_2 matrix. All in all, depending on the magnitude of I_D, σ and $\tilde{T}$ demonstrate strikingly different temporal behavior during the SH induced IMT and backward recovery to the insulating phase after the cessation of the I_D-pulse. We have developed a phenomenological model and confirmed the observations by comparing them with the earlier IMT Raman micro-mapping images obtained at various temperatures, before and after the IMT.

8.7 References

[1] F. J. Morin, "Oxides which show a metal-to-insulator transition at the Neel temperature," *Physics Review Letters*, vol. 3, pp. 34-36, 1959.

[2] K. Schneider, "Optical properties and electronic structure of V2O5, V2O3 and VO2," *Journal of Materials Science: Materials in Electronics*, vol. 31, no. 13, pp. 10478-10488, 2020.

[3] Z. Shao, X. Cao, H. Luo and P. Jin, "Recent progress in the phase-transition mechanism and modulation of vanadium dioxide materials," *NPG Asia Materials*, vol. 10, no. 7, pp. 581-605, 2018.

[4] Y. Zhang, W. Xiong, W. Chen and Y. Zheng, "Recent progress on vanadium dioxide nanostructures and devices: Fabrication, properties, applications and perspectives," *Nanomaterials*, vol. 11, no. 2, p. 338, 2021.

[5] K. Liu, S. Lee, S. Yang, O. Delaire and J. Wu, "Recent progresses on physics and applications of vanadium dioxide," *Materials Today*, vol. 21, no. 8, pp. 875-896, 2018.

[6] D. Malarde, M. J. Powell, R. Quesada-Cabrera, R. L. Wilson, C. J. Carmalt, G. Sankar, ... and R. G. Palgrave, "Optimized atmospheric-pressure chemical vapor deposition thermochromic VO2 thin films for intelligent window applications," *ACS Omega*, vol. 2, no. 3, pp. 1040-1046, 2017.

[7] H. Ren, O. Hassna, J. Li and B. Arigong, "A patterned phase-changing vanadium dioxide film stacking with VO2 nanoparticle matrix for high performance energy-efficient smart window applications," *Applied Physics Letters*, vol. 118, no. 5, p. 051901, 2021.

[8] F. Qaderi, T. Rosca, M. Burla, J. Leuthold, D. Flandre and A. Ionescu, "Millimeter-wave to near-terahertz sensors based on reversible insulator-to-metal transition in vanadium dioxide," 2022.

[9] J. Liang, K. Zhang, T. Su, S. Wang and X. Yu, "Design and fabrication of frequency-responsive terahertz transmittance modulator based on vanadium dioxide spherical films," *Optics Communications*, vol. 488, p. 126834, 2021.

[10] G. Wu, X. Jiao, Y. Wang, Z. Zhao, Y. Wang and J. Liu, "Ultra-wideband tunable metamaterial perfect absorber based on vanadium dioxide," *Optics Express*, vol. 29, no. 2, pp. 2703-2711, 2021.

[11] R. Cabrera, E. Merced and N. Sepúlveda, "A micro-electro-mechanical memory based on the structural phase transition of VO2," *physica status solidi (a)*, vol. 210, no. 9, pp. 1704-1711, 2013.

[12] J. Jiang, G. Chugunov and R. R. Mansour, "Fabrication and characterization of VO2-based series and parallel RF switches," 2017.

[13] T. Driscoll, H. T. Kim, B. G. Chae, M. Di Ventra and D. N. Basov, "Phase-transition driven memristive system," *Applied Physics Letters*, vol. 95, no. 4, p. 043503, 2009.

[14] S. H. Bae, S. Lee, H. Koo, L. Lin, B. H. Jo, C. Park and Z. L. Wang, "The memristive properties of a single VO2 nanowire with switching controlled by self-heating," *Advanced Materials*, vol. 25, no. 36, pp. 5098-5103, 2013.

[15] H. Coy, R. Cabrera, N. Sepúlveda and F. E. Fernández, "Optoelectronic and all-optical multiple memory states in vanadium dioxide," *Journal of Applied Physics*, vol. 108, no. 11, p. 113115, 2010.

[16] L. Pellegrino, N. Manca, T. Kanki, H. Tanaka, M. Biasotti, E. Bellingeri, ... and D. Marré, "Multistate memory devices based on free-standing VO2/TiO2 microstructures driven by Joule self-Heating," *Advanced Materials*, vol. 24, no. 21, pp. 2929-2934, 2012.

[17] S. Carapezzi, E. Corti, A. Nejim, S. Karg and A. Todri-Sanial, "TCAD electrothermal simulations of self-oscillations in vanadium dioxide devices for oscillatory neural networks," 2021.

[18] A. A. Sharma, J. A. Bain and J. A. Weldon, "Phase coupling and control of oxide-based oscillators for neuromorphic computing," *IEEE Journal on Exploratory Solid-State Computational Devices and Circuits*, vol. 1, pp. 58-66, 2015.

[19] N. Shukla, A. Parihar, E. Freeman, H. Paik, G. Stone, V. Narayanan, ... and S. Datta, "Synchronized charge oscillations in correlated electron systems," *Scientific Reports*, vol. 4, no. 1, pp. 1-6, 2014.

[20] X. Hong, D. J. Loy, P. A. Dananjaya, F. Tan, C. Ng and W. Lew, "Oxide-based RRAM materials for neuromorphic computing," *Journal of Materials Science*, vol. 53, no. 12, pp. 8720-8746, 2018.

[21] C. Zhang, C. Koughia, O. Güneş, J. Luo, N. Hossain, Y. Li, ... and S. Kasap, "Synthesis, structure and optical properties of high-quality VO2 thin films grown on silicon, quartz and sapphire substrates by high temperature magnetron sputtering: Properties through the transition temperature," *Journal of Alloys and Compounds,* vol. 848, p. 156323, 2020.

[22] C. Zhang, C. Koughia, Y. Li, X. Cui, F. Ye, S. Shiri, M. Sanayei, S.-J. Wen, Q. Yang and S. Kasap, "Near-zero IR transmission of VO2 thin films deposited on Si substrate," *Applied Surface Science*, vol. 410, p. 415, 2018.

[23] Y. Zhao, J. Hwan Lee, Y. Zhu, M. Nazari, C. Chen, H. Wang, ... and Z. Fan, "Structural, electrical, and terahertz transmission properties of VO2 thin films grown on c-, r-, and m-plane sapphire substrates," *Journal of Applied Physics*, vol. 111, no. 5, p. 05, 2015.

[24] Z. Xiang, Z. Wu, C. Ji, Y. Shi, J. Dai, Z. Huang, ... and Y. Jiang, "Low temperature fabrication of high-performance VO2 film via embedding low vanadium buffer layer," *Applied Surface Science*, vol. 517, p. 146101, 2020.

[25] F. Ureña-Begara, A. Crunteanu and J. P. Raskin, "Raman and XPS characterization of vanadium oxide thin films with temperature," *Applied Surface Science*, vol. 403, pp. 717-727, 2017.

[26] T. D. Vu, S. Liu, X. Zeng, C. Li and Y. Long, "High-power impulse magnetron sputtering deposition of high crystallinity vanadium dioxide for thermochromic smart windows applications," *Ceramics International*, vol. 46, no. 6, pp. 8145-8153, 2020.

[27] S. Yu, S. Wang, M. Lu and L. Zuo, "A metal-insulator transition study of VO2 thin films grown on sapphire substrates," *Journal of Applied Physics*, vol. 122, no. 23, p. 235102, 2017.

[28] B. G. Chae, H. T. Kim, S. J. Yun, B. J. Kim, Y. W. Lee, D. H. Youn and K. Y. Kang, "Highly oriented VO2 thin films prepared by sol-gel deposition," *Electrochemical and Solid-state Letters*, vol. 9, no. 1, p. C12, 2005.

[29] J. C. Manifacier, J. Gasiot and J. P. Fillard, "A simple method for the determination of the optical constants n, k and the thickness of a weakly absorbing thin film," *Journal of Physics E: Scientific Instruments*, vol. 9, no. 11, p. 1002, 1976.

[30] C. Koughia, O. Gunes, C. Zhang, S. J. Wen, R. Wong, Q. Yang and S. O. Kasap, "Topology of conductive clusters in sputtered high-quality VO2 thin films on the brink of percolation threshold during insulator-to-metal and metal-to-insulator transitions," *Journal of Vacuum Science & Technology A: Vacuum, Surfaces, and Films*, vol. 38, no. 6, p. 063401, 2020.

[31] J. Rozen, R. Lopez, R. F. Haglund Jr. and L. C. Feldman, "Two-dimensional current percolation in nanocrystalline vanadium dioxide films," *Applied Physics Letters*, vol. 88, no. 8, p. 081902, 2006.

[32] Y. J. Chang, C. H. Koo, J. S. Yang, Y. S. Kim, D. H. Kim, J. S. Lee, T. W. Noh, H.-T. Kim and B. G. Chae, "Phase coexistence in the metal–insulator transition of a VO2 thin film," *Thin Solid Films*, vol. 486, no. 1-2, pp. 46-49, 2005.

[33] V. G. Karpov and D. Niraula, "Resistive switching in nano-structures," *Scientific Reports*, vol. 8, no. 1, pp. 1-10, 2018.

[34] Y. Zhou, X. Chen, C. Ko, Z. Yang, C. Mouli and S. Ramanathan, "Voltage-triggered ultrafast phase transition in vanadium dioxide switches," *IEEE Electron Device Letters*, vol. 34, no. 2, pp. 220-222, 2013.

[35] A. Joushaghani, J. Jeong, S. Paradis, D. Alain, J. S. Aitchison and J. K. Poon, "Wavelength-size hybrid Si-VO 2 waveguide electro absorption optical switches and photodetectors," *Optics Express*, vol. 23, no. 3, pp. 3657-3668, 2015.

[36] I. Valmianski, P. Y. Wang, S. Wang, J. G. Ramirez, S. Guénon and I. K. Schuller, "Origin of the current-driven breakdown in vanadium oxides: Thermal versus electronic," *Physical Review B*, vol. 98, no. 19, p. 195144, 2018.

[37] A. Zimmers, L. Aigouy, M. Mortier, A. Sharoni, S. Wang, K. G. West, ... and I. K. Schuller, "Role of thermal heating on the voltage induced insulator-metal transition in VO2," *Physical Review Letters*, vol. 110, no. 5, p. 056601, 2013.

[38] J. G. Ramírez, R. Schmidt, A. Sharoni, M. E. Gómez, I. K. Schuller and E. J. Patino, "Ultra-thin filaments revealed by the dielectric response across the metal-insulator transition in VO2," *Applied Physics Letters*, vol. 102, no. 6, p. 063110, 2013.

[39] J. M. Goodwill, G. Ramer, D. Li, B. D. Hoskins, G. Pavlidis, J. J. McClelland, ... and M. Skowronski, "Spontaneous current constriction in threshold switching devices," *Nature Communications*, vol. 10, no. 1, pp. 1-8, 2019.

[40] V. I. Polozov, S. S. Maklakov, A. L. Rakhmanov, S. A. Maklakov and V. N. Kisel, "Blow-up overheating instability in vanadium dioxide thin films," *Physical Review B*, vol. 101, no. 21, p. 214310, 2020.

[41] B. Fisher, L. Patlagan, A. Eyal and G. M. Reisner, "The insulator–insulator and the insulator–mixed-metal–insulator transitions in self-heated AlxV1− xO2 single crystals and their visualization," *physica status solidi (a)*, vol. 218, no. 9, p. 2000820, 2021.

9. Conclusions and Future Work

9.1 Conclusions

This dissertation has covered the fabrication of vanadium dioxide (VO_2) thin films and their structural, optical and electrical characterizations under various fabrication conditions towards obtaining films with optimum characteristics as well as providing more physical insight into the insulator-to-metal (IM) and metal-to-insulator (MI) phase transitions. The conducted studies in this work have can be categorized as follows. The first attempt was to study the effect of substrate biasing on the quality of the VO_2 thin films. The second step focused on the investigation of the effect of substrate temperature on the structural, optical and electrical properties of the VO_2 thin films. Thirdly, the near-epitaxial growth of VO_2 films on single-crystal silicon (100), quartz and r-cut sapphire substrates was studied. The fourth study examined the topology of infinite conductive clusters during IMT and MIT. The fifth study focused on the self-heating-induced electrical and optical switching of VO_2 films grown on c-cut sapphire substrates. These studies are summarized in the two sections introduced below.

9.1.1 Fabrication of VO_2 Thin Films Under Different Deposition Conditions

VO_2 thin film fabrication was carried out under two different deposition conditions which involved varying the substrate biasing and the substrate temperature. The effect of substrate biasing on the quality of VO_2 thin films grown on single-crystal Si (100) and r-cut sapphire substrates was investigated under four different biasing voltages, which were 89 V, 126 V, 146 V and 173 V. The examination of the surface morphology of the materials through Raman, SEM and XPS showed that increasing substrate bias leads to a drop in the deposition rate, which is accompanied by an increase in the grain size. The latter was attributed to secondary nucleation. The reduced deposition rate resulted in thinner films. Furthermore, it was observed that the optical properties degraded with increasing substrate biasing. On the other hand, the transition temperature was increased by 14 K and the hysteresis width broadened with increasing substrate bias voltage. The Swanepoel model was applied to the transmittance spectrum of the films to extract the indirect bandgap of 0.6 ± 0.05 eV, where the attenuation of light in the films was not only related to band-to-band absorption but also affected by surface scattering.

The second study on the fabrication of VO_2 films involved the effect of substrate temperature (T_S) on the phase transition qualities of VO_2 thin films. The examination of the films included structural investigation using XRD, SEM and XPS as well as the characterization of optical and electrical phase transition properties. It is observed that the quality of VO_2 thin films degraded as the substrate temperature was reduced to 500 °C, where the T_S below this value favoured the growth of V_2O_5 phase. For VO_2 films prepared at low T_S, reduced optical and electrical phase transition properties such as broadened hysteresis, and transition temperature that shifted towards low temperatures (i.e., T_t around 320 K for films on Si and r-cut sapphire substrate prepared at T_S = 500 °C) were observed. The degrading of the optical transmittance throughout the NIR regime reflects the worsening of the optical modulation efficiencies of the films with decreasing T_S. SEM surface images showed that the grain size became smaller with decreasing T_S. The worsening of the optical and electrical properties was related to structural defects and unrelaxed lattice strain in the film.

The third study focused on the preparation of VO_2 films on three different single-crystal substrates, silicon, quartz and sapphire have been commonly used in semiconductor research and development applications that are based on VO_2 films. The reason for the silicon substrate was to attempt to incorporate VO_2 films into the standard microelectronics technology, which is almost totally based on silicon. This study aimed to determine the best substrate that would deliver the highest quality of VO_2 thin films under uniform deposition conditions using the DC magnetron sputtering technique. The optical characterization experiments have shown a high switching contrast (on silicon: 56%, on sapphire: 52% at a wavelength of λ = 2500 nm) and a near-zero IR transmission in the switched metallic phase. The highest quality film was achieved on r-cut sapphire substrate as it displayed the narrowest hysteresis width and highest sharpness in the optical phase transition, which was very close to their bulk single-crystal form. The SEM images revealed that the films grown on sapphire substrates had a flat surface with no grain boundaries. The outcomes were related to the significantly reduced imperfections in the film with similar grain orientation between the VO_2/sapphire interface due to epitaxial growth during high-temperature (650 °C) deposition. The refractive index (n) and extinction coefficients (K) of VO_2 films extracted agreed with those obtained in previously published works. In addition, this study revealed the coexistence of insulating and metallic phases by Raman mapping of the VO_2 films under various temperatures, below and above MIT, during the heating and cooling of the films. This outcome

gave an incentive to study the phase transition phenomenon in VO_2 films by means of the percolation theory. Moreover, the Manifacier technique was applied in the presence of absorption for extracting optical constants of a thin film to n and K. The dispersion data were obtained (n and K vs. λ) for the films deposited on quartz and sapphire substrates. From the extinction coefficient K, the absorption coefficient α was obtained. Additionally, from the dependence of the α on the photon energy, it was shown that as-prepared VO_2 films had an indirect bandgap of 0.52 eV and a direct bandgap of 2.6 eV.

9.1.2 Investigation of Phase Transition in VO_2 Thin Films

In this work, two different physical phenomena were studied. The first phenomenon focused on the IM and MI phase transitions in VO_2 thin films. In this respect, both phase transitions were considered to take place by means of percolating infinite conductive clusters. The experimental data on the temperature (T) dependence of both electrical conductivity (σ) and optical transmittance ($\tilde{T}$) was used to examine the phase transition phenomenon. In this regard, classical effective medium approximations (EMAs) such as the Maxwell-Garnet equation and Bruggeman rule were taken into consideration as a conventional approach. Nevertheless, the EMAs were not able to explain the behavior of partial metallic concentration (mixed phase region) during IMT and MIT. However, the percolative theory was considered to explain the data. In this regard, Efros-Shklovskii (ES) theoretical model was taken into account to examine the temperature dependence of partial metallic concentration during the IMT and MIT. The analyses showed that the metallic infinite conductive cluster (ICC) had a two-dimensional expansion throughout the volume of the film during the IMT. On the other hand, during the MIT, the appearance and formation of the insulating phase were three-dimensional and resembled Swiss cheese structure. The difference in the topology of ICC was related to the local mechanical stresses present in the insulating and metallic phases of the material, tensile and compressive, respectively.

The second investigation focused on the self-heating-induced electrical and optical switching in a high-quality VO_2 film by the driving constant currents (I_D). The observations showed that depending on the magnitude of I_D, the σ and $\tilde{T}_r$ have demonstrated a remarkable difference in their temporal behavior not only during the self-heating (SH) induced MIT but also

after the removal of I_D. The difference between the electrical and optical switching at I_D between 100 and 150 mA was attributed to the local formation of a hot ultra-thin channel with metallic conductivity. On the other hand, the modulation of transmittance was obtained to be clear for I_D between 175 and 500 mA as the effect of SH became more prominent throughout the volume of the film. These observations were explained by building a simple model based on the percolation theory. The outcome of the model was compared and verified with the results of the structural MIT obtained from the Raman mapping.

9.2 Future Works

9.2.1 Elemental Doping in VO_2 Thin Films

Elemental doping stands as an important topic in research on VO_2 thin films because it can be used to manipulate the phase transition properties of VO_2. As mentioned in this thesis, the main goal of doping is to either elevate or reduce the phase transition temperature (T_{MIT}) by preserving optimal hysteresis width and transition sharpness. Among various elements that have been already considered as dopants, we propose the study of Nb and Ge doping in VO_2 thin films. These elements carry particular interest not only for shifting the T_{MIT} to higher (Ge doping) or lower (Nb doping) temperatures but also there is limited work no these particular elements and what effect they really have on the properties of VO_2 films. There is particular interest in doping in VO_2 thin films with Nb and Ge by means of ion implantation. Until now, a comprehensive investigation of optical, electrical and structural characterization of VO_2 films implanted with Ge and Nb has not been reported. Particularly, there are only a few reports on Ge doping in VO_2 films [1–3]. A comprehensive characterization should consist of optical transmittance, electrical resistivity, excess $1/f$ noise characteristics, thermoelectric (Seebeck) effect, and structural characterization using atomic force microscopy (AFM), Rutherford backscattering (RBS), Raman spectroscopy, scanning electron microscopy (SEM), x-ray diffraction (XRD) and x-ray photoelectron spectroscopy (XPS).

9.2.2 Excess Noise in VO_2 Thin Films

Excess noise is an undesirable component of electronic fluctuations in electronic devices and systems. This phenomenon represents fluctuations that are above shot and thermal noise. Excess noise is likely to cause distortions in signal transfers which lead to false output signals of electronic devices. One form of excess noise is flicker noise (or $1/f$ noise). Noise characterization is essential in developing models to eliminate noise and produce high signal-to-noise ratio systems. The noise spectral power density of has a spectrum that has a frequency dependence of the form f^{α} where α is between ≈ 1 and 2. Until now, there have been only two reports on the topic, one of which has been by Andreev et al. [4] on a single-crystal VO_2, and the other by Topalian et al. [5] on VO_2 film on a sapphire substrate as a lithographic micro-structure. It is proposed that excess noise of bulk VO_2 films be investigated at various temperatures by use of co-planar gold electrodes separated by varying distances. This study can shed light on the conductivity fluctuations in the semiconducting and metallic phases in larger volumes of VO_2.

9.2.3 VO_2 Thin Film-Based Diffraction Gratings

A second proposal for future work is to fabricate light-intensity modulators based on diffraction gratings (DGs) for optical switching applications. The functionality of these devices is based on the diffraction of light on locally induced MITs produced by electrochromic and thermochromic switching. For electrochromic switching applications, the electric field required to induce MIT can be applied by forming numerous grid-like contacts with approximately micrometer scale (2−10 μm contact width and contact separation). On the other hand, thermochromic switching may be used to modulate the light intensity transmitted through the gratings by means of heating. Figure 9.1 (a) and (b) deliver a simple illustration of electrochromic and thermochromic DGs, respectively. In the fabrication of such diffraction gratings, we propose two methods to fabricate. The first approach to building such devices is to deposit VO_2 films on platinum (Pt) gratings with separate microscale (i.e., 10-μm) grid width and separation with 90 pairs ED-IDE1-Pt) manufactured by Micrux Technologies [6]. The alternative approach is to design diffraction gratings with various grid widths and separations in micrometer scale (e.g., 10 μm).

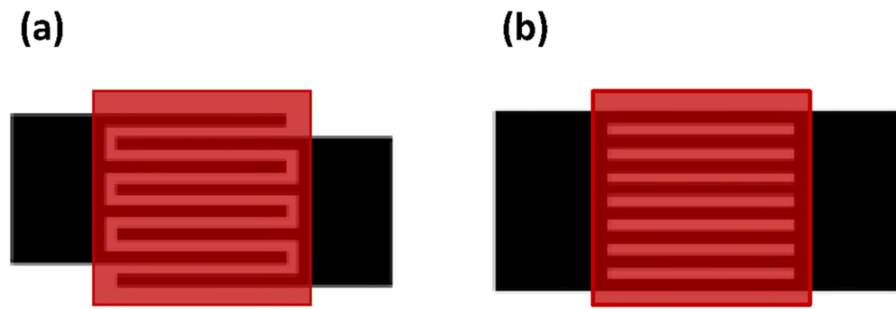

Figure 9.1 (a) Simple sketch of electrochromic diffraction gratings of electric constants for switches using electric field induced MIT (b) thermochromic diffraction gratings for thermally induced MIT. Black layers represent the gratings, and the red layers represent VO_2 films.

9.2.4 Multilayered VO_2 Thin Film Structures

As a last recommendation for future work, we express our interest in fabricating multilayer VO_2 thin film devices for dielectric mirror applications or similar photonic components. Multilayered VO_2 (A) with a transitional metal oxide (B) would produce a broad hysteresis with different refraction indexes at each layer. Such devices are potential candidates for achieving simultaneous data processing and storage. One of the main challenges is the compatibility of the material for layer B with VO_2 given that VO_2 needs to be deposited at a substrate temperature of 650 °C. Another challenge can be identified as the selection of the layer thickness and material B (i.e., transition metal oxide semiconductor such as SiO_2), which affects the structure and optical properties of the resulting AB, ABAB and ABABAB multilayered films. In the case of successful fabrication, the devices are expected to pass NIR light within a certain bandwidth of wavelength (e.g., 800-1500nm) and reflect other light with wavelengths which do not fall in the spectrum.

9.3 References

[1] H. A. M. Futaki, "Effects of various doping elements on the transition temperature of vanadium oxide semiconductors," *Japanese journal of Applied Physics*, vol. 8, no. 8, p. 1008, 1969.

[2] A. Krammer, F. T. Demière and A. Schüler, "Infrared optical properties of doped and pure thermochromic coatings for solar thermal absorbers," in *Proceedings of SWC2017*, 2017.

[3] M. E. Uslu, I. B. Misirlioglu and K. Sendur, "Crossover of spectral reflectance lineshapes in Ge-doped VO2 thin films," *Optical Materials*, vol. 104, p. 109890, 2020.

[4] V. N. Andreev, B. P. Zakharchenya, Y. S. Kapshin, V. A. Noskin and F. A. Chudnovskil, "Low-frequency noise in vanadium dioxide undergoing a metal–semiconductor phase transition," *The Journal of Experimental and Theoretical Physics (English translation)*, vol. 79, p. 1353, 1980.

[5] Z. Topalian, S. Y. Li, G. A. Niklasson, Granqvist, C. G. and L. B. Kish, "Resistance noise at the metal–insulator transition in thermochromic VO2 films," *Journal of Applied Physics*, vol. 117, no. 2, p. 025303, 2015

[6] Micrux Technologies, "Thin-film InterDigitated Electrodes," ED-IDE1-Pt Thin-film Platinum InterDigitated Electrode [Online], 2020. Available: https://www.micruxfluidic.com/en/electrochemical-solutions/thin-film-electrochemical-sensors/interdigitated-electrodes-ide/. [Accessed 5 February 2023].

Appendix A

Technical Information on the SPT-320 Magnetron Sputtering System and the Purpose-built Optoelectronic Characterization System

A.1 Process Flow of SPT-320 Magnetron Sputtering System

Figure A.1 shows the process flow chart of the Plasmionique SPT-320 magnetron sputtering system. The control system consists of an SV-42 Power distribution box, a computer, two DC power supplies (DC1 and DC2) three RF power supplies (RF1, RF2 and RF3), a TV1 control, a control box (CO-42A), and a heater box (HC-42).

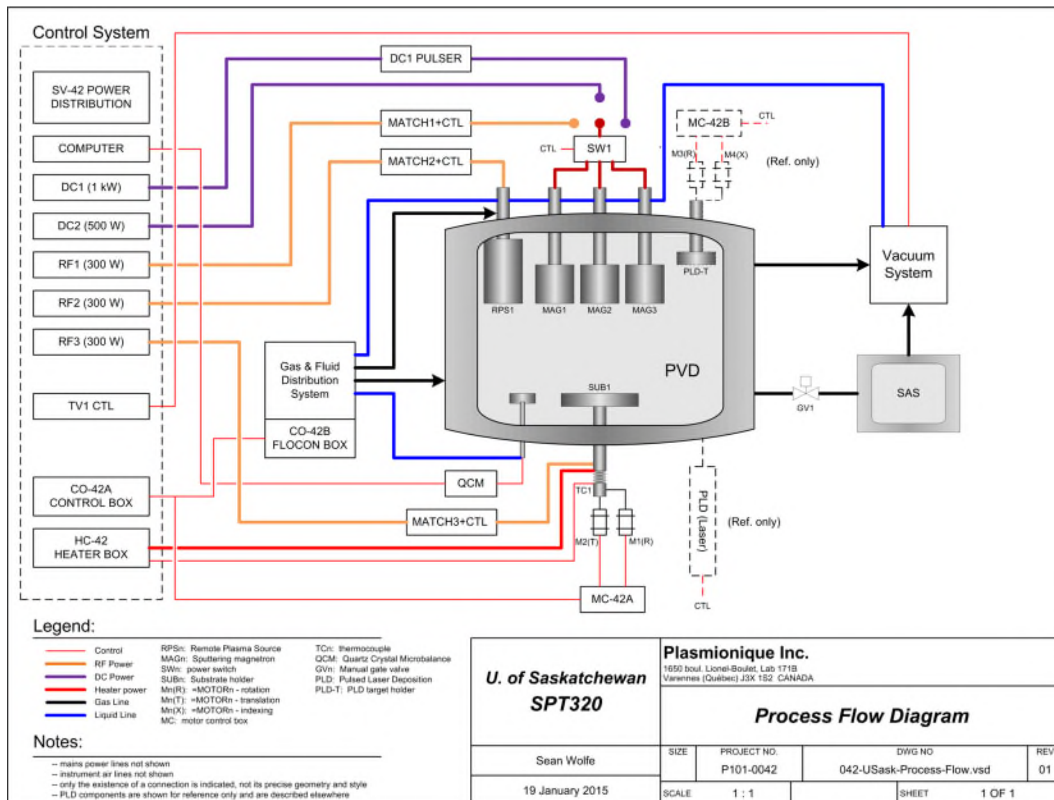

Figure A.1 Process flow diagram of SPT-320 magnetron sputter deposition system produced by Plasmionique Inc. for the Department of Mechanical Engineering at the University of Saskatchewan.

A.2 Technical Details of the Optoelectronic Characterization System

A.2.1 Electrical Circuitry for Constant Current Application

Figure A.2 shows the electronic circuit that was built to measure the *I-V* characteristics of VO_2 thin films. The input to the circuit is a rectangular waveform in time. The circuit with operational amplifier (opamp) O1 functions as a constant current generator in which the current depends on the input voltage generated by an Analog Discovery 2 waveform generator (AD2-WFG). As a result, the sample is driven by a constant current (in the range between 100mA to 500mA). The applied current is limited by a 100 Ω, 3W–current limiting resistor (R9 in Figure A.2) where the 60V DC voltage line reaches the sample. This resistor limits the current through the sample to 0.6 A and is meant to protect the sample from destruction in case of failure in the current generator circuit. The voltage drop across the sample is the difference between Output1 and Output2. The current through the sample is V_{input}/R_4.

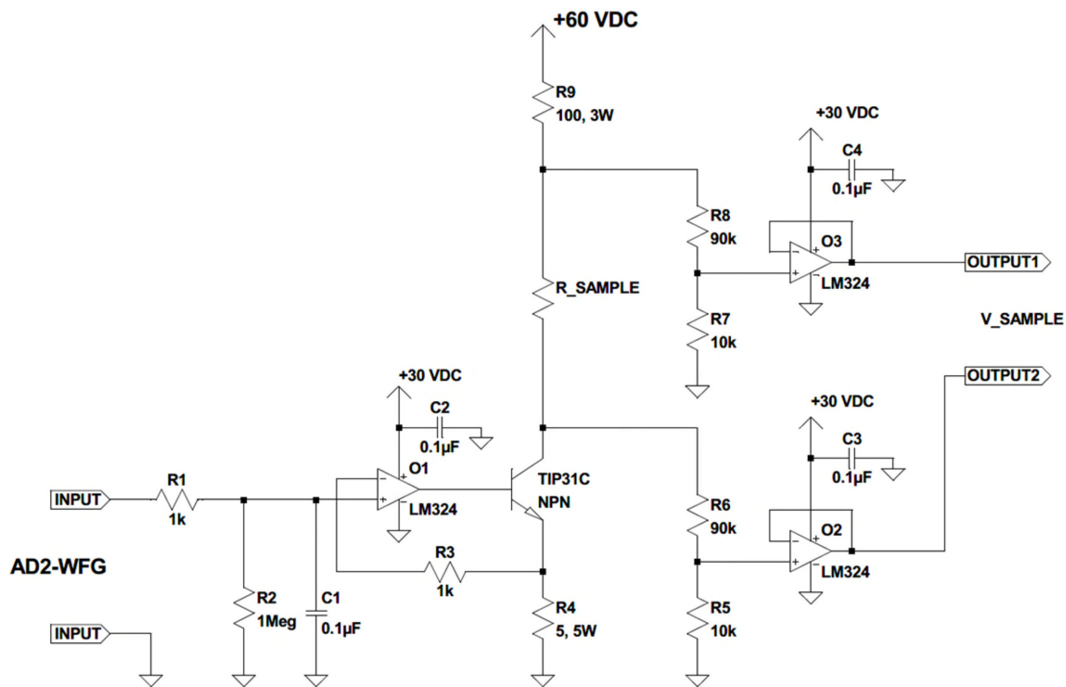

Figure A.2 Electrical circuit designed to pass constant current through a VO_2 film.

The signal generated by the Analog Discovery 2 waveform generator (AD2-WFG) is fed into an opamp-bipolar circuit that functions as a constant current source. The input voltage V_{input} is the signal from the AD2 waveform generator. The opamp/bipolar transistor circuit is designed

so that the output current is given by V_{input}/R_4. The output from the opamp $V_o = A(V_p - V_n)$. The current in the collector of the bipolar transistor is I_o. The voltage across R_4 is fed back to the negative input of the opamp to provide negative feedback. Thus $V_n = R_4 I_o$. Thus,

$$V_o = A\left[V_{input} - I_o R_4\right]$$

and since A is very large (100 dB),

$$I_o \approx \frac{V_{input}}{R_4}$$

It can be seen that the constant current that is generated through the sample depends on the input voltage from AD2 divided by R_4.

A.2.2 Photodiode Circuitry for Observation of Optical Transmittance

Figure A.3 shows the photodetector circuit used to detect the light passing through the sample. It uses an InGaAs photodetector that responds in the IR region of interest (1550 nm). The objective is to measure the relative change in the transmitted light intensity rather than the absolute value. During the experiments, the position of the sample, the photodetector and the light source (1550 nm-laser diode) are aligned and maintained fixed.

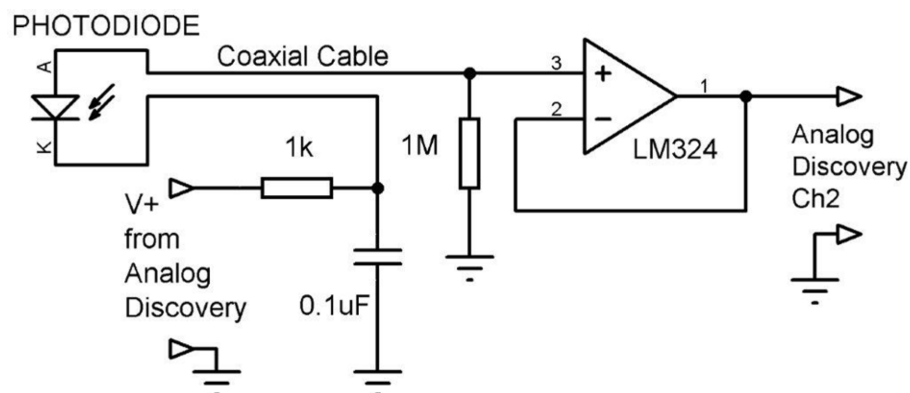

Figure A.3 The circuit used to measure the transmittance of VO_2 thin films. The light incident on the photodiode produces a photocurrent that is fed into a large load resistor, which is 1 MΩ. The photocurrent and hence the voltage across the load resistor is a function of incident light power, light wavelength, and responsivity.

The responsivity is a measure of the sensitivity of the photodiode to the incident light power; it is the ratio of the photocurrent to the incident light power. A 1 MΩ-load resistor is used to convert the photocurrent to voltage. The voltage signal is coupled, through a voltage follower, into one of the channels of a Digilent AD2-WFG. The waveform is then recorded, stored, and displayed by using Waveforms 2015 software. The change in the voltage reading from the photodiode is interpreted as the change in transmitted light intensity. The applied reverse bias to the photodiode was 5V.

A.2.3 Electrical Circuitry for Temperature Measurement

Figure A.4 shows the circuit used to measure the temperature of the sample. The temperature sensor is a small 100 Ω-platinum thermistor (Pt-100, with TCR 3851 ppm/°C) and the thermistor is attached to the back side of the sapphire substrate. The 0.5 mm-thick c-cut sapphire substrate has good thermal conductivity (23.1 parallel to the optical axis, 25.2 perpendicular to the optical axis[10]) so the VO_2 film and the substrate are assumed to be at the same temperature. The resistance of the Pt-100 thermistor changes with temperature. A calibration curve was obtained

[10] https://www.advaluetech.com/technical-single-crystal-sapphire. (Accessed on 5 February 2023).

that related the resistance of the Pt-100 thermistor to the temperature of the sapphire substrate. Since we need to measure the resistance of the Pt-100 thermistor during the experiments, a constant reference voltage of 4.096 V was used with a large resistor (5000 Ω) to pass an approximately constant current (≈ 4.096 V/ 5000 Ω) through the thermistor. This value of the current is small enough to prevent the self-heating of the Pt-100 thermistor. The voltage drop across the resistor is amplified 31 times by the non-inverting amplifier built with LM324 and recorded by the Analog discovery module. The voltage across the thermistor is proportional to the resistance of the thermistor and this voltage was then amplified and fed into one of the channels of the logger. The temperature data is acquired by an AD2-WFG logger and saved in a Labview program.

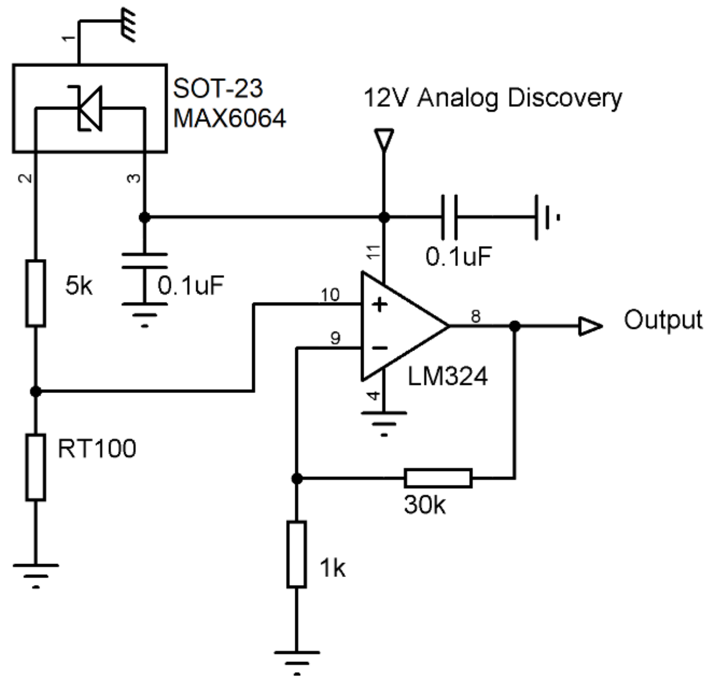

Figure A.4 The circuit used to measure the temperature of the VO_2 sample.

A constant reference voltage is obtained from an IC SOT-23 MAX6064. This IC provides a reference voltage of 4.096 V. The voltage reference IC is powered by applying +5 V from a Digilent Analog Discovery voltage supply. An approximately constant current, 4.096 V/5000 Ω is passed through the thermistor so that the voltage across it is proportional to its resistance. As the resistance of the Pt-100 resistor changes, the voltage at the non-inverting input changes. The signal

is converted to temperature with the use of an $R(\Omega) - T(°C)$ calibration curve and saved in a Labview program.

Figure A.5 (a) shows an image of a Digilent Analog Discovery 2, a multi-functional instrument. The electronic core of the instrument is the Xilinx® Spartan®-6 FPGA (XC6SLX16-1L). The instrument consists of various devices which includes a two-channel oscilloscope, a two-channel arbitrary function generator, a stereo audio amplifier, a 16-channel digital logic analyzer, a 16-channel pattern generator, two programmable power supplies (0…+5V, 0…-5V), a network analyzer etc. More information about the feature of this instrument can be found on the company's website[11]. Two scope channels were used to read the change in VO_2 sample resistance and optical transmittance for self-heating measurements explained in Chapter 8. An additional Digilent Analog Discovery 2 to read the sample temperature which was recorded in a Labview program shown in Figure A.8. Figure A.5 (b) shows the block diagram of Digilent analog discovery 2.

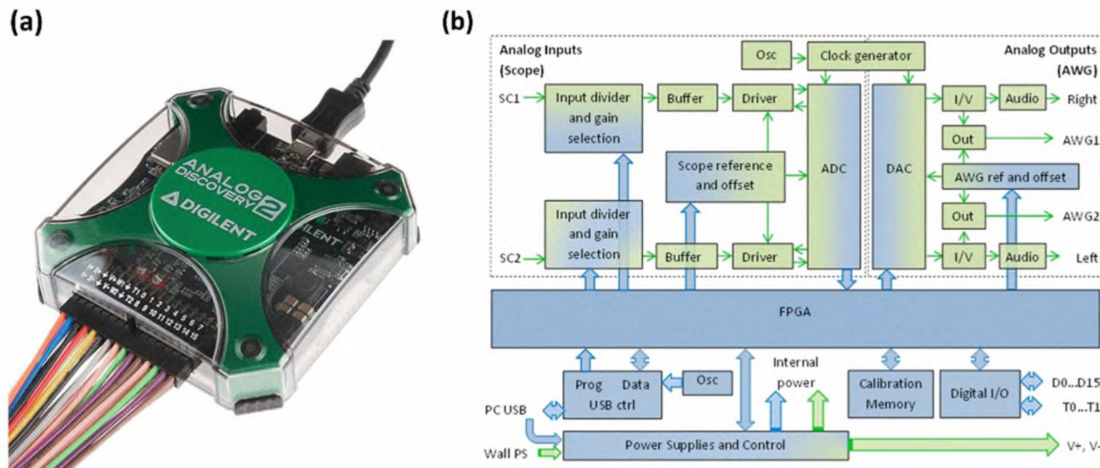

Figure A.5 An image of a Digilent Analog Discovery 2. (b) A block diagram of the Digilent Analog Discovery 2.

The experimental procedure can be explained as follows:

[11] https://digilent.com/reference/test-and-measurement/analog-discovery-2/reference-manual. (Accessed 5 February 2023).

1) 1550 nm laser diode would be enabled, positioned and fixed on a rail, which enables the light to pass between the two coplanar electrodes deposited on the VO_2 film.

2) During the experiments the system would be covered with a box to isolate the system from the variation of the ambient temperature and undesirable airflow.

3) The VO_2 sample would be heated up to 330 K (near IMT) temperature setpoint by use of a Labview program that commands an Omega® CN16Pt-330 PID controller and a DC power supply.

4) Once the temperature reached the setpoint, the PID control was disabled. By use of a Labview program, the DC power supply would be kept enabled to supply the heating unit as the PID command was disabled.

5) A square pulse of selected amplitude was applied, the amplitude and duration of which were controlled by Analog Discovery 2 software (Waveforms 2015).

6) The signals representing sample transmittance, resistivity and temperature would be logged and saved in the associated software programs and extracted for analysis.

7) After the pulse, the sample temperature would recover back to the initial setpoint temperature since the heating unit would still be supplied by the DC power supply.

A.2.4 Labview Programs

There are two Labview programs that were used simultaneously for measurements:

1) One was used to regulate the substrate temperature by controlling an Omega® PID temperature controller which regulates the heating of the sample through a DC voltage supply. The program controls the power supply DPD4304 to keep the temperature constant. The power supply powers the heater (PR1 given in Figure 8.1). The other Pt-100 resistor (PR2 given in Figure 8.1) is connected to the Omega® temperature controller, and the program reads the temperature from the controller through the USB port. Note that the controller does not control the temperature, instead it acts as a thermometer.

2) The other Labview program is created to read the substrate temperature during the measurements.

Figure A.6 shows the waveform chart that displays the substrate temperature reading with a setpoint temperature stabilized at 330 K (57 °C). Two COM posts are used to communicate with the GW Instek GPD4304 DC voltage supply and the Omega® PID controller. The control loop parameters (loop time, proportional, integral and derivative coefficients) are optimally set which the heating/cooling of the sample flows a linear ramp to a certain setpoint (desired temperature). As given in the figure, near the “Stop” button, different outputs are defined for these parameters for the current iteration of the PID loop. These outputs are used for tuning the temperature controller. With the optimal PID parameters set, the program is able to control the temperature of the system. The desired setpoint is set after determining the optimal PID parameters.

The “Output” displays the current power supply output voltage. The “Error, C” shows the difference between the set point and the “PV, C” (process value) gives the current sample temperature. The “Exit” button is used to exit the program while leaving the voltage supply on at a constant value to keep the substrate temperature steady around the setpoint of 330 K. Once the “Stop” button is clicked the program is disabled. However, with the “Exit” button on, a constant supply voltage is left on to keep the substrate temperature around 330 K.

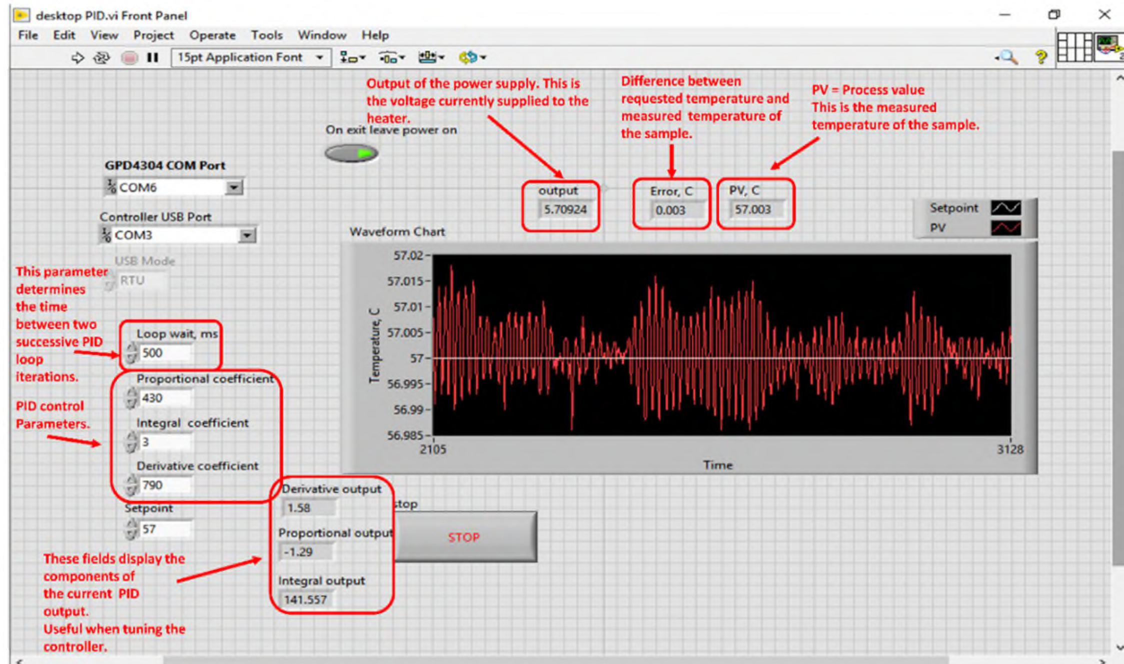

Figure A.6 The front panel of PID control. GDP4304 COM Port is used to communicate with the GW Instek GDP4304 DC voltage supply. COM3 port is used to communicate with the Omega® PID temperature controller.

Figure A.7 shows the block diagram of the Labview program used to regulate the substrate temperature. The PID software can be explained as follows. First, communication with the power supply (GDP4304) is established. Also, communication with the Omega® PID temperature controller is established to monitor current temperature reading. The temperature reading coming from the Omega® PID controller is used as an input to be displayed in the front panel of the Labview program. When the program is activated the PID parameters are delivered to the GDP4304 DC power supply. The PID output is a number with magnitude and sign depending on the magnitude and the sign of the difference between the real sample temperature and the set point. In this setup the maximum power is limited to 1 W to avoid damage to the Pt-100 thermistor, in which the usable range output voltage from the DC power supply is between 0 – 10 V. Also, in this setup, the PID regulation range was set to ± 1000 (PID output). Thus, a number larger than + 1000 should cause the heater to work with the full power of 1 W (output voltage 10 V) and a number smaller than - 1000 should turn the heater off (set the power supply output voltage to 0 V). That is done by the true case of the case structure. The calculations around the false case of

the same case structure map the - 1000 to + 1000 range of the PID output to 0 to 10 V range of the output voltage of the power supply. Thus, - 1000 corresponds to 0 V, + 1000 corresponds to 10 V, and the PID output of 0 corresponds to 5 V. The negative numbers are mapped to the range 0 – 5 V and the positive numbers to the range 5 – 10 V.

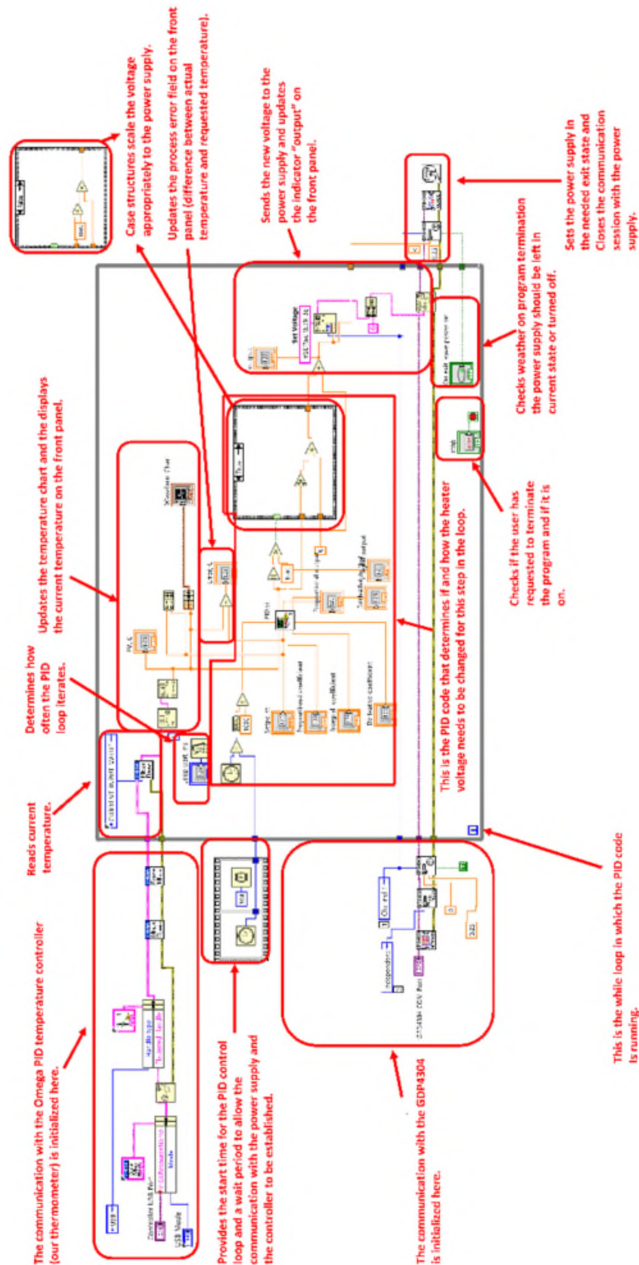

Figure A.7 Block diagram of the Labview program used to control the substrate temperature.

Before entering the loop, the program establishes communication with the Omega® PID controller and with the power supply these are the sections at the bottom of the while loop. Similar section on the top of the while loop closes the communication with the controller. In the loop, the program reads the current temperature and determines what corrections need to be applied to the output voltage of the power supply. Then, it communicates with the power supply to update the voltage value and also update the display shown in Figure A.6.

Figure A.8 shows a test run of the substrate temperature measurement of VO_2 film stabilized around 303 K (60 °C). The acquisition time is adjusted for 20 s. Pre-trigger time is adjusted to 2 s and the sampling rate is 400.

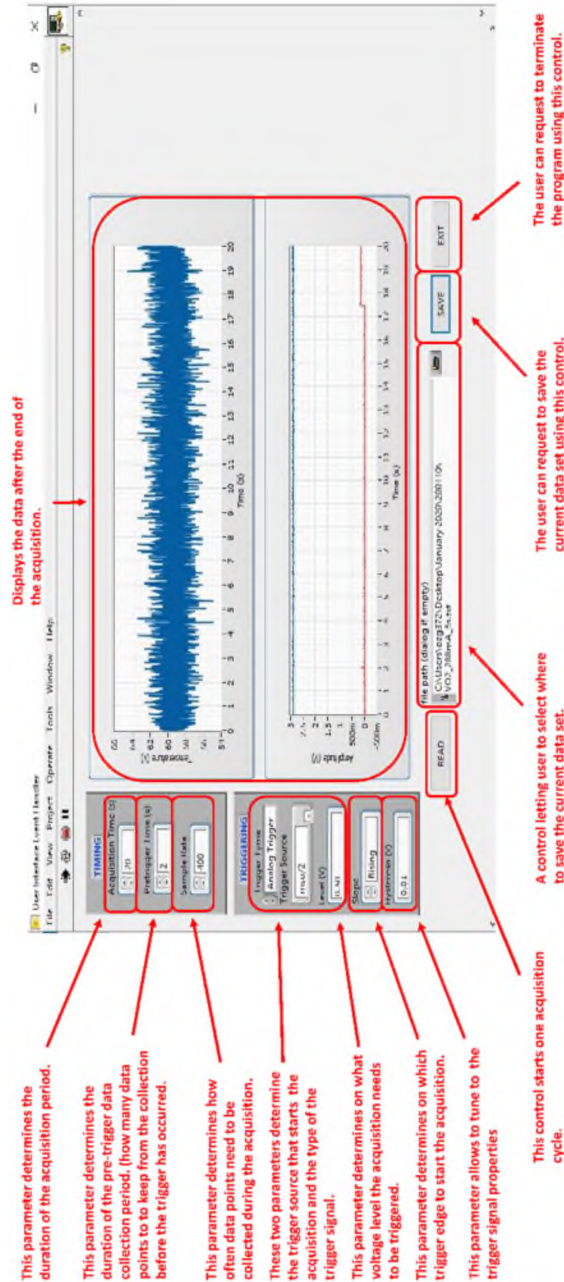

Figure A.8 The user interface of the Labview program is used to measure the substrate temperature (top reading). Significant noise in the temperature reading, which is inevitable, may be due to the vibrations coming from the temperature measuring circuit. The bottom reading (red data) shows the voltage across a 5 Ω-5 W resistor connected in series to the VO_2 film.

A.2.5 Waveforms 2015 – Digilent Analog Discovery2 Software

Figure A.9 illustrates a square five-second (5 s) current pulse which is set in the waveform generator bar in Waveforms 2, software of Digilent Analog Discovery 2. The software has multiple channels of monitoring signals or applying a waveform. Such options are scope, logger, supplies, and waveform generator. In the scope, the applied pulse across the sample is monitored. The logger is used to monitor the resistance and transmittance reading. The supplies tool is used to supply + 5 V through the Digilent Analog Discovery module to the voltage reference used. The waveform generator is used to apply a square current pulse to the sample.

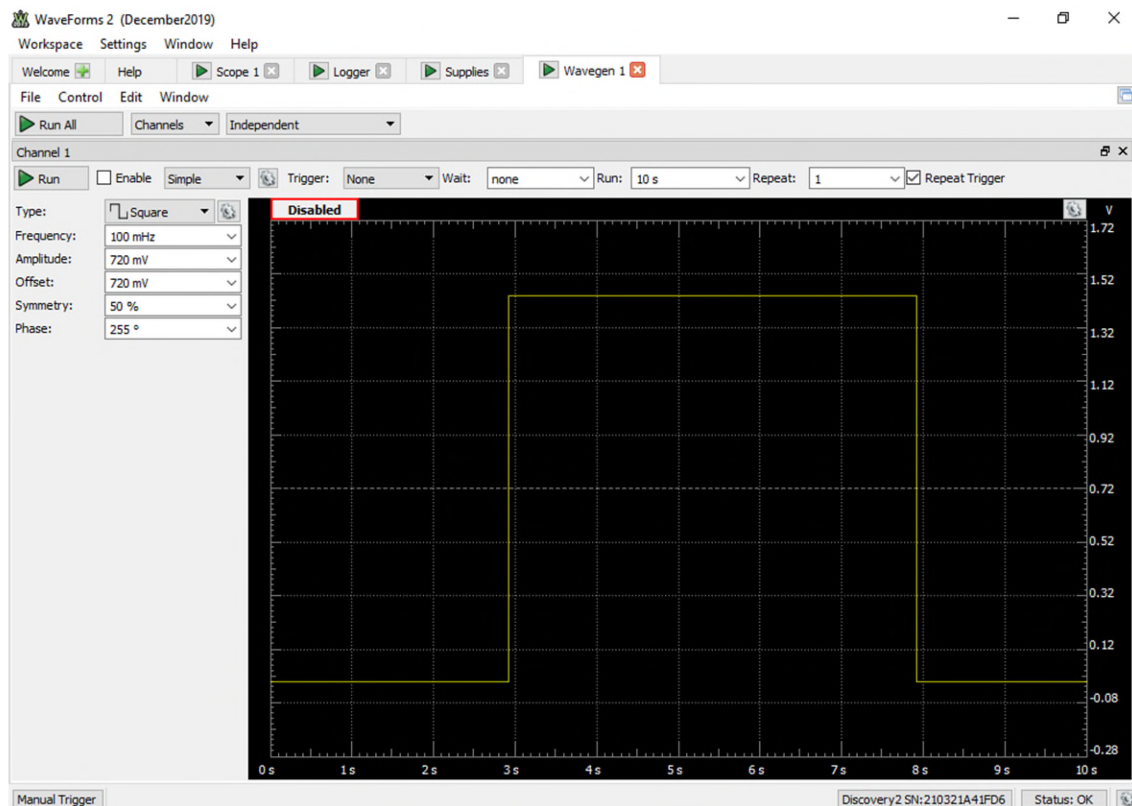

Figure A.9 Square pulse of a total amplitude of 1.5 V set to generate 300 mA with a 5 s-pulse period.

Figure A.10 shows the scope window in the Waveforms 2015 software. The defined pulse in Figure A.9 is applied for only one run using the "Single" button. Before applying the square (DC) pulse, the amplitude and the pulse duration are set in the "Wavegen1" given in Figure A.9. The "Run" button "arms" the Analog discovery to apply the pulse. By pressing the "Single" button

given in Figure A.10 the pulsing is enabled for one single run. Hence, the application of the pulse and the change in optical transmittance and the voltage across the sample are monitored within a defined time range.

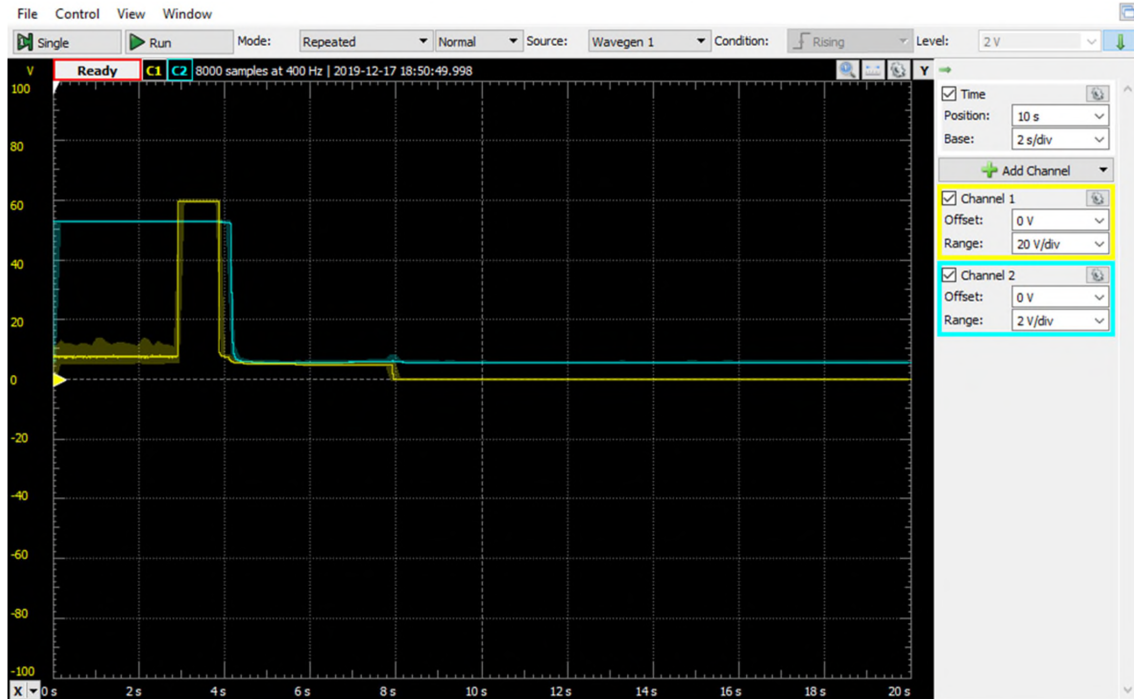

Figure A.10 Scope panel was used to monitor the change in optical transmittance (blue) and voltage reading across the sample (yellow).

Appendix B

Mapping of IMT and MIT transitions using Raman spectroscopy

Figure 6.14 and Figure 6.15 clearly show the disappearance of the Raman signal during the insulator-to-metal transition. Therefore, a zero Raman signal can be taken as a criterion for the full conversion of VO_2 into the metallic state. Figure B.1 (a) shows that for large signals coming out of the 25 × 25-pixel array, this criterion is quite reliable. However, for an individual pixel, the interpretation becomes more ambiguous during IMT as the Raman signal decreases and eventually "sinks" into the electronic noise as shown by Figure B.1 (b) – (d). Hence, the question arises of the definition of the "zero signal" in the presence of noise. To answer this question, we developed a special statistical procedure. For all spectra (for every pixel at every temperature) we calculated correlation coefficients (CCs) using the spectrum shown in Figure B.1 (a), i.e., spectrum corresponding to the guaranteed semiconducting state.

The results of these calculations are presented in Figure B.2 in the form of histograms. As one can see at 24 °C (well below IMT), the histogram is a narrow peak spreading from 0.60 to 0.77 which indicates the presence of a strong correlation. Meanwhile, at 90 °C (well above IMT), the histogram becomes broader and spreads from 0.11 to 0.24 showing the absence of correlation. Comparing these results, we can conclude that all pixels with a CC > 0.60 show predominantly semiconducting properties, while the pixels with CC < 0.24 are predominantly metallic.

It is worth noting here that the maximum of the histogram at 24 °C is at 0.69, and at 90 °C it is at 0.08. At intermediate temperatures, the maxima of histograms fall within the 0.69 – 0.08 interval with their position depending on sample thermal prehistory (heating or cooling) as shown in Figure B.2 for 65 °C measurements. For pixels undergoing IMT/MIT, i.e., containing a mixture of metal and semiconductor phases, we offer another criterion that allows us to define the dominance of a certain phase. We have created an "artificial mixture" of 50% semiconductor and 50 % of metal by summing in equal proportion spectra measured at 24 and 90 °C. We have calculated the CCs of these spectra with base spectrum from Figure B.1 (a) and we have found the

average value of the CCs to be equal to 0.55. This way we were able to create the following scale for mapping insulator-to-metal and metal-to-insulator transitions of VO_2 using Raman spectroscopy:

(i) CC > 0.60, semiconductor phase

(ii) 0.60 > CC > 0.55, more semiconductor than metal phase

(iii) 0.55 > CC > 0.24, more metal than the semiconductor phase

(iv) CC < 0.24, metal phase

The results of the mapping are shown in Figure 6.15.

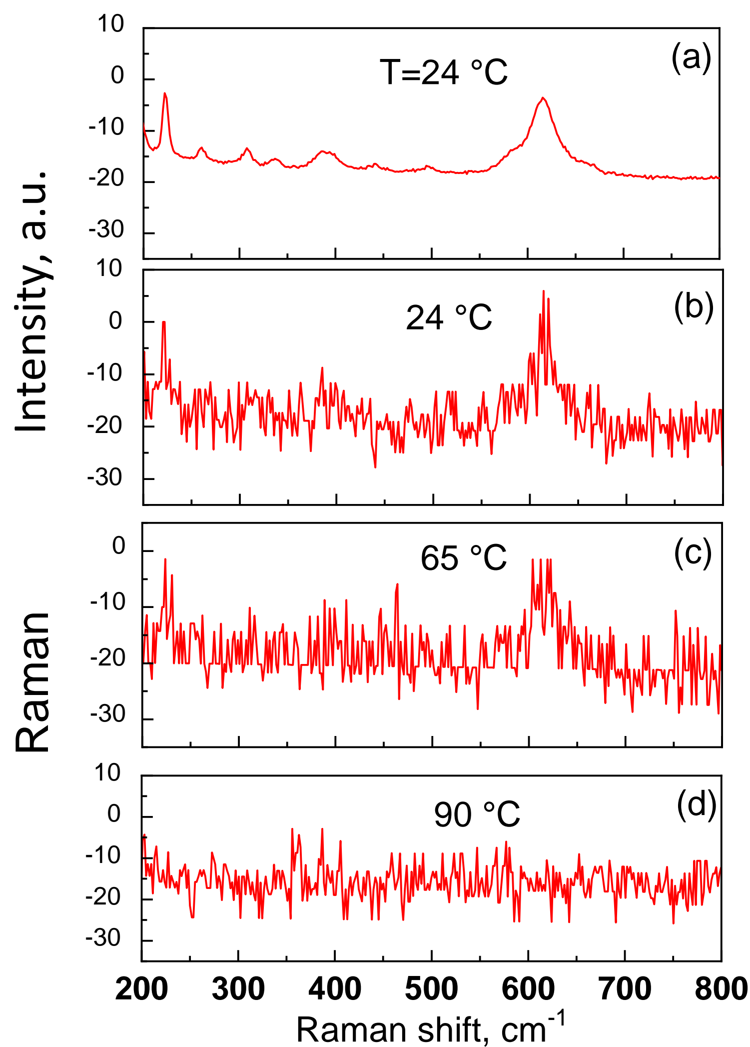

Figure B.1 (a) Raman spectrum measured for an array of 25 × 25 = 625 pixels at 24 °C. (b) – (d) Typical Raman spectra collected at different temperatures for an individual pixel as it undergoes a transformation from semiconducting (b) to metallic (d) phase.

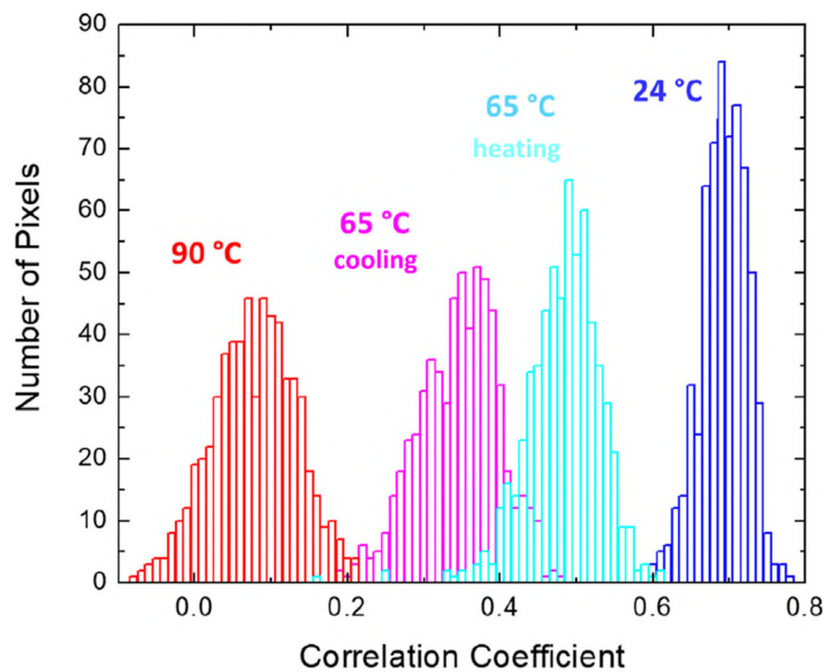

Figure B.2 Histograms of correlation coefficients (CC) of the Raman spectra in Figure B.1, measured at different temperatures.